

**PROBES OF QUARK MATTER FORMATION IN
HIGH ENERGY ^{16}O - NUCLEUS COLLISIONS**

Yves Sirois

**Physics Department
McGill University, Montreal**

**A thesis submitted to the Faculty
of Graduate Studies and Research
in partial fulfillment of the
requirements for the PhD degree**

March 7, 1988

(c) Yves Sirois, 1988

— Abstract

I present the measurements, analysis and results obtained with the NA34 experiment at the CERN European laboratory, on the global characteristics of particle production in ultra-relativistic oxygen-nucleus collisions, at incident energies of 60 and 200 GeV/nucleon. The observed properties of the particle flow are analysed in the framework of phenomenological models inspired by quantum chromodynamics. From this analysis, novel information emerges concerning the mechanisms and space-time evolution of the soft-hadronic processes in short-lived extended volumes of matter at extreme densities and temperature. We consequently study the parameters and critical conditions under which nuclear collisions could allow the observation of a phase transition from hadronic matter towards a new state of deconfined quark-gluon plasma matter

Résumé

Je présente les mesures, analyses et résultats obtenus dans l'expérience NA34 au laboratoire européen du CERN, et concernant les caractéristiques globales de la production de particules dans les collisions ultra-relativistes oxygène - noyau à des énergies incidentes de 60 et 200 GeV/nucléon. Les propriétés observées du flot de particules sont analysées dans le cadre de modèles phénoménologiques inspirés de la chromodynamique quantique. De cette analyse découle une compréhension accrue des mécanismes et de l'évolution spatio-temporelle des processus d'interactions hadroniques molles dans un volume étendu de matière soumis temporairement à des densités et des températures extrêmes. Nous étudions finalement les paramètres et les conditions critiques pour lesquels les collisions nucléaires pourraient conduire à l'observation d'une transition de phase de la matière hadronique vers un plasma de quarks et de gluons déconfinés.

Preface

In this thesis, I present the results of a research conducted within the HELIOS Collaboration, an experiment of the first generation devoted to the study of extended volume of matter under extreme densities and temperature. This exploratory research is fundamentally motivated by the possibility of using ultra-relativistic nuclear collisions to create short-lived systems where hadronic matter would undergo a phase transition towards a new state of deconfined quark-gluon plasma matter. The installation of the HELIOS multi-purpose set-up started in 1984 in the north fixed target area of the Super Proton Synchrotron at the CERN European laboratory in Genève. The experiment (NA34) was fully operational in november and december 1986 for three weeks of data taking with incident oxygen ions of 60 and 200 GeV/nucleon, colliding on aluminium, silver or tungsten target nuclei¹. The design of the detectors and the corresponding choice of physics observables were largely dictated by the very complex nature of the nuclear collisions. These collisions involve a very large number of valence and sea quarks, and are dominated by soft-hadronic processes which are intimately connected to the confinement problem and thus outside the proper domain of perturbative quantum chromodynamics (QCD) applicability.

In a global strategy for the creation of a quark-gluon plasma in nuclear collisions and its unambiguous identification, one has to reach the appropriate critical initial conditions, demonstrate the achievement of some degree of thermalization in a system with fluid properties and, finally, measure signals directly probing the very nature of the hot and dense matter, or sensitive to the character of the phase-transition between quark matter and normal hadronic matter. The guidelines for the experimental selection of the most significant observables will emerge from the introduction chapter in which I will briefly review the theoretical expectations concerning the critical parameters, the nature of the phase transition and the probing signals. Moreover, I will insist on the necessity to understand the mechanisms by which the system develops a collective behaviour starting from the space-time evolution of the microscopic elementary interactions. The global characteristics of the energy and multiplicity flow will appear to be closely related to crucial thermodynamic variables such

¹ Throughout this thesis, following the universal practice of the high energy physics community, energies will be given in GeV ($1\text{GeV} = 10^9\text{eV} = 1.602 \times 10^{-13}\text{J}$), distances in fermi ($1\text{fm} = 10^{-15}\text{m}$), and cross-sections in barn ($1\text{b} = 10^{-28}\text{m}^2$). A complete list of equivalents in the SI (international system of metric units) can be found in the "Review of Particle Properties" by M. Aguilar-Benitez et al., Phys. Lett. B170(1986)1

as the initial energy density or the entropy.

In chapter 2, I will study the multi-particle production in "conventional" models for soft-hadronic interactions. These models will provide the "background" above which one hopes to find experimental evidence for new phenomena. There is no unique model to describe the mechanisms and evolution of the multiple soft processes within matter brought to extreme conditions, and one shall gain new information by comparing the observed properties of the particle flow with predictions made in the framework of various models, in particular the framework of QCD-inspired phenomenological models.

I will then show, in chapter 3, how the HELIOS experimental set-up addresses the various stages of our search for the quark matter. I will describe in some details the multiplicity and calorimetry detectors which were used as the main sources of information, and describe a spectrometer in which we performed individual particle identification over a limited solid angle. A particular attention will be given to the calorimeters for which I participated in general studies, reconstruction, and optimization of the performances.

The treatment of the 1986 ^{16}O -nucleus data and the associated correction procedures based on Monte Carlo simulations will be the subject of chapter 4. The presentation of the experimental results, their interpretation based on a comparison with microscopic models, and the discussion on the implications for the production of the quark-gluon plasma, will form the chapter 5. Conclusions will be presented in chapter 6.

The success of the experimental work presented in this thesis is the result of the effort of a large collaboration of which I would like to thank all members². The measurements were made possible by the dedication of the CERN technical staff who contributed to the superb performance of the PS-SPS accelerator complex, and by the support of the CERN DD division staff.

I am deeply grateful to my supervisor, Professor Claude Leroy of McGill University, for his invaluable, continuous and active support, and for his most appreciated constructive comments during the completion of this thesis.

I am indebted to Dr C W Fabjan, Dr W. Willis and our spokesman Prof. H. Specht for their encouragements and trust, and for many knowledgeable discussions. I express my gratitude to Dr R. Wigmans for his most fruitful collaboration in various calorimeter studies. I would like also to express my gratitude to Dr G. London and Dr J.P. Pansart for providing multichain Monte Carlo parton model data tapes.

² The complete list of members of the HELIOS Collaboration can be found in ref [126].

I would like to thank the National Science and Engineering Research Council of Canada, McGill University and the Carl Reinhart foundation for their financial support.

Finally, I would like to dedicate this thesis to my wife Louise for her invaluable continuous moral support and for her precious help in typing this manuscript.

Contents

Abstract	ii
Résumé	iii
Preface	iv
Chapter 1: Introduction: from colour confinement to quark matter	1
1.1 Strongly interacting matter at high density	1
1.2 The QCD-phase transition	2
1.3 Production and signals of quark matter formation in nuclear collisions	5
1.4 Space-time evolution of hadronic interactions in nuclear collisions	7
1.4.1 Critical initial conditions in the fragmentation regions	8
1.4.2 Critical initial conditions in the central region	11
1.4.3 Thermalization and expansion	14
Chapter 2: Models for particle production in ultra-relativistic nuclear collisions	19
2.1 Introduction	19
2.2 Nucleon collisions and global particle flow characteristics	20
2.3 Energy conservation and nuclear stopping power	26
2.4 Hadronic formation time	29
2.5 QCD-inspired multiple soft-hadronic interactions models	32
2.5.1 The Dual Parton Model	33
2.5.1.1 The Dual Parton Model for hadron-hadron interactions	33
2.5.1.2 Extension of the Dual Parton Model to hadron-nucleus collisions	39
2.5.1.3 The Dual Parton Model for nucleus-nucleus collisions	45

Chapter 3: Observables in HELIOS experiment	48
3.1 The hadronic and nuclear beams	48
3.2 Survey of the experimental set-up	49
3.3 The beam telescope and general trigger system	50
3.4 The silicon detectors for the charged multiplicity measurements	52
3.5 The 4π calorimetry	53
3.5.1 General description and mechanical properties	53
3.5.2 The absorbent, the readout, and the light collection uniformity	57
3.5.3 Signal handling and energy calibration	69
3.5.4 The calorimeter performances	76
3.5.5 The transverse energy flow trigger	80
3.6 The External Spectrometer	85
Chapter 4: Data reduction and analysis	86
4.1 The selection of ^{16}O – nucleus interactions	86
4.2 The differential transverse energy distributions	93
4.2.1 The E_T trigger efficiency	93
4.2.2 The subtraction of empty target contamination	95
4.2.3 The absolute normalization	97
4.3 The transverse energy pseudorapidity distributions	97
4.4 The Monte Carlo corrections on transverse energy flow	99
4.5 The multiplicity differential and pseudorapidity density distributions	102
4.6 Deconvolution of the differential cross-sections for finite resolution	109
Chapter 5: Experimental results and discussion	111
5.1 Introduction	111
5.2 Transverse energy production in ^{16}O – nucleus collisions at 60 and 200 GeV/n	112
5.2.1 The differential cross-sections $d\sigma/dE_T$	112
5.2.2 Qualitative features and geometrical parametrizations	119
5.2.3 The A -dependence of the transverse energy production	124
5.2.4 Fractional E_T density in pseudorapidity	126
5.3 Charged multiplicity flow in ^{16}O – nucleus collisions at 60 and 200 GeV/n	129
5.3.1 The differential cross-sections $d\sigma/dN^{\text{ch}}$	129
5.3.2 Fractional multiplicity density in pseudorapidity	133
5.4 Comparison with Monte Carlo multichain Dual Parton models	138

5.5 Estimate of energy density achieved for the 200 GeV/n data	145
5.6 Multiplicity dependence of the transverse momentum	148

Chapter 6: Conclusion	152
-----------------------------	-----

References	155
------------------	-----

Figures

1.	Energy density as a function of temperature in lattice QCD calculations.	3
2.	Phase diagram of nuclear matter.	4
3.	Schematic representation of a nuclear collision in the target nucleus rest frame.	8
4.	Phenomenological estimate of the initial energy density in fragmentation regions.	11
5.	Schematic representation of a nuclear collision in the center-of-mass frame.	12
6.	Measured average transverse momentum versus energy density.	16
7.	Predicted average transverse momenta versus energy density.	16
8.	Participating nucleons and inelastic scatterings in O - Pb collisions.	21
9.	Central rapidity multiplicity density versus the number of participants.	27
10.	Mean baryon rapidity shift and the stopping power of nuclear matter.	28
11.	The rapidity density of negatively charged particles in (p - Xe)/(p - p) collisions.	29
12.	Two chain diagrams for soft particle production in hadronic collisions.	35
13.	Predicted rapidity distribution of particles for a p - p collision.	37
14.	Four chain contributions in p - p interactions.	38
15.	Double-scattering diagram in a p - A interaction.	39
16.	Dual Parton Model comparison to p - A pseudorapidity distributions.	43
17.	MCFM predictions for the rapidity density ratio (p - Xe)/(p - p).	44
18.	DPM comparison to charged particles production in α - α collisions.	46
19.	Layout of HELIOS (NA34) experimental set-up.	49

20.	Block diagram of the trigger logic main components.	51
21.	Layout of the charged multiplicity detectors.	52
22.	Overview of the calorimetric components.	54
23.	Artist's view of the calorimetrized dipole magnet.	55
24.	Isometric view of a U/Cu/scintillator module	56
25.	e/h ratio and resolution for U/scintillator calorimeters.	60
26.	Optical spectra for butyl - PBD scintillating agent.	61
27.	Influence of the scintillators attenuation length on the resolution.	62
28.	Set-up for optical measurements,	63
29.	The light yield of an irradiated scintillator plate.	64
30.	Light attenuation curves for radiation damaged and undamaged plates.	65
31.	Uniformity of the light collection in a module tower.	66
32.	Schematic view of the set-up for calibration with cosmic muons.	67
33.	The optical quality versus uranium radioactivity doses.	68
34.	Attenuation of light along the wavelength shifters.	69
35.	Event-by-event correlation between electromagnetic and hadronic signals.	71
36.	Resolution and e/ π versus the gain ratio B/A.	73
37.	Measured versus incident energy for electromagnetic showers.	75
38.	The U/scintillator modules response to hadronic showers.	77
39.	The e/ π signal ratio as a function of energy.	78
40.	Single particle fractional energy resolution for a U/scintillator module.	79

41.	The μ/e signal ratio as a function of the incident energy.	80
42.	The splitting of the PM anode signal and the weighting resistors.	82
43.	Example of the performances of the energy flow trigger logic.	84
44.	Plan view of the external spectrometer set-up.	85
45.	Mass spectrum built from the measured total energy.	87
46.	The raw E_{tot} response versus E_{T}	87
47.	dE/dx plotted against E_{tot} for high- E_{T} events.	88
48.	Silicone-ring contribution to the empty target contamination.	89
49.	Correlation cuts in the (E_{T} , multiplicity) planes	91
50.	Ratio of the $^{16}\text{O} - \text{W}$ E_{T} distributions for various target thicknesses.	92
51.	Overlap of the dN/dE_{T} distributions for the various E_{T} thresholds.	94
52.	The (target)/(no-target) ratio of the $1/\text{flux } dN/dE_{\text{T}}$ distributions.	96
53.	Mapping of the calorimeter towers in pseudorapidity and azimuth.	98
54.	Average correction factors for the pseudorapidity density of E_{T}	101
55.	Raw E_{T} versus raw multiplicity	103
56.	The pulseheight distributions in silicon segments for high multiplicity events.	105
57.	Correction curves for the raw multiplicities	107
58.	Estimated true resolution functions for the charged multiplicity.	108
59.	Main steps of the deconvolution procedure for resolution corrections.	110
60.	Transverse energy distributions for $^{16}\text{O} - \text{nucleus}$ collisions at 60 GeV/n.	117
61.	Transverse energy distributions for $^{16}\text{O} - \text{nucleus}$ collisions at 200 GeV/n.	118

62.	Geometrical overlap cross-sections.	120
63.	Geometrical parametrization fits to the transverse energy.	121
64.	WNM and AQM fits of the E_T distributions.	123
65.	A - dependence of the E_T production.	125
66.	Distributions of the E_T density in pseudorapidity for $^{16}\text{O} - \text{W}$ collisions.	127
67.	Charged multiplicity distributions for $^{16}\text{O} - \text{nucleus}$ collisions at 60 GeV/n.	130
68.	Charged multiplicity distributions for $^{16}\text{O} - \text{nucleus}$ collisions at 200 GeV/n.	131
69.	Pseudorapidity distributions for central O - W collisions.	133
70.	The charged multiplicity pseudorapidity density distributions.	135
71.	The mean charged particles pseudorapidity versus E_T	137
72.	IRIS predictions for the $d\sigma/dE_T$ distributions at 200 GeV/n.	139
73.	Effects of the inclusion of a finite formation time on the $d\sigma/dE_T$ distribution.	141
74.	IRIS prediction for central O - W $dE_T/d\eta$ distribution.	142
75.	IRIS predictions for the $dN/d\eta$ distributions.	144
76.	$\langle E_T \rangle$ /charged particles versus E_T in central pseudorapidities.	149
77.	(+/-) particle ratio and mean momenta versus E_T	150
78.	p_T spectrum of negative particles in $^{16}\text{O} - \text{W}$ collisions.	151

Tables

1.	Calibration factors for the uranium modules.	74
2.	^{16}O - Al transverse energy differential cross-section.	112
3.	^{16}O - Ag transverse energy differential cross-section.	113
4.	^{16}O - W transverse energy differential cross-section.	114
5.	^{16}O - Al transverse energy differential cross-section.	115
6.	^{16}O - Ag transverse energy differential cross-section.	115
7.	^{16}O - W transverse energy differential cross-section.	116
8.	Parametrization of the $d\sigma/dE_T$ distributions.	122
9.	Target mass dependence of the E_T production.	128

Chapter 1

Introduction: from colour confinement to quark matter

1.1 Strongly interacting matter at high density

The fundamental theory of strong interaction is widely believed to be quantum chromodynamics (QCD), a theory of coloured quarks interacting with massless vector fields, the gluons. Although being very similar in spirit to quantum electrodynamics (QED), it differs in particular in the fact that there are three colours instead of one electric charge. Unlike the QED $e^{i\phi}$ gauge factors, the SU_3 transformations do not commute with each other. So gluons, unlike photons, are themselves charged. This leads to important differences in the way one performs charge renormalization. In QED, the virtual pairs screen the charge so that the effective charge increases as we get closer to a point charge. In QCD the result is inverted and the effective charge decreases, a behaviour called asymptotic freedom or antiscreening. There the lowest order interaction is just the one gluon exchange, while in the next orders the interactions are essentially modified due to vacuum and matter polarizations. The complicated field theory for the QCD vacuum presumably provides for the colour confinement: the absence of quarks and gluons in the observed physical spectrum.

Quarks and gluons are normally colour confined within hadrons. Absolute confinement implies not only that some work should be done to extract quarks from hadrons, but also that the work would be infinite, a fact taken into account in bag and string models. Due to asymptotic freedom, it is believed that asymptotically dense matter should be in a phase consisting of unbound quarks and gluons; a phase called the QCD (quark-gluon) plasma [1], in analogy with similar phenomena in atomic physics. Deconfinement in strongly interacting matter can be viewed as the QCD version of an insulator-conductor transition in atomic physics: at low density, quarks and gluons form colour-neutral bound states, and hence hadronic matter is a colour insulator. At sufficiently high density or temperature, the hadrons will interpenetrate each other and the colour antiscreening will lead to a phase transition from a colour insulator to a colour conducting plasma. Such extreme energy densities and temperatures have probably prevailed in the very early baryon free universe, about 10^{-5} sec after the big bang. A transition from the deconfined quark matter to deconfined singlet states occurred as the universe expanded and cooled down. There, the vacuum with its vanishing "dielectric" constant for the colour field was created and the primordial quark-gluon plasma condensed into colourless hadrons. In our cold universe quark matter may be formed in the

central regions of supernovas, which are submitted to sudden compression through gravitational collapse, or in the very high baryon density regions of the core of neutron stars.

1.2 The QCD-phase transition

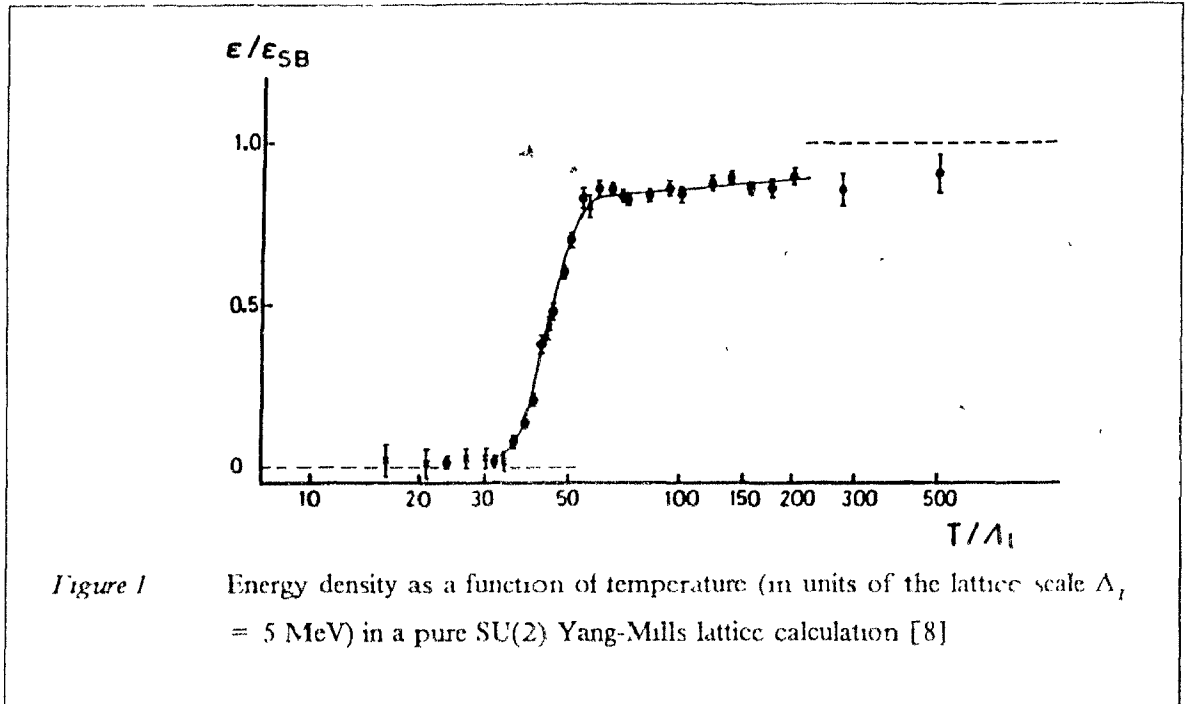
Within the framework of QCD, there is impressive evidence that a deconfinement phase transition from hadronic matter into the quark matter should occur at baryon number densities³ of $n = 5 - 10n_0$ and/or very high temperature $T \approx 150 - 220$ MeV (i.e. $\sim 2 \times 10^{12}$ °K) [2] [3]. Assuming the existence of quark matter and hadronic matter as an input, the two-phase nature of strongly interacting matter has been studied in a great variety of phenomenological models [4]. Such models are based for instance on the MIT bag model (see ref. [5] [6]), or they approach the phase transition either from the confined hadron matter (using the effective relativistic field theory [5]) or from the high temperature plasma phase (far enough from the non-perturbative effects of the transition region to make use of perturbative QCD [7] [5]). Nevertheless, the main quantitative information on critical parameters and the proof of the very existence of a phase transition have emerged from investigations within gauge theory on the lattice (see reviews in ref. [3] [6]). The lattice regularization of QCD has the unique advantage of offering the possibility to follow physical observables through the transition region, from absolute confinement to quark-gluon plasma. Besides, it fundamentally requires only Λ_{QCD} , the characteristic scale of QCD, as a "free" parameter.

The physical observable we are mostly interested in is the energy density ϵ . It is to be expressed in terms of thermodynamic variables, as a function $\epsilon(\mu, T)$ of the temperature T and the chemical potential μ . This function⁴ should exhibit a "discontinuity" at the phase transition for critical temperature T_c and/or chemical potential μ_c . In lattice QCD, the study of this function is unfortunately (at present) restricted to $\mu \equiv 0$. This corresponds to a situation where the net baryon number density is vanishing and only gluons and $q - \bar{q}$ pairs may be included. In practice there is severe and yet unsolved theoretical difficulties which hamper the inclusion of light quarks on the lattice [5]. The most significant results have thus been obtained for pure SU(N) Yang-Mills gluon matter. The applications of the lattice approach using SU(2) or SU(3) have been shown to give essentially the same results [4] [3] so that the more extensive Monte Carlo calculations have been performed with the smaller colour group. In all cases, one observes a rapid variation of the energy density and a sharp peak of the specific heat, which both signal the phase transition, at critical temperatures within an interval from $T_c = 150$ to 220 MeV. (One finds $T_c \sim 200$ MeV for SU(2)

³ $n_0 = 0.15 fm^{-3}$ is the nuclear ground state mean baryon number density

⁴ See ref. [6] for the detailed theoretical formulation.

and $T_c \sim 160$ MeV for SU(3).) The dramatic rise of the energy density ϵ in Figure 1 on page 3 corresponds to the many degrees of freedom being "liberated" and, at high T the energy density follows the Stefan-Boltzman ϵ_{SB} behaviour of a non-interacting gluon gas.



The introduction of fermions on the lattice has only been done in the "quenched" approximation where the quarks acquire a large mass $m_q \gg T_c$ so that an $1/m_q$ expansion converges. Despite this limitation, it has revealed the possibility of another distinct phase transition at high temperature where chiral symmetry would be restored. At the deconfinement transition the hadrons would melt into massive constituent quarks and massless pions and then, at the chiral phase transition, pions would disappear and leave a gas of massless quarks and gluons. The temperature separation between those two transitions and their nature (first order with large latent heat releases, or second order) is still under debate [2] [3]. With the inclusion of fermions on the lattice, the Stefan-Boltzman limit for the energy density is given by [6]

$$\epsilon_{SB} = \left(\frac{\pi^2}{15} \right) \frac{T^4}{(hc)^3} \left(N^2 - 1 + 7 \frac{NN_f}{4} \right)$$

Using this formula to estimate the critical energy density, we find for SU(3) with two quark flavours ($N_f = 2$) that a critical temperature of $T_c \sim 160$ MeV corresponds to a critical energy density of $\epsilon \sim 2.5 \text{ GeV}/\text{fm}^3$.

Very similar ϵ_c is obtained at $\mu = 0$ and finite T from simple two-phase phenomenological approaches based on the bag model [4], and also at $T = 0$ and finite baryon densities where one finds $\epsilon_c \sim 1-2 \text{ GeV}/\text{fm}^3$ with a broad phase coexistence region of the quark-gluon and hadron plasma [5].

Combining the actual knowledge on the critical parameters at finite temperature or finite baryon densities (see ref [6]), the phase diagram of nuclear matter could resemble that of Figure 2.

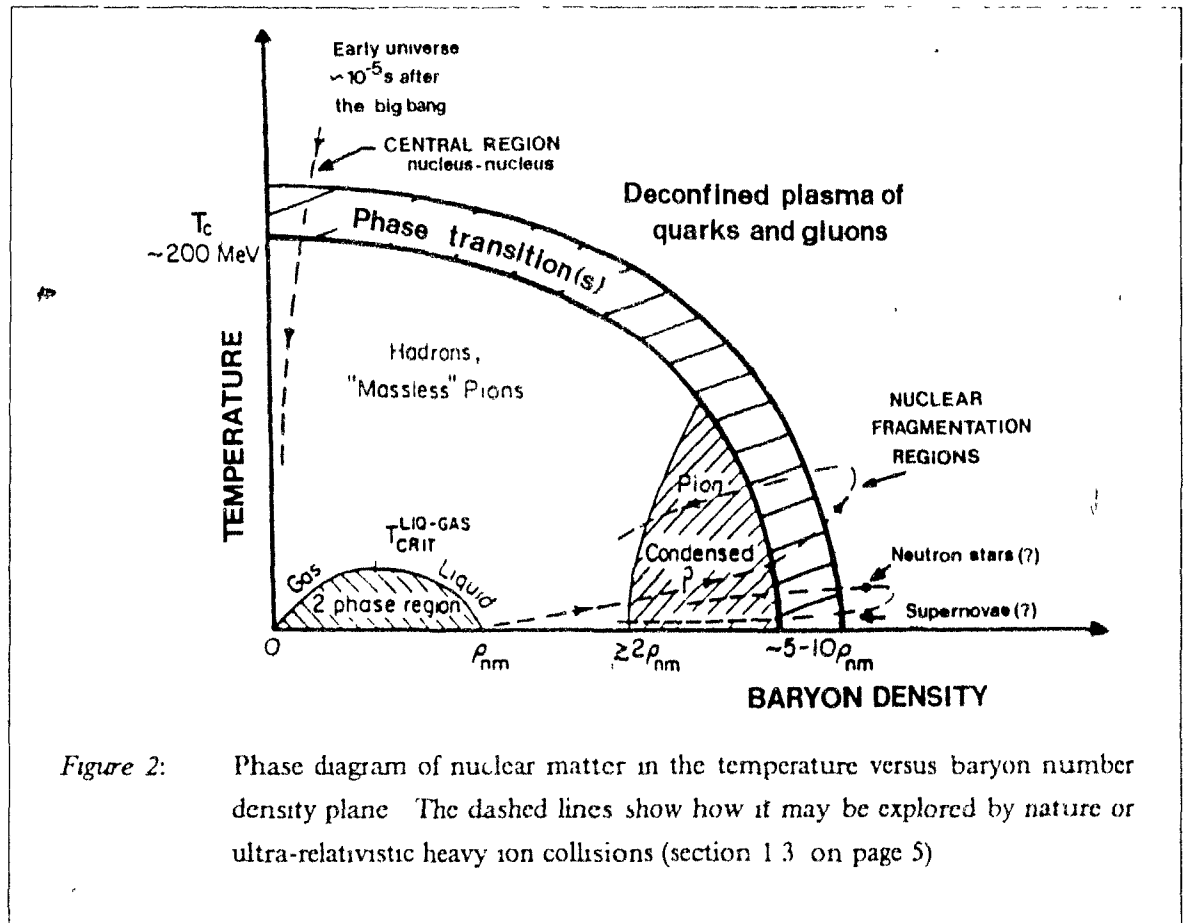


Figure 2: Phase diagram of nuclear matter in the temperature versus baryon number density plane. The dashed lines show how it may be explored by nature or ultra-relativistic heavy ion collisions (section 1.3 on page 5)

The confined hadron matter at low n_b and T will proceed through complicated phase transitions, as the energy density is raised to $\epsilon_c \sim 1-3 \text{ GeV}/\text{fm}^3$ with increasing n_b and/or T , towards deconfinement

1.3 Production and signals of quark matter formation in nuclear collisions

By compression and heating of cold nuclear matter, ultra-relativistic nucleus - nucleus collisions could allow the study of both low and high baryon number density hot matter. In these collisions, the beam and target nuclei fragments (together with some inelastically produced particles) form two hot dense fireballs presumably joined by a central hot firetube of mesonic matter. As will be seen in next section, critical densities and temperatures sufficient to produce short lived extended volumes of quark - gluon plasma matter are expected both in the fragmentation region [9], where the plasma is associated with large baryon density characteristic of the core of neutron stars, and in the central region [10] with small net baryon number, thus reproducing the conditions of the strong interaction physics which took place in the very early universe. The production of such a volume with a distance scale very large ($\gg 1$ fm) compared to the hadron size could be identified by the manifestation of collective phenomena and via direct probes, revealing novel non-perturbative aspects of QCD. Various signatures are suggested to recognize the formation of a deconfined state of matter in the fragmentation region or in the baryon free central region. The signals are related either to the transition between phases or they reveal some properties of the quark-gluon phase by which it can be distinguished from the hadron gas phase

Photons and leptons are considered to be amongst the best probes [11] for investigating the hadronic phases. They act as good thermometers of the initial hot quark - gluon plasma phase from where they mostly emanate. They probe the entire volume of the plasma, and due to their relatively small rescattering cross-sections compared to hadrons, they retain a memory of the plasma less confused by the expansion processes. Lepton pairs are emitted from inside the plasma by virtual photons. In this context, ordinary perturbative QCD Drell-Yan lepton pair production is the background for the electromagnetic radiation from the thermalized phases. The thermal radiation is expected to dominate for large Feynman x_F where the continuum would then give a measurement of the temperature of the plasma. Direct photons from quark bremsstrahlung also act as thermometers. For these, the background originates from QCD - Compton direct photon production. The dependence of the photon or dilepton emission on the pion multiplicity per unit rapidity allows us to determine whether the emission is due to hard processes or whether it is collective in nature [12]. The production from hard processes is independent of pion multiplicity whereas it increases quadratically with pion multiplicity for collective processes. This dramatic difference provides a clear test for collective behaviour but is mute about the degree of thermalization. If the mixed pion-quark phase lasts much longer than the pure QGP phase and extends over a larger region, it may be easier to observe such lepton signals from the mixed phase.

The correlation between identical particles measures the size and shape of the interaction volume. The large spatial extent of the pion-quark mixed phase should show up in pion interferometry experiments. Two or three particle correlations are also sensitive to the degree of phase coherence at freeze-out time when the particles are emitted.

The production of strange particles may provide information on the transient QGP [13]. If thermalization or chemical equilibrium is effective in the QGP, abnormally large abundance of strange particles, such as K , $\bar{\Lambda}$ and $\bar{\Sigma}$, is expected. In an environment rich in u or d quarks, Pauli's principle suppresses appearance of further $u\bar{u}$ and $d\bar{d}$ pairs relative to strange particles. Abnormally large antihyperons to antiprotons ratio or large $\bar{\Lambda}$ abundance should then result from the plasma hadronization. If the expansion rate is larger than the annihilation rate, large amount of strange quarks will survive the expansion and enhanced K/π ratio would be a good signal for QGP formation.

Another fundamental observable is the "melting" of resonances which was first discussed in terms of ρ and ω [14] but may be more striking for the J/ψ and ψ' [15]. Resonances can no more be formed in the plasma as the confinement bags are "melted" away by the Debye screening of the quark colour charge. In the high temperature QGP (at $T \sim 1.3 T_c$) the screening radius falls to 0.2 - 0.3 fm while, for instance, the J/ψ radius increases above 1 fm ($\geq 3 \cdot r_{J/\psi}^{(0)}$) so that $c\bar{c}$ bound states cannot exist. The suppression of the resonances will have to compete against $q\bar{q}$ recombination at the hadronization point in the mixed phase and in the pion gas. This is especially true for light resonances. For heavy mesons such as the J/ψ the contamination from $q\bar{q}$ recombination will be strongly reduced. During the time it takes for the evolution of the thermalized plasma towards the hadronization phases, the quarks and antiquarks of the lowest- p_T pairs created initially have been brought to large distance separation and they cannot recombine with each other. The c and \bar{c} quarks will hardly find the needed \bar{c} and c companions as the presence of these companions is thermally reduced by a factor e^{-m/T_c} . For a critical temperature of $T_c \sim 200$ MeV this implies that the J/ψ production via hadronization is reduced by approximately four orders of magnitude.

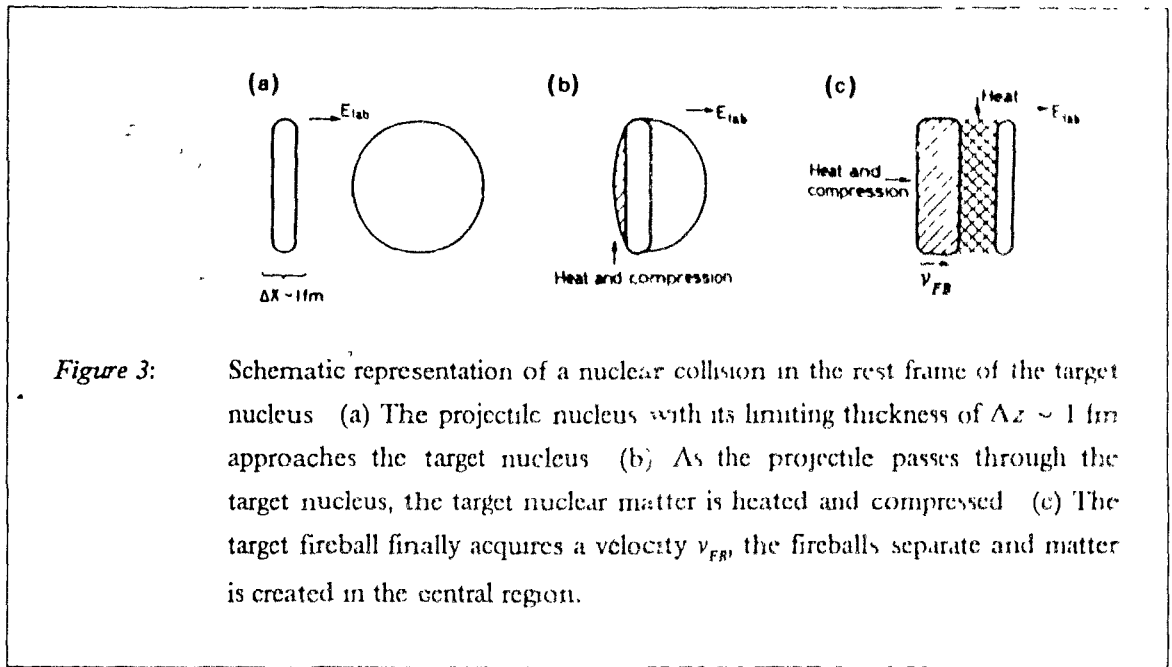
1.4 Space-time evolution of hadronic interactions in nuclear collisions

Precise theoretical quantitative estimate of the production rate of leptons and hadrons requires to understand the dynamics of the expanding quark matter. The space-time evolution of a nucleus-nucleus collision will generally depend on pre-equilibrium effects, initial conditions, transport scenario, hadronization and final state interactions. The fundamental stimulus for starting a detailed theoretical and experimental investigation of these questions came when one realized that ultra-relativistic nuclear collisions could allow the thermalization of large volumes of matter in which the critical conditions for quark-gluon plasma formation would be satisfied.

In the center of mass (c.m.) frame of a nucleon collision, the colliding nuclei form two Lorentz contracted pancakes approaching one another. As a consequence of the uncertainty principle, the pancakes cannot be contracted below a limiting thickness. This phenomenon arises because the nucleon's low longitudinal momentum degrees of freedom ($q\bar{q}$, gluons), which contribute to the nucleus wave function, cannot be resolved within a distance scale smaller than $\Delta z \sim \hbar/p_L$ (of order 1 fm). The collision between these two contracted pancakes will result in the formation of two hot receding fireballs with longitudinal momentum and baryon number close to that of the projectile or target nuclei (\equiv nuclear fragmentation regions). This nuclear transparency is due to Lorentz invariance and the uncertainty principle. The interactions of the incoming nucleons with the target nucleons, at rest in the laboratory frame, produce colour field chains linking the incident quarks to quarks of the target nucleons. The chains linked to fast forward moving ($p_L^{lab} \gg p_T^{lab}$) virtual fragments, which contain the quantum numbers of the valence constituents of the projectile pancake, will have no time to materialize while the incident nucleus is traversing the target nucleus. These chains have a proper formation time τ_0 , a consequence of the uncertainty principle, which is stoutly dilated to $\tau^{lab} \sim p_L^{lab} / p_T^{lab} \tau_0$. While the contracted incident pancake traverses the target nucleus, the incident nucleons, which have a mean free path in nuclear matter of order $\lambda_{nuc} \approx 1.6$ fm, will undergo several inelastic collisions when traversing, for instance, the 7.1 fm radius of a heavy target nucleus such as ^{208}Pb . The high momentum component of an incident nucleon's wave function will pass through the target nucleus largely unperturbed by the multiple inelastic collisions, and will travel with the beam fireball until hadronization. The eventual rescattering of the resulting secondary particles within the fireballs will play an important role in the thermalization of the energy in the fragmentation regions. The multiple scattering processes mainly involve the low momentum component of the nucleons wave functions, i.e. the quarks, antiquarks and gluons of the virtual cloud attached to the valence quarks, and remove relatively little energy from the fast forward moving valence fragments while giving rise to chains mostly populating the central region. These chains engender the formation of a hot firetube of mesonic matter [10] linking the fragmentation fireballs. Some of the low momentum components of the incident pancake scraped off by the target nuclei will remain "trapped" in the target nucleus and will heat the target fireball. It is this heating mechanism together with a nuclear shock compression, that contributes to the extreme energy density achievable in the fragmentation regions [9].

1.4.1 Critical initial conditions in the fragmentation regions

The heating and compression of the fireballs are better describable in the referential frame where the target nucleus is originally at rest. A central symmetric $A \rightarrow A$ collision is schematically represented in Figure 3.



We can estimate the magnitude of the shock compression suffered by the target nucleus by treating the projectile as a slab of negligible thickness sweeping the target nucleus at the velocity of light. The projectile scatters first on the closest encountered target nucleons. These target nucleons acquire a longitudinal velocity v_{FB} which is, on average, the velocity given to the target nuclear fireball. The second "row" of target nucleons will then be struck after the time interval it takes for the thin projectile slab to travel the average longitudinal distance that separates the first and second "rows". This implies, for a projectile with velocity $\sim c$, that the longitudinal separation between two nucleons is changed by $\Delta z = (1 - v_{FB}/c)z$. When the beam nucleus has traversed the target nucleus, the original radius $R_0 \sim 1.2 A^{1/3} \text{ fm}$ of the target nucleus has been compressed to $R_0(1 - v_{FB}/c)$ for a recoil compression of $\rho/\rho_0 = 1/(1 - v_{FB}/c)$ in the laboratory rest frame. The density of the target fireball in its rest frame, which is moving with a laboratory velocity v_{FB} , has thus increased by a compression factor:

$$\kappa \equiv \frac{\rho_{FB}}{\rho_0} = \frac{1}{\gamma_{FB} \left(1 - \frac{v_{FB}}{c}\right)} = \gamma_{FB} + (\gamma_{FB}^2 - 1)^{1/2} \quad (1)$$

In order to evaluate the effect of compression it is then sufficient to know the average velocity of the target fireball. Note that formula (1) can be further rewritten (omitting the speed of light constant, c , for convenience) in terms of the laboratory rapidity of the fireball by using $y_{FB} \equiv 1/2 \ln \{ (E + p_L)/(E - p_L) \}$ and $E = \gamma_{FB} \cdot m$ and the fact that for $p_L^2 \ll m^2$, $p_L \sim m \sqrt{(\gamma_{FB}^2 - 1)}$, which yields $\kappa \sim e^{y_{FB}}$

The evaluation of γ_{FB} for various colliding nuclei, has been performed in ref [9], where a detailed study of the heating's contribution to the energy density is also made. This study requires to identify the slow virtual fragments that have a chance to be trapped and may then transform their kinetic energy into heating of the fireball. The prescription in ref. [9] uses general arguments based on time dilatation, proper formation time, and known properties of hadronic fragmentation (assuming universality from high Q^2 data) for quantitative calculations. In order that a slow virtual fragment be allowed to materialize inside the target nucleus, it should have separated from his parent by a distance equal or greater than the QCD formation length⁵ $\tau_0 \sim \hbar/p_L \sim \Lambda_{QCD}^{-1} \sim 1$ fm. If this condition is satisfied at a time when the fragment is still inside the target nucleus, it may rescatter and emit its own tertiary fragments. For a fragment having longitudinal velocity $v \sim c$ emitted with p_L and p_T , the condition that it be separated from its parent by τ_0 before it escapes from the target nuclei sets a constraint on its transverse momentum

$$p_T \geq \frac{p_L}{R_0} (\tau_0) \quad (2)$$

Note that in terms of the fragment's rapidity, this condition is written $y \leq \ln(2 R_0/\tau_0)$, which reduces to (2) for $p_T^2 \gg m^2$. The condition that the fragment be still in the target nuclei further imposes a limit on the longitudinal momentum

$$p_L \leq m\kappa \frac{R_0}{\tau_0} \quad (3)$$

where m is an effective fragment-mass and κ is our compression factor. Using the constraints of equations (2) and (3), together with fragments momenta obtained by extrapolating structure functions from e^+e^- data, ref. [9] evaluates the equivalent total number of particles of different

⁵ If the separation is less than ~ 1 fm, the virtual fragment would be included as a parton excitation of the projectile. Such excitations are emitted only after the passage of the projectile through the target nucleus.

flavors trapped and the total energy M_{FB} trapped per incident nucleon.

Taking into account the compression and heating mechanisms, the initial energy density of the fireball in a symmetric A - A collision is simply expressed as

$$\epsilon_{FB} = \frac{A \cdot M_{FB}}{V_A / \kappa} = n_{nm} \cdot M_{FB} \cdot \kappa = n_{nm} \cdot M_{FB} \cdot e^{\gamma_{FB}} \quad (4)$$

where n_{nm} is the nuclear matter ground state baryon density, $n_{nm} \sim 0.15 \text{ fm}^{-3}$. The quantitative calculations [9] show that for A - A collisions at c.m. energies of $30 \text{ GeV} \leq \sqrt{s} \leq 70 \text{ GeV}$ with A varying from ^{56}Fe to ^{238}U : the recoiling target nucleons are relativistic and carry an average longitudinal momentum of $\bar{p}_l \sim 1.9 \rightarrow 2.4 \text{ GeV/nucleon}$, and 95 \rightarrow 97% of them are trapped; the pions carry $\bar{p}_l \sim 1.8 \rightarrow 3.8 \text{ GeV/nucleon}$ and 2.6 \rightarrow 3.5 pions/nucleon are trapped; there is only 0.1 \rightarrow 0.2 kaons/nucleon trapped, the target fireball is relativistic with $\gamma_{FB} \sim 1.7 \rightarrow 2.0$ ($\Rightarrow \kappa \sim 3.1 \rightarrow 3.7$) and it has trapped a total energy of $M_{FB} \sim 2.7 \rightarrow 3.6 \text{ GeV/nucleon}$. From these results we find using equation (4), an estimate for the energy density reachable in the fireballs of

$$\epsilon_{FB} \sim 0.15 \cdot (2.7 \rightarrow 3.6) \cdot (3.1 \rightarrow 3.7) \text{ GeV/fm}^3 \sim 1.3 \rightarrow 2.0 \text{ GeV/fm}^3 \quad (5)$$

Such energy densities are well within the region of the critical values required for the deconfinement phase transition. A useful approximate phenomenological formula for equation (4) is given in ref. [16].

$$\epsilon_{FB} \sim \beta \cdot n_{nm} \cdot (2A^{1/3} - 1) \text{ GeV/fm}^3 \quad (6)$$

where β is a parameter of order one. In the general case of a central collision between uneven nuclei $A \rightarrow B$ with $A < B$, equation (6) becomes

$$\epsilon_{FB} \sim \beta \cdot n_{nm} \cdot \left\{ 1 + 2 \left(B^{1/3} - \frac{B^{1/3}}{A^{1/3}} \right) \right\} \text{ GeV/fm}^3 \quad (7)$$

The predictions of equations (6) and (7) are shown in Figure 4 on page 11 for A - B collisions with $A = B$ and $A = ^{16}\text{O}$, together with the quantitative estimates of ref. [9].

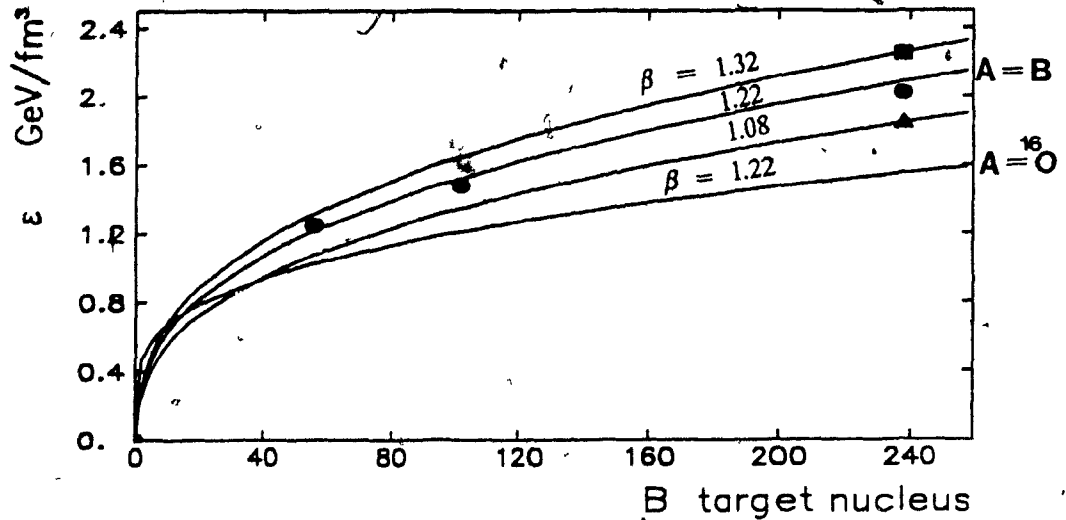
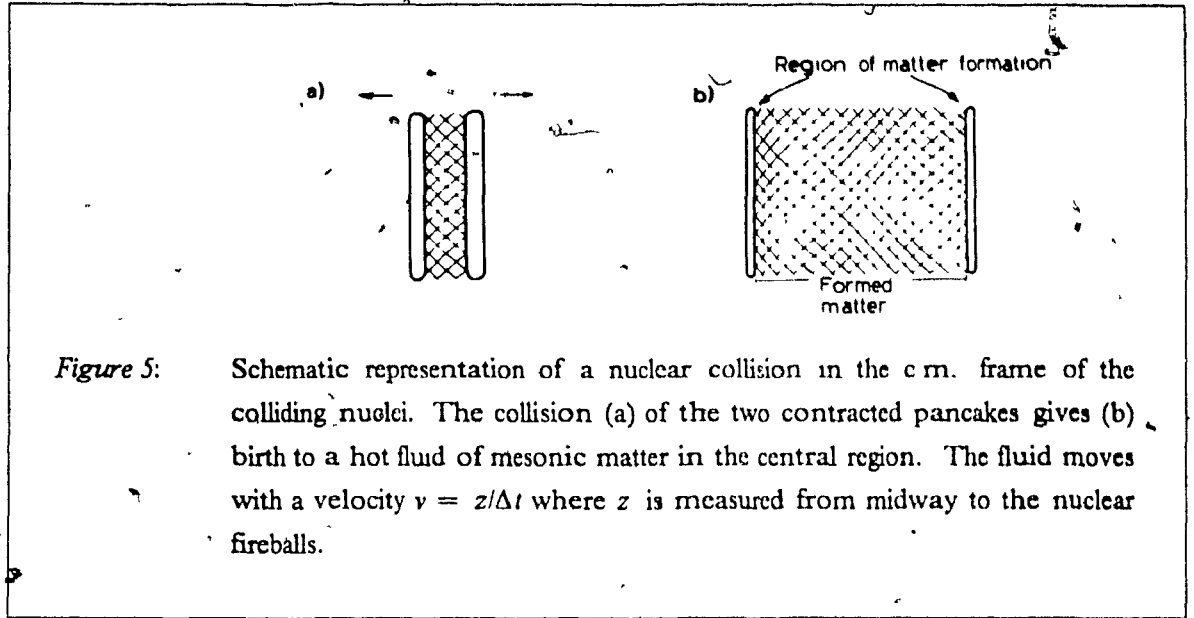


Figure 4: Phenomenological estimate of the initial energy density reachable in the fragmentation regions. Quantitative estimates [9] are shown for $A-B$ collisions at $\sqrt{s^n}$ of 30 GeV/nucleon (closed triangle), 50 GeV/nucleon (closed circles) and 70 GeV/nucleon (closed box) together with the predictions from equation (6) with $\beta = 1.08, 1.22$ and 1.32 respectively. The prediction of equation (7) for ^{16}O -nucleus collisions is also shown for $\beta = 1.22$.

1.4.2 Critical initial conditions in the central region

I shall now come back to the central region for which I have already mentioned that the slow virtual fragments contributed to the formation of a hot region of mesonic matter. In order to study this region, the main additional concept introduced in Bjorken's scaling hydrodynamics [10] [17] is the appearance at sufficiently high energy of a "central plateau" structure for the particle production as a function of the rapidity variable, similar to the one observed in nucleon-nucleon collisions. This is motivated by the assertion [10] that the space-time evolution of the system should look essentially the same in all c.m.-like frames, i.e. in all frames where the fireballs are contracted pancakes receding in opposite direction at nearly the speed of light. A cylindrical symmetry property, imposed as initial condition, leads to simple solution of the hydrodynamic equations in which the entropy per unit rapidity is constant. This implies in turn that the particle production per unit rapidity, which is proportional to the entropy, does not depend on the details of the hydrodynamic evolution but only on the initial energy and entropy deposition in the early stage of the collision. A schematic representation of the geometry in the c.m. frame of the colliding pancakes is given in Figure 5 on page 12. Near the collision axis the fluid expansion is longitudinal and homogeneous. At midway the fluid remains at rest while at longitudinal distance z from that midpoint it moves with

longitudinal velocity $z/\Delta t$, where Δt is the time elapsed since the pancakes collided.



At early time τ_0 after the collision, in a rest frame centered at $y = 0$ (i.e. around the midpoint), a thin slab of thickness d has a volume in fm^3 of

$$V_{\tau_0} \approx \pi R_{\text{min}}^2 d = \pi (r_0 \cdot A^{1/3})^2 \cdot d$$

where $r_0 \cdot A^{1/3}$ is the radius of the smallest nuclei in fm, with $r_0 \sim 1.2$ fm. Now the distance d can be rewritten in terms of the slab surface velocity as $d \sim 2v\tau_0 \sim c\tau_0\delta y$. The early energy density is then obtained from

$$\varepsilon_{\tau_0} V_{\tau_0} \sim \frac{dE}{dy} \delta y \sim \bar{m}_T c^2 \frac{dN}{dy} \delta y$$

which gives [10]

$$\varepsilon_{\tau_0} \sim \frac{\bar{m}_T c^2}{c\tau_0 \pi (r_0 \cdot A^{1/3})^2} \frac{dN(y=0)}{dy} \text{ GeV/fm}^3 \quad (8)$$

where in the baryon free central region, dN/dy is the pion multiplicity density at $y \sim 0$ ($\sim 3/2 dN^{\text{ch}}/dy$) and $\bar{m}_T c^2 = (\bar{p}_T^2 c^2 + m_\pi^2 c^4)^{1/2}$ is the average transverse mass of the pions. An estimate of

the early entropy can then be obtained in a simple manner. I have mentioned in section 1.2 on page 2 the results from lattice QCD calculations showing that above the critical temperature the system can be described as an ideal gas of massless quarks and gluons, with the energy density ϵ following the simple Stefan-Boltzman limit $\epsilon \sim aT^4$. Moreover, it is known from the combined first and second laws of thermodynamics, that for such a system at phase equilibrium:

$$TS = U + PV \Rightarrow s = \frac{4}{3} \frac{\epsilon}{T} \sim \frac{4}{3} a T^3 \quad (9)$$

where $P = \epsilon/3$ was used. From equations (8) and (9) one obtains, using $\bar{m}_T \sim T$, an estimate of the early entropy density:

$$s_{\tau_0} \sim \frac{4}{3} \frac{1}{c \tau_0 \cdot \pi (r_0 \cdot A^{1/3})^2} \frac{dN(y=0)}{dy} \text{ fm}^{-3} \quad (10)$$

This equation together with equation (8) provide crucial links between the observable characteristics of the particle flow and the initial thermodynamic properties of the hot central firetube. In principle, Bjorken's formula (8) is only applicable as such in an ultrarelativistic scaling regime where the central region is well decoupled from the target fragmentation regions. In such a regime, a rough estimate of the achievable energy density may be obtained via an extrapolation based on p-p data. For that one may use the very high energy limit of the Dual Parton Model (section 2.5.1.3 on page 45) for which the particle density in the central region scales like

$$R \equiv \frac{dN_{AB}/dy}{dN_{pp}/dy} \sim v_{AB}$$

where v_{AB} is given by [18] $v_{AB} = AB \sigma_{pp}/\sigma_{AB}$. Here σ_{pp} is the p-p inelastic cross-section (~ 32 mb) and σ_{AB} is the nucleus-nucleus inelastic cross-section (parametrized in ref. [19] as $\sigma_{in}(mb) = 65.9(A^{1/3} + B^{1/3} - 11)^2$). We furthermore use the charged pions mean transverse momenta of $\bar{p}_T \sim 340$ MeV/c characteristic of p-p data, and assume that the thermalization time τ_0 is approximately the same as the particle formation time in p-p collisions, i.e. $\tau_0 \approx 1$ fm/c. Under these assumptions, the energy density $\epsilon_{Bjorken}$ (equation (8)) for an $^{16}\text{O} - ^{208}\text{Pb}$ collision is evaluated to be:

$$\epsilon_{Bjorken} \sim \frac{0.37 \text{ GeV}}{1 \text{ fm} \times 28.7 \text{ fm}^2} \times 16 \times 208 \times \frac{32 \text{ mb}}{3545 \text{ mb}} \times \frac{3}{2} \times \frac{dN_{pp}^{ch}(y=0)}{dy} \text{ GeV/fm}^3 \quad (11)$$

$$\epsilon_{Bjorken} \sim 0.58 \frac{dN_{pp}^{ch}(y=0)}{dy} \text{ GeV/fm}^3$$

The charged multiplicity density in p-p collisions is dependent⁶ on the available \sqrt{s} . For ultra-relativistic energies (say $\sqrt{s} \sim 50-100 \text{ GeV}$), $dN_{ch}^{pp}(y=0)/dy \geq 3 - 6$ which leads using (11) to energy densities of $\epsilon_{Bjorken} \geq 1.7 - 3.5 \text{ GeV}^4/\text{fm}^3$, well within the critical domain for a deconfinement transition

The Bjorken formula (8) is considered as representing a "lower bound" to the initial energy density since, in more realistic models, part of the initial energy is spent in the form of work done by the fluid during expansion [20]. Taking this into account, the energy density is expressed as

$$\epsilon_0 = (\text{Constant} \times \epsilon_{Bjorken})^{1/\nu}$$

where ν is the sound velocity in the fluid. Conversely, equation (10) provides an "upper bound" on the initial entropy density since there are additional sources of entropy (e.g. viscous heating and the phase transition from the quark to hadronic phase [20])

1.4.3 Thermalization and expansion

Considerable theoretical efforts have been devoted to the study of the quark matter formation and evolution in nuclear collisions, from pre-equilibrium to final state interactions. These efforts have not yet resulted in a universal description allowing us to make unique quantitative statements about the true significance of the various direct quark matter probes (section 1.3 on page 5). They have nevertheless considerably improved our understanding of the role and importance of different parameters, and revealed the possibility to use macroscopic properties of the particle flow to pre-select the most interesting event candidates

In the quark-gluon plasma formation stage, the beam kinetic energy is converted into internal excitation energy and this energy becomes thermalized (entropy production). Rapid local thermodynamic equilibrium is usually assumed as it leads to simple dynamical models of the collisions based on hydrodynamics. However the validity of this assumption remains to be checked. Important efforts have to be devoted to the questions of how to characterize the quanta which have a chance to thermalize and on what time scale the equilibrium is reached [21]. The question of the energy density soon after thermalization can be investigated by solving the kinetic equations, given the pre-equilibrium conditions, but it requires a detailed knowledge of the microscopic processes by which the quanta exchange energy, momentum and quantum numbers. An ambitious but necessary program is to address these questions in the framework of microscopic parton models [22]

⁶ The dependence on \sqrt{s} of the average charged multiplicity in p-p collisions is well described as $\langle n_{ch} \rangle = 0.88 + 0.44 \ln s - 0.118 (\ln s)^2$

Similarly the role of the rescattering of secondaries, within the interaction volume, has to be investigated

The latter global evolution of the system will be determined by conservation laws and the equation of state of matter which will provide a system of hydrodynamic equations. In most hydrodynamical studies of nuclear collisions, the initial conditions for the hydrodynamic evolution of the matter produced in the central rapidity region are imposed to be invariant under a Lorentz boost in the beam direction [10]. This symmetry constraint on the initial conditions has been motivated by the apparent formation of a central rapidity plateau in hadron-hadron particle distributions. Thus a superposition of rapidity distributions measured in hadron-hadron interactions is often taken to define the initial conditions for hydrodynamic treatment of a nucleus-nucleus interaction. The validity of these assumptions is connected to the more general question of knowing to what extent one can infer the properties of nucleus-nucleus collisions from the superposition of the physics of hadron-hadron collisions. This question calls for experimental data on global energy flow and particle multiplicity. The global properties of this particle flow may be dependent on nature of dissipative processes, as well as on the mechanism by which proceeds the transfer of the energy and entropy into the longitudinal and transverse directions [23]. The study of the transfer to transverse expansion has led to the conjecture that [24] the energy density of the mixed phase might vary considerably as hadronic matter is converted into quark matter and that this could result in a change of slope in the curve of transverse momentum versus multiplicity. Such a behaviour may have been observed in very high energy nucleus-nucleus collisions by the IACRF cosmic ray experiment [25]. Their results are shown in Figure 6 on page 16 where \bar{p}_T is plotted versus the energy density estimated using Bjorken's formula (8). Also shown are results from the UA1 Collaboration [26] for which the small rise of \bar{p}_T may be explained by the contribution of mini-jets.

From the detailed theoretical predictions [27] [28] the \bar{p}_T is expected to increase while ϵ and P increase, until reaching the region (corresponding to a mixed phase) of a first order transition in which \bar{p}_T remains constant (i.e. P and T both remain constant while ϵ continues to increase). A steeper rise is finally expected in the pure plasma phase. The \bar{p}_T enhancement is predicted to be greater for larger masses (Figure 7 on page 16) and the eventual observation of such a mass dependence could signal the existence of collective flow in the final state of heavy ion collisions.

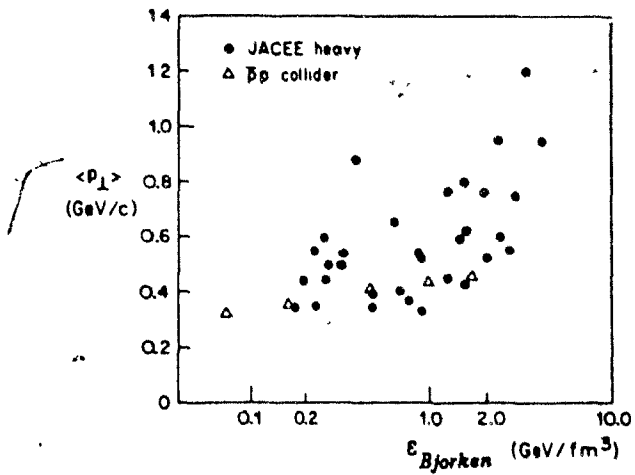


Figure 6 The average transverse momentum \bar{p}_T versus the energy density $\epsilon_{Bjorken}$. The results are measurements from highly relativistic nuclear collisions (closed circles) [25] and $p-\bar{p}$ collisions (open triangles) [26].

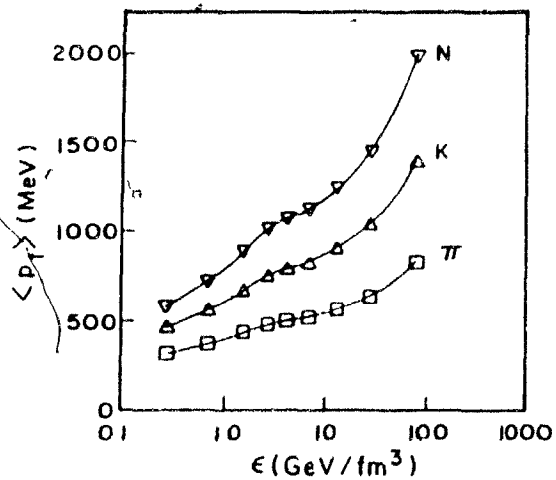


Figure 7. The average transverse momentum \bar{p}_T versus the energy density ϵ for pions, kaons and nucleons. The predictions are from the model of ref. [28] for a first order phase transition.

In the hadronization phase prior to the final freezeout into free streaming particles, it is known that the virtual particles created will materialize in a sequence dictated by time dilatation and the uncertainty principle, but little is known about how the energetic environment of hadronic matter affects the materialization [29]. The initial distribution of virtual particles could be changed by interactions with the surrounding matter and this could lead to observable difference in the rapidity distributions. The hadronization of the quark-gluon plasma may proceed from its outer surface or correspond to a hadronization transition from inside the plasma due to the rapid cooling caused by the longitudinal expansion. The hadronization mechanism has been studied using fluid mechanics theory, in the framework of the combustion theory, and with phenomenological microscopic models inspired by QCD [23]. The studies within the combustion theory have led to speculation on the possibility of large event-by-event fluctuations resulting from explosive deflagration or detonation during final state materialization [30], or isolated maxima of width $\delta y \sim 1$ in the rapidity distribution dN/dy of hadrons engendered by the deflagration of quark-gluon plasma droplets [31]. Note that large event-by-event fluctuations may also be linked to the plasma formation process [32]. Both experimental information and parton models extrapolations from hadron physics are essential tools for identifying such abnormal events or explicitly collective effects of unknown character.

In this exploratory phase of the quark matter search, a clear strategy for the first generation of ultra-relativistic heavy ion experiments is, while being alert for signals directly probing the quark matter phase or phase transition, to measure with great precision the energy and particle flow and related event-by-event correlations. The distributions and fluctuations will give information on crucial thermodynamic variables defining conditions of the plasma formation. Comparisons to extrapolation from hadron-hadron physics, based for instance on parton models, will allow characterization of events which are most likely candidates for plasma formation. Nucleus-nucleus interactions are dominated by low- p_T processes. These are intimately connected with the quark confinement problem and outside the proper domain of perturbative QCD applicability. Nevertheless, a number of QCD-inspired phenomenological models have been developed to describe low- p_T particle production in terms of the quark structure and fragmentation functions. The most successful of these models, the Dual Parton Model and the String Fragmentation Model (see section 2.5 on page 32), have been incorporated in Monte Carlo event generators and thus extensively compared to a variety of processes in hadron-hadron and light nuclei collisions. These models should be used with a minimum of ad hoc assumptions to predict the various features of nucleus-nucleus collisions from hadron-hadron physics. The description of nuclear collisions within conventional low- p_T particle production is the "background" against which the effects of quark-gluon plasma formation have to be found. A further constraint on the parton models is the necessity to reproduce the right correlation between the energy lost by the leading baryons and the distribution of produced particles in phase space. Here, parton models become not only tools for identifying deviations from standard physics but also tools for optimization of the conditions for the formation of the quark matter. The leading baryon spectrum can be studied in parton models framework to provide us with the baryon densities in the different regions of phase space and the energy lost by the leading baryons during the collision. These are two basic parameters for quark-gluon plasma

formation.

Given the assumption of thermalization, precise experimental information on energy and particle flow in rapidity provides information on thermodynamic properties like the energy density and the entropy and, thus, will help to establish the equation of state. The mean transverse momentum of particles produced in very high energy nucleus-nucleus collisions may be directly related to the energy per unit entropy of the hot matter originally formed and also, together with the rapidity density of particles, to the initial energy density.

Chapter 2

Models for particle production in ultra-relativistic nuclear collisions

2.1 Introduction

In order to be able to discriminate the signals pointing to a possible formation of quark matter in nucleus-nucleus collisions, we will need to compare the observed energy and particle flow to extrapolations made within the framework of conventional models for soft-hadronic processes. These extrapolations based on known characteristics of particle production in hadron-hadron collisions will tell us what to expect a priori from conventional physics. The search for deviations from such conventional "background" is a necessary pathway towards identification of effects resulting from quark-gluon plasma production. Unfortunately, there exists yet no unique way to derive a "conventional" picture of ultra-relativistic nuclear collisions.

First of all, the nuclei themselves are no trivial tools. Predictions for the mean behaviour and fluctuations of observables depend on a precise description of the instantaneous distribution of nucleonic matter in the colliding nuclei, and the comparison with experimental data requires a knowledge of the effective sampling of impact parameters. Once the "geometry" of the nuclear collisions is under control, we need a detailed description of the mechanism of multiple interactions which took place and of the resulting particle production. For these, one can rely on a wide variety of more or less fundamental theoretical approaches, with more or less predictive power.

The theoretical models can be roughly classified into two classes. In a first class of models (section 2.2 on page 20), an incoming hadron is assumed to interact in a sequential cascading way with several nucleons of the target nucleus. During this propagation through nuclear matter, the projectile hadron never loses its identity. In this case, except for energy-momentum conservation, a multiple collision is a superposition of individual independent collisions. On the contrary, one can adopt a picture where the collision breaks completely the hadronic projectile into partonic fragments which subsequently undergo interactions with other target nucleons. In such models (section 2.5 on page 32) one no longer has a simple superposition. The space-time development of the multiple interactions will be function of the basic dynamics of the hadronic interactions.

2.2 Nucleon collisions and global particle flow characteristics

The simplest superposition models are the Wounded Nucleon and Nucleon Collision models, for which the basic assumption is that for a certain class of phenomena, the underlying quark-gluon structure of hadrons is not revealed or plays no significant role in the mechanism of the multiple soft-hadronic collisions. These models pretend to be interested only in global properties of the nucleus-nucleus collisions, which they deduce by convoluting a parametrization of the average behaviour of p_T , E_T or the multiplicity distribution observed in hadron-hadron or hadron-nucleus collisions. In the most naive versions of the models, a drastic oversimplification is made by neglecting energy-momentum conservation. One starts with a description of the colliding nuclei A and B in terms of the nucleonic density profiles ρ_A and ρ_B . A geometrical cross-section is calculated via a convolution which involves either the sum $\rho_A + \rho_B$ to calculate the probability of having N_w participating nucleons, or the product $\rho_A \cdot \rho_B$ to calculate the probability for the incoming nucleons to suffer N_c collisions. The geometrical probability distribution is then folded with a simple parametrization of $p-p$ data. The resulting spectrum may provide simple heuristic descriptions of distributions measured in nucleus-nucleus collisions.

The calculation of N_c is the starting point of the Nucleon Collision Model (NCM). In this simple model [15] [34] the number of collisions experienced by an incident nucleon arriving with impact parameter b on a target nucleus A is estimated as

$$n(b) = \sigma_{nn} \int \rho_A(z) dz \quad (12)$$

where ρ_A is the target nuclear density profile (taken as trapezoidal in [34]) and z is the incidence axis. This relation implies that an incident nucleon is imagined to interact successively with all target nucleons it encounters within a cylinder of cross-sectional area σ_{nn} , the inelastic nucleon-nucleon cross-section. The quantity $n(b)$ has large RMS spread around the average over impact parameter, \bar{n} , which corresponds to $\bar{n} = A \cdot (\sigma_{nn}/\sigma_{nA})$. For a projectile nucleus B centered at impact parameter b , the total number $N(b)$ of nucleon-nucleon collisions is constructed by making (over the allowed impact parameter domain for the individual nucleons) the product $n(b')$ times the effective number of participating incident nucleons:

$$N_{eff}(b) = \int dx \int dy \int dz_1 \rho_A(x, y, z_1) \int dz_2 \rho_B(x, y, z_2, b) \quad (13)$$

The folding of equations (12) (13) gives

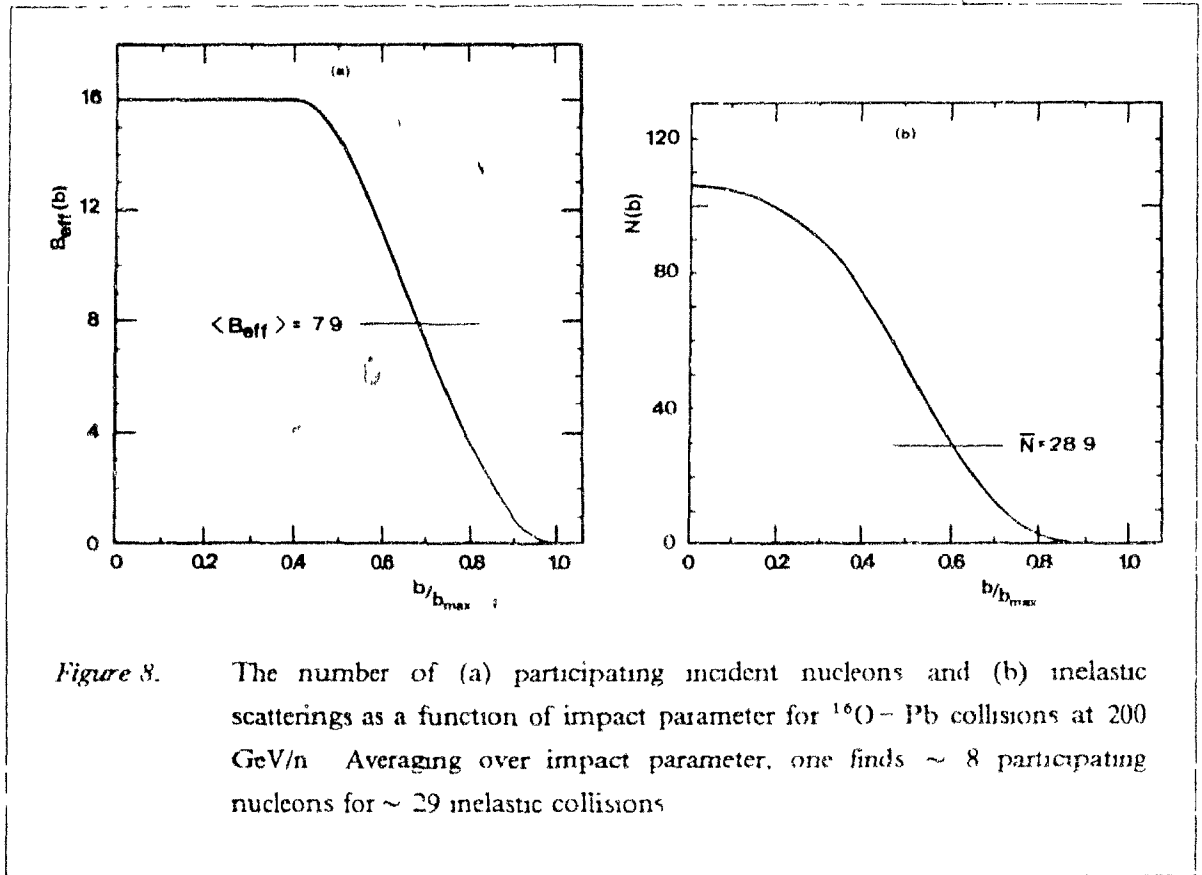
$$N(b) = \sigma_{nn} \int dx \int dy \int dz_1 \rho_A(x, y, z_1) \int dz_2 \rho_B(x, y, z_2, b)$$

or in abbreviated notations

$$N(b) = \sigma_{nn} \int dS \xi_A \xi_B \quad (14)$$

where S is the surface of the interaction volume orthogonal to the incidence axis, and ξ_A, ξ_B are the projected "density" per unit area

The number of participating incident nucleons $B_{\text{eff}}(b)$ and the total number of inelastic collisions $N(b)$ are shown as a function of impact parameters in Figure 8, for ^{16}O on ^{208}Pb at 200 GeV/n incident energy [34]. For central collisions ($b \leq 3\text{fm}$), all incident nucleons participate and undergo ~ 7 inelastic collisions.



In order to construct observable distributions, the NCM makes the ad hoc assumption of a scaling with the total number of inelastic collisions. For instance, a transverse energy differential cross-section is built on the assumption that each independent collision has a probability of

$$p_0(E_T) = \frac{f(E_T)}{\varepsilon_0} e^{-E_T/\varepsilon_0}$$

to contribute by the amount E_T . The function $p_0(E_T)$ is chosen to fit $p-p$ data. The fluctuations of these "elementary" contributions depend on the choice of $f(E_T)$, which is taken as 1 in [33] for a variance of ε_0^2 , and $4E_T/\varepsilon_0 \cdot e^{-E_T/\varepsilon_0}$ in [34] for a variance of $\varepsilon_0^2/2$. The total number of collisions is then allowed to be subject to poissonian fluctuations such that for a given impact parameter, one has an E_T distribution of [34]:

$$p(E_T) \sum_m \frac{e^{-N(b)} N^m(b) (2E_T/\varepsilon_0)^{2m-2}}{m!(2m-1)!}$$

where the sum over m ranges from 1 to infinity. The differential cross-section is finally obtained by averaging over impact parameters. Such a simple one parameter fit was performed on experimental data for $^{16}\text{O}-\text{Pb}$ collisions at 200 GeV/n measured in the pseudorapidity region $2.2 < \eta_{lab} < 3.8$ [35]. The fit [34] with $\varepsilon_0 = 0.79$ GeV gave a reasonable description of the data. This value of ε_0 may be compared to the corresponding value for $p-p$ collisions, which is found [34] to be 1.2 GeV in the pseudorapidity domain considered.

The incapacity to maintain the parameters values from nucleon-nucleon collisions is an incurable disease of the NCM. In general, different data sets will require different values of ε_0 [34] and the introduction of a variance parameter ω such that

$$\overline{E_T} = N \varepsilon_0$$

$$\sigma^2 = \omega \varepsilon_0 \overline{E_T}$$

The values of neither ε_0 nor ω can be deduced in a straightforward manner from $p-p$ data. A partial cure may be the introduction of an additional parameter, to take into account the energy losses between successive intranuclear scatterings, such as a damping factor $1/\kappa$ for the relative contribution $C(v)$ of the v^{th} scatter. This kind of linear fall-off $C(v) \propto v/\kappa$ has been used to reproduce the A -dependence of the transverse energy distribution in $p-A$ collisions [36]. For $B-A$ collisions, this prescription would require to keep trace of the whole multi-collision history in order to "correctly" weight the interaction between already multi-scattered nucleons.

In the Nucleon Collision model, any given nucleon may undergo an unlimited number of contributing scatters independently of its history. Furthermore, without any self-consistent

justification, the total number of scatters N_c is assumed to play a fundamental role in nucleus-nucleus collisions, similar to its presumed role in p-A collisions [37]. There N_c is linearly related to the total number of participating ("Wounded") nucleons,

$$N_c = N_w - 1,$$

so that either N_c or N_w may be used. For a nucleus-nucleus collision, there is no unique relation between N_c and N_w .

In the Wounded Nucleon Model (WNM) [38], the conjecture is made that a more fundamental role is played by the total number of wounded nucleons N_w . The observable properties of a nucleus-nucleus collision are assumed to be obtained by N_w convolution of the corresponding properties measured in p-p collisions. Here again, the model offers no self-consistent justification for the average scaling with N_w . This ad hoc choice implies that a nucleon-nucleon scatter will contribute only if one of the interacting nucleons is not already wounded, although a given nucleon may "wound" an unlimited number of nucleons. The WNM assumption that each wounded nucleon contributes independently to the observable particle flow implies that the overall produced particle multiplicity should increase linearly as a function of the number of participants. Hence, when comparing the particle production in nucleus-nucleus and nucleus-nucleon collisions, the prediction is that

$$R(pA / pp) = \frac{N_w^{pA}}{N_w^{pp}} = \frac{1}{2} (N_c + 1) \sim \frac{1}{2} \left(\frac{A \sigma_{pp}}{\sigma_{pA}} + 1 \right) \quad (15)$$

This linear relation between the particle production and the thickness of the target nucleus is in good agreement with experimental observations [39] [40] up to $N_w^{pA} \sim 4$. Note that such a A-dependence is dramatically weaker than what was predicted by naïve intranuclear cascade models in which all particles created in the primary collision were allowed to interact immediately with other nucleons in the nucleus [41].

Given the assumption that each wounded nucleon acts as an independent source, a distribution such as a transverse energy differential cross-section can be built from a convolution of the form [36]

$$\frac{d\sigma^{AB}}{dE_T} = \sigma_{in}^{AB} \sum_{w=2}^{A+B} a_w \cdot f_w(E_T) \quad (16)$$

The nuclear inelastic cross-section σ_{in}^{AB} is calculated using the Glauber multiple scattering model [42] for which the scale is fixed by the free nucleon-nucleon inelastic cross-section ($\sigma_{in}^{nn} \sim 32$ mb at $\sqrt{s} \sim$

19.4 GeV). The colliding nuclei are described in terms of Wood-Saxon nuclear density profiles. The probability a_w that N_w nucleons get wounded in the A-B collision is written as

$$a_w = \sum_{w_A} P_A(w_A) P_B(w-w_A)$$

where $P_A(w_A)$ is the probability that w_A nucleons of nucleus A get wounded [43]. A parametrization of the experimental nucleon-nucleon $d\sigma^m/dE_T$ distribution leads to an expression of the form

$$f_w(E_T) = \frac{\alpha^{\frac{w}{2}(\beta+1)}}{\Gamma\left(\frac{w}{2}(\beta+1)\right)} \cdot e^{-\alpha E_T} \cdot E_T^{\left(\frac{w}{2}(\beta+1)-1\right)} \quad (17)$$

for the contribution to equation (16) from the n_w wounded nucleons. The parameters α and β in (17) are given by the fit to the p-p data or are left as free parameters.

An extension of the WNM to introduce the quark-gluon structure of hadrons is made in string models such as the Additive Quark Model (AQM) [44] [45] [46]. In AQM, the first stage of the nuclear collision is a set of parallel collisions of constituent quarks. Coloured strings are assumed to span between the participating quarks and the fragmentation of the strings gives rise to the particle production in the central region. During the multiple scattering processes, several strings may be connected to any given quark and one postulates that these eventually coalesce into one string prior to fragmentation. The effective total number of coloured strings is thus equal to the total number of wounded valence quarks of the incident protons and all strings are assumed to contribute with equal weights independently of the number of "parent" strings from which they were formed. The building of an observable particle distribution can then proceed [42] as for WNM, except that now the sum in equation (16) runs from $w = 1$ to $3 \cdot A$ wounded quarks, a_w is the probability to have N_w wounded quarks [47], and the scale is fixed by the quark-quark cross-section ($\sigma^{qq} \sim 1/9 \sigma_n^m$).

The attempt to account for the particle production (in central regions) by a simple counting of the total number of wounded nucleons or by counting the "gluon strings", together with the assumption that all wounded nucleons or strings can be considered as equivalent independent sources of particles, allowed a reasonable description [46] of multiplicity distributions for p- α and α - α collisions at $\sqrt{s} = 44$ and 31 GeV/n and provided there a simple explanation for the nuclear enhancement at large E_T [36]. On the other hand, one cannot find a coherent set of values for the α and β parameters that simultaneously fits the characteristics of the particle flow (e.g. $d\sigma/dE_T$ distributions) measured in nucleon-nucleon, nucleon-nucleus and nucleus-nucleus collisions [42] [48] [49]. The global shape of the distributions is generally reproduced to an extent such that one may nevertheless use the models as a basis for a compact parametrization of the data [50] [51]. The

models furthermore provide simple rough estimates of average quantities characterizing the particle production. It is worth noting here that in some very limiting cases, as we will see in 2.5.1.3 on page 45, the more fundamental underlying constituent quark dynamics will result indeed in an approximate scaling with N_w in the central rapidity region. In the WNM, the mean number of participants from projectile A and target B is

$$\bar{N}_A = A \frac{\sigma_{in}^{pB}}{\sigma_{in}^{AB}} \text{ and } \bar{N}_B = \frac{B \sigma_{in}^{pA}}{\sigma_{in}^{AB}} \quad (18)$$

where σ_{in}^{AB} is the $A \rightarrow B$ production inelastic cross-section, i.e. excluding the cases of a nuclear breakup without meson production. This cross-section is thus a fraction of the total inelastic cross-section as measured in emulsion experiments and which is known to be parametrized [52] as

$$\sigma_{in}^{TOT} = \pi \rho_0^2 \left(A^{1/3} + B^{1/3} - \frac{c}{A^{1/3} + B^{1/3}} \right)^2 \quad (19)$$

with $\rho_0 \sim 1.3$ fm and $c \sim 4.45$. The formula (19) deviates slightly from the pure geometrical cross-section ($\sigma_{in} = \pi \rho_0^2 (B^{1/3} + A^{1/3})^2$) for a spectator-participant picture with straight line trajectories, since the outlines of the boundary between spectators and participants are blurred by the finite scattering angles. This is taken into account by the last term in (19). The σ_{in}^{AB} in (18) corresponds to σ_{in}^{TOT} minus the contribution from nuclear breakup and from electromagnetic dissociation. A useful parametrization is [19]

$$\sigma_{in}^{AB} = 65.9 (A^{1/3} + B^{1/3} - 1.11)^2 \text{ in mb} \quad (20)$$

One can use WNM to derive simple expressions for quantities such as the average transverse energy produced in a nuclear collision [49]:

$$\bar{E}_T^{AB} = \frac{(\bar{N}_A^{AB} + \bar{N}_B^{AB})}{(1 + \bar{N}_B^{AB})} \bar{E}_T^{pB} = (\bar{N}_A^{AB} + \bar{N}_B^{AB}) \frac{\bar{E}_T^{pp}}{2} \quad (21)$$

For an $^{16}\text{O} - ^{208}\text{Pb}$ collision at 200 GeV/n incident energy, we thus expect (from (20) and (18) and using $\sigma_{in}^{pO} \sim 292$ mb and $\sigma_{in}^{pPb} \sim 1770$ mb) an average of ~ 7.9 participating incident nucleons leading to an average transverse energy production of $\bar{E}_T(O-Pb) \sim 12.5 \bar{E}_T(p-p)$. Note the average number of participating incident nucleons coincides with the prediction (see Figure 8 on page 21) of the NCM.

2.3 Energy conservation and nuclear stopping power

The simple "counting rules" of the NCM (number of inelastic scatterings), the WNM (number of participants) and the AQM (number of strings for the central region) are merely useful parametrizations which are seen to be of limited applicability as soon as the particle production is studied in greater details. First of all, the energy conservation has been omitted and it will play a fundamental role even in collisions initiated by ultra-relativistic (i.e. $\sim 10^2$ GeV/nucleon) incident projectiles. This might be seen, for instance, in $p-A$ data when the thickness of the target nucleus is brought to a value leading to a sizeable number of participating target nucleons (N_w larger than ~ 4) [53] [36]. The central multiplicity density in $p-A$ collisions is seen to increase in proportion with the number of participants up to $N_w \sim 4$, above which it is increasingly suppressed compared to the naive scaling. This is seen in Figure 9 on page 27, which shows a compilation of p -emulsion data made by Brody et al. [36] which they use to study the effect of the inclusion in WNM and AQM of an additional parameter representing the weakening of the contribution from successive inelastic collisions.

A "damping" coefficient is found to be necessary to avoid an overestimation by the WNM of both the A -dependence of the central multiplicity and the "nuclear enhancement" as measured [54] at high transverse energy with the ratio $(d\sigma/dE_T)_{pA} / (d\sigma/dE_T)_{pp}$. The interpretation of the suppression mechanism in such comparison is however not unique, as one cannot distinguish between the effect on the particle production of the energy loss of the leading baryon during the multiple scattering process, and a limitation of the effective number of collisions allowed for the incident projectile. This latter case follows from the "counting rules" of a model like AQM since the total number of contributing collisions is limited to 3 (valence quarks) for an incident baryon. Neither WNM nor AQM (with or without an "energy conservation" parameter) seem to be able to simultaneously reproduce the observed nuclear enhancement and the damping of the multiplicity at central rapidity [36], and the suppression via a valence quark counting in the AQM leads to an underestimation of the rise of the central rapidity multiplicity density.

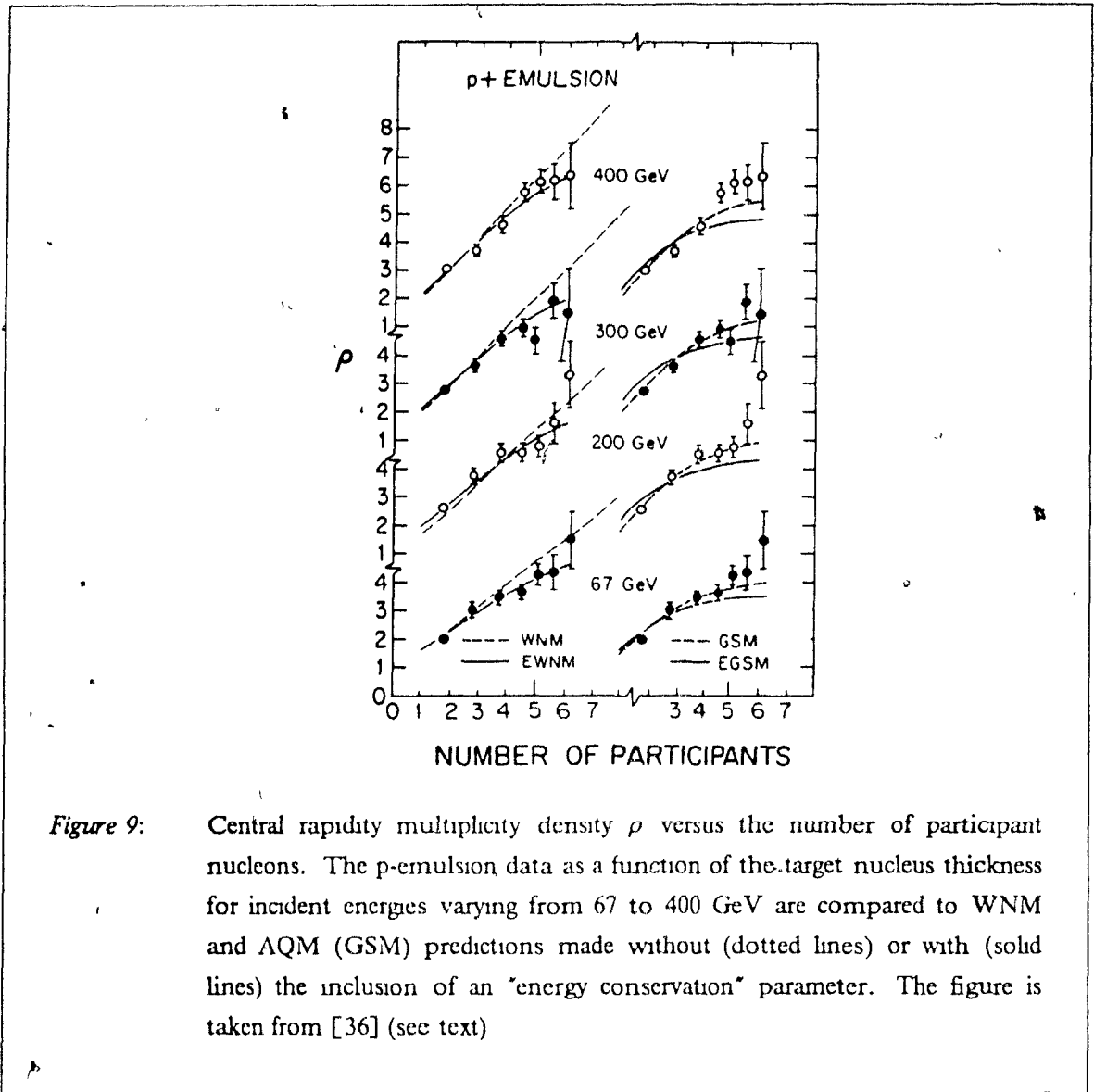
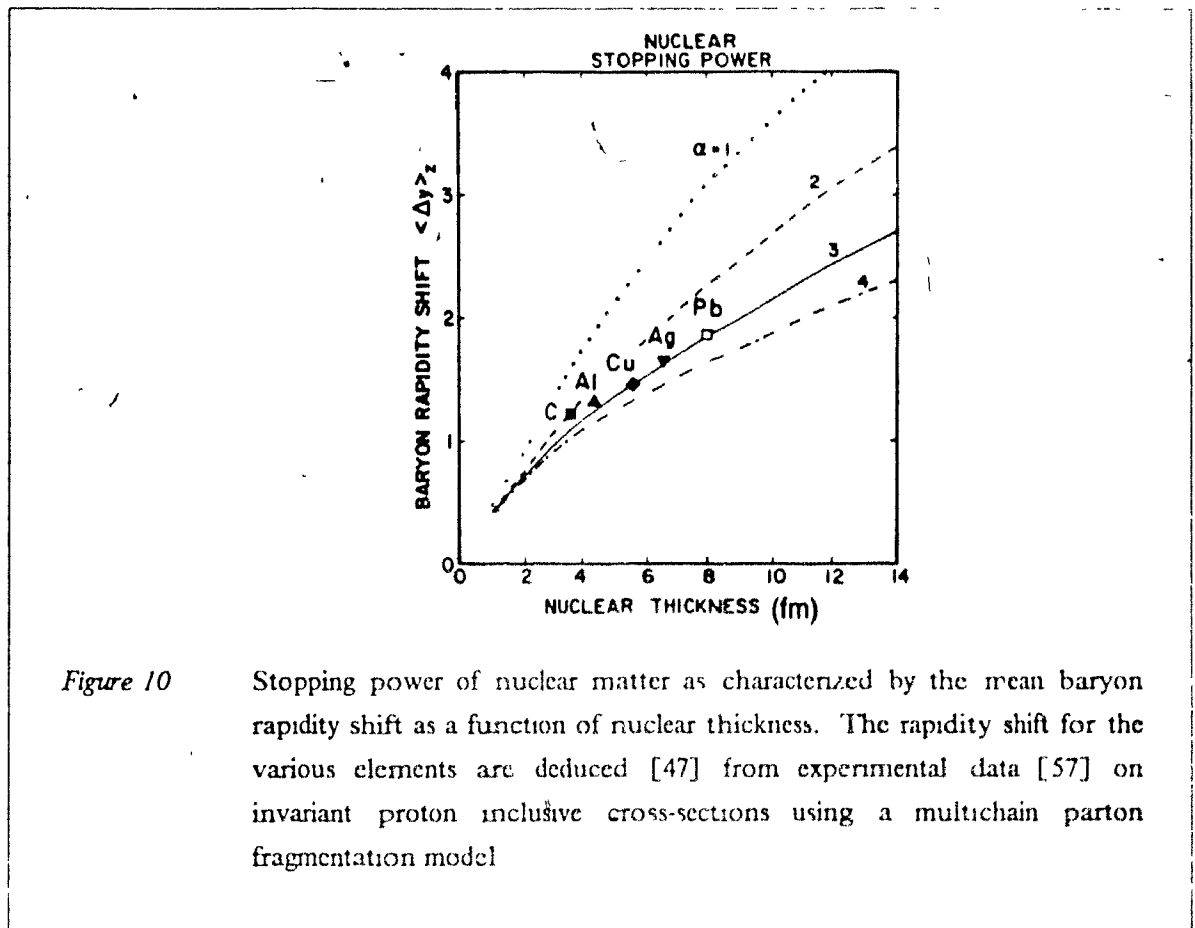


Figure 9: Central rapidity multiplicity density ρ versus the number of participant nucleons. The p-emulsion data as a function of the target nucleus thickness for incident energies varying from 67 to 400 GeV are compared to WNM and AQM (GSM) predictions made without (dotted lines) or with (solid lines) the inclusion of an "energy conservation" parameter. The figure is taken from [36] (see text)

The crucial role of the energy-momentum conservation is better manifested in its contribution to the increasing rapidity shift of the incident baryons (so-called stopping power) when brought to traverse an increasing target nucleus thickness. As mentioned in chapter 1, the nuclear stopping power is a necessary ingredient of any attempt to estimate the most favorable experimental conditions under which one may hope to generate a local deconfinement of quarks and gluons [55] [47]. It allows to evaluate the expected rapidity gap between the baryon rich nuclear fireballs, and the deposited energy which is available for particle production. Considerable theoretical efforts [55] [47] [56] have been devoted to the understanding, in terms of nuclear stopping power, of the A-dependence of the inclusive invariant cross-sections $E \frac{d^3\sigma}{dp^3} (= 2E/\sqrt{s} \times d^2\sigma/dx_F dp_T^2)$. These cross-sections, as measured for $p + A \rightarrow p + X$ and $p + A \rightarrow \pi^+ + X$ as a function of Feynman $x_F = 2p_L/\sqrt{s}$ (in the p-p center-of-mass frame) at 100 GeV incident energy [57], are found to be

increasingly weighted towards lower x_F with increasing target mass. From the displacement, one can extract a function $Q_n(\Delta y)$ giving the probability that the projectile loses $\Delta y = y - y_{beam}$ after n scatters. Although the translation into such a stopping power function is model dependent, most models agree in assessing for a relatively "large" nuclear stopping power, giving rise to mean rapidity losses which vary from $\Delta y \sim 1.2$ to $\Delta y \sim 1.8$ as the mean number of scatters increases from ~ 1.7 (^{12}C) to ~ 3.8 (^{208}Pb). Figure 10 shows the results of the calculations made by Daté et al. [47], who interpreted the data [57] in the framework of a multichain parton fragmentation model. Their calculated mean rapidity shift of ~ 1.8 in the case of ^{208}Pb (averaged over all impact parameters) would correspond to a shift reaching $\Delta y \sim 2-3$ units when an incident nucleon passes through the entire 8 fm diameter of a Pb target nucleus.



The extrapolation from the nucleon-nucleus information, to predict the stopping power of nuclear matter in the context of a nuclear collision, is hampered by the fact that little is known on the extent to which the stopping properties of the target nucleus may be felt differently by the successive layers of incident nucleons.

2.4 Hadronic formation time

The proton-nucleus data have also revealed that the particle production mechanisms deviate in another fundamental aspect from "trivial" superposition of free $p-p$ interactions. This is seen, for instance, when normalizing the overall rapidity density distributions of produced particles measured in p -nucleus collisions to the one measured in $p-p$ interactions, i.e. in measurements of the ratio $R = \rho_{pA}(y)/\rho_{pp}(y)$. The best measurement of such ratio was performed by a streamer chamber experiment [58] where the momenta and identification of charged particles could be made over the whole solid angle for 200 GeV/c protons and antiprotons incident on H, Ar and Xe targets. The results for negatively charged particles produced in p -Xe collisions are shown in Figure 11.

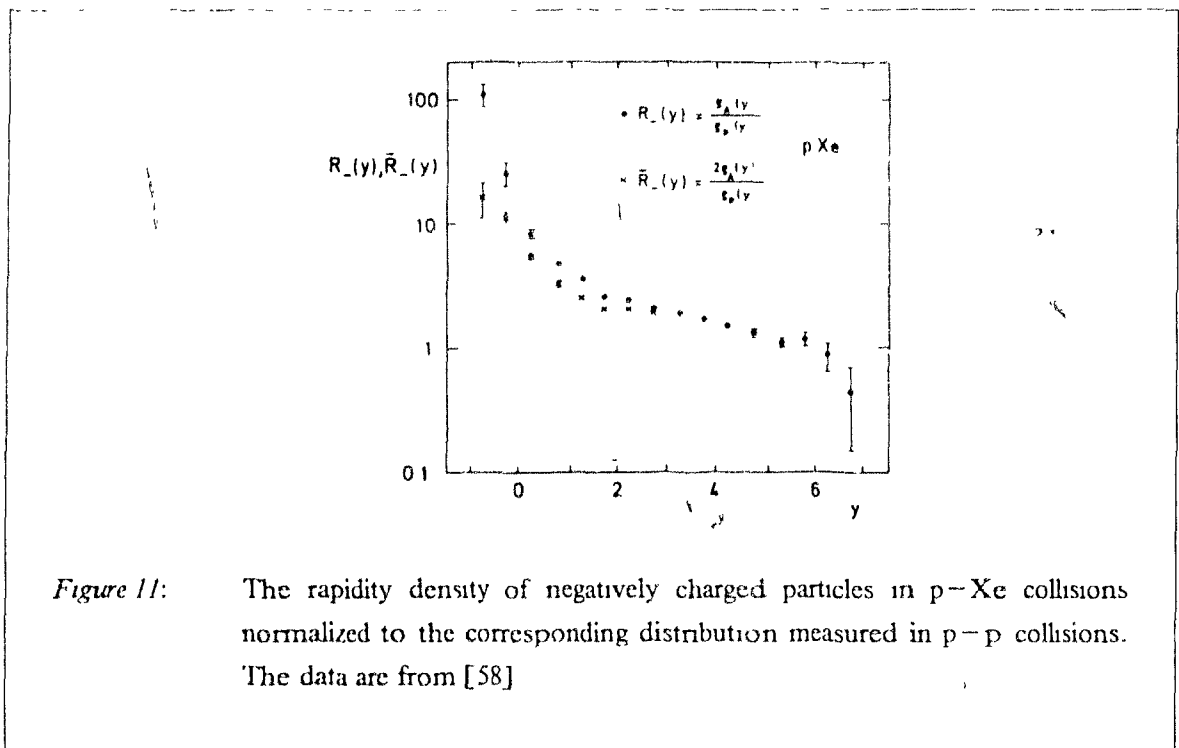


Figure 11: The rapidity density of negatively charged particles in p -Xe collisions normalized to the corresponding distribution measured in p - p collisions. The data are from [58]

The ratio distribution in Figure 11 shows a depletion ($R < 1$) at large forward rapidities corresponding to the beam fragmentation region. It slowly rises to reach a kind of plateau at central rapidities around $y_{lab} = 3$ ($y_{c.m.} = 0$ in the nucleon-nucleon c.m. frame). In this central region, the A -dependence of the particle production is compatible with the expectations from a naive counting of the "wounded" nucleons or "gluon strings" (eq. (15)), i.e. it scales in proportion to slightly more than half the number ν of inelastic scatters. The particle multiplicity density finally rises much faster than ν in the target fragmentation region. The general trend of such distributions was originally one of the motivations supporting the AQM assumption that valence quarks played a fundamental role in the collision process. This was generally simply argued [59] [18] by extending the simple counting

rules over the full rapidity. While the particle production in the central region would arise mainly from the breaking of the coloured strings, it would be dominated in the nuclear fragmentation region by the fragmentation of quarks which exchanged coloured gluons (wounded quarks [60]) and by the fragmentation of the spectator quarks in the wounded nucleons. A simple rough estimate obtained by counting strings, wounded and spectator valence quarks [18] leads to a prediction of $R^T \sim A (\sigma_{pp}/\sigma_{pA}) = \nu$ in the target fragmentation region, $R^C \sim 1/2(\nu+1)$ in the central region, and $R^B \sim 1.2s$ ($s \equiv$ spectator quarks) in the beam fragmentation region ($\Rightarrow R^B \leq 1$). In attempting to develop a more complete physical picture of the multiple collisions in the framework of the AQM, one has to implement the fragmentation and energy loss mechanisms which are not directly given by the model [47]. Some extensions of the AQM were found to provide a good description of the multiplicity rapidity dependence down to $y \sim 1$ [45] [58], but all failed in reproducing the maximum ($R^T \gg \nu$) in the target fragmentation region. The very high particle density in the target fragmentation region has been interpreted as evidence for large amount of cascading inside the target nucleus by the slow secondaries. The fact that this cascading appeared to be restricted to slow secondaries argued for the validity of the formation zone concept [61] [9] [41]. In the various theoretical approaches, the mechanisms responsible for the existence of this formation zone, an effect also called longitudinal growth, have been discussed in terms of the general principles of quantum mechanics and field theory, but generally speaking they can all be traced to an argument involving the uncertainty principle and the Lorentz time dilatation. The secondaries have a characteristic formation time τ_0 in their own rest frame which is dilated in the target rest frame to $t = \tau_0 \cdot E/m_T c^2 = \tau_0 \cosh(y)$. Above a certain energy E_c , which is given by the requirement $c\tau_0 = c\tau_0 \cdot E_c/m_T c^2 \approx r_0 A^{1/3}$, there is no cascade of secondaries and they escape the target nucleus as virtual fragments (for $m_T c^2 \sim 400$ MeV this corresponds to a critical rapidity of $y_c = \cosh^{-1}(L_c/m_T c^2) \sim 1$ to 2).

With the inclusion of the formation zone concept, the multiplicity overestimations of the naive cascade models could be explained, and needless to say, a number of improved cascade models were proposed as valid interpretation of the particle flow properties in p-nucleus collisions [41]. Similarly, numerous models relying on basis ranging from collective hydrodynamic to microscopic parton concepts have attempted to explain these observed properties [39] [62] [63]. As I am presenting in this thesis results of an experiment of the of the first generation on ultra-relativistic nuclear collisions, and since the actual hadron-hadron and hadron-nucleus data do not allow yet to completely discriminate between the various possible physical approaches for describing the nuclear collision process, one should be aware that there will be no unique interpretation of our results. The hadron-hadron and hadron-nucleus data nevertheless brought forward some constraints that guide the choice of a high energy nuclear collision model, which might be considered as representing the most reasonable extrapolation from "known" properties of soft-hadronic interactions. We shall minimally request that such a model provides a clear mechanism for the stopping of the incident nucleons and the corresponding rapidity displacement of the particle production, while preserving the approximate scaling of the central multiplicity and allowing for a

straightforward implementation of the hadronic formation time concept and eventual cascading of secondaries. Furthermore, it should require a minimal set of parameters and these should be severely constrained by the data. These conditions are fulfilled by the QCD-inspired models presented in the following sections and used as tools for the physics comparison with the data in chapter 5.

2.5 QCD-inspired multiple soft-hadronic interactions models

The particle production at low transverse momentum is the dominating observable feature from ultra-relativistic hadron-hadron to nucleus-nucleus collisions. The soft-hadronic processes responsible for this production are believed to be closely related to the quark confinement problem. The low momenta transferred are probing a domain where the strong interaction coupling constant is very large, thus forbidding a perturbative QCD treatment. Nevertheless, QCD-inspired models maintaining a close correspondence to the phenomenology used for hard processes have successfully been developed to explain soft-hadronic interactions. It is remarkable that the dominant contributions to phenomena in the low- p_T regime could depend on essentially free-parton probabilities. The understanding of the philosophical and practical implications of this is one of the major achievements of early recombination [64] and fragmentation [65] [66] [67] models. These two classes of models were able to reproduce the main observed features of the inclusive particle production, although with apparently contradictory viewpoints.

In the recombination models, the inclusive distributions are given by the parton structure functions, $f^q(x)$, of a fast forward-moving valence quark which recombines (according to a priori unknown recombination functions) with a slow ($x_2 \sim 0$) sea quark to produce the outgoing hadron. This approach, for which $x = x_1 + x_2 \sim x_1$, leads to an inclusive differential cross-section (e.g. in $p_T^2 \sim \pi^2 X$) of the form

$$\frac{d\sigma^{F \rightarrow H}}{dx} \sim f_F^q(x) \sim (1-x)^3 \quad (22)$$

in agreement with experiment. It is this discovery [68] of experimental evidence for a striking similarity between hadron-hadron low- p_T hadronic spectra at large x and the structure function of pointlike constituents measured in deep inelastic scattering which originally motivated the recombination approach. In the detailed application of the recombination models, the sea quark is allowed to carry a non-zero momentum fraction and adjustable parameters are required to describe the joint $q - \bar{q}$ recombination function.

The fragmentation models were stimulated by the observation [65] of an equally striking similarity of the Feynman x -distributions of hadrons in soft hadronic collisions to parton fragmentation functions measured in hard processes. These models are, in principle, made parameter free by using a colour separation mechanism and parton fragmentation functions fixed by measurement in $e^+ e^-$ or deep inelastic scattering. A straight-forward application of the phenomenology of quark fragmentation at large p_T to low- p_T reactions would disagree with equation (22) [69], so a mechanism known as the quark "held back" effect was incorporated. A valence quark is "held back" and the inclusive distribution is described by the fragmentation functions of the remaining fast-forward moving quark (or diquark) system. The attempts to provide a firmer

theoretical basis to the held-back mechanism, by invoking the concept of stretching the colour flux tube [70] [71] or through the Dual Model [72] [73], are at the origin of the most successful fragmentation models: the Lund Model [65] [70] [71] [74] [75] and the Dual Parton Model (see section 2.5.1) developed at Orsay.

The Lund and the Dual Parton models differ in philosophy and in the details of their predictions but nevertheless have similarities. In analogy to the physics of $e^+ e^-$ annihilation, both models consider a "perturbative phase" or parton shower responsible for colour separation followed by a fragmentation, described by strings or chains, of the partonic state into hadrons. In the fragmentation regions they behave like the early fragmentation models, in the sense that meson fragmentation looks like quark fragmentation and proton fragmentation is similar in hadronic collisions and in deep inelastic scattering.

The fragmentation models have the advantage over the recombination models of being formulated in a general framework allowing a unified description of the central and fragmentation regions. Moreover they can be extended to hadron-nucleus and nucleus-nucleus interactions without introducing new physical concepts or assumptions. I shall concentrate on the Dual Parton fragmentation model in the following sub-sections. Concerning the still open debate between fragmentation and recombination, I refer to a recent comprehensive review by K. Fialkowski and W. Kittel [62] and the criticisms of various protagonists [76]. Let me also mention that there has been claims that from the point of view of the Dual Topological Unitarisation scheme, the recombination and fragmentation are essentially equivalent parton interpretations of the same dual cylinder component [73].

2.5.1 The Dual Parton Model

2.5.1.1 The Dual Parton Model for hadron-hadron interactions

The confinement related non-perturbative effects in soft-hadronic interactions do not allow a simple extension of the perturbative treatment of quantum chromodynamics (QCD) which provides a firm basis for the parton description of hard processes. A possible solution comes from the study of the correspondences between QCD and the Dual Topological Unitarization scheme (DTU). It is such a study which constitutes the foundation of the Dual Parton Model [67] [72] [73] [77].

In the DTU scheme, given the large values considered for the strong coupling constant, one tries to find a different expansion parameter allowing a perturbative treatment. This is achieved by decomposing the scattering matrix S into an infinite number of topological components. The topological expansion [78] is carried in powers of $1/N$, where N is the number of flavours and the ratio of the number of colours over the number of flavors is maintained fixed [79] [80]. This

expansion in terms of diagrams with increasing complex topology is expected to converge rapidly, and the graphs with the simplest topologies are assumed to dominate [73]. The fixed ratio N_c/N_f permits the introduction of corrections imposed by unitarity [80], and a conceptual link between gauge theories and Regge field theories is obtained. The relative weights between the various terms of the expansion can be determined within the framework of Regge field theory. The first two dominating components correspond through unitarity to Reggeon and Pomeron exchange and one can develop a partonic fragmentation interpretation of these exchange processes [72] [73] [77]. The hadronic scattering amplitudes, at the lowest order in DPU, can thus be considered as providing the "zeroth order" approximation to QCD.

The requirements of a good correspondence to dual-Regge models lead naturally to a situation where the dressed quarks, which saturate the whole momentum of a hadron, behave rather asymmetrically, one fast and the other ones slow [72] [77]. This is the salient feature of the leading order colour separation mechanism in the Dual Parton Model [77]. The interaction (colour exchange) between two nucleons separates the valence quarks of each nucleon into two coloured systems that share the nucleon momentum, one slow with the quantum numbers of a valence quark and the other fast with those of a diquark. In order to neutralize these coloured systems, two multiparticle chains are formed stretching from one nucleon to the other as seen in (a) (Figure 12 on page 35). The corresponding diagrams for the separation of a meson into a quark and antiquark coloured system is shown in (b) (Figure 12 on page 35).

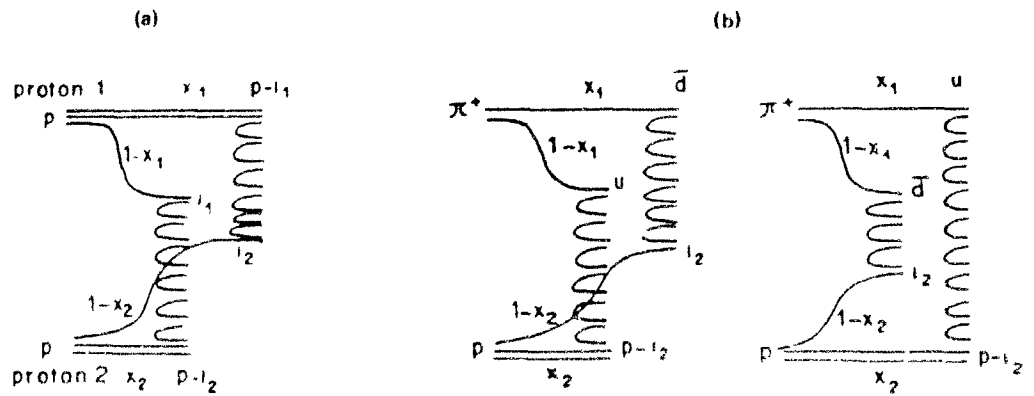


Figure 12 Two chain diagrams for soft particle production in hadronic collisions. In a $p-p$ collision, fig (a), the quarks i_1 and i_2 are "held back" and 4 coloured systems are produced, $i_1, i_2, p-i_1$ and $p-i_2$. The two multiparticle chains are $(p-i_1, i_2)$ and $(i_1, p-i_2)$, each corresponding to 3 colour separation. In a $\pi-p$ collision, fig (b), there are two diagrams corresponding to holding back the quark and holding back the antiquark.

Squaring the diagrams of Figure 12 and summing over the intermediate states, as required by unitarity, gives the cylinder topology of the Pomeron in the Dual Model [77]⁷

In order to specify the colour separation mechanism quantitatively, one introduces the function $\rho_{i_1 i_2}(x_1, x_2)$ which is the probability that the interaction between the colliding nucleons breaks them into two diquark systems with momentum fractions x_1 and x_2 , and two quarks with momentum fractions $(1-x_1)$ and $(1-x_2)$ and with flavors labelled i_1 and i_2 respectively. The function $\rho_{i_1 i_2}(x_1, x_2)$ is assumed to be proportional to the product of the valence quarks distribution functions of the colliding hadrons [77]. The derivation of these momentum distributions, which is based upon the dominance of the Regge singularities studied in appropriate rapidity intervals, gives [81] [82]:

$$\rho^q(x_i) \sim (x_i)^{-1/2} (1-x_i)^{3/2} \quad (23)$$

for a valence quark i in a baryon, and

⁷ Although the Pomeron contribution is of order $1/N^2$, it is found [81] to dominate over the Reggeon contribution which is of order $1/N$ and contains one chain for two back-to-back jets.

$$\rho^q(x_i) \sim (x_i)^{-1/2}(1-x_i)^{-1/2} \quad (24)$$

for a valence quark or antiquark i in a meson.

The model is completed by fixing the rules by which the partons hadronize into observable particles. In most applications of the Dual Parton model, one assumes that the fragmentation functions are universal such that they scale from high Q^2 to low Q^2 processes⁸, i.e. the rapidity density of each chain depends on the nature of the systems at the chain ends but not on the soft or hard nature of the process which produces them. The fragmentation functions are taken from e^+e^- data when the appropriate data is available, or else they are derived from counting rules $\{\sim(1-x)^n\}$. They may also be based on event-by-event Monte Carlo methods for hadronization. Once the fragmentation rules are specified, an inclusive spectrum is simply given by a convolution of quark momentum distribution functions and quark fragmentation functions with weights given by the structure functions. This gives for a $p-p$ collision an equation like

$$\frac{1}{\sigma} \frac{d\sigma}{dy} = \frac{dN}{dy} = \iint dx_1 dx_2 \rho(x_1) \rho(x_2) \cdot \left[\frac{dN_1}{dy}(y - \Delta_1, \bar{P}_1) + \frac{dN_2}{dy}(-y, -\Delta_2, \bar{P}_2) \right]$$

$$\text{with } \Delta_{1,2} = \frac{1}{2} \ln \left(\frac{1 + \beta_{1,2}}{1 - \beta_{1,2}} \right)$$

where $\bar{P}_1(\bar{P}_2)$ is the c.m. momentum of chain 1 (2), β_1 and β_2 are the Lorentz boosts required to go from the c.m. frame of each chain to the overall c.m. frame of the hadronic collision; and $\Delta_1(\Delta_2)$ is the corresponding shift in rapidity for the densities dN_1/dy (dN_2/dy) coming from chain 1 (2) (see ref. [67] for the detailed relations). A schematic representation of the corresponding rapidity distributions in the c.m. frame of a $p-p$ collision is given in Figure 13 on page 37.

⁸ Apart for the scaling violations resulting from the off-shellness of the quarks in hard processes [77]

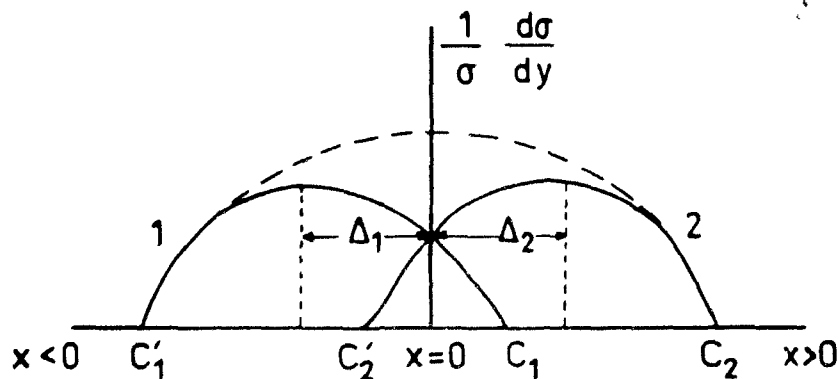


Figure 13: The rapidity distribution of particles in each chain and their sum (dashed line) for a $p-p$ collision. The labels C_1 , C_2 , C'_1 and C'_2 represent the four coloured objects at the chains ends (two valence quark and two diquark systems) and $\Delta_{1,2}$ is the distance between the c.m. of a chain and the overall c.m. A rise of the central "plateau" will eventually arise from an increasing overlap between the two chains

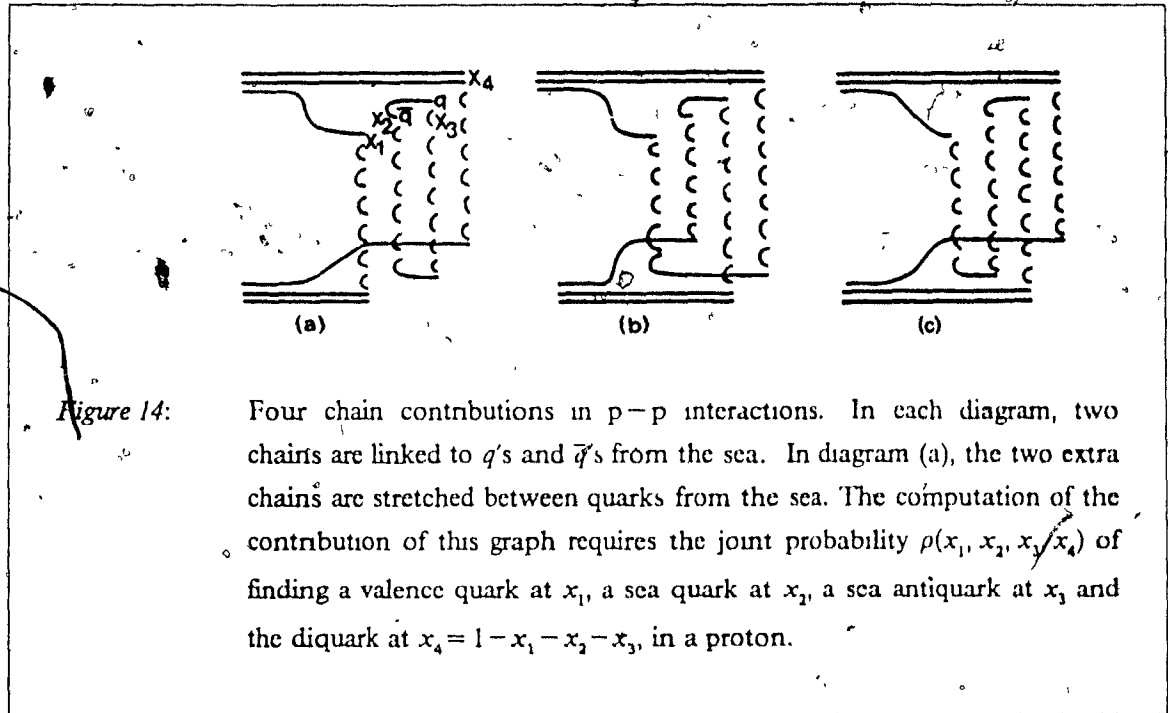
Coming back to the momentum distributions of eqs. (23) and (24), one remarks that the singularity at $x=0$ forces an "held back" slow valence quark in the central region. This implies that the remaining diquark system, which also contains the gluons and the sea, will carry away most of the incoming momentum. The fragmentation of the fast diquark system will often produce a fast "leading" baryon.

The two-chain structure of the colour separation in the leading diagrams, together with the "held back" mechanism and the leading baryon effect, gave to the Dual Parton model a qualitative and quantitative understanding of all low- p_T multiparticle production data up to the highest c.m. energies at the ISR⁹, $\sqrt{s} \sim 60$ GeV. There, the model reproduced the shape and the energy dependence of inclusive spectra both in the fragmentation and central regions [67] [77] [83], as well as the ratio of $\pi-p$ to $p-p$ cross-sections [77] and the relative particle flavor composition in $\bar{p}-p$ and $p-p$ collisions [84].

With increasing \sqrt{s} for the hadronic collisions, the high order terms required by unitarity in the $1/N$ expansion will play an increasingly important role. They correspond to a situation where sea quarks get sufficiently energetic to produce new chains and contribute to the increase of particle

⁹ The CERN Intersection Storage Ring.

production. These higher order terms are related to multiple Pomeron exchange and their relative contributions are calculated within Regge theory [81]. Figure 14 shows four chains diagrams (order $1/N^4$) contributions for $p-p$ collisions.



The sea quark momentum distribution is of the order [81] $\rho(x) \sim 1/x$, and is thus sharply peaked near $x \approx 0$. The chains stretched between sea quarks are in general short and concentrated in the central region so that

$$\bar{x}_{sea} < \bar{x}_{valence} \ll \bar{x}_{diquark}$$

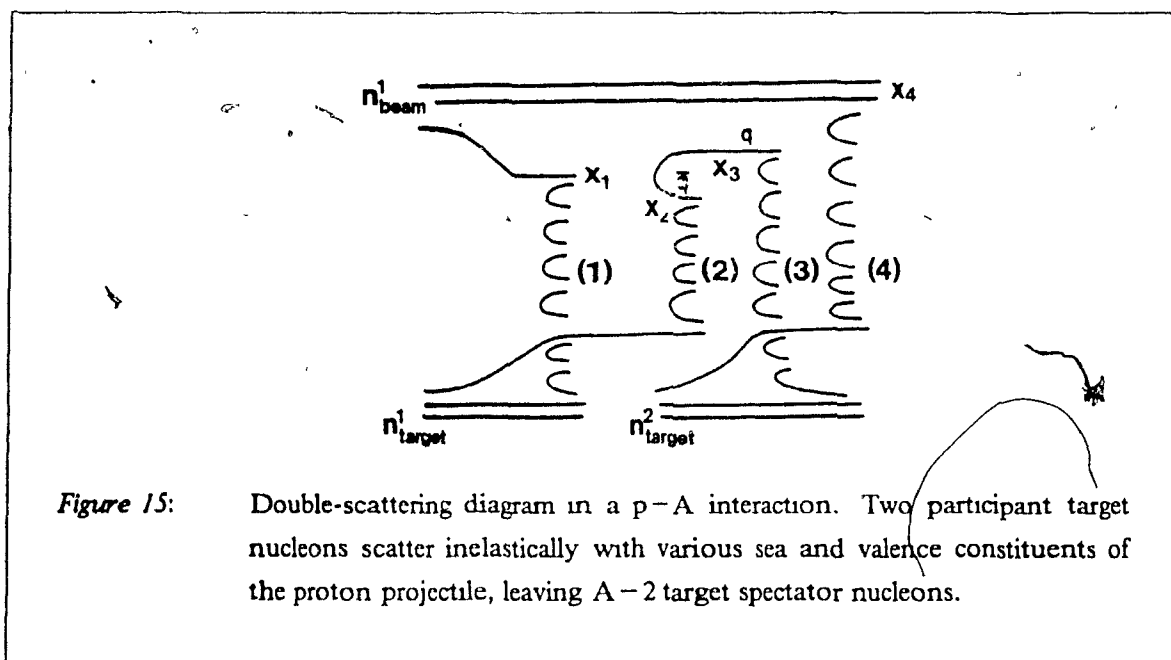
The multichain (> 2) contribution is below the 10% level for hadron-hadron collisions at the highest ISR cm energies [85], but is essential at SPS¹⁰ collider energies where it reaches 30% for $\sqrt{s} = 540$ GeV [81]. In the collider energy domain, various theoretical developments along the lines of the multichain Dual Parton Model were shown to be in reasonable agreement with data for the average multiplicities [86], the rapidity distributions (both inclusive and semi-inclusive) [87], KNO scaling violations and the energy and rapidity dependence of multiplicity moments [85] [88], the long-range rapidity and forward-backward multiplicity correlations [89], the energy dependence of heavy flavour production [85], and the diffractive particle production [88] [90]. With the addition

¹⁰ The CERN Super Proton Synchrotron.

of some intrinsic momentum at chain ends (due to semi-hard scattering or multiple gluon emission), the multichain Dual Parton Model also reproduces the correlation between transverse momentum and multiplicities of secondaries [91].

2.5.1.2 Extension of the Dual Parton Model to hadron - nucleus collisions

The Dual Parton Model can be generalized in a straightforward manner to hadron - nucleus interactions. For this case, in contrast with hadron - hadron interactions, multi-chain diagrams will play an important role. Although such diagrams correspond to higher order corrections in the $1/N$ expansion, they are enhanced in interactions with a nucleus due to trivial combinatorial factors resulting from the possibility of linking the various chains to different nucleons in the nucleus. This is seen for example in Figure 15 showing a double-scattering diagram in a proton - nucleus interaction.



The n inelastic collisions of an incident hadron projectile with n target nucleons correspond to a n - Pomeron exchange¹¹ leading to the formation of $2n$ chains. Here again, the large momentum separation between the systems at the end of each chain will cause the stretching and evolution of the chains, via a colour-confining mechanism, into a jet of hadrons.

¹¹ The associated dual diagram has a complicated topology with $n - 1$ "handles" [92]

In a $p-A$ multiple scattering process (e.g. Figure 15 on page 39), there are four types of chains involved. Chain 1 (4) is stretched between a valence quark (diquark) of the proton projectile and a valence diquark (quark) of a target nucleon. Chains 2 and 3 involve respectively an antiquark (quark) of the projectile sea and a valence quark (diquark) of a target nucleon. For any total number n of inelastic scatterings, the chains 1 and 4 can only appear once (neglecting possible rescattering of fragments) while chains of type 2 and 3 appear $n-1$ times each. The rapidity density of the produced hadron h in an inclusive reaction $p + A \rightarrow h + X$ is thus given by [92] [82] :

$$\begin{aligned} \frac{dN^{pA \rightarrow hx}}{dy}(y) &= \frac{1}{\sigma_{in}^{hA}} \frac{d\sigma^{pA \rightarrow hx}}{dy} \\ &= \sum_{n=1}^A \frac{\sigma_n}{\sigma_{in}^{hA}} \cdot \{N_1^h(y,n) + n_4^h(y,n) + (n-1)[N_2^h(y,n) + N_3^h(y,n)]\} \end{aligned} \quad (25)$$

The inclusive particle spectra N_α^h for chains of type $\alpha = 1, 2, 3$ and 4 is written as

$$N_\alpha^h(y,n) = \int_0^1 dx \int_0^1 dx' \rho_n^c(x) \rho_n^{c'}(x') N_{cc'}(y-\Delta, P)$$

for a chain stretched between a constituent c (quark or diquark of the projectile) at x and a constituent c' (quark or diquark of a target nucleon) at x' . The expressions for the c.m. momentum $P(x, x')$, and for the rapidity interval $\Delta(x, x')$ between the c.m. of the chain and the overall c.m., can be found in ref. [82]. The function $\rho_n^c(x)$ is the $2n-1$ integral over all variables, the variable x of the constituent c of the joint momentum distribution function $\rho(x_1, x_2, \dots, x_n)$ excepted. This latter function being the probability of finding in a proton a valence quark at x , $n-1$ sea quark-antiquark pairs at $x_1, x_2, \dots, x_{2n-1}$, and the diquark at x_{2n} . It can be written in terms of a product of functions derived from single quark momentum distribution functions, as

$$\rho_n(x_1, x_2, \dots, x_{2n}) = C_n f_v(x_1) f_s(x_2) \dots f_s(x_{2n-1}) f_{qq}(x_{2n}) \cdot \delta(1 - \sum_{i=1}^{2n} x_i)$$

with

$$f_v(x) \simeq (x^2 + \mu^2/P^2)^{-1/4}$$

$$f_{qq}(x) \simeq x^{1.5}$$

$$f_s(x) \simeq (x^2 + \mu^2/P^2)^{-1/2}$$

where μ is a transverse mass (~ 0.3 GeV) and P the hadron center of mass momentum.

In order to characterize the main consequences of the above theoretical formulation on the particle production, we define the ratio

$$R(y) = \frac{\left[\int \frac{dN^{pA}}{dy} dy \right]}{\left[\int \frac{dN^{pp}}{dy} dy \right]} = A^{\alpha(y)}$$

In the projectile fragmentation region, $\alpha(y)$ is negative due to the n -dependence of $N_4(y, n)$ arising from energy-momentum conservation. In the Dual Parton Model, the energy carried away via the $2n-2$ sea quark chains resulting from n inelastic scatterings in the target nucleus, is mainly provided by removing energy from the fast diquark in chain 4, which is the only important contribution in the fragmentation region. As the number n increases, chain 4 becomes shorter and consequently $N_4(y, n)$ decreases. If the rapidity distribution N_4 was independent of n , there would be no A -dependence in the projectile fragmentation region, i.e. $\alpha(y) = 0$. At larger y , there will be a cross-over point for which $R(y_0) = 1$. It will occur at a value y_0 independent of the overall c.m. energy and A [82]. In the central region, $\alpha(y)$ is positive and the functions $N_n^h(y, n)$ should only slightly depend on n . Neglecting this weak dependence and using

$$\sigma_{in}^{hA} = \sum_{n=1}^A \sigma_n$$

$$\sum_{n=1}^A n \sigma_n = A \sigma_{in}^{pp}$$

equation (25) becomes

$$\frac{dN^{pA-hx}}{dy}(y) = N_1^h(y) + N_4^h(y) + (v-1)[N_2^h(y) + N_3^h(y)] \quad (26)$$

where the average number of inelastic scatterings is taken as $\bar{n} \equiv v = A \sigma_{in}^{pp} / \sigma_{in}^{pA}$. Here the rapidity densities of chains 1 and 4 are identical to those in a $p-p$ collision, and therefore the average multiplicities follow

$$\bar{N}_1 = \bar{N}_4 = \bar{N}_{pp} / 2 \quad (27)$$

where \bar{N}_{pp} is the average p-p multiplicity. If we further neglect the difference between the valence and sea quarks, i.e. $N_3(y) \sim N_1(y)$, and consider the fact that the chains of type 2 are very short since they have a quark or an antiquark at both ends, i.e. $N_2(y) \sim 0$, we get for the central region from equations (26) and (27) that

$$R \equiv \frac{\bar{N}^{pA}}{\bar{N}^{pp}} = 1/2 (v + 1) \quad (28)$$

In the very high energy limit, all chains will develop independent plateaus of identical heights and the contributions of chains 2 can no longer be neglected. In this limit [82], $R \approx v$. This corresponds to the input assumption of the naive Nucleon Collision Model (2.2 on page 20) for p-A collisions, and at asymptotic energies one approaches an $A^{1/3}$ dependence.

The extension of the Dual Parton model to p-A collisions has been implemented in Multichain Monte Carlo models which have proven to provide good agreement to exclusive and inclusive particle production cross-sections [93], and to forward-backward correlations and the A-dependence of single particle distributions [94]. Moreover, the Dual Parton Model provides a satisfactory description of experimental data on charged multiplicity rapidity distributions. This is seen for instance in Figure 16 on page 43 which shows the fit [82] to pseudorapidity charged multiplicity distributions for central collisions with various nucleus at nucleon-nucleon $\sqrt{s^{nn}} = 20 \text{ GeV}$.

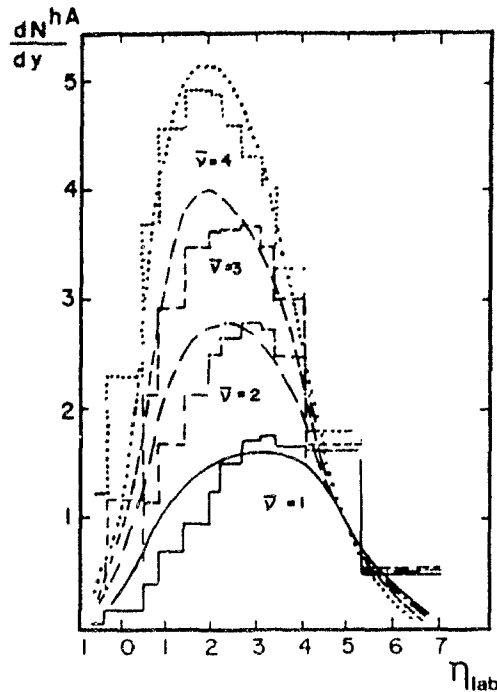


Figure 16: The Dual Parton Model comparison to p-A pseudorapidity charged multiplicity distributions [95] at $\sqrt{s^m} = 20 \text{ GeV}$.

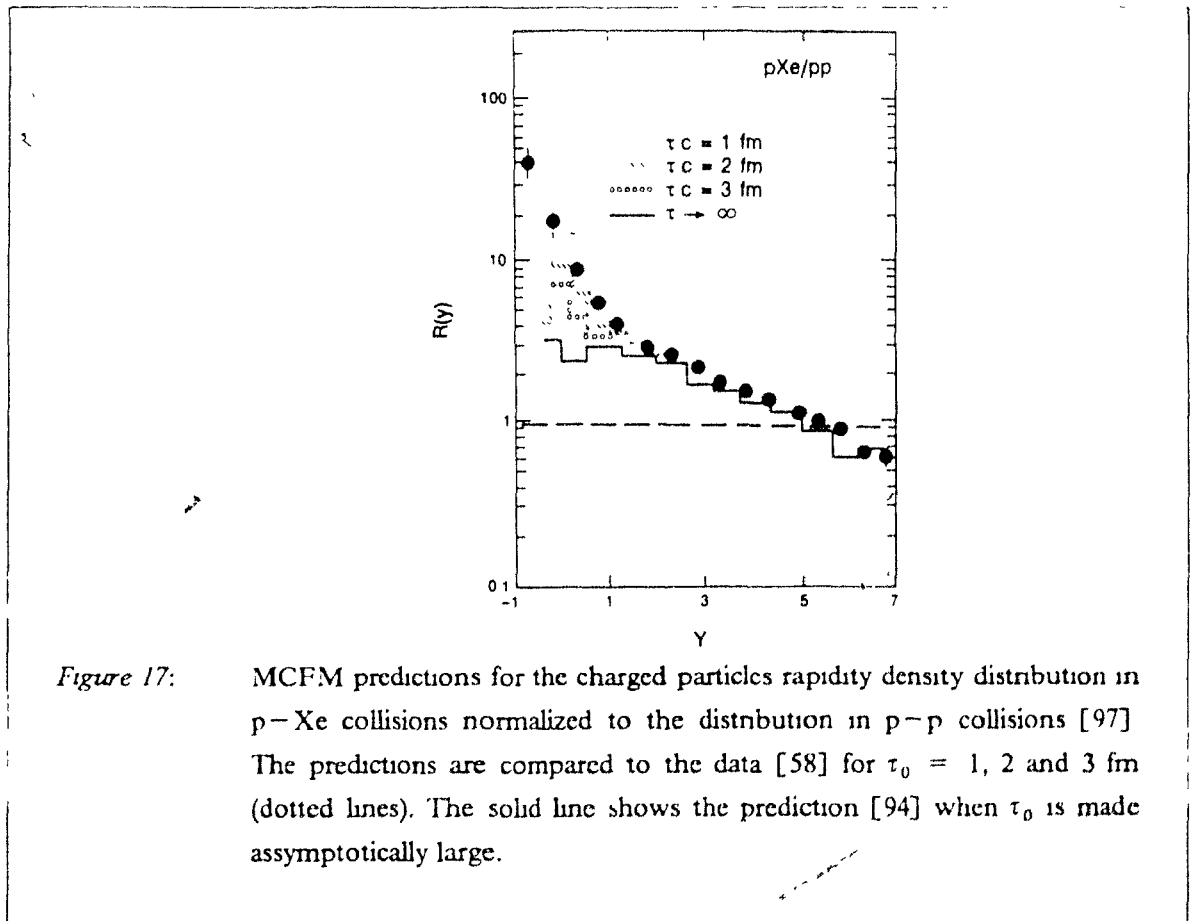
The apparent failure of the model for reproducing the experimental A-dependence in the target fragmentation region may be due to effects of cascading of slow secondaries.¹² These contributions are neglected in the Dual Parton Model as the model does not provide characteristic timescales for hadronization. The effect of the rescattering of the secondaries has been studied with the Dual Monte Carlo Multi-Chain Fragmentation Model (MCFM) developed by Ranft [97]. The DPM was adapted to take into account leading order corrections due to secondary interactions inside the target nucleus via the introduction of an empirical formation time parameter. The virtual secondaries were not permitted to reinteract before an average time τ_0 in their own rest frame, after which they were considered to be present as complete hadronic states. Before they are completely formed, in the context of the DPM, the virtual fragments might be understood as states consisting only of "free" quarks, without the full system of sea quarks, antiquarks and gluons. It is this absence of soft

¹² Similar conclusions are reached in a different extension of the dual approach, developed by Chao et al [96]. They assume that from the first interaction, the chain system linking the fast projectile diquark to a valence quark from a target nucleon can be treated as an "excited projectile system". This excited projectile system has no time to hadronize between successive collisions and it undergoes v collisions giving rise to v "excited target systems". The model naturally gives the high energy limit of equation (28)

components in the hadronic quantum state which is responsible for the reduced probability of hadronic interactions. The MCFM allows one to follow the full space-time history of the collisions, i.e. the vertex coordinates of the elementary collisions in which the nucleons are engaged are known and the energies and momenta of the secondaries are specified. The trajectories of the secondaries are followed in space-time and, in the rest frame of the target nucleus, the particles may reinteract after a dilated time interval of $\gamma\tau_0$. Most slow secondaries thus have a chance to reinteract while most fast secondaries are created outside the target nucleus volume. The influence of the formation time τ_0 on the contribution of rescattering to the particle production is shown in Figure 17 where the predictions of MCFM are compared to the measured [58] rapidity density ratio

$$R(y) = \frac{(dN_{pXe}^{ch}/dy)}{(dN_{pp}^{ch}/dy)}$$

The relative increase of the charged multiplicity density in the target fragmentation region for $p-Xe$ collisions is well reproduced for values of the formation time parameter ranging from $\tau_0 c = 1$ to 2 fm.



2.5.1.3 The Dual Parton Model for nucleus - nucleus collisions

In further extension of the model to nucleus-nucleus collisions [98] [99], the colour separation mechanism follows immediately from the "rules" developed for hadron-nucleus. For example, let us consider the configuration in which n_A nucleons of nucleus A interact inelastically (get "wounded") with n_B nucleons of nucleus B, via a total of n inelastic collisions. The available fragments will be n_A (n_B) valence quarks and diquarks from nucleus A (B). In the case where $A \leq B$ and $n_A < n_B$, the chains involving valence constituents are n_A chains of type $(qq)_A - q_B^v$ and n_A chains of type $q_A^v - (qq)_B$, $n_B - n_A$ chains of type $\bar{q}_A^v - q_B^v$ and $n_B - n_A$ chains of type $q_A^v - (qq)_B$, where the indices v and s are labelling valence and sea quarks. The valence constituents are thus contained in $2n_A + 2(n_B - n_A) = 2n_B$ chains. Having taken care of all valence constituents and since the dual formulation requires that the n inelastic scatterings lead to $2n$ chains, the remaining $2n - 2n_B$ chains will have to be of the type $\bar{q}_A^s - q_B^s$ (or $q_A^s - \bar{q}_B^s$). As seen for the hadron-nucleus case, in order to make quantitative predictions concerning for instance rapidity density distributions, one would need to know the joint momentum distribution function giving the probability for each valence or sea quark involved to carry a certain momentum fraction, averaged over all possible configurations for a given impact parameter. In other words the rapidity distribution from a given chain depends not only on n_A , n_B and n , but also on new indices specifying the ordering and the number of inelastic collisions that each of the n_A and n_B wounded nucleons has undergone. The resulting full combinatorial complications and the corresponding chain configurations probabilities have been worked out under simplifying assumptions in ref. [100], but generally it can only be handled in Monte Carlo applications of the Dual Parton Model. For the moment the problem shall be restricted to the attainment, for averages at fixed impact parameter (i.e. central collisions), of approximate formulas when drastically neglecting energy-momentum conservation. In such a case, the rapidity density is written as [99]

$$N^{AB}(y) = \bar{n}_A \cdot \{vv\} + (\bar{n}_B - \bar{n}_A) \cdot \{sv\} + (\bar{n} - \bar{n}_B) \cdot \{ss\} \quad (29)$$

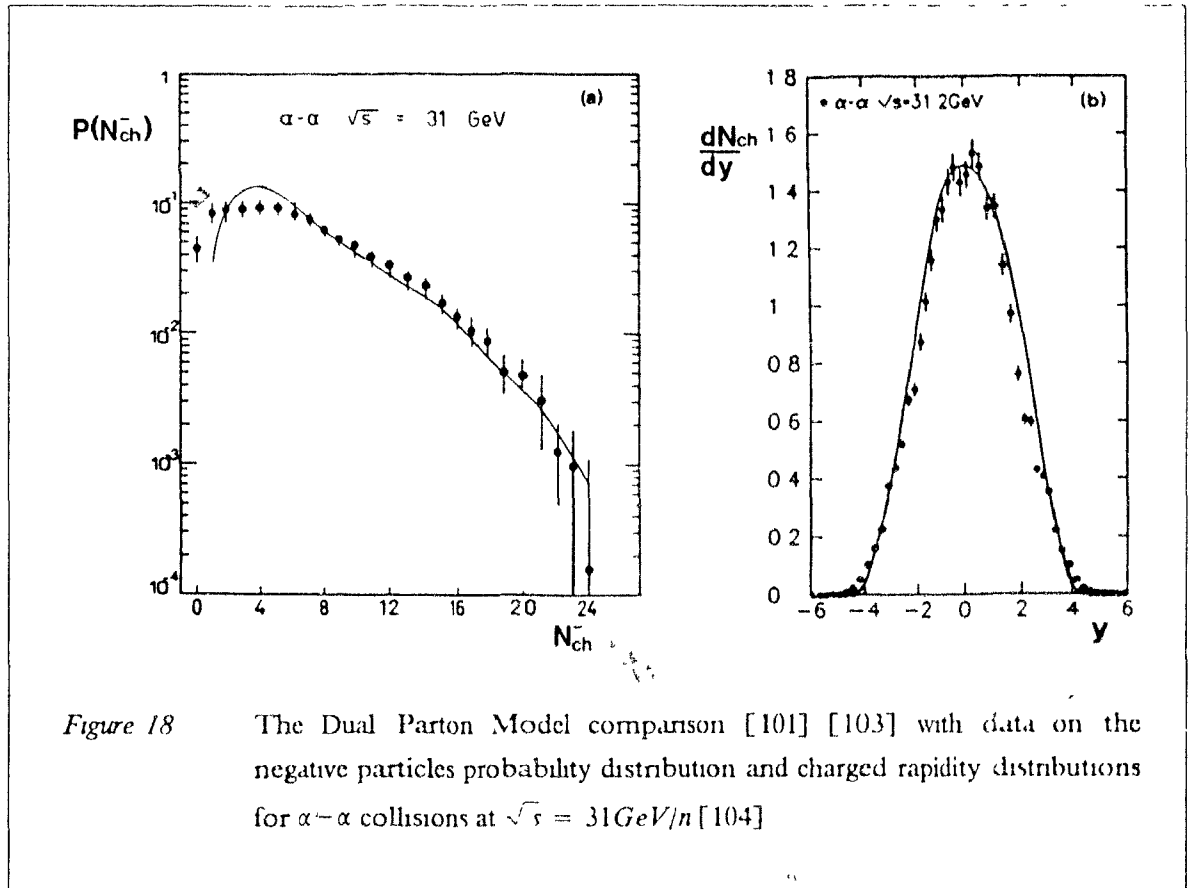
where

$$vv(y) \equiv N^{(qq)_A - q_B^v}(y) + N^{q_A^v - (qq)_B}(y) \quad (30)$$

$$sv(y) \equiv N^{\bar{q}_A^v - q_B^v}(y) + N^{q_A^v - (qq)_B}(y)$$

$$ss(y) \equiv N^{\bar{q}_A^s - q_B^s}(y) + N^{q_A^s - \bar{q}_B^s}(y)$$

These approximate equations have been found to provide good agreement with nucleus-nucleus rapidity distributions measured in cosmic ray experiments in the TeV/nucleon range [99] and with negative particles multiplicity, total energy and probability distributions in α - α collisions at nucleon-nucleon $\sqrt{s} = 31 \text{ GeV}$ [98] [99] [101] [102] [103]. Some of the results for α - α collisions are shown in Figure 18



Using the notations (30), the approximate formula (29) may be rewritten [99] in terms of the mean nucleon-nucleon rapidity distribution as

$$\frac{dN_{AB}}{dy} = \frac{dN_{NN}}{dy} \left[\bar{n}_A + (\bar{n}_B - \bar{n}_A) \cdot \frac{sv(y)}{v(y)} + (\bar{n} - \bar{n}_B) \cdot ss(y) \right] \quad (31)$$

This can be compared to the corresponding formula in the simple Wounded Nucleon Model (section 2.2 on page 20)

$$\frac{dN_{AB}}{dy} = \frac{dN_{NN}}{dy} \left[\bar{n}_A + (\bar{n}_B - \bar{n}_A) \beta(y) \right] \quad (32)$$

where $\beta(y)$ is a function to be extracted from hadron - nucleus data. The difference between (31) and (32) resides in the additional sea quark term in (31). The basic ad hoc assumption within the Wounded Nucleon Model of an approximate scaling in terms of the number of wounded nucleons, thus finds a support only if $\bar{n} - \bar{n}_p$ is small enough (i.e. close to one scatter per participating target nucleon) and/or if the sea quark - antiquark densities can be neglected. The latter condition is fulfilled outside the central rapidity region for nucleon - nucleon $\sqrt{s} \leq 40 GeV$ [99], but there the energy-momentum conservation should be properly treated and so the approximations leading to (31) may not be justified

In Chapter 5, I will describe and make use of multichain Monte Carlo models based on the colour separation mechanism of the Dual Parton Model. The predictions of these models, the IRIS event generator developed by Pansart [105] and the Dual Monte Carlo Multi-Chain Fragmentation Model developed by Ranft [97], will be compared to the data

Chapter 3

Observables in HELIOS experiment

3.1 The hadronic and nuclear beams

The HELIOS experimental set-up is installed in the H8 beam line at the CERN Super Proton Synchrotron (SPS). The SPS nominally operates at intensities up to 10^{12} protons per burst (2.4 sec) with a maximal momentum of 450 GeV/c. An attenuated primary beam of $\sim 10^6$ protons can be deflected in H8. By means of a production target, beams of secondary high energy hadrons with momentum of 200 GeV/c at rates of $\sim 10^7$ per burst are also available.

In late 1986, the CERN accelerator complex proceeded to the extraction and acceleration of fully stripped oxygen ions. The acceleration chain comprised a linear accelerator (Linac1), which first brought the nuclei to an energy of 12 MeV/nucleon, and transferred them in a synchrotron from where they were injected at 260 MeV/nucleon in the CERN Proton Synchrotron (PS). The nuclei were boosted up to 10 GeV/nucleon in the PS before injection in the SPS where they were finally accelerated to energies of up to 200 GeV/nucleon. Intensities of $\geq 10^8$ ions per burst (4.2 sec) were transported in the SPS where high rate was a minimum requirement for adequate beam control. In view of the large cross-section and high multiplicity expected in nucleus-nucleus collisions, this intensity was reduced for HELIOS activities by a factor $\sim 10^3$. This reduction was achieved on the extracted ion beam by means of steel-septum magnets, and in the H8 secondary transport beam system by using cylindrical and slit collimators. The physics data taking profited from beams of $\geq 10^5$ ions per burst focused, at the target position, in a ellipsoidal profile with gaussian spread of $(\sigma_x, \sigma_y) \sim (0.5\text{mm}, 1.2\text{mm})$. In the following sections, after a brief general overview of the HELIOS experimental set-up, I will describe the detector components used to measure observables relevant for the study of ultra-relativistic ion collisions.

3.2 Survey of the experimental set-up

The HELIOS multi-purpose detectors were designed to operate both with hadrons and nuclei incident beam. Using the proton beam, the lepton program of the experiment aims at settling open questions in the production of electrons, muons and neutrinos in $p-p$ and $p-A$ interactions. Prominent among these are e/μ universality, anomalies in the production of single leptons, contribution of charm decay to lepton pair (Drell-Yan) production, and "anomalous" low mass pairs. The HELIOS ion program involves ultra-relativistic nucleus-nucleus collisions where both compression and heating should allow the production of states of high-energy densities over extended volumes. High densities are a necessary condition for the creation of a plasma of "deconfined" quarks and gluons.

A schematic top view of the set-up is shown in Figure 19.

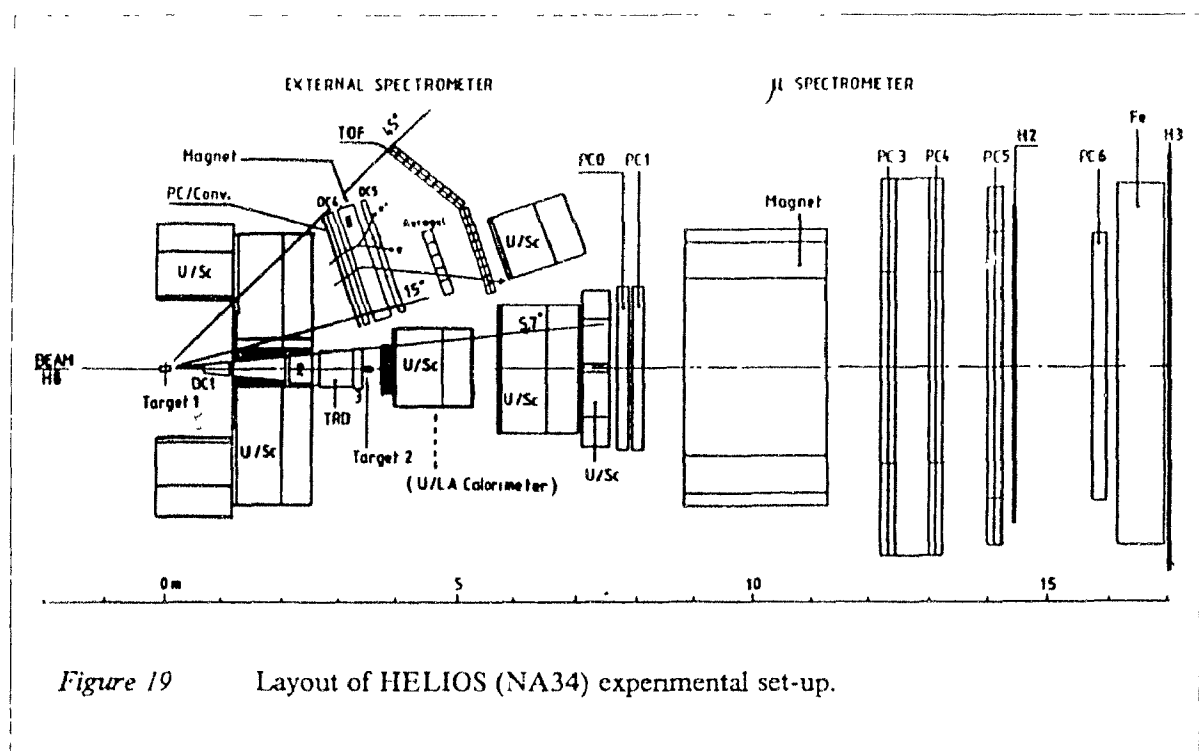


Figure 19 Layout of HELIOS (NA34) experimental set-up.

The experimental design for the lepton program consists of four major components: the target-vertex trigger system including silicon charged multiplicity counters, the compact electron spectrometer utilizes drift chambers with high multitrack capability, a "weak field" calorimetrized magnet, transition radiators and fast high resolution liquid argon calorimetry; the Uranium/Scintillator calorimeters extend the energy coverage for accurate measurement of missing energy; the muon spectrometer, comprising a magnetic spectrometer and an hadron filter. The 4π -coverage of the

calorimeter for the measurement of the energy flow, in the center-of-mass (c.m.) frame, is a powerful tool in the ion program, allowing a full reconstruction of the events topologies as well as providing a trigger on transverse energy in various pseudorapidity intervals. The main other component for the heavy ion physics program is an external spectrometer that views the target through a slit in the calorimeter wall. It uses Time-Of-Flight and Threshold Cherenkov detectors giving good $\pi/\kappa/p$ separation, two proportional chambers spaced by a thin converter for photon detection and drift chambers coupled with a magnet for electron momentum analysis.

3.3 The beam telescope and general trigger system

Two small scintillator counters placed at 23.0 cm and 21.5 cm before the target are used to define the arrival of a beam nucleus and to provide a determination of its charge by dE/dx measurement. The first beam scintillator is 5 mm thick and has a cross-sectional area of $6 \times 6 \text{ mm}^2$ which ensures a full overlap with the beam profile. This counter is thick enough to give good time resolution as its signal defines the time reference t_0 ($\equiv 0$ sec) of the experiment. A coincidence between the two beam scintillator counters generates a valid beam strobe only if a beam coincidence has not occurred within the before protection interval $\Delta = 500$ ns. The basic requirement defining a valid interaction in the passive target is a coincidence between a valid beam and a minimum charged track multiplicity detected in a silicon array located at 9.0 cm behind the target. The silicon pad array provides a fast analog output whose amplitude is proportional to the number of low level discriminators set in the region $\eta_{lab} > 5$ ($\theta > 0.77^\circ$). This signal is discriminated to provide the multiplicity identifying an interaction. A valid interaction further requires no other interaction in the before protection interval $\Delta = 1200$ ns.

The components of the trigger logic relevant for the present discussion are shown in Figure 20 on page 51.

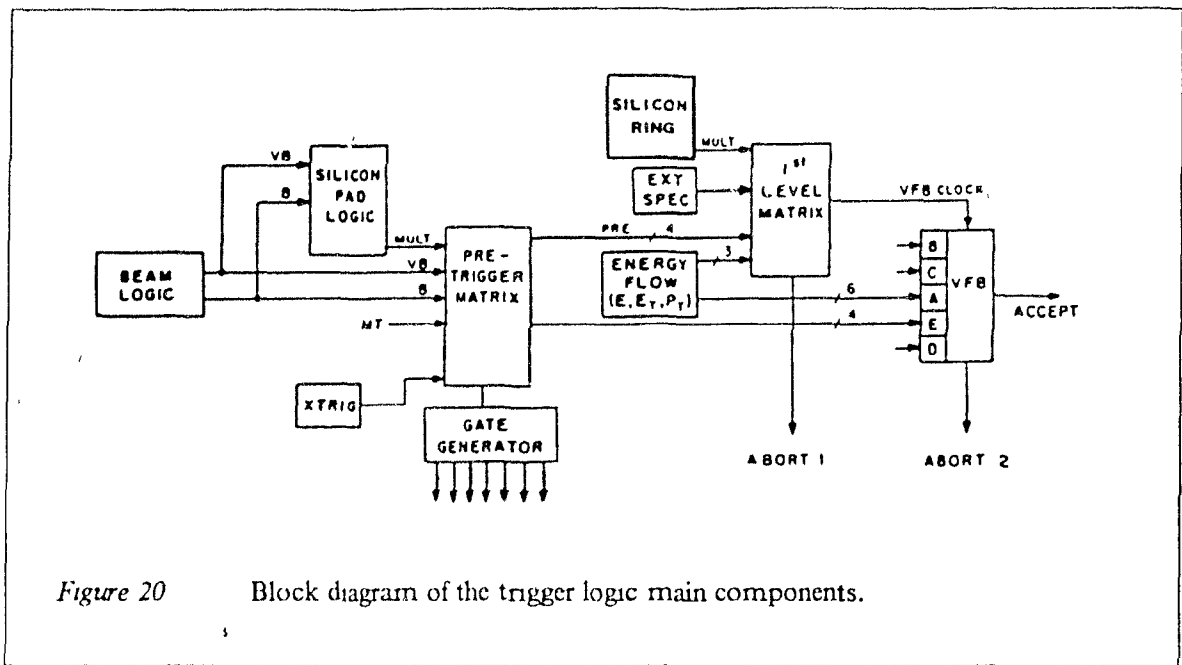


Figure 20 Block diagram of the trigger logic main components.

The beam logic and the silicon logic are the main components of the pre-trigger which causes the information from each of the detectors to be stored in ADC's, DTR's, TDC's, etc. This happens at approximately $t = t_0 + 340 \text{ ns}$. A pre-trigger may also be an artificial "empty" pre-trigger generated randomly and used for controlling pedestal stability of various detectors components. A late beam or late interaction abort is issued if a beam coincidence occurs within an after protection interval of $\Delta = 300 \text{ ns}$ or if an interaction occurs within $\Delta = 700 \text{ ns}$. After the pre-trigger, the energy flow logic begins to process the calorimeter information which is digitized and combined to obtain values of E_{tot} , E_T , and p_T . These values are compared to the lowest threshold in a comparator and, if a threshold requirement is satisfied, a trigger flag signal is generated. This decision happens at $\sim 800 \text{ ns}$ after the beam particle crossing. If an abort is to be issued, a fast clear order is given to the units that stored information at pre-trigger time. An excess dead time of $\geq 1.2 \mu\text{s}$ is inserted to permit the data acquisition electronics to clear and to ensure stable pedestal values in the charge sensitive ADC's. After all the subsystems have completed their trigger evaluations, a Very Fast Bus is clocked to reach a final decision. There, the relative population of various types of triggered events is weighted via downscale factors n_i so that only every $n_i + 1$ event of type i is effectively stored on a buffer to be transferred to magnetic tape in between beam bursts.

3.4 The silicon detectors for the charged multiplicity measurements

A fine granularity measurement of the charged multiplicity flow is obtained in the pseudorapidity¹³ region $0.9 < \eta_{lab} < 5.0$ with a set of silicon detectors equipped with a segmented pad readout and placed at 3 and 9 cm behind the target. Both detectors were centered on the nominal beam axis, to a precision of few microns, by the means of an optical telescope.

A 300 μm thick silicon pad (Si-pad) detector [106] covering $2.5 < \eta_{lab} < 5.0$ is centered on the beam axis 9.0 cm behind the target. It consists of an array of 400 silicon pad segments varying in size from $0.02 \times 0.167 \text{ cm}^2$ to $0.167 \times 0.66 \text{ cm}^2$. The pseudorapidity coverage for the multiplicity measurement is extended to the region $0.9 < \eta_{lab} < 2.8$ by a 250 μm thick silicon ring (Si-ring) detector placed at 3.0 cm behind the target, and made of 384 segments approximately equally spaced in pseudorapidity. Both silicon detectors were operated at full depletion and the boundaries between individual segments are made of 40 μm of fully active oxide. The layouts of the Si-pad and Si-ring detectors are shown in Figure 21.

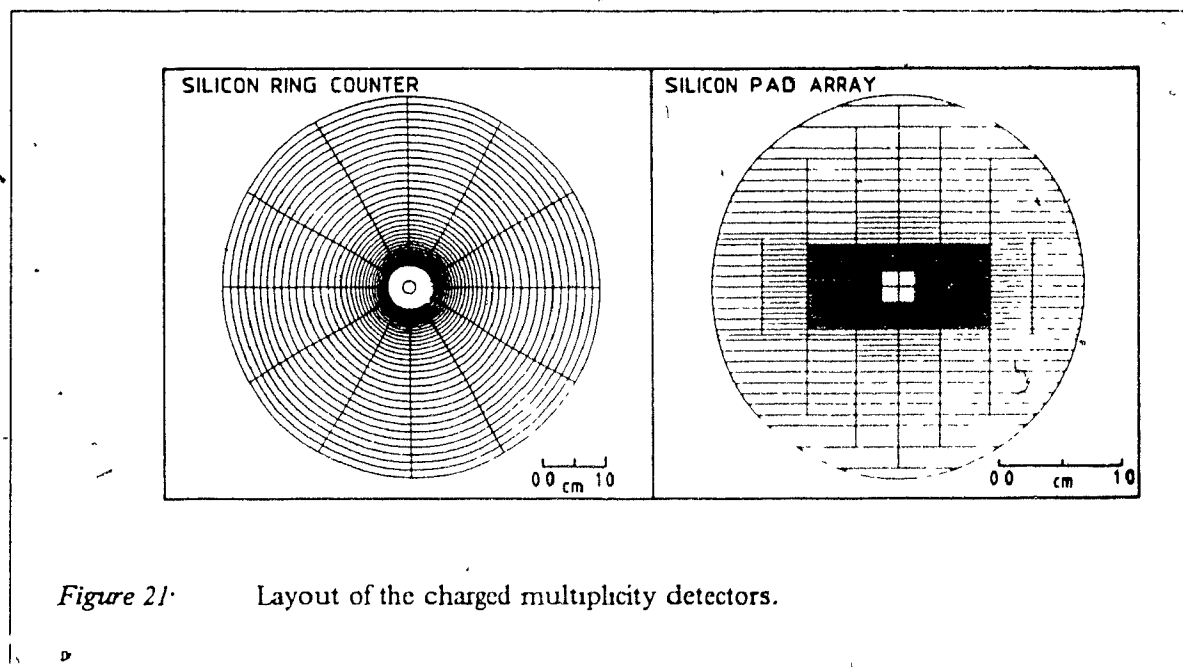


Figure 21. Layout of the charged multiplicity detectors.

The pad (ring) elements are connected to preamplifiers via a two-step bonding, firstly from the silicon to a ceramic overlay, and then to a printed circuit board with connectors for flexible jumpers. The

¹³ The pseudorapidity η_{lab} is defined as $\eta_{lab} = -\ln\{\tan(\theta_{lab}/2)\} = \ln\{(p+p_L)/p_T\}$. For $m = 0$ it is equivalent to the Lorentz invariant (omitting c 's) $y = 1/2\ln\{(E+p_L)/(E-p_L)\} = \ln\{(E+p_L)/m_T\}$.

overlay is made of standard 600 μm "thick film" ceramic on which a gold paste was deposited by serigraphic method. The motherboard is made of G10 (G30) material. This material has thermal properties compatible with the ones of ceramic.

The signal from each individual pad or ring segment is sent to charge integrating ADC's and to discriminators (the readout chain of the Si-ring detector includes a charge sensitive preamplifier, an intermediate amplifier followed by a shaper and peak sensitive ADC). As mentioned in the previous section, the discriminators allow the formation of a fast analog sum used for trigger purposes. Each of the pad or ring segment was individually calibrated by fitting a modified Landau function to the pulseheight distribution measured in low multiplicity events [106] [107]. For the segments of both detectors, the signal-to-noise ratio, taken as the ratio of the most probable energy loss to the r.m.s. width of the pedestal, is ≥ 10 for single particles. This is slightly degraded for actual high multiplicity events due to possible charge contamination coming from neighbouring elements (charge-sharing resulting from the passage of a particle near the border ($\leq 20 \mu\text{m}$) of a segment). More details on the silicon detectors design and performances can be found in [106] [107]. During the 1986 heavy ion data taking period, about 25% of the active area of the Si-pad and 30% of the active area of the Si-ring were not operational due mainly to broken bonds on the detectors themselves. The detectors were otherwise stable during the data taking period and no degradation of performances due to radiation damage was observed.

3.5 The 4π calorimetry

3.5.1 General description and mechanical properties

The measurement of the energy flow is performed in calorimeter elements covering $\sim 4\pi$ in the c.m. frame. The target is surrounded by an almost hermetic "box" of calorimeter modules that covers opening angles from $\sim 6.3^\circ$ ($\eta_{lab} = 2.9$) up to $\sim 95.7^\circ$ ($\eta_{lab} = -0.1$). The perpendicular distance from the target to the various walls of the box is approximately 120 cm in all directions. The forward region ($\eta_{lab} \geq 2.9$) is covered by calorimeter modules placed further downstream. An overview of all calorimeters is shown in Figure 22 on page 54.

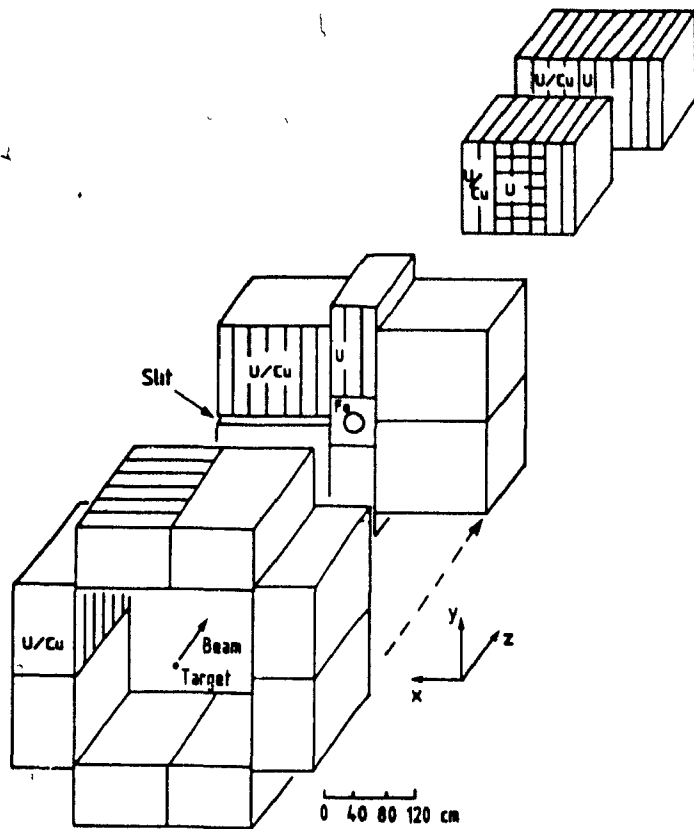
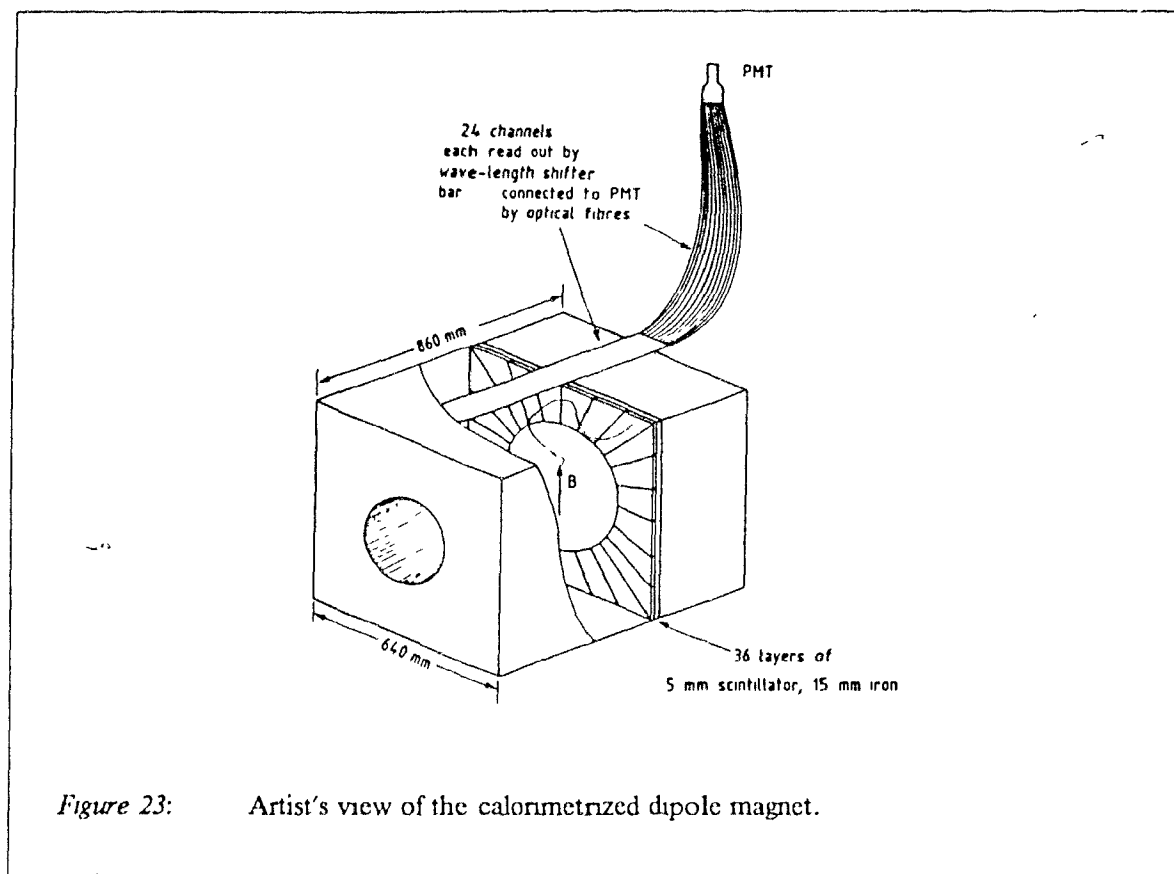


Figure 22: Overview of the calorimetric components of the experimental set-up. The target is surrounded by a calorimetrized dipole magnet, U/scintillator and U/Cu/scintillator modules covering the full solid angle in the c.m. frame of a nucleus-nucleus collision at 200 GeV/nucleon. The external spectrometer, not shown here, views the target through the 20 msr slit.

The forward region of the box ($2.2 < \eta_{lab} < 2.9$) is occupied by a calorimetrized dipole magnet (Figure 23 on page 55). It consists of an iron yoke of cross-section $64.8 \times 64.8 \text{ cm}^2$ with a maximum depth of 32 interaction lengths (λ_i) into which is bored the 6.3° conical hole. The sampling consists of 1.5 cm Fe plates alternating with 0.5 cm scintillator plates.



It is divided azimuthally into 24 "petals" covering $\sim 15^\circ$ each, and read out by plastic Wave Length Shifter (WLS) bars coupled to the PMs via light-guides made of 1 mm diameter optical fibres about 1 m in length. Optical fibres were used because some degree of flexibility was needed due to severe space constraints

The rest of the box is built up from U/scintillator and U/Cu/scintillator modules (Figure 24 on page 56). Both types of modules consist of metal plates interleaved with 0.25 cm thick scintillator plates. These modules are divided into an electromagnetic and a hadronic section. The electromagnetic section is 6.4 radiation lengths deep and contains 0.2 cm thick depleted U plates. The hadronic section for the U/scintillator modules is 4.0λ , deep and contains 0.3 cm U plates. The hadronic section for the U/Cu modules is 3.8λ , deep and the U plates alternate with 0.5 cm Cu plates in the ratio 2:1.

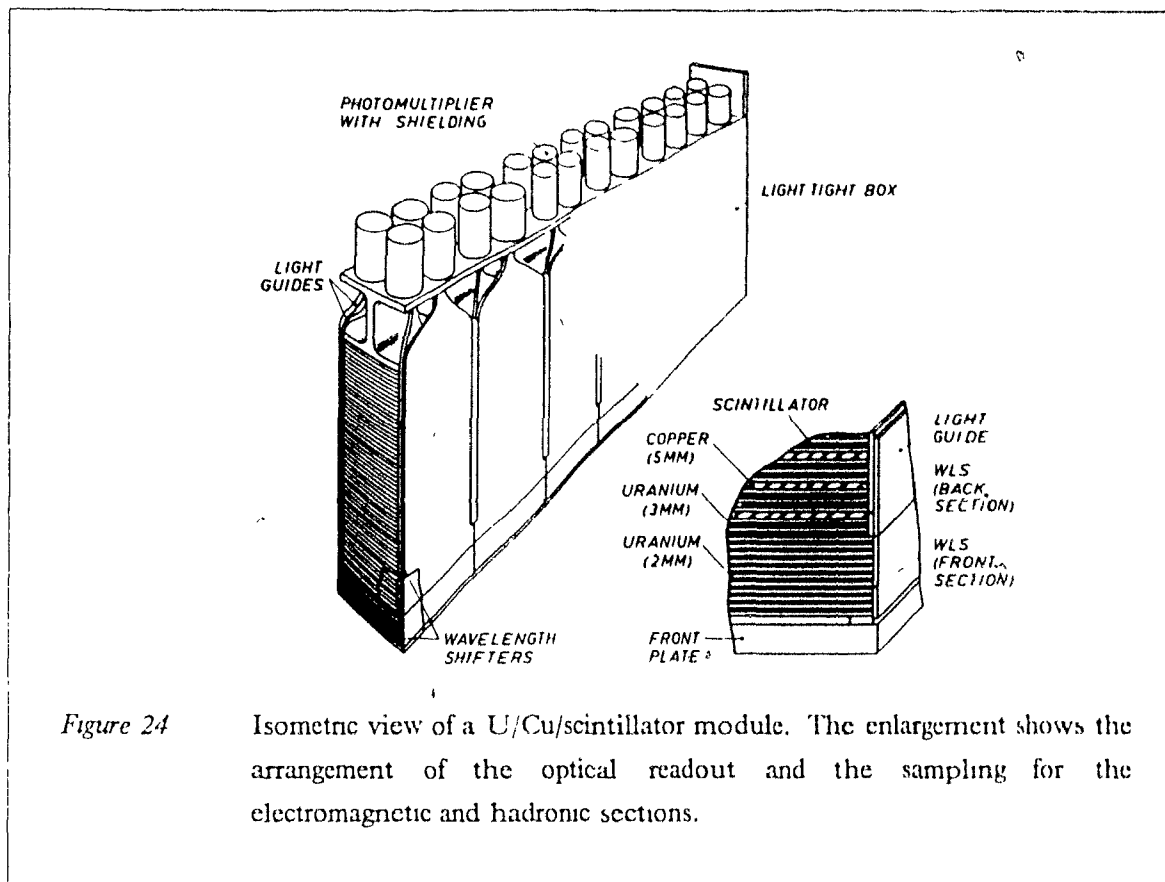


Figure 24

Isometric view of a U/Cu/scintillator module. The enlargement shows the arrangement of the optical readout and the sampling for the electromagnetic and hadronic sections.

In both sections, the scintillator plates ($\sim 120 \times 20 \text{ cm}^2$) are read out on both sides by six independent 0.2 cm WLS plates, producing a $20 \times 20 \text{ cm}^2$ tower structure and giving 24 channels per module. The modules containing only uranium metal plates have the advantage of giving more uniform response to electromagnetic and hadronic showers, and so were placed in a region where we expect the maximum transverse energy deposition.

A substantial fraction of the incident energy is carried away by particles passing through the forward conical hole and is detected in the downstream U modules which provide $10.5\lambda_1$ of sensitive depth. In order to limit the light sharing between the towers of the most forward modules, the 6 towers are optically decoupled by slits of 0.5 mm width made in the scintillator plates with a 600 W CO_2 laser. Polished surfaces of high quality can thus be obtained inside the slits. In order to avoid cross-talk by light refraction, reflectors of aluminized Mylar were mounted inside the slits. The light containment in optically decoupled towers will allow better energy localization in the very high energy and multiplicity environment of the forward rapidities.

A slight overpressure of nitrogen is maintained in each individual module to avoid radiation induced deterioration of the optical components.

3.5.2 The absorbent, the readout, and the light collection uniformity

In general, the relationship between the signal in the readout and the true energy deposited in a calorimeter depends strongly on the type, energy, and shower history of the individual incident particles. The design criteria governing the choice of the absorbent and readout media and nature of the light collection system, are based on an attempt to maintain good energy resolution while approaching the ideal situation of exact linearity and equal response ($e/\pi = 1$) for electromagnetic and hadronic showers. This is particularly important in a large multiplicity environment (e.g. heavy ion collisions) where clusters due to individual particles are not resolved

While constructing the U/scintillator modules, we reviewed and optimized the properties of the optical readout system, and investigated the fundamental mechanisms governing the response of a sampling calorimeter to electromagnetic and hadronic showers. I shall mainly summarize here the results that had direct implications for the treatment of the calorimeter information in the ion physics program. That concerns results that directly influence the signal handling and energy calibration procedure (section 3.5.3 on page 69) or the data analysis and Monte Carlo simulations of the calorimeter response (Chapter 4). A more general account of the above mentioned calorimeter studies would clearly be outside the scope of this thesis and we shall mainly refer to recent publications for a more detailed discussion

The choice of absorbent and readout material and thicknesses determines the intrinsic quality of the resolution and linearity of a sampling calorimeter. The reference scale for the calorimeter response can be defined as the response to an idealized exactly minimum ionizing particle¹⁴ (\equiv mip). The fraction of the total energy deposited that a mip spends for ionization loss in the active medium is simply calculable from well known mean dE/dx values in different materials [108]. For example, the mean energy loss of a mip is $(\Delta\bar{E})_0 = 20.66$ MeV/cm in uranium and 2.29 MeV/cm in our PMMA scintillator readout material. Hence, for a (3mm U)/(2.5mm scintillator) sampling, a mip deposits 8.6% of its energy in the active layer. The response of a calorimeter is characterized by comparing this number to the fraction of the energy deposited in the active layer by electromagnetic (e/mip ratio) or hadronic (h/mip) showers.

For electromagnetic showers, the overall e/mip ratio can be rewritten as a sum over the sampling layers n of an effective ratio $\{e/\text{mip}\}^{\text{eff}}(n)$ multiplied by the shower profile $\Delta E_n/E$:

$$\left(\frac{e}{\text{mip}}\right)^{\text{overall}} = \sum_n \left\{ \frac{e}{\text{mip}} \right\}^{\text{eff}}(n) \cdot \frac{\Delta E_n}{E}$$

¹⁴ minimum ionizing particle

Both the overall e/mip ratio and the evolution of the effective e/mip as a function of shower depth are of interest. It is a well known experimental fact that the overall e/mip ratio¹⁵ for a sampling calorimeter with $Z^{absorbent} \geq Z^{readout}$ satisfies $e/mip \leq 1$ [109] and varies roughly linearly with the ratio $Z^{readout}/Z^{abs}$. There are various contributions to this fact. A contribution comes from the so-called "transition effect" [110]. The high-Z absorbent material has a critical energy ϵ (i.e. energy below which the electron loses more energy by ionization than by bremsstrahlung) much lower than that of the low-Z readout material. The equilibrium number of secondary electrons scales with the critical energy of a medium and a rapid reduction of the number of electrons will occur as the shower passes the boundary between high-Z and low-Z material. This reduction is thought to happen because the materialization rate per radiation length (X_0) of the photons remains unchanged at crossing while the collision losses of the electrons suddenly increase by a large factor. In our calorimeter modules, the readout medium has only a thickness of $0.0073 X_0$, and for $\epsilon^{readout}/\epsilon^{abs} \sim 4$ we only expect a small ($\leq 5\%$) change of the electron flux. The shower development will be essentially governed by the properties of the $\sim 1 X_0$ thick absorbent material. Other contributions [111] to the relative suppression of the electron response may come from the decrease of the average track length (which scales like E/ϵ) in the readout due to the larger critical energy, or from the effect of multiple scattering which tends to increase the effective path length in the high-Z absorbent relative to the low-Z readout. We investigated another possible source of suppression coming from the low energy photons in the tail of the electromagnetic shower. It turned out that the response to low energy γ 's (≤ 1 MeV) is a dominant source of suppression of the electromagnetic signal. EGS4 Monte Carlo simulations [112] indicate that $\sim 40\%$ of the shower energy is deposited by particles that are softer than ~ 1 MeV. Because of the photoelectric effect which dominates for low energy photons and which cross-section scales with Z^5 , the photons interaction cross-section is very much larger for the high-Z absorbent than for the low-Z readout (see for instance the mass attenuation coefficients in [113]). Most of the soft photons will transfer partly (Compton effect) or totally (photoelectric effect) their energy to the electrons of the absorbent media. These electrons are generally stopped before they can reach the readout media. Quantitative results concerning the effect of the low energy photons suppression mechanism were presented in refs [113] [114]. Among the most important effects is the fact that the e/mip ratio will strongly vary with the absorbent plate thickness for sufficiently thin plates ($\leq 1 X_0$), and more abruptly for larger ($Z^{abs} - Z^{readout}$) differences. This is due to the increased probability for the soft photons to transfer their energy to electrons close to the surface of the absorbent plate, i.e. electrons that can escape the absorbent and contribute to the measured signal. Hence the e/mip ratio can be "tuned" for sufficiently thin absorbent plates, but at the expense of a sizeable contribution to the multiparticle resolution (e/mip then function of the angle of incidence). In our modules, the absorbent plates are sufficiently thick to minimize the

¹⁵ In most cases, relativistic muons are used and the energy dependent e/μ ratio is measured. In order to be able to compare different results, the energy deposition of the muons should be corrected back for the rise of the average energy loss due to energy (and material) dependent effects such as δ -ray production, bremsstrahlung, e^+e^- pair production, etc.

contribution of the e/mip fluctuations to the energy resolution¹⁶. Another important effect is the decrease of the effective e/mip ratio with increasing shower depth due to the increasing fraction of the shower energy carried by slow particles. As will be seen in section 3.5.3 on page 69 this has important consequences when attempting to use electromagnetic showers to intercalibrate a longitudinally segmented calorimeter.

In order to optimize the performances for the detection of hadronic showers, in terms of linearity and energy resolution, a calorimeter should have equal relative response to the purely electromagnetic (e.g. π^0) and hadronic components of the showers. This allows to minimize the degradation of the energy resolution and linearity caused by the large event-by-event fluctuations, and average logarithmic increase with energy, of the fraction of the shower's energy used for π^0 production. For most sampling calorimeters with $Z^{had} \geq Z^{em}$, one typically finds [109] that $e/h \equiv (e/mip)/(h/mip) > 1$. The suppression of the hadronic shower response is caused by the substantial fraction (25→30%) of the energy that is transferred by its hadronic component to hardly detectable (muons, soft neutrons and gammas, neutrinos) or invisible (binding energy in nuclei breakup) energy. A compensation for this undetectable energy was first achieved in Uranium/scintillator calorimeters [115] and was attributed to the role played by detectable products (soft evaporation neutrons and γ 's) of induced uranium fission. In order to gain a better understanding of the nuclear-physics mechanisms governing the development of the hadronic component of hadronic showers, we proceeded to a detailed analysis of the "fingerprint" of reaction products left after the passage of a shower in uranium calorimeters. The method allowed us, for instance, to separate the contribution of fast charged particles induced fissions from neutron-induced fissions, and to measure the total neutron "production". One of the main outcomes [116] of this activation analysis was the finding that the total number of fissions per GeV was significantly lower ($\sim 10/\text{GeV}$ and $\sim 90\%$ neutron-induced) than usually assumed and dependent on the calorimeter sampling configuration. The total neutron production was measured to be of the order of ~ 45 per GeV, and only $\sim 20\%$ of those induced a fission before being slowed down and captured. From the analysis, we inferred that fission alone could not account for the compensation in U/scintillator calorimeters, and we were led to conjecture that a dominant role could be played by evaporation neutrons and cascade neutrons and protons from spallation reactions [116]. Detailed phenomenological studies [113] confirmed the importance of the contribution from densely ionizing protons ($p/mip \gg e/mip$) liberated in the spallation reactions and from neutrons (via energy transfer to recoil protons in the low-Z readout media). The dominant role of spallation products in the compensation mechanism allowed to envisage non-uranium compensating calorimetry. This was recently achieved with a Pb/scintillator hadronic calorimeter [117]. Figure 25 on page 60 shows the predictions of [113] for the e/h ratio and energy resolution as a function of the sampling fraction in U/scintillator calorimeters. The optimal performances are achieved with uranium plates thickness of 2–3mm for a 2.5mm scintillator

¹⁶ Useful parametrizations for the energy resolution of sampling calorimeters for electromagnetic showers are given in refs [111] [109]

plate. These values correspond to our choice for the readout and absorbent thicknesses.

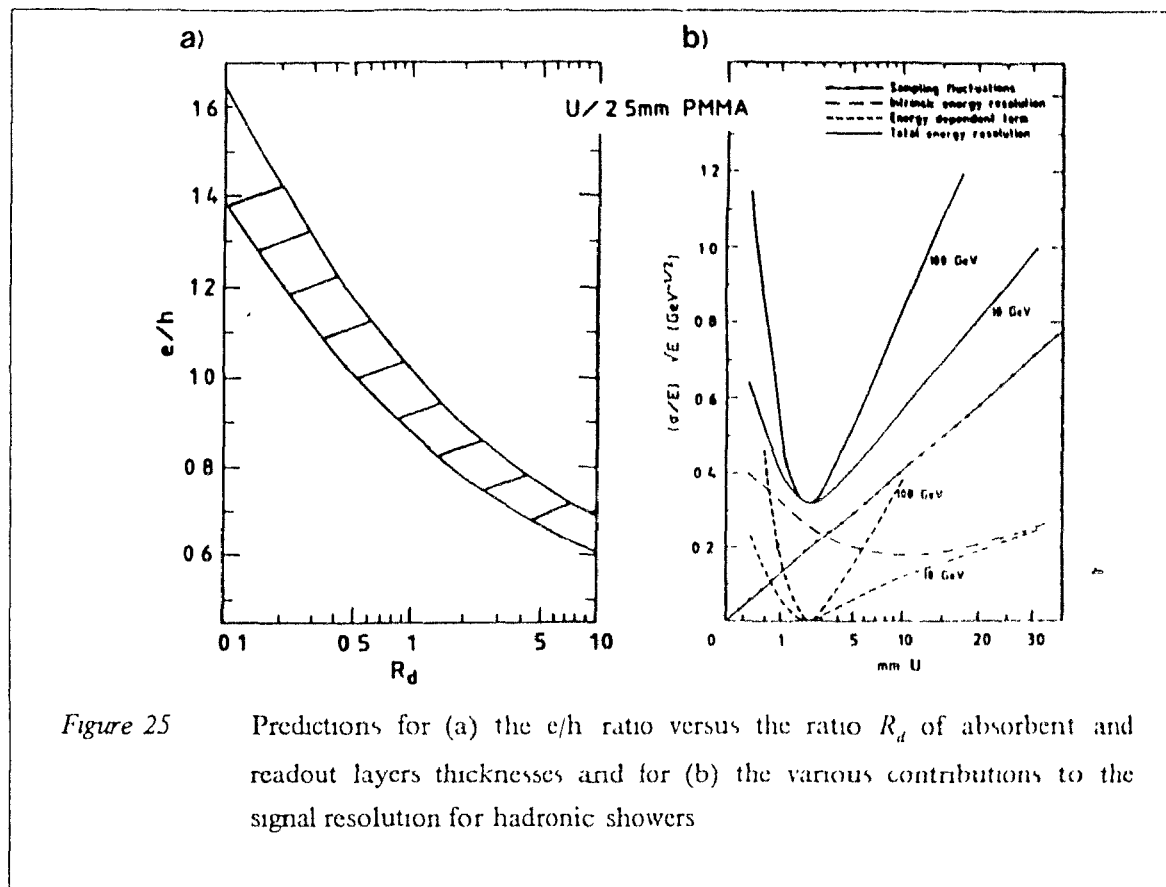
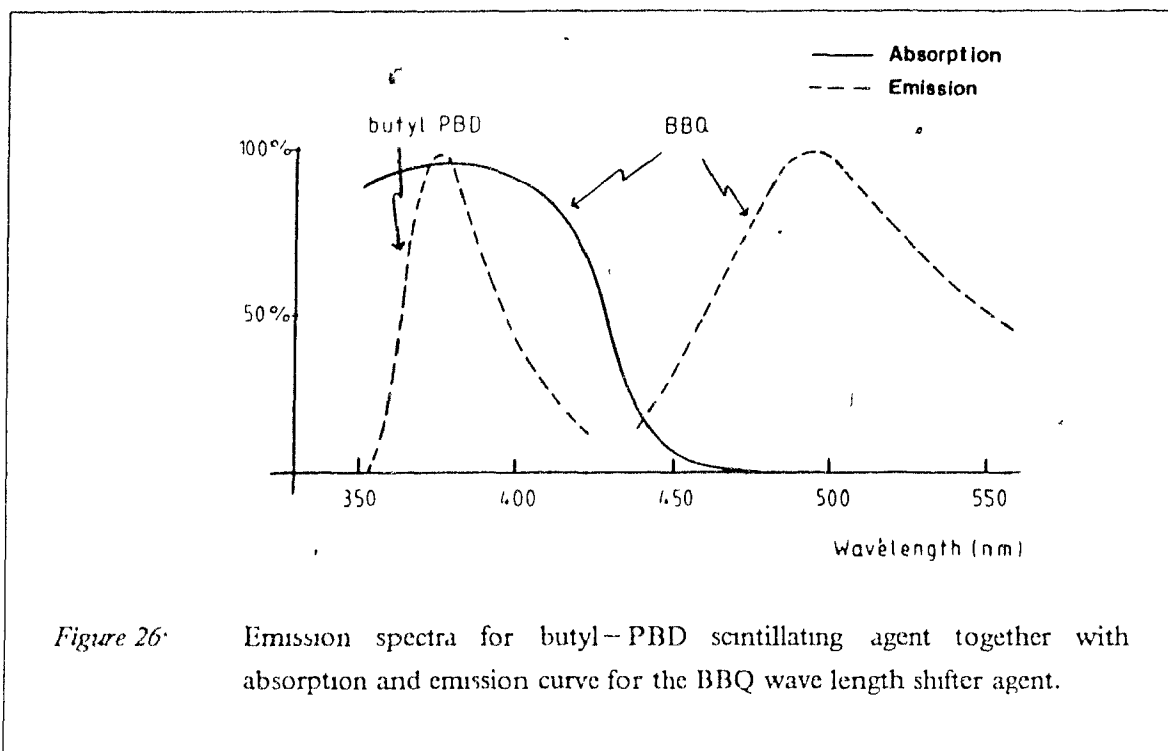


Figure 25 Predictions for (a) the e/h ratio versus the ratio R_d of absorbent and readout layers thicknesses and for (b) the various contributions to the signal resolution for hadronic showers

Having fixed the absorbent and readout media characteristics, there remains to optimize the optical readout quality by a careful tuning of the scintillator–WLS–photomultiplier (PM) combination. In the modules containing Uranium, the scintillator plates basic matrix is PMMA¹⁷ to which is added 1% of PBD–butyl scintillating agent and 10% of naphthalene to increase the ultraviolet (UV) light yield. The scintillator light is carried into the WLS plates where it is converted from ultraviolet to green. The emission spectrum of the PBD–butyl peaks at ~ 368 nm and is well matched to the absorption efficiency of the WLS (Figure 26 on page 61).¹⁷

¹⁷ Polymethyl Methacrylate



The WLS plates are made of Plexiglass to which 80 mg/l of BBQ¹⁸ shifting agent is added. The BBQ fluorescent chemical has an emission spectrum peaked at 500 nm (Figure 26). Its concentration is optimized to both maximize the absorption of the incoming UV light and minimize the self-absorption for the re-emitted green light which has to travel along the WLS plate towards the PM. In order to reduce the sensitivity to the Cherenkov light production by electrons of leaking showers, the thin WLS plate is further doped with a chemical absorbing part of the Cherenkov light before it is converted by the BBQ. The green light from the WLS is brought to the PM by means of a light-guide made of UV absorbing acrylic glass. A 3 mm thick disk of elastic silicone rubber doped with a UV absorbing chemical provides the optical coupling between the light-guide and the PM, and acts as a UV filter with an absorption edge at ~ 390 nm. The optical readout produces approximately 1.5 photoelectrons per mip per scintillator plate.

The optical attenuation length λ_{att}^{scint} in the scintillator has to be long enough to avoid a significant degradation of the energy resolution. A too strong attenuation would lead to a reduced number of photoelectrons per unit of deposited energy and a signal amplitude that would depend on the distance from the light source(s) to the WLS plate. The influence of λ_{att}^{scint} on the energy resolution is shown in Figure 27 on page 62, as a result of a Monte Carlo calculation taking into account only the effects of fluctuations in the light yield for particles entering the calorimeter cell at

¹⁸ Benzimidazo-benzisoquinoline-7-one

random impact points. These fluctuations essentially add a constant term to $\sigma/\sqrt{E} = C_1$, transforming it into

$$\frac{\sigma}{\sqrt{E}} = C_1 \oplus C_2 \sqrt{E}$$

where \oplus means adding in quadrature.

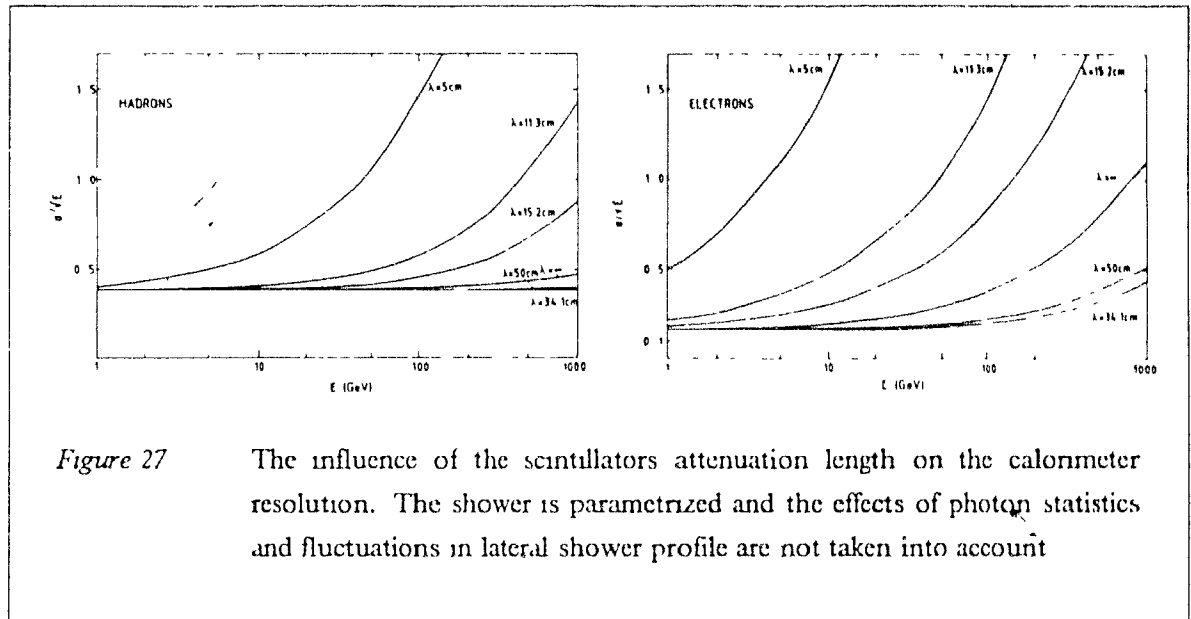


Figure 27 The influence of the scintillators attenuation length on the calorimeter resolution. The shower is parametrized and the effects of photon statistics and fluctuations in lateral shower profile are not taken into account

As $\lambda_{\text{att}}^{\text{scint}}$ decreases, the energy resolution degrades significantly with increasing energy. The scintillator plates of the U/scintillator modules have $\lambda_{\text{att}}^{\text{scint}} \sim 35$ cm, which is a compromise allowing good shower localization while maintaining a uniform total response (no observable contribution to σ/\sqrt{E} below 100 GeV) in a tower cell.

The U/Cu/scintillator modules were used for 5 years in the axial field spectrometer operating at the CERN Intersecting Storage Rings and their overall performance was found to have considerably deteriorated since their construction. We found that this was due to radiation damage causing severe degradation of the optical properties of the scintillator plates [118]. The main contribution to the radiation dose comes from β 's and γ 's from $^{234}\text{Pa} \rightarrow ^{234}\text{U}$ decay in the decay chain of ^{238}U , giving a dose¹⁹ that amounts to 10 Gy/y. The radiation damage occurred for an integrated dose which was orders of magnitude smaller than what was currently believed to be a safe level. This suggested that

¹⁹ 1 Gray (Gy) = 1 J/kg = 100 rad

dose rate was a dominating factor. We found that the UV light continuously produced by the ^{238}U radioactivity, in combination with oxygen diffusing into the scintillator plate, was responsible for the ageing [118]. The radioactivity induces production of UV light by the PBD-butyl. The UV light breaks up the molecular oxygen into its atomic constituents. The ionized singlet oxygen leads to the formation of chemically aggressive free radicals which attack the PMMA polymer chain. The impact of a given total absorbed dose is limited by the supply of oxygen via diffusion from the surrounding atmosphere. The contribution of diffusing oxygen was measured in tests performed at a dose rate more comparable to natural ^{238}U radioactivity. For these we used a 7 mCi ^{90}Sr β -source at 93 mm from scintillator plates placed in a box that could be flushed with air, nitrogen or oxygen. Each irradiation was carried up to an accumulation of 115 Gy in the center of the plate, as determined by LiF counter based on thermoluminescence induced by ionizing radiation. The light yield was then measured by scanning with a collimated β -source along the long axis of the scintillator plate with the set-up shown in Figure 28.

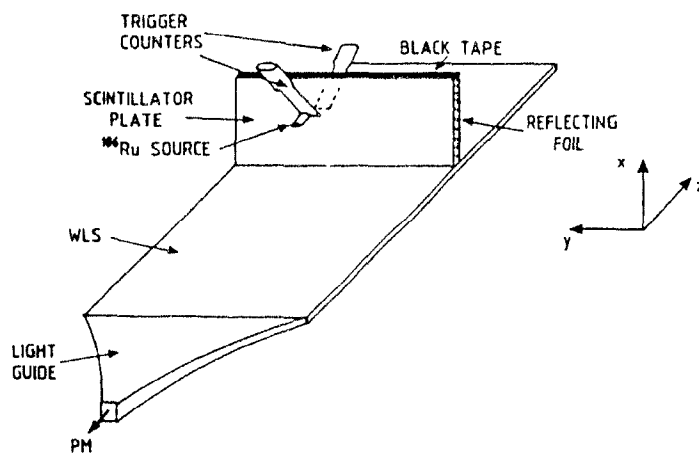


Figure 28: Set-up for optical measurements. Electrons from β -decay of ^{106}Ru create scintillation light in an area of $1 \times 1 \text{ cm}^2$ defined by two small scintillator trigger counters that sandwich the plate and define the trigger. As in a calorimeter module, the plate is coupled by a WLS bar (else covered by black foil) and a light guide to a PM. The source-trigger counter system can be moved by stepping motors in the X-, Y- and Z-directions

Figure 29 on page 64 shows the light yield measurement in air, oxygen and nitrogen environment.

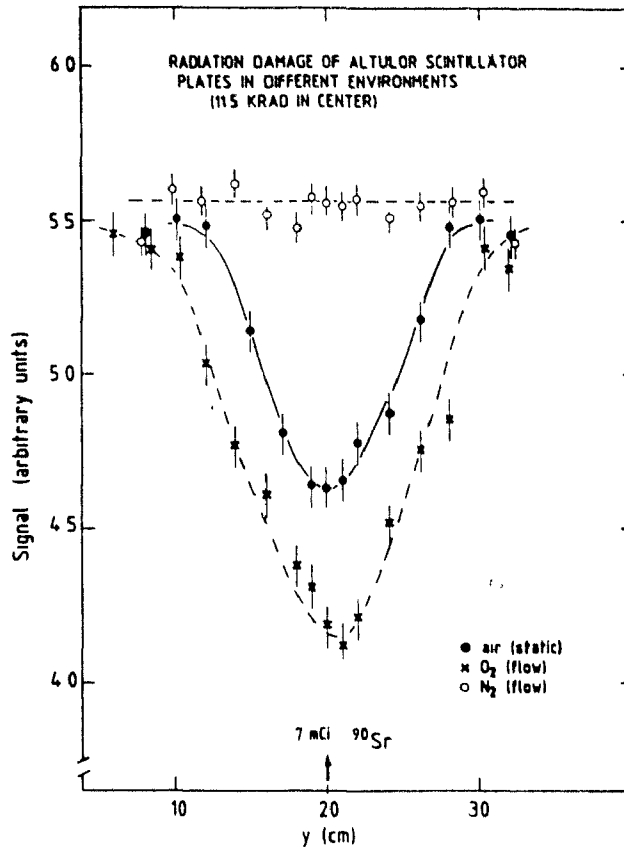


Figure 29 The light yield of an irradiated scintillator plate (⁹⁰Sr, 115 Gy) as a function of Y (at 10 cm from the WLS) for air, nitrogen and oxygen environment. The curves are drawn to guide the eye

The radiation damage decreases with decreasing concentration of oxygen and no observable ageing (< 10 % of the effect in air) is measured in the case of nitrogen environment.

The light attenuation characteristics of a scintillator plate from a U/scintillator module and of radiation damaged plates from a U/Cu/scintillator module (integrated dose of ~25Gy in an air environment) are shown in Figure 30 on page 65.

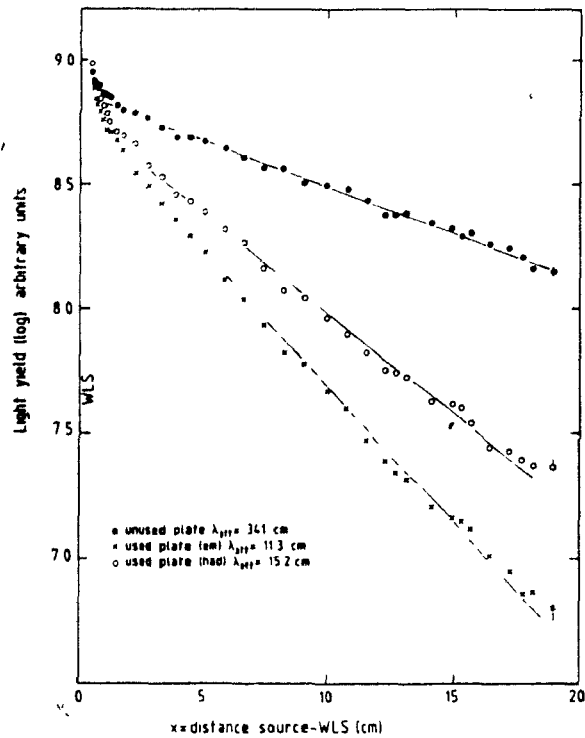


Figure 30: Light attenuation curves for radiation damaged and undamaged scintillator plates.

The attenuation lengths are considerably shorter for the radiation damaged plates but measurements close to the WLS yield the same signal. In other words, the light production by ionizing particles is unaffected whilst the losses between the impact point and the WLS have changed considerably. This confirms that it is the basis matrix (PMMA) which is deteriorated. Instead of being transparent to the UV light produced by the scintillating agent, it absorbs this light and re-emits in the yellow part of the spectrum which, of course, cannot be converted by the WLS. The effect of light attenuation on the response in a tower versus the impact point is shown in Figure 31 on page 66.

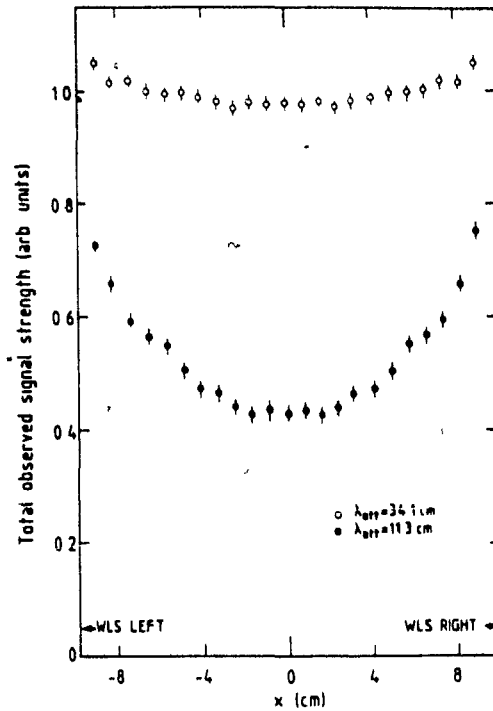


Figure 31: Uniformity of the light collection in a module tower having radiation damaged (closed circles) and undamaged (open circles) scintillator plates.

For U/scintillator modules in nitrogen atmosphere, the non-uniformity is below the 1–2% level, while for U/Cu/scintillator modules the relative response varies by up to a factor 3.

The radiation damage being uniform over the surface of the scintillator plates, it will still be possible to ensure a correct signal to energy conversion in U/Cu/scintillator modules when averaging over random impact points. The knowledge of the optical properties of the scintillator plates in the various U/Cu/scintillator modules will be an essential ingredient for the response function studies that are necessary for a proper reconstruction of the transverse energy flow. These properties were deduced from the measurement of the light sharing amongst the different channels of a module traversed by a mip. The measurements were performed with cosmic muons using the set-up shown in Figure 32 on page 67

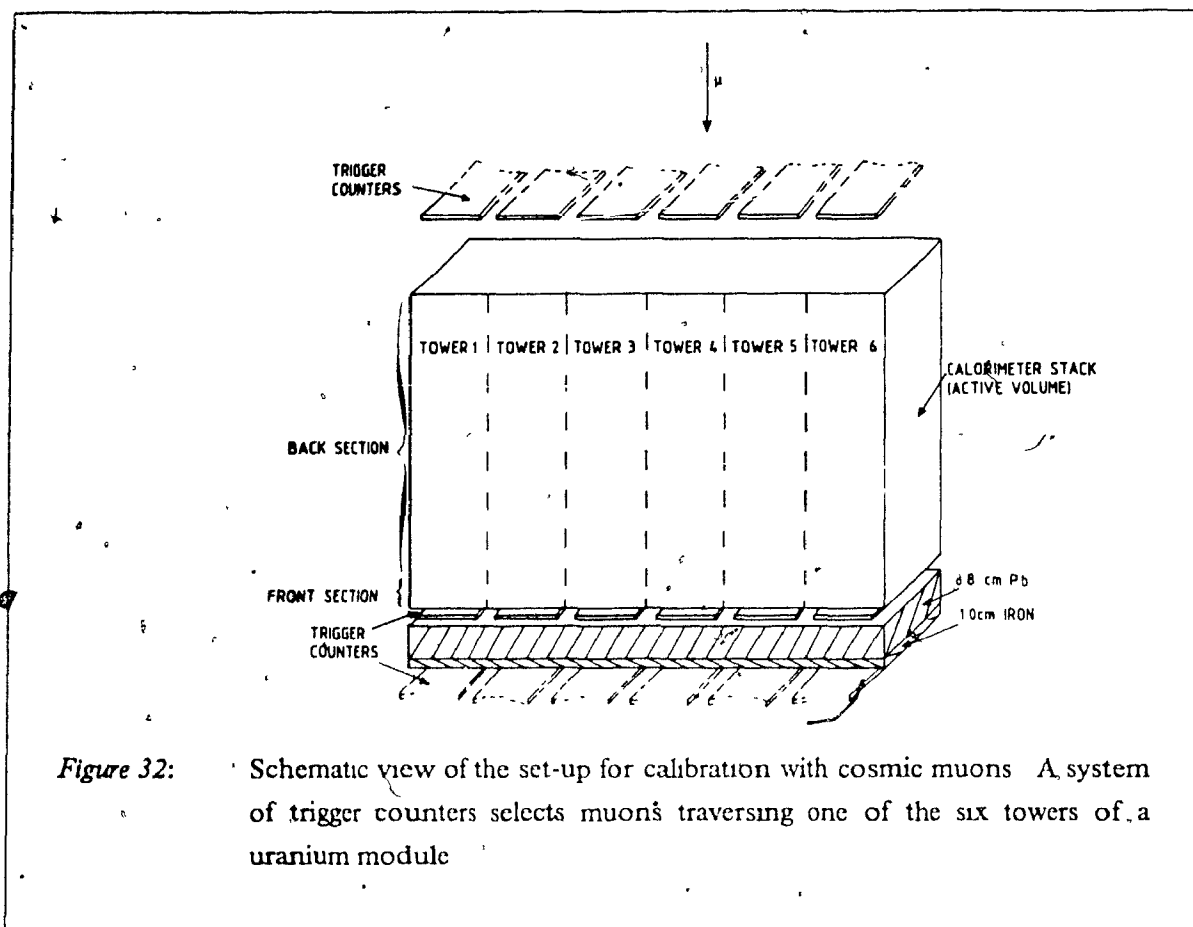


Figure 32: Schematic view of the set-up for calibration with cosmic muons. A system of trigger counters selects muons traversing one of the six towers of a uranium module.

The light sharing characteristics as a function of integrated dose rate are shown in windows (a), (b) and (c) of Figure 33 on page 68. The deduced relation [118] between λ_{on} and the absorbed dose is plotted in (d).

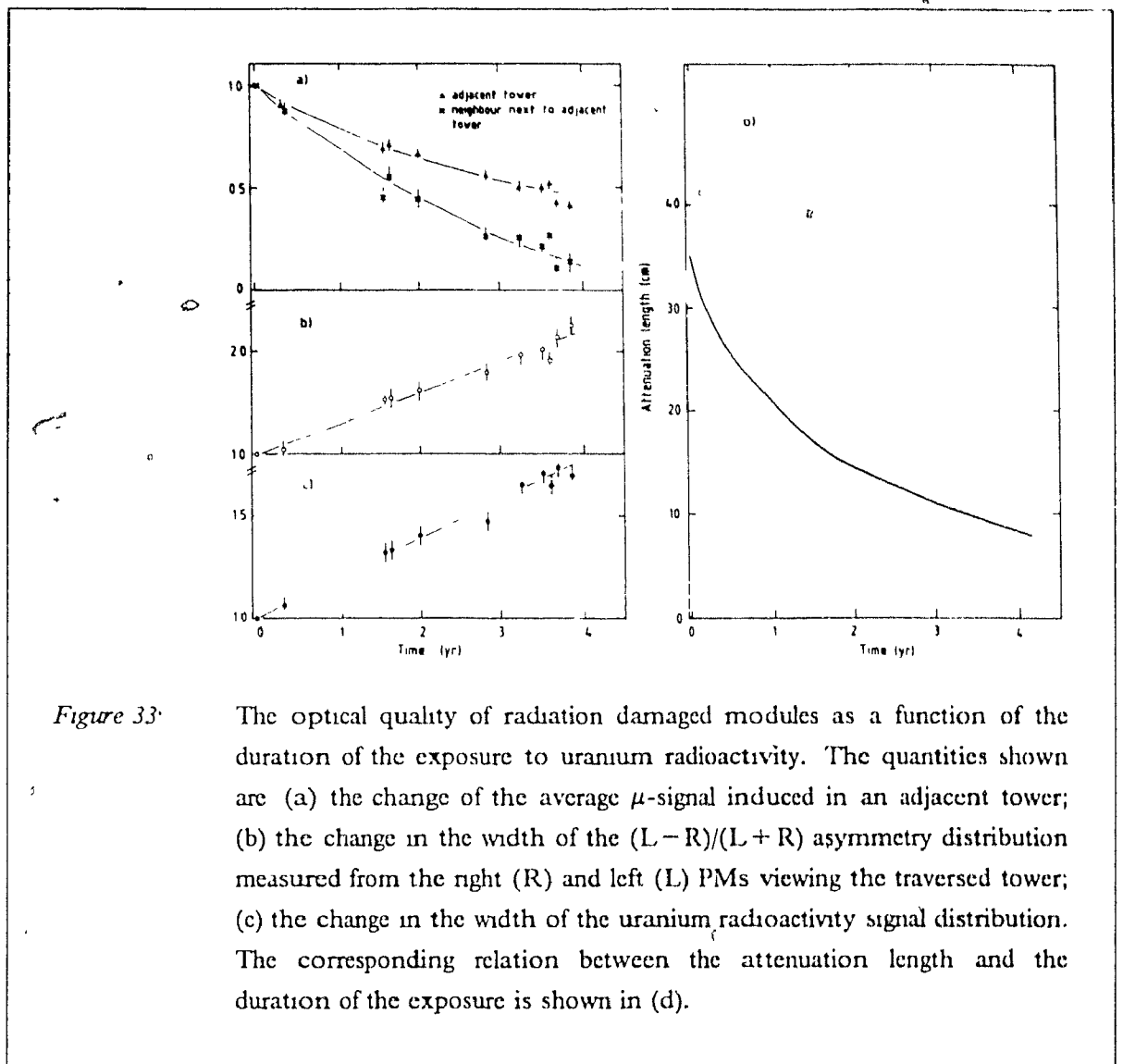


Figure 33

The optical quality of radiation damaged modules as a function of the duration of the exposure to uranium radioactivity. The quantities shown are (a) the change of the average μ -signal induced in an adjacent tower; (b) the change in the width of the $(L-R)/(L+R)$ asymmetry distribution measured from the right (R) and left (L) PMs viewing the traversed tower; (c) the change in the width of the uranium radioactivity signal distribution. The corresponding relation between the attenuation length and the duration of the exposure is shown in (d).

The WLS plates, which are doped with a UV absorbing chemical and did not suffer from radiation disease [118], generate non-uniformities as a function of depth due to light attenuation along the way to the PM tubes. The effective attenuation is a combination of bulk attenuation and losses due to surface imperfections. The response versus the position, along the WLS, of the light conversion was measured using the set-up of Figure 28 on page 63 adapted to closely reproduce the configuration in a uranium module. This response curve plotted in Figure 34 on page 69 shows a $\sim 10-15\%$ non-uniformity which is tolerable for our module's typical range of energy measurements.

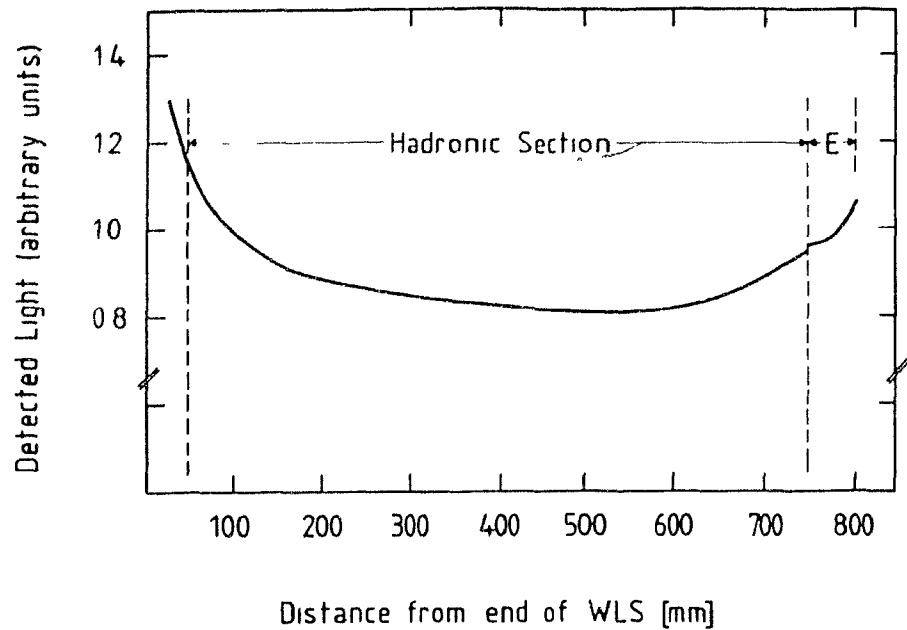


Figure 34: Attenuation of light along the wavelength shifter for the electromagnetic and hadronic sections of a module

This level of non-uniformity is to a certain extent fortuitous since the light losses due to bulk attenuation are partially compensated by reflections from the edge of the WLS [115].

3.5.3 Signal handling and energy calibration

High precision calorimetry requires a major effort concerning the energy calibration which tasks are, on one hand, to tune the PMs so that the energy deposition of a given particle always produces the same signal (measured in picoCoulombs) independent of the calorimeter module in which it is detected, and on the other hand, to set the absolute energy scale. The gain balancing for the uranium modules profits from the natural radioactivity of the uranium plates which provides a convenient, stable and homogeneously distributed source of signals. The relative gain of the two sections (electromagnetic and hadronic) is set using minimum ionizing muons. We use light diodes and radioactive sources for the PM gain balancing in the magnetized calorimeter. The absolute energy scale for all calorimeters is determined using electrons

The detailed calibration procedure has to cope with: instability of the PMs, which require frequent checking and adjustment; attenuation of light in the scintillator plates and in the WLS, which implies that the calorimeter response depends on the impact point of the particle, the angle of

incidence and, for hadron showers, the depth at which the shower starts developing; and the absolute signal-to-energy conversion which is in general quite different for muons, electrons, photons and hadrons (for hadrons the signal in a calorimeter is in general not proportional to the particle incident energy). Moreover, maintaining on-line an equal energy response (i.e. equal gains in MeV/pC) in each individual calorimeter channel is essential since one third of each PM anode signal is diverted into first analogue summing circuits for triggered event selection. Two thirds of the anode current are sent to charge integrating analogue-to-digital converters (ADC), for off-line analysis.

We have developed the following calibration procedure

i) We first calibrate the charge-ADC channels by using a precision pulse generator to accurately determine the charge equivalent per ADC count of each individual channel (nominally 4 counts/pC for our Lecroy 2282 charge-ADC's)

ii) We then balance the current output of all PM's by measuring the signal resulting from the natural radioactivity of uranium ("uranium noise"). In order to get signals that are sufficiently accurate with respect to the ADC pedestals, a relatively long gate time of 10 μ s is used instead of the 0.13 μ s which is the standard value for shower detection. The high-voltage applied on each PM that reads out towers of the same structure-type is adjusted to obtain a pre-defined mean integrated charge for the uranium noise signal distribution. We nominally require in the 10 μ s gate an average integrated charge of 24.11 pC (70-40 pC) for the electromagnetic (hadronic) section of the U/Cu/scintillator modules and 24.11 pC (116-16 pC) for the electromagnetic (hadronic) section of the U/scintillator modules. The measurement of these averages is performed to better than 1% by allowing for sufficient readings. This procedure ensures an equalization of the gains (same relative MeV/pC conversion factors) for all towers of a given type. These gains are function of the number of scintillator plates, the amount of uranium and the uranium plates thicknesses.

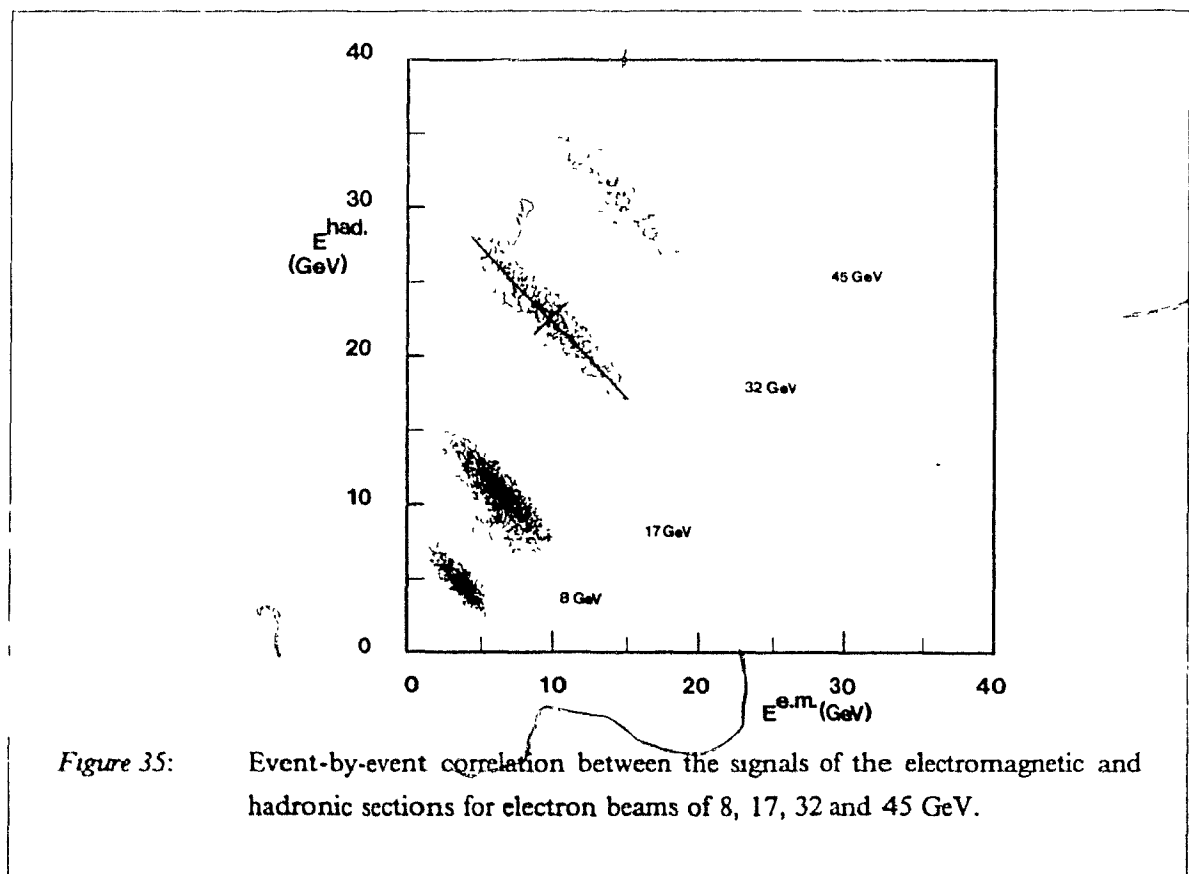
iii) We finally determine the absolute values of the ratios MeV/pC by exposing the various types of modules to beams of different energies. Since the electromagnetic sections are thin (6.4X₀), the charged particles will in practice always produce a signal in both the electromagnetic and hadronic sections of a module, and therefore one can only calibrate both sections simultaneously.

We used tagged electron beams from the CERN SPS, at energies of 8, 17, 24, 32 and 45 GeV, and cosmic muons, to derive the absolute values of the calibration constants. The electromagnetic showers have the advantage of depositing their energy over a limited volume, easily contained within the modules, with comparable fractions in the two sections. We investigated various procedures to obtain the absolute calibration constants. The simplest one consisted of solving a system of

equations of the form $E_k = AS_k^{em} + BS_k^{had}$, where E_k is a given incident energy, and S_k^{em} (S_k^{had}) is taken either as the mean signal from the electromagnetic (hadronic) section or as the peak values of the signal distributions (e.g. obtained from a gaussian fit up to $\pm 3\sigma$). Alternatively, the calibration constants A and B for the electromagnetic and hadronic sections were calculated by minimizing the width of the total signal distribution, i.e. by minimizing the quantity

$$Q = \left(\sum_{j=1}^n E(\text{beam}) - A \sum_{i=1}^n S_{ij}^{em} - B \sum_{i=1}^n S_{ij}^{had} \right)^2 \quad (33)$$

where Σ^{em} and Σ^{had} are the sums of all the ADC counts in the towers i of the electromagnetic and hadronic sections that contribute to the measured signal for event j . In all cases, these different methods yielded similar results, both when A and B are left as free parameters or when an additional constraint of the type $A = \text{Const} B$ is imposed. I shall here concentrate on the more precise and powerful minimization method. This method can provide an independent solution for any given mono-energetic beam since, as seen in Figure 35, the fluctuations on the energy sharing between the electromagnetic and hadronic sections are much larger than those resulting from energy resolution. It thus allows a complete study of systematic deviation:



A universal calibration together with good error estimates is obtained via a global minimization over many j different energies of the reduced χ^2 , $\chi^2 = \sum (Q / \Delta E)^2$, where ΔE is an estimate of the sampling resolution ($\Delta E \sim 0.19\sqrt{E}$)

We first studied the situation where A and B are left as free parameters. We observed that the values of A and B found when calibrating with electrons were slightly dependent on the incident energy, and that the B/A ratio was inconsistent with the one observed for a muon intercalibration. The fact that different A and B factors, and also a different B/A ratio, have to be used for different electron energies leads to a violation of the fundamental requirement of signal linearity for electron shower detection. One cannot find calibration constants that fulfill this requirement and optimize the energy resolution for electromagnetic showers at the same time. The ratio B/A went up with the energy by about 20% over the energy range studied. Cosmic muons only allow to derive a value for B/A, since the energy deposited in the modules depends in a complicated way on the unknown energy of the muon. The B/A ratio from muon calibration was found to be $\sim 21\%$ larger than the (average) value from the electron runs. These effects result from the combination of problems of instrumental and physics origin. The instrumental contribution arises from the light attenuation in the WLS of the hadronic section. The light production by both muons and uranium noise is uniform as a function of depth. Light from the electron shower tail is produced in the part of the hadronic section furthest from the PM, and is therefore more attenuated than the average for uranium noise and muons. From the measured WLS attenuation characteristics, we found that an effect of 10–15% has to be expected on the B value for electrons. The longitudinal inhomogeneity of the WLS might be resolved by properly filtering the light transmitted from the scintillator into the WLS [119]. The physics contribution is related to the fact that in a sampling calorimeter, the fraction of the electromagnetic shower energy converted into a measurable signal changes with depth. In the case of uranium absorber a very considerable decrease occurs. This effect is due to the soft γ component of the shower, for which the calorimeter response (signal per unit of energy) is much lower than for minimum ionizing particles (mip's). This means that a given amount of energy deposited by the fast (more mip-like) part of the shower in the electromagnetic section will yield a larger signal than the same energy deposited by the soft tail in the hadronic section. The effect of this on our calibration result is energy-dependent: if the electron energy is increased, the particles in the fraction of the shower deposited in the hadronic section become on average more energetic, which results in a larger response. As observed, the B/A ratio is then expected to increase with incident energy. This phenomenon creates a very fundamental problem: the relation between the energy deposited by the shower and the resulting calorimeter signal is different for the two sections of the calorimeter and, moreover, energy-dependent. This was clearly confirmed by EGS4 calculations with which we simulated the development of electromagnetic showers in our calorimeter. Averaged over all energies, the hadronic/electromagnetic signal ratio is predicted to be 30% smaller than the ratio of the energies deposited in the two sections. The combined instrumental and shower ageing contributions explain the experimentally observed discrepancies between the electron and muon calibrations and the energy dependence of A and B in the electron calibration.

The relation between the B/A value and the energy resolution, and e/π signal ratio, is shown in Figure 36 (the dashed line is our chosen B/A value). Window (a) of that figure shows what happens to the σ_{RMS} of the signal distribution, which corresponds to the quantity that we minimized in order to find B and A from the electron measurements. The minima are found for values of B/A lower than the corresponding value for a muon intercalibration (which gives B/A = 4.0) and the minimum shifts with energy. Because of the arguments just given, the σ_{RMS} found as a minimum value cannot be interpreted as an energy resolution but as the width of the distribution of the total number of ADC counts

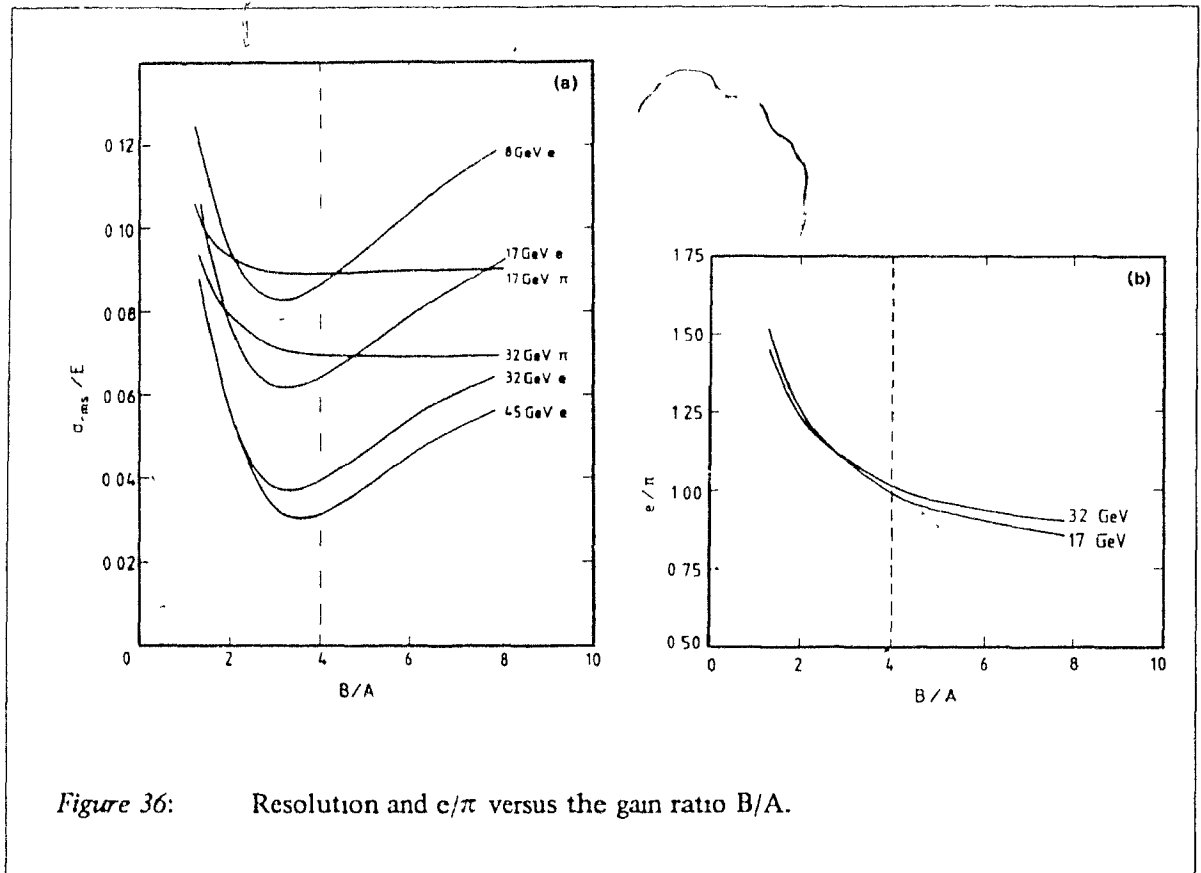


Figure 36 (a) also shows that the hadronic energy resolution is very insensitive to the forward-backward gain balancing. This is because the energy fraction deposited by hadrons in the electromagnetic section ($0.2\lambda_{int}$) is very small. This also explains what is observed in Figure 36 (b), where the effect of the B/A value on the e/π signal ratio is shown. The e/π signal ratio obviously decreases as more weight is given to the part of the shower detected in the hadronic section.

In summarizing we remark that showers cannot be used to intercalibrate sections of a longitudinally segmented calorimeter, and that in such a calorimeter intercalibrated with muons, only

the total shower energy recorded is meaningful, while the signals in the individual segments cannot be fully interpreted as energy information. Therefore, the shower-age dependence of the calorimeter response also implies that the weighting factors used in algorithms [119] to improve the energy resolution off-line using the longitudinal shower information, should be energy dependent.

In practice, we decided to use the B/A value from the muon calibration, fixing the A and B values such as to reproduce best the electron beam energies over our measured range. This guarantees proportionality between the total electron signal (expressed in energy units) and the particle energy. Any other choice would only have had a limited meaning for electrons of a particular energy. An inevitable consequence of this choice is that the apparent energy deposited by electromagnetic showers in separate segments is slightly offset with these calibration constants. This is also valid for hadronic showers, where the calorimeter response analogously decreases with increasing shower depth. The calibration constants obtained for $B/A \equiv 4.0$ are given in Table 1.

Table 1 Calibration factors for the uranium modules.

Module type	Required signal for uranium noise equalization pC/10 μ s	Calibration factors MeV/pC	Correlation coefficient ρ
U/Cu/scintillator	em	24.11	15 844 ¹⁾
	had	70.40	63.377
U/scintillator	em	24.11	14.844 \pm 0.634
	had	116.16	59.376 \pm 2.535
U/scintillator	em	24.11	16.191 \pm 0.606
(decoupled towers)	had	116.16	67.765 \pm 2.408

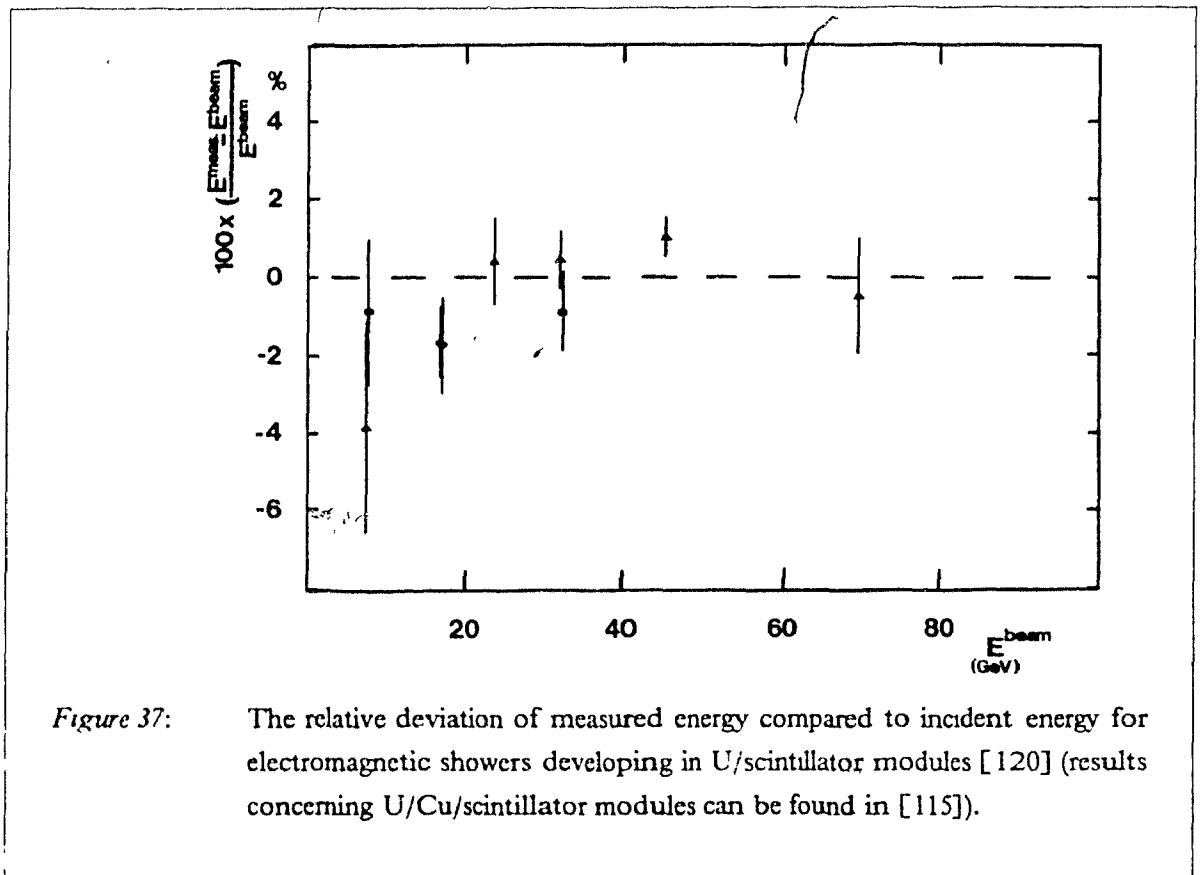
1) Provided by the R807 Collaboration.

The quoted errors on A and B are rather large but these parameters have a very strong negative correlation (-92%) so that the event-by-event reconstruction of the energy $E = A \cdot S^{em} + B \cdot S^{had}$ is precise to

$$(\Delta E)^2 = (\Delta A \cdot S^{em})^2 + (\Delta B \cdot S^{had})^2 + 2\rho(\Delta A \cdot S^{em})(\Delta B \cdot S^{had})$$

which corresponds to a 3-4 % uncertainty. The mean energies are, however, reconstructed to better than 2%.

A small but significant difference between the calibration constants for different modules was found. This may be explained by the fact that the electrons deposit their energy in a limited region of the calorimeter volume and therefore the signal relative to uranium noise is rather sensitive to anomalies in, for example, the thickness of the active or passive layers. The observed difference between the A and B values for the module with the optically decoupled towers, and the uranium module with the unmodified scintillator plates, is also partly due to the fact that the reflection of the aluminized mylar foils in the slits is not perfect (i.e. the locally produced light from showers differs from the uniformly distributed light generated by uranium decay), yielding somewhat larger (by 8%) A and B values for the decoupled towers. The calorimeter modules are shown to respond linearly to electromagnetic showers as a function of energy (Figure 37) to a precision of 1-2%.



Once the values for A and B are fixed, the uranium noise signal can be used to set and maintain the required gain. The gain stability is checked daily by measuring the uranium noise signal (nominally $\sim 7\mu\text{A}$ for a hadronic tube at standard voltage), which is maintained at a fixed number of

ADC counts for each specific channel.

The response of the 24 tubes of the MAGCAL is checked and maintained by two systems: light diodes and a radioactive source. One fibre of each light guide is coupled to a light diode. The light passes down the fibre, along the WLS bar, where it is reflected at the end and returns back to the PM. In order to control systematic effects in the light diodes, each diode feeds four channels and the temperature of the diodes is monitored. To check the scintillator response, a 740 MBq ^{60}Co source is pulled round the front face of the MAGCAL. This source samples the first few layers of scintillator. The absolute energy scale was set by scanning the different types of petals with a 8 GeV electron beam.

3.5.4 The calorimeter performances

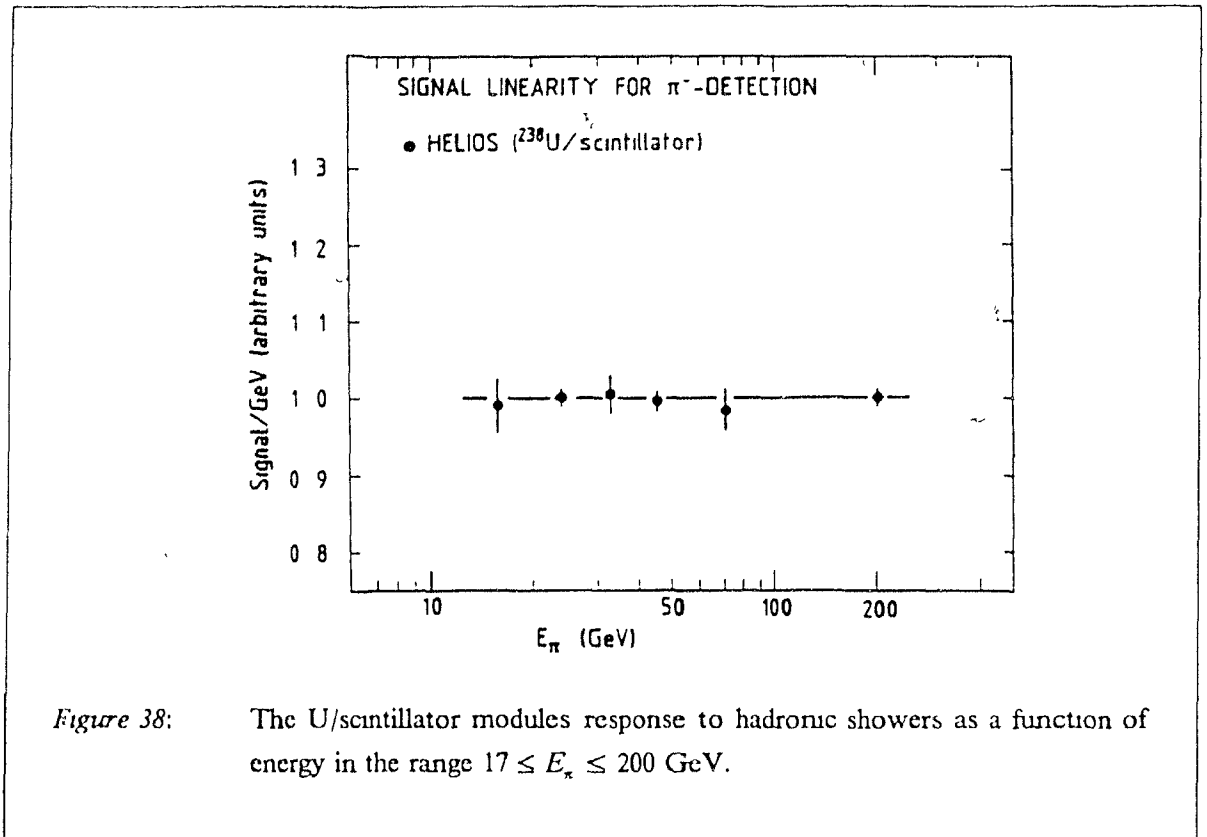
The calorimeter performances were measured with beams of electrons and pions at 8, 17, 24, 32, 45, 70 and 200 GeV/c, incident on the forward beam modules ($2 \times 4.2\lambda$, thick). The beam intensity was maintained at low values of 10^2 to 10^4 particles per 2.6s burst. The set-up to define the arrival of a beam particle is the one described in 3.3 on page 50, with a before-and-after protection of $\pm 1\mu\text{s}$. It is worth mentioning that the light production induced by a shower extends significantly beyond the width of our standard charge integration gates (130ns) for both electromagnetic and hadronic showers, and that the fraction of the light that is produced after 130ns is measured to be slightly larger for hadronic showers. The main contribution to the slow component of the signals comes from the fluorescence mechanism in the wavelength-shifter plates. The small difference in the time structure of electromagnetic and hadronic showers may be due to the process of capture of thermalized neutrons which plays a significant role in the energy deposition [116] for hadronic showers and has a $1\mu\text{s}$ time scale [121].

We recorded typically $\geq 10^4$ events at each energy.²⁰ The electrons and pions were separated efficiently (up to 45 GeV) using the tagging information coming from a Cherenkov differential counter with achromatic ring focusing (CEDAR). Further particle identification was provided by the longitudinal and transverse characteristics of the showers [120] (e.g. requiring $> 30\%$ of E_{TOT} in the electromagnetic section leaves a pure sample of electrons, whilst requiring $< 3\%$ leaves a pure sample of pions).

The linearity of the calorimeter response for the detection of pions was investigated in the energy range from 17 to 200 GeV. The results are shown in Figure 38 on page 77. Over the energy range considered, there is no indication of a deviation from proportionality larger than the 2% overall

²⁰ There were not enough pion events available at 8 GeV and electron events at 200 GeV for them to be used in the analysis.

precision.



Since the fraction of the total energy spent by a hadronic shower on π^0 production increases logarithmically with energy, one can approach linearity for hadronic showers only if the intrinsic response to the purely electromagnetic (i.e. π^0 induced) and purely hadronic components are equal, i.e. $(e/\pi)^{\text{intr}} = 1$. For a perfect detector that does not suffer from inhomogeneities in the light collection, this condition is equivalent to the requirement that the measured average responses to electrons and charged pions be equal ($(e/\pi)^{\text{meas}} = \text{constant} = 1$). In our uranium modules, the measured e/π value is sensitive to the effective light attenuation in the WLS bars reading the hadronic sections. This measured ratio is plotted in Figure 39 on page 78 as a function of energy in the range $17 \leq E_\pi \leq 200$ GeV (the electron value at 200 GeV was obtained by assuming that we could extrapolate the linear behaviour observed for electrons from 8 to 70 GeV).

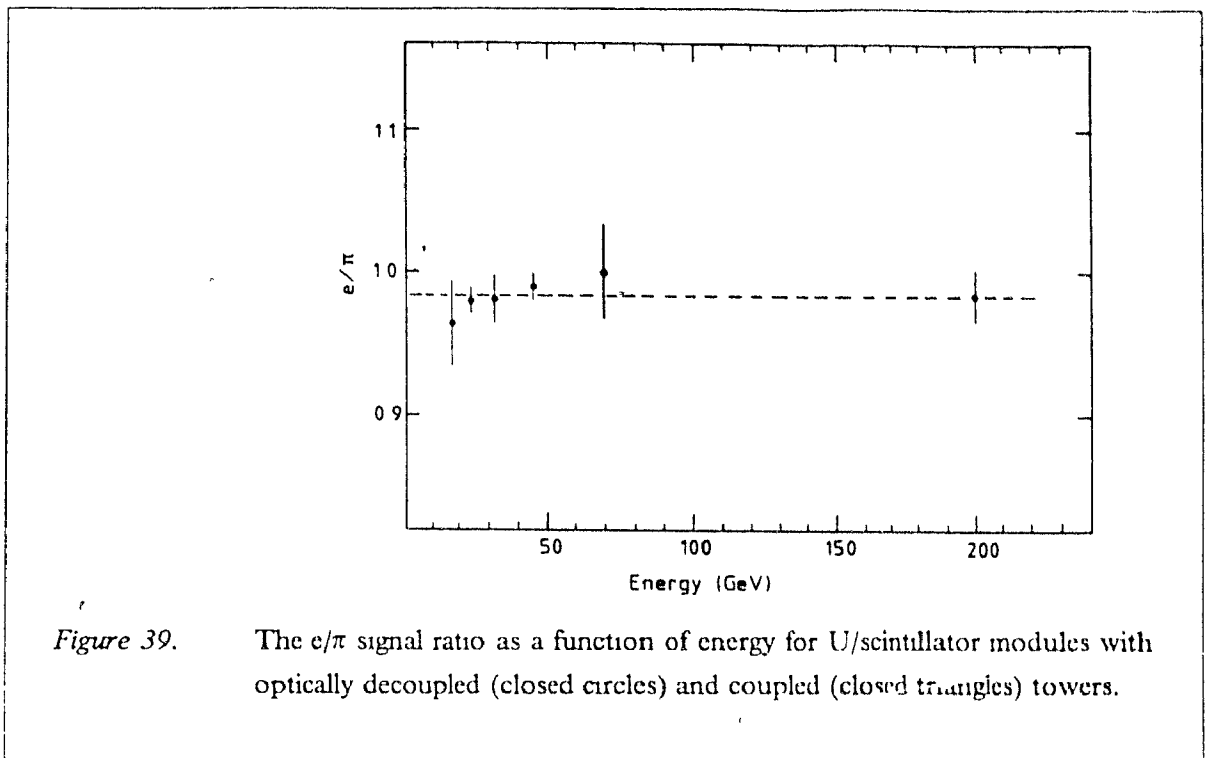


Figure 39. The e/π signal ratio as a function of energy for U/scintillator modules with optically decoupled (closed circles) and coupled (closed triangles) towers.

Over the energy range studied, the $(e/\pi)^{meas}$ ratio is constant within experimental uncertainties. An average value of 0.98 ± 0.01 (1.01 ± 0.02) is found for U/scintillator modules with optically decoupled (coupled) towers. This indicates that $(e/\pi)^{meas} \sim (e/\pi)^{intr} \sim 1$. The results stand in contrast to non-compensating Fe/scintillator calorimeters where $(e/\pi)^{meas}$ varies by $\sim 20\%$ over similar energy range [122].

The best resolution performances are expected for a calorimeter with $(e/\pi)^{intr} \sim 1$. Only then will the effect of the non-gaussian event-by-event fluctuations in the fraction of energy spent on π^0 production be minimized, and the energy resolution for hadronic showers be following a scaling law $\sigma \sim f(E) \cdot \sqrt{E}$. The measured energy resolution for electromagnetic and hadronic showers is shown in Figure 40 on page 79. The σ of the signal distribution was determined from a Gaussian fit over the approximate range $[\text{mean} \pm 3\sigma]$.

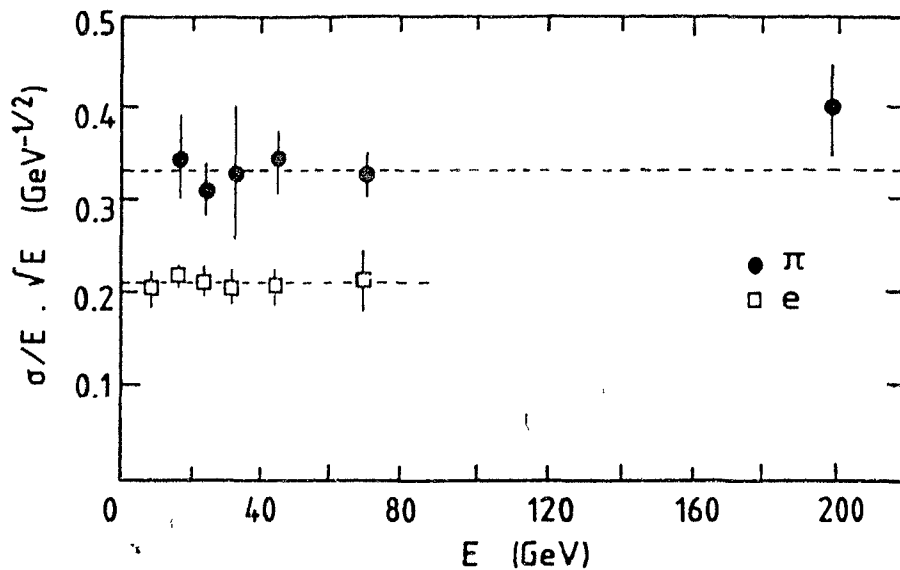


Figure 40 The single particle fractional energy resolution $(\sigma/E) \cdot \sqrt{E}$ as a function of energy for electrons (open squares) and pions (closed circles). The results were obtained with a U/scintillator module having optically decoupled towers

Within experimental uncertainties, the value of σ/\sqrt{E} is independent of the particle energy for both electromagnetic and hadronic showers. A least squares fit to the data points gives $\sigma/E = (0.337 \pm 0.013) / \sqrt{E}$ for pions and $\sigma/E = (0.215 \pm 0.007) / \sqrt{E}$ for electrons (E in GeV). The hadronic resolution value compares favorably to results for non-compensating calorimeters, for which the value is much larger and severely degrades with increasing energy [122]. A complete table of results concerning the energy resolution, signal linearity and e/π for U/scintillator modules (with optically coupled and decoupled towers) is given in [120]. Results concerning the U/Cu/scintillator modules can be found in [115]. The energy resolution of the magnetized calorimeter was measured to be $\sigma/E = 0.25 / \sqrt{E}$ for 8 GeV electrons.

Besides electrons and pions, the test beams also contained muons (easily recognized by their fractional energy deposition) which made it possible to study, as a function of energy, the relative calorimeter response to muons and electrons (i.e. μ/e ratio) in the same experimental conditions. Having set the absolute energy scale with electrons, we determined the (μ/e) ratio by comparing the apparent energy deposited by the muons to the 1.802 GeV that a minimum ionizing particle would lose when passing through the $8.4 \lambda_i$ of the forward beam modules. The results are shown in Figure 41 on page 80.

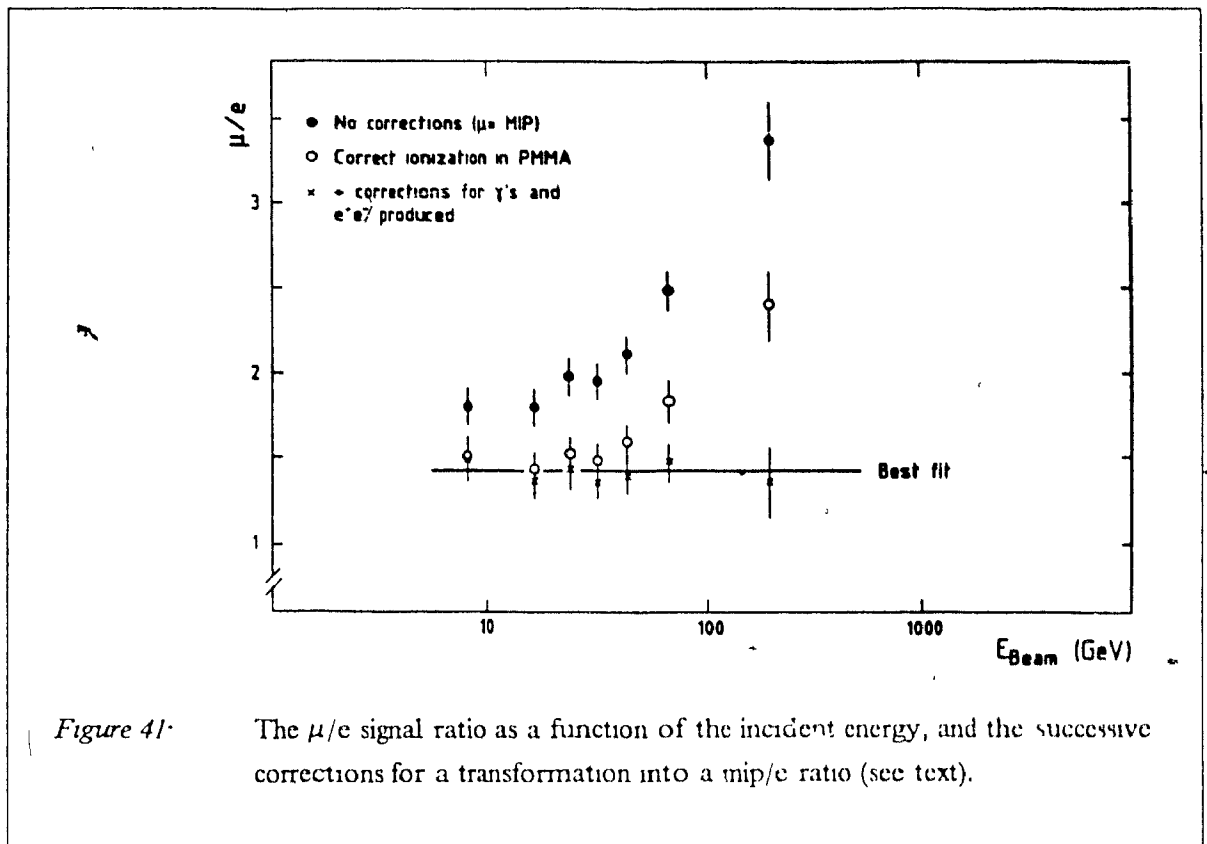


Figure 41. The μ/e signal ratio as a function of the incident energy, and the successive corrections for a transformation into a mip/e ratio (see text).

The apparent increase in the energy loss (closed circles) is due to δ -ray emission (relativistic rise), bremsstrahlung and pair production. The energy dependence is partly removed when correcting [120] for the relativistic rise (open circles). When further removing the contribution due to bremsstrahlung and pair production, the μ/e ratio (non equivalent to a true mip/e ratio) is found to be energy independent (crosses). A least square fit gives $\text{mip}/e = 1.43 \pm 0.10$.

3.5.5 The transverse energy flow trigger

The Energy Flow Logic (EFL) can provide a trigger on the total transverse energy of an event, in selected regions of pseudorapidity. The fast hard-wired on-line value of E_T is formed by diverting one third of the anode signals of the various calorimeters, suitably weighted by resistors, into fast analogue summing circuits [120].

The weights were found by Monte Carlo simulation where the E_T produced by the event generator HJET [123] was compared to the simulated energy response in the calorimeter. For any event k , the visible generated E_T is given by

$$E_T^k = \sum_j E_j^k \sin \theta_j^k = \sum_j \left(\sum_i D_{ij}^k \right) \sin \theta_j^k \quad (34)$$

where θ_j is the opening angle for particle j , and its associated total energy E_j (kinetic energy in the case of baryons) is decomposed in terms of a sum over D_{ij} , the energy deposited in each tower i . The reconstructed E_T is written as

$$E_T^k = \sum_i w_i S_i^k = \sum_i w_i \left(\sum_j L_{ij}^k + \Delta U_i^k \right) \quad (35)$$

where the w_i are the desired weights and S_i^k is the energy corresponding to the signal measured in tower i for event k . This energy is further decomposed in a sum over the contribution of all particles to the light output L_{ij} , and ΔU_i takes into account the uranium "noise" fluctuations around the average radioactive signal. The final weights were obtained by averaging over a large number of events with a statistical weighting of the contribution of each event to tower i assumed to be proportional to the signal S_i . From equation (34) and (35), this gives

$$w_i = \frac{\sum_k \sum_j D_{ij}^k \sin \theta_j^k}{\sum_k \left(\sum_j L_{ij}^k + \Delta U_i^k \right)} \quad (36)$$

The showers in the calorimeter were simulated using a shower parametrization tuned to fit the measured longitudinal and lateral properties. We adopted and adapted the parametrization from Böck et al. [124] for the longitudinal shower development. The electromagnetic showers are parametrized by

$$dE = C_1 E t^{\alpha-1} e^{-\beta t} dt$$

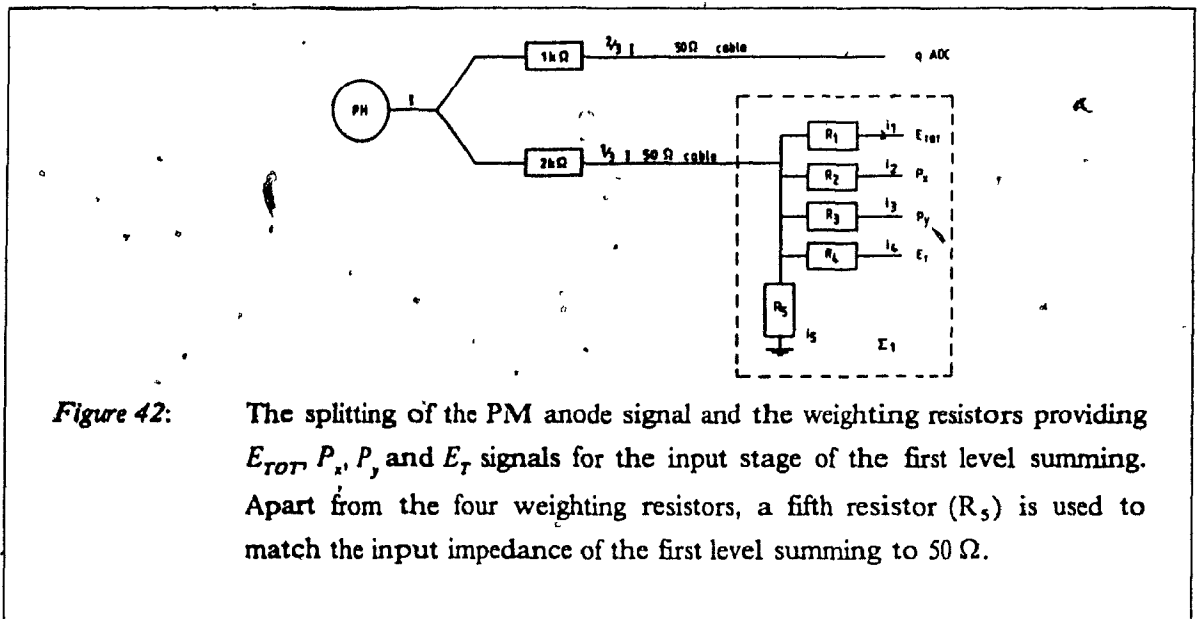
where C_1 is a normalization constant, α and β are dimensionless energy dependent parameters, and t is the depth in units of the radiation length X_0 , the characteristic scale of an electromagnetic shower.

The hadronic showers have a similar "electromagnetic" component (mainly for the π^0 production in the primary interactions) and a "hadronic" component with the absorption length λ_0 as characteristic scale,

$$dE = C_2 E \left[w t^{\alpha-1} e^{-\beta t} dt + (1-w) s^{\beta-1} e^{-s/\lambda_0} ds \right]$$

where C_s is a normalization constant, α , β , γ and δ are energy dependent parameters, t is in units of X_0 and s in units of λ_0 . The parameter w fixes the relative weight of the "electromagnetic" and "hadronic" components. The Monte Carlo simulation procedure took into account the geometrical position of the energy deposition, the effects introduced by the finite spatial and energy resolution of the calorimeter, and by light attenuation in the scintillators.

From the weights provided by the Monte Carlo, we deduced the weighting resistor values for each individual input line (PM). The physical quantities (E_{TOT} , P_x , P_y , E_T) for the trigger were obtained by analogue summing over the suitably weighted pulse heights. The sums were performed in three or four stages of electronic summing units (termed Σ_1 to Σ_4). The splitting of the PM signal and the input stage to the first level summing are shown schematically in Figure 42.



In order to achieve the desired accuracy in the trigger signals, high precision resistors (differing by less than 1% from their nominal values) were used for the splitting of the primary current and for the weighting factors. The E_{TOT} quantity, which may be used at trigger level for pile-up rejection, is obtained by adding the individual pulse heights with equal weights, and the gain of the summing chain is adjusted according to whether the signal is digitized in a 7-bit or 9-bit flash-ADC. The signals for the E_T quantity correspond to a product of the E_{TOT} signals with weights of which the geometrical part is proportional to $\sin \theta_i$ (the detailed cabling and summing layout can be found in [120]). The energy coming from the hadronic or electromagnetic sections of the modules are summed separately in up to 4 Σ_1 units per quadrant per component (box sides, box forward wall, beam modules). The outputs are fed into the second level summing (Σ_2) which calculates the

electromagnetic or hadronic sums for each quadrant of a calorimeter component. The sum over the four quadrants of a component is then made in Σ_3 units and the electromagnetic and hadronic values are added in Σ_4 units. The output of the Σ_4 is sent, via a differential driver unit, to 150 ns shaping amplifiers in the counting room, and from there, via adapter units which provide for fine adjustment of the summing chain gain, into the FADCs and the digital part of the EFL. The gains of the summing units corresponding to a given calorimeter component are optimized to keep the electronic noise at a minimum and at the same time use the full FADC range for the signals expected from that component. The overall energy scale is fixed by the calibration of the charge ADCs. The signals for each physical quantity and for each calorimeter component, digitized in the flash-ADCs, is finally treated by digital comparators for use in the parallel trigger processor. Digital ADDER modules provide values for the physical quantities E_{tot} , P_x^+ , P_x^- , P_y^+ , P_y^- and E_T . These values are then compared to a set of pre-determined thresholds in order to decide whether a trigger condition is satisfied or not. The digital EFL units are under CAMAC control which allows, via selection of ADDER inputs, to trigger for instance on E_T in sub-regions of the overall angular coverage. Moreover, there are five available thresholds on each COMPARATOR module so that a great variety of EFL triggers can be defined. Both 7-bit and 9-bit FADCs are used, in order to cope better with the dynamic range of the energy sum signals.

The performances of the energy flow logic are studied by a comparison with off-line analysis of the detailed charge-ADC information. Figure 43 on page 84 (a) shows a sample of events, for 200 GeV/nucleon ^{16}O incident on a 5% Pb target, selected with a set of four different E_T thresholds in the pseudorapidity region $-0.1 < \eta_{\text{lab}} \leq 0.8$ (i.e. sides of the box). For these events, the correlations between the transverse energy flash-ADC sums and the corresponding charge-ADC sums are shown in (b). A one-to-one correspondence is observed over the full range. The dispersion around the mean correlation axis is mainly caused by the independent reading of the fluctuations in the calorimeter uranium radioactivity signals. A small contribution to the dispersion arises from the limited systematic precision of the resistors forming the on-line E_T weights.

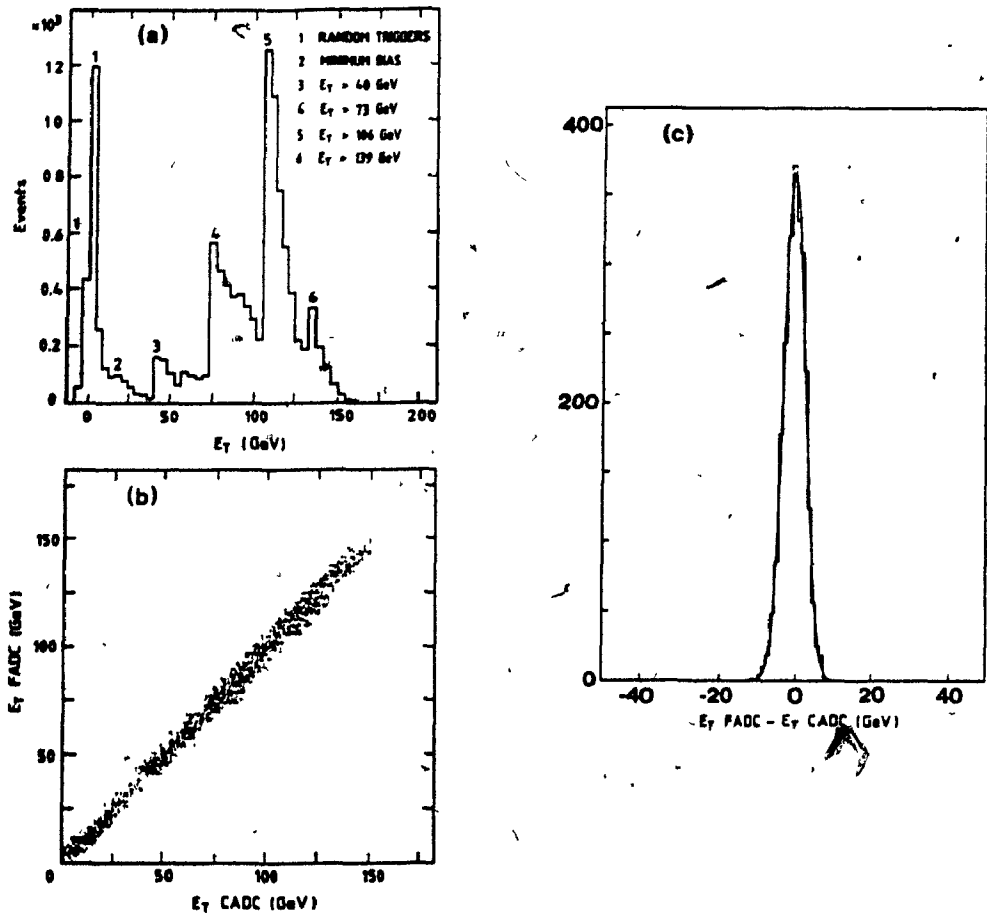
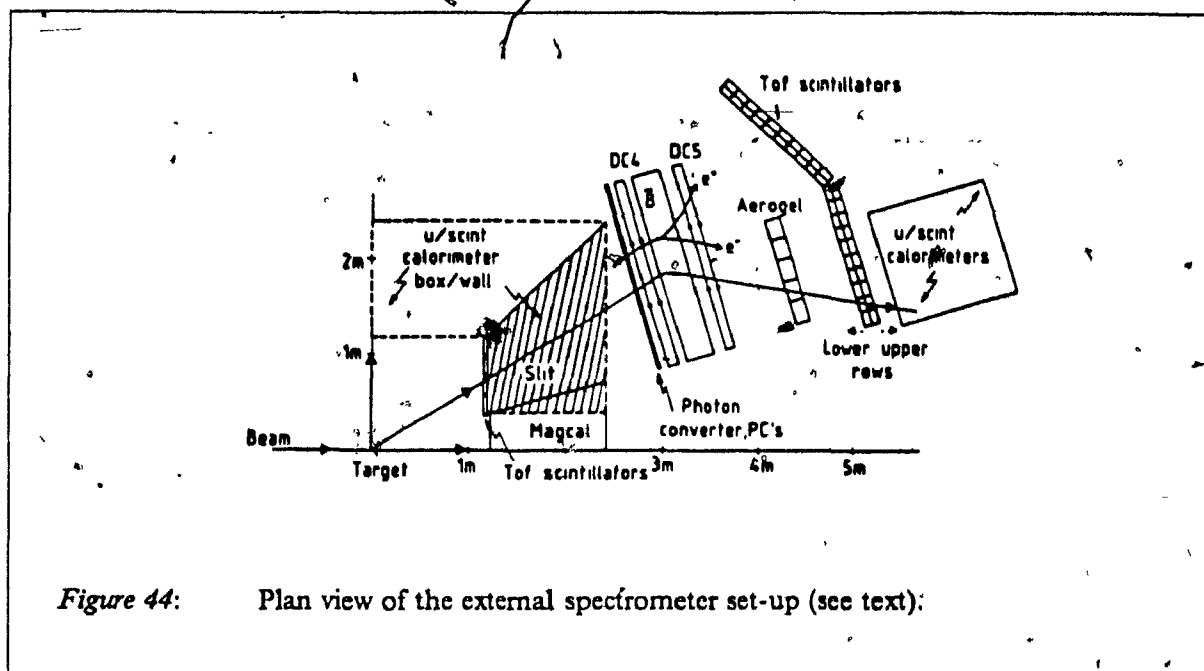


Figure 43: Example of the performances of the energy flow trigger logic. The transverse energies for a sample of events (a) are shown in a correlation plot (b) of the flash-ADC sums versus the analyzed charge-ADC values. The dispersion (c) is mainly caused by the uranium noise fluctuations (see text).

A typical flash-ADC - charge-ADC asymmetry distribution is shown in Figure 43 (c) for one of the trigger thresholds. The asymmetries have a fitted gaussian width (solid curve) of ~ 2.7 GeV corresponding to the quadratic sum of a 2.6 GeV contribution from uranium noise and an apparent ~ 0.7 GeV contribution from electronics and weighting resistors. The uranium noise thus constitutes the ultimate limitation on the transverse energy resolution.

3.6 The External Spectrometer

We conclude this chapter with a brief description of the external spectrometer (Figure 44), which performs individual particle measurements within a small solid angle (20 mrad) through the horizontal slit of the wall ($0.9 \leq \eta_{lab} \leq 2.0$).



The momentum measurement of charged particles is performed using a 7 KG magnet with a transverse momentum kick of $\sim 75 \text{ MeV}/c$, and two high resolution drift chambers. The drift chambers furthermore provide an adequate pointing through the slit as they allow measurement of the horizontal coordinate via drift time ($\sigma_x \approx 180 \mu\text{m}$) and of the vertical coordinate via charge division ($\sigma_y \approx 1.0 \text{ cm}$). An array of time-of-flight counters gives particle identification in the non-relativistic domain, whereas a set of Aerogel Cherenkov counters can separate π , K and protons up to $\sim 3 \text{ GeV}/c$. Photon measurements are made possible by a $5\% X_0$ converter placed immediately in front of the first drift chambers. The converter is sandwiched by two planes of multiwire proportional chambers, allowing a localization of the conversion point.

Chapter 4

Data reduction and analysis

I summarize here the analysis procedures developed for the treatment of the energy and multiplicity flow data concerning ^{16}O -nucleus collisions.

4.1 The selection of ^{16}O -nucleus interactions

The oxygen beam data taken with the Al, Ag, and W targets correspond to an integrated incident flux of 8.5×10^8 , 4.8×10^8 and 1.6×10^9 nuclei at 60 GeV/nucleon, and to 7.9×10^8 , 3.8×10^8 and 2.3×10^9 nuclei respectively at 200 GeV/nucleon incident beam energy.

A fraction of the oxygen ions of the primary beam get broken into nuclear fragments during extraction from the main accelerator ring to the beam transport line of the experiment. The fragments having the same rigidity as oxygen may be transported down to the detectors, so that the ion beam reaching the experiment contains a mixture of nuclei with $A/Z = 2$. The beam composition for an unbiased subsample of the observed incident flux is shown in Figure 45 on page 87 for the 200 GeV/nucleon beam, in a "mass spectrum" obtained by measuring the total energy in the full 4π -calorimetry. The ^{16}O nuclei identified by total energy were found to represent $\geq 94\%$ of the incident flux for both 60 and 200 GeV/nucleon beams.

The selection windows in \bar{E}_{tot} were wide enough to cope with a slight change (2-3%) of the raw response as a function of transverse energy (Figure 46 on page 87) or multiplicity. This change is due to the increasing absolute amount of energy deposited in regions where the hadronic response is suppressed ($e/\pi = 1.11$ for U/Cu/scintillator modules and 1.4 for the magnetized calorimeter) or reaching inert volume of the backward calorimetry (the edges of the "box", the support frame of the modules, the horizontal slit, etc.).

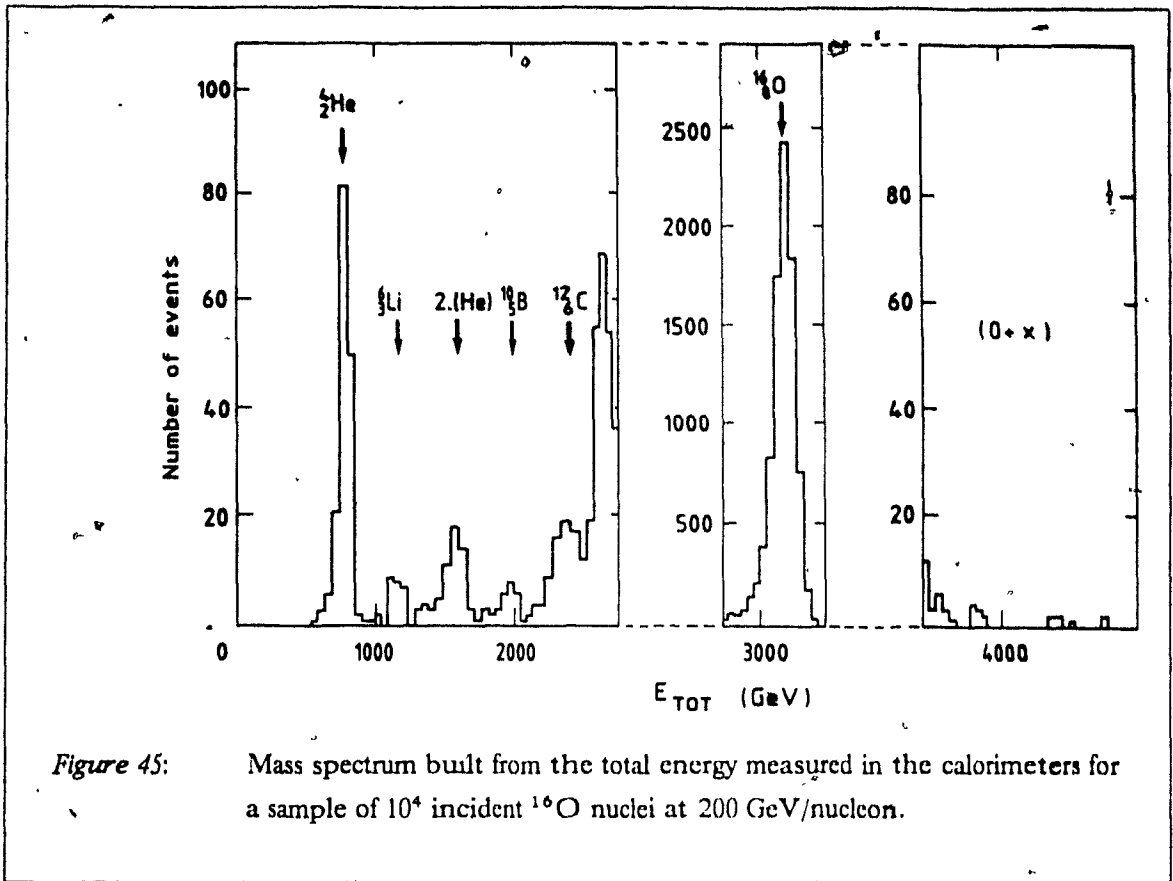


Figure 45: Mass spectrum built from the total energy measured in the calorimeters for a sample of 10^4 incident ^{16}O nuclei at 200 GeV/nucleon.

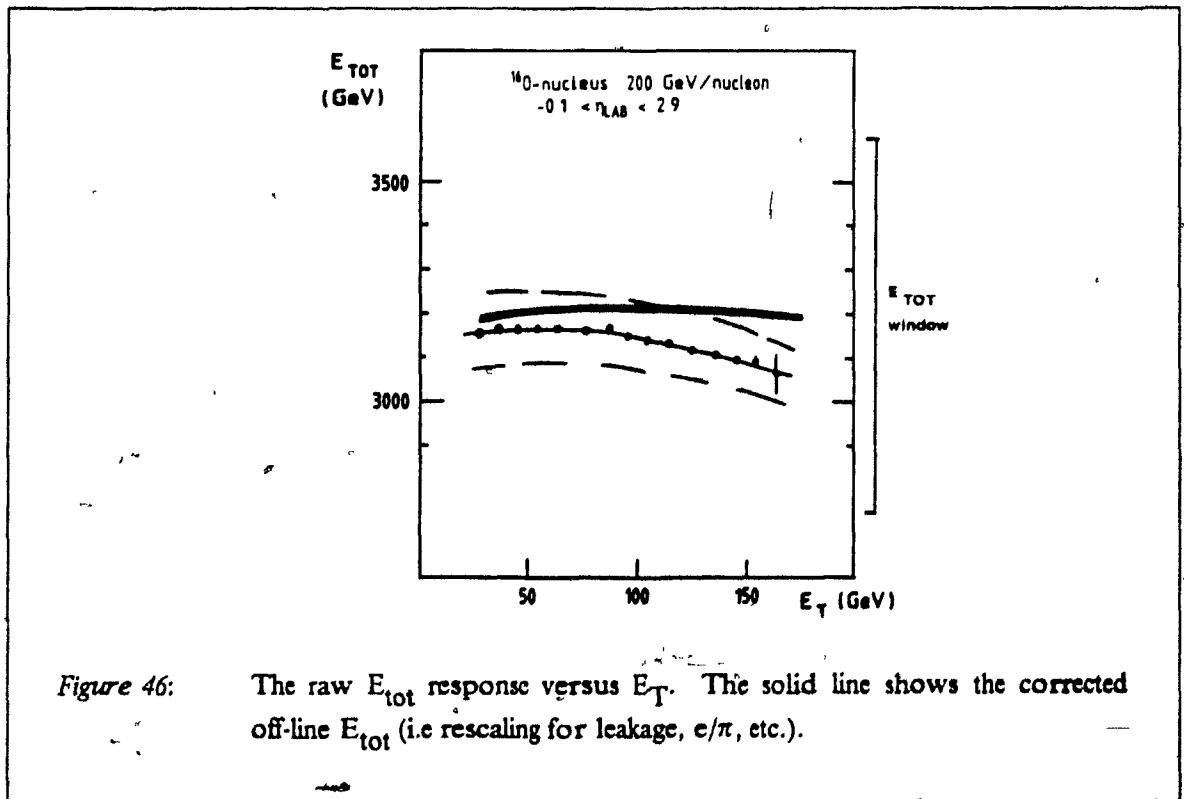


Figure 46: The raw E_{tot} response versus E_T . The solid line shows the corrected off-line E_{tot} (i.e. rescaling for leakage, e/π , etc.).

A fraction of the identified ^{16}O nuclei were broken during beam transport, or interacted in the few metres of air or in the beam scintillator before reaching the target. These upstream interactions were tagged by the measurement of ionization losses in the beam scintillators, which provided a powerful discrimination between an ^{16}O and the sum of all (or part) of its fragments. This is illustrated in Figure 47 where the ionization measured in a scintillation counter before the target is plotted versus the total energy in the calorimeter for events with $E_T \geq 100$ GeV.

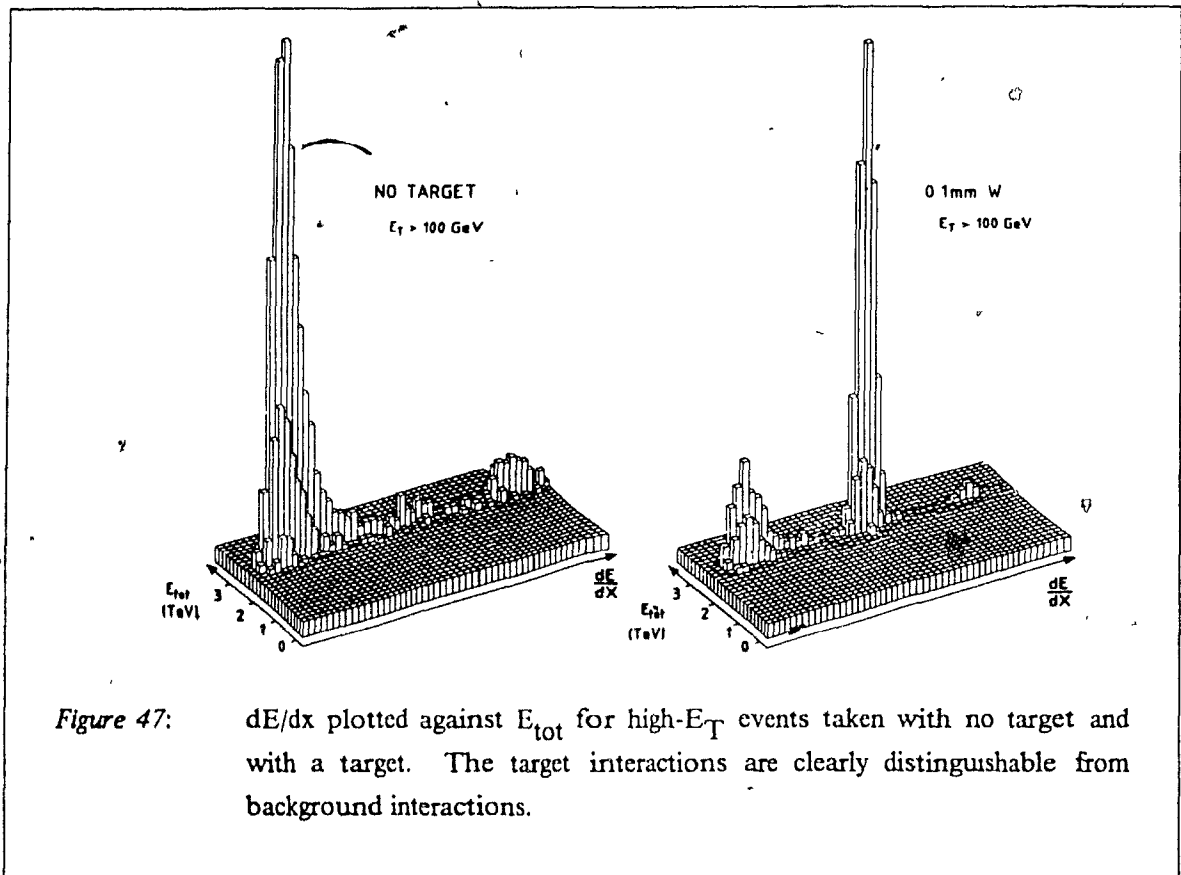
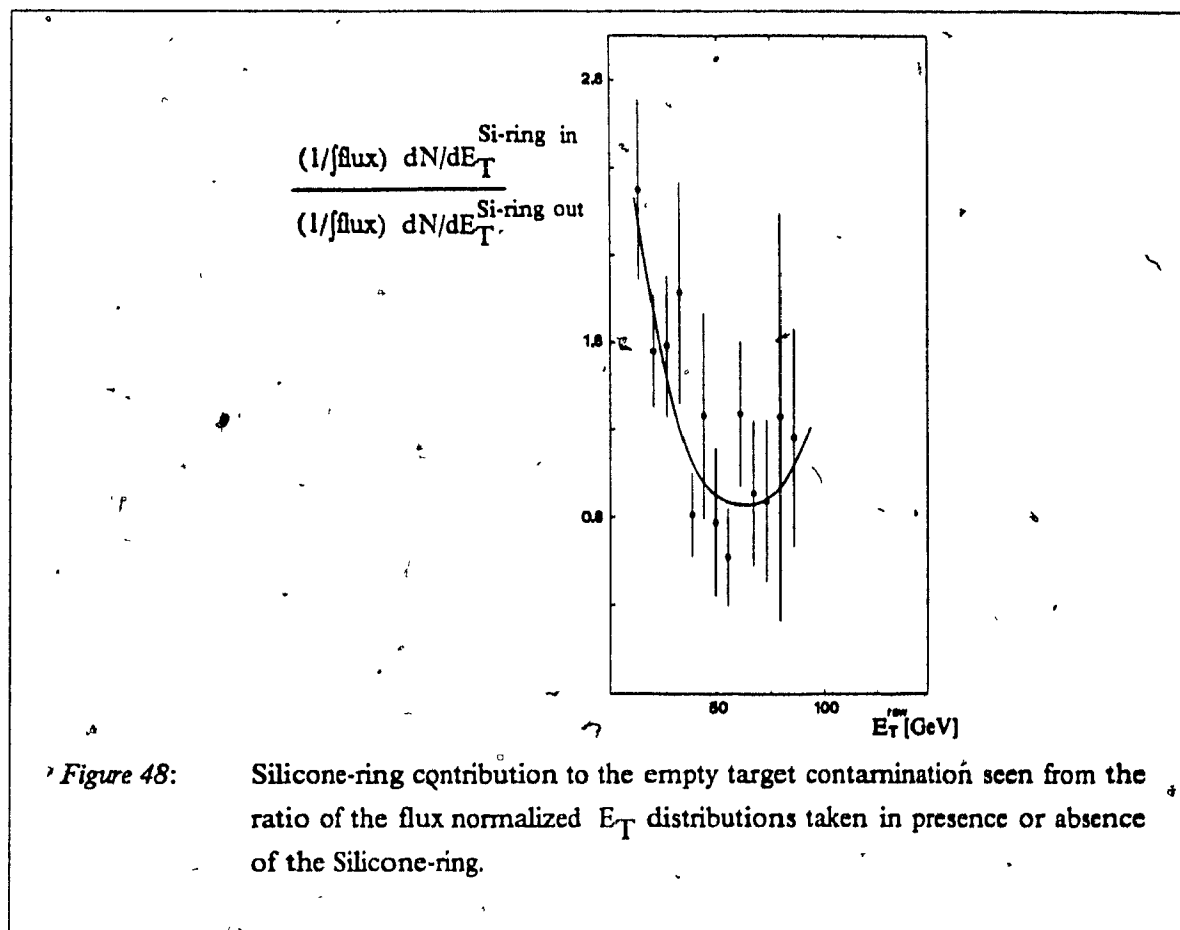


Figure 47: dE/dx plotted against E_{tot} for high- E_T events taken with no target and with a target. The target interactions are clearly distinguishable from background interactions.

From the dE/dx measurement, we find that 9.3% (6.2%) of the oxygen ions are destroyed by early interactions at 60 GeV/nucleon (200 GeV/nucleon). Only a small fraction of these early interactions, 10 to 20%, actually generate an interaction trigger in the experiment. The cuts in total energy E_{tot} and dE/dx , used in the subsequent analysis to identify the sample of ^{16}O candidates reaching the target, select $89.1 \pm 1.4\%$ ($87.5 \pm 1.3\%$) of the incident flux at 60 GeV/nucleon (200 GeV/nucleon). Finally, concerning the dE/dx selection, I shall mention that during the short period of data taking no significant degradation of the beam scintillator response due to radiation damage was observed.

The ^{16}O nuclei selected by the E_{tot} and dE/dx requirements may still interact in the multiplicity detectors behind the target. It turned out that the oxygen beam slight misalignment ($r = 0.5$ mm at

the target mid-plane) and rather wide oval profile (2.4 mm^2) allowed a significant amount of interactions in the innermost material of the Si-ring²¹. This is seen for instance in Figure 48 where we compare the flux normalized empty target data taken in presence and absence of the Si-ring detector.



The apparent thickness of the empty target is found to increase by 30 to 50% when the ring is mounted on the beam telescope. However, as E_T rises, the interactions in the multiplicity detector exhibit increasingly recognizable pathological properties; for example, an interaction in the Si-ring gives no detected multiplicity there, high multiplicity in the Si-pad, and large E_T in the pseudorapidity region overlapping the Si-ring. We can profit from such behaviour to develop simple empirical cuts. By comparing empty target and target data after dE/dx and E_{tot} selection, we defined allowed regions in correlation plots between the E_T measured in $-0.1 < \eta_{\text{lab}} < 2.9$, the charged multiplicity measured in the Si-ring covering $0.9 < \eta_{\text{lab}} < 2.8$ and the charged multiplicity in the

²¹ The central material in the Si-ring represents an average thickness of $0.01 \lambda_1$ for oxygen ions.

Si-pads covering $2.5 < \eta_{lab} < 5.0$. In windows (a) to (f) of Figure 49 on page 91, we show such correlations for empty and .1 mm W target at 200 GeV/nucleon.

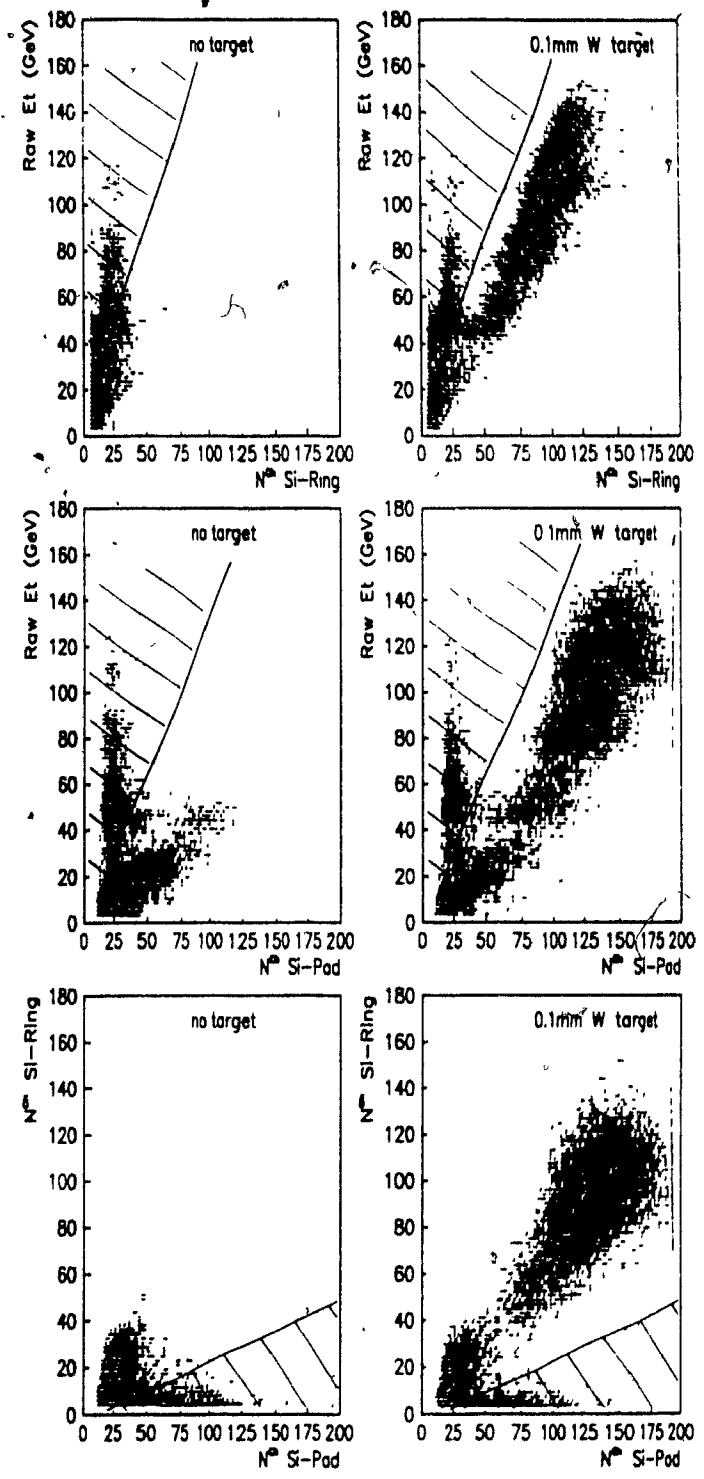
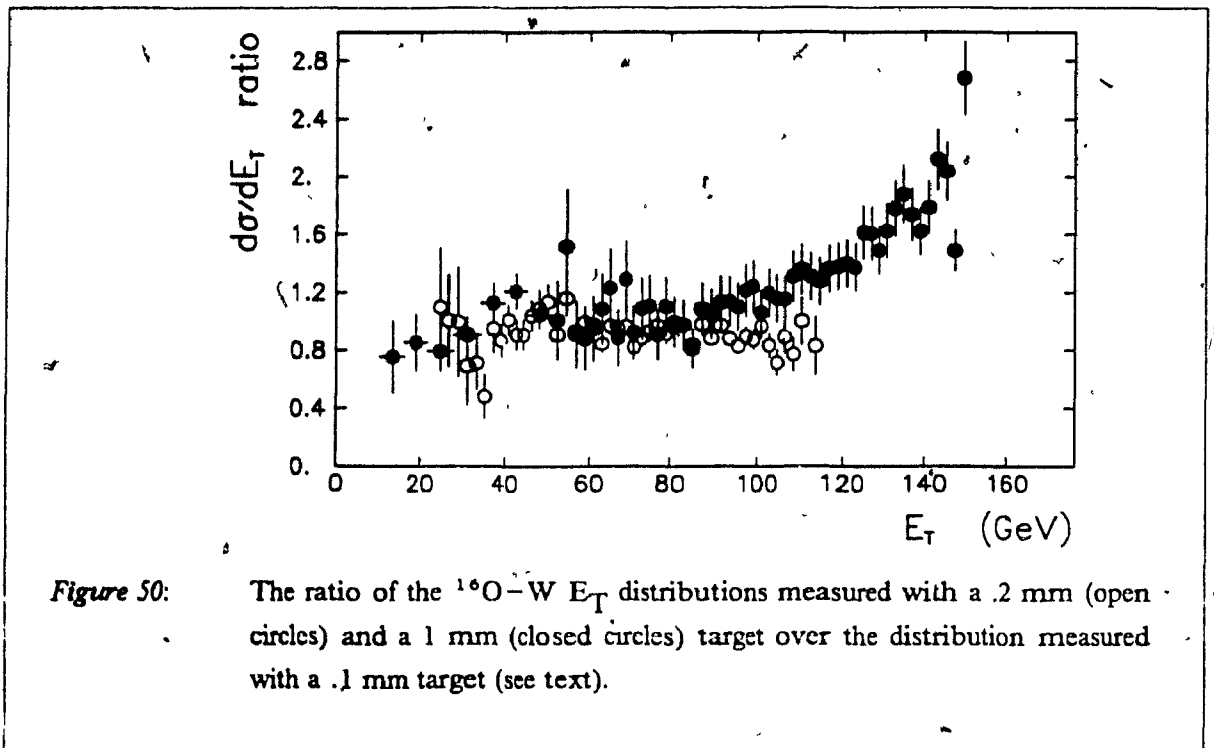


Figure 49: Correlation cuts in the (E_T , multiplicity) planes defined empirically from a comparison of target and no target data.

The efficiency losses (i.e. fraction of good events removed) introduced by the correlation cuts are negligible for $E_T > 30$ GeV. For events with lower E_T , we will estimate the losses empirically by comparing the measured distributions with the ones obtained using thick targets ($> 2\% \lambda_i$ for ^{16}O). For thick targets, we can perform an analysis without the correlation cuts since the background is relatively suppressed. The use of thick target information calls for a detailed study of multiple collision effects. The secondaries from the first interaction may interact with another nucleus in the target causing an upward fluctuation of multiplicity and transverse energy. We have to ensure that such contributions are negligible in the E_T region where we shall use the thick target information, and also that they can be neglected for thin target over the full dynamic domain covered by the E_T triggers. These questions can be investigated by plotting the ratios of the transverse energy probability distributions measured with thick targets over the one measured with thin targets. Such ratios are shown in Figure 50 where the E_T distributions for $^{16}\text{O}-\text{W}$ collisions obtained with .2 mm (60 GeV/nucleon) and 1 mm (200 GeV/nucleon) targets were divided by the distribution measured with the .1 mm target. The .2 and 1 mm data were analyzed without applying the correlation cuts, and the ratios were calculated after having subtracted the no-target contamination (section 4.2.2 on page 95) and normalized for the true beam fluxes and target thicknesses (section 4.2.3 on page 97).



The ratios $R^{1\text{mm}/.1\text{mm}}(E_T^{RAW})$ and $R^{.2\text{mm}/.1\text{mm}}(E_T^{RAW})$ are both compatible with 1.0, within statistical errors, below $E_T^{RAW} \sim 100$ GeV. This indicates that our correlation cuts are soft enough to avoid significant

efficiency losses. Above this value of E_T^{RAW} , the probability to measure a given E_T is relatively increasingly larger for the 1 mm W target. This relative increase happens in a region of E_T where the probability distribution falls steeply (see Figure 51 on page 94) so that even small upward fluctuations are sufficient to produce a fast rise in the ratio. Correspondingly, the fact that, within statistical errors, the ratio $R^{2mm,1mm}(E_T^{RAW})$ is compatible with 1.0 over the full E_T range indicates the perturbation from multiple collision on the E_T production can be safely neglected for the .1 mm W target. Similarly, for the other thin targets used (.5 mm Al and .2 mm Ag), the contamination from multiple collisions is maintained well below the achievable statistical precision over the full domain covered in energy and multiplicity flow.

After having applied the E_{tot} , dE/dx and correlation cuts, the $^{16}O - Al$, $^{16}O - Ag$, and $^{16}O - W$ data samples at 60 GeV/nucleon consist of 11167, 19166, and 75889 events respectively. At the incident energy of 200 GeV/nucleon the data consist of 2921, 5817, and 103417 events for the Al, Ag, and W target respectively. The events are distributed over the full E_T range by triggering on a charged multiplicity requirement $N^{ch} \geq 10$ and using a set of four E_T -thresholds (e.g. $E_T \geq 42, 76, 108, 136$ GeV for the W target). At this point, the remaining empty target contamination (to be subtracted) corresponds to an apparent thickness of approximately 0.9%.

4.2 The differential transverse energy distributions

4.2.1 The E_T trigger efficiency

The E_T trigger required the total analog sum in the region $-0.1 < \eta_{lab} < 2.9$ to exceed a threshold value. Good statistical coverage over a wide E_T domain was achieved by appropriate down-scaling of events satisfying several different E_T thresholds. The resulting raw distributions for the various thresholds are shown in Figure 51 on page 94, in the case of a W target for 200 GeV/nucleon ^{16}O beam.

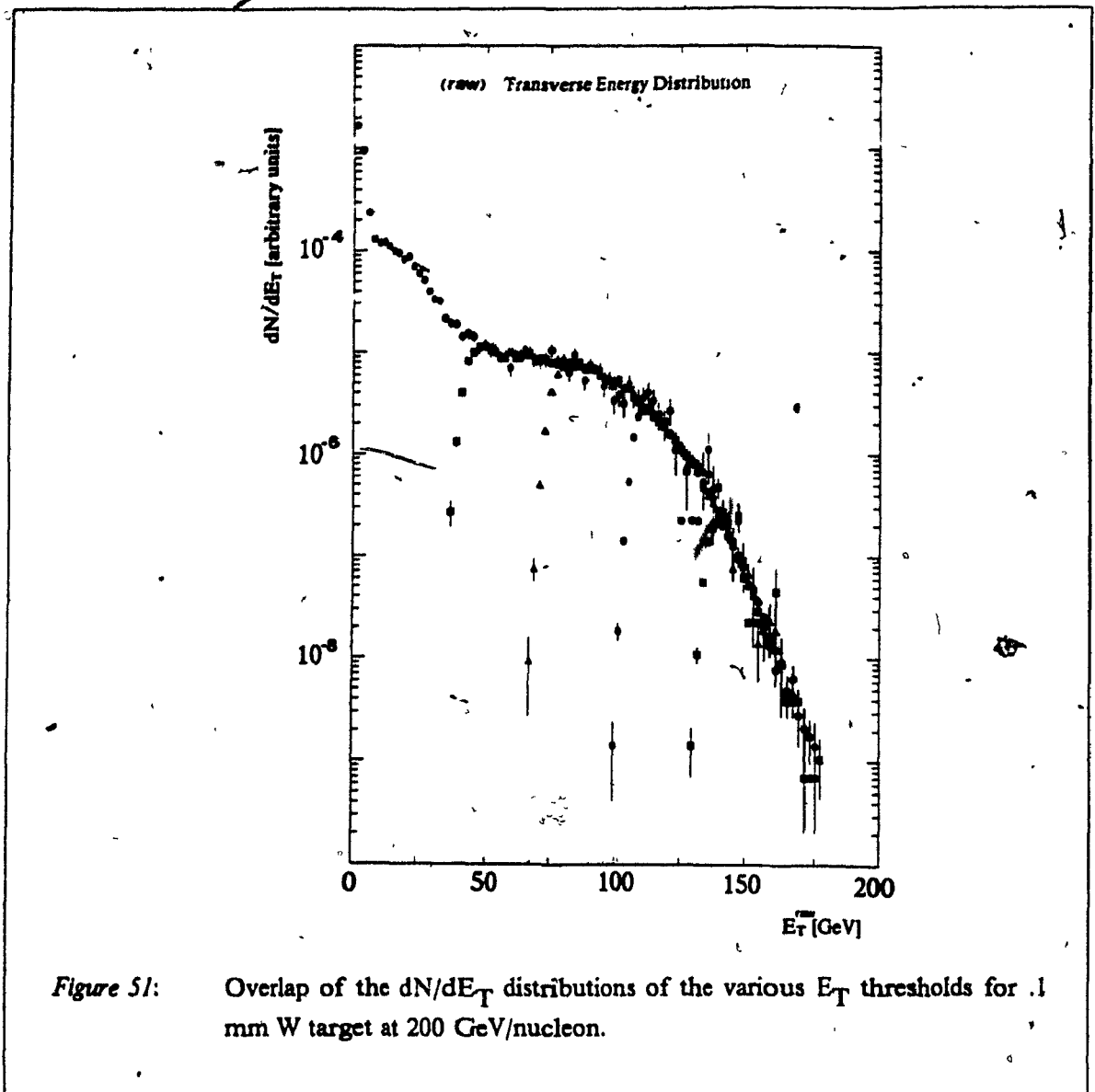


Figure 51: Overlap of the dN/dE_T distributions of the various E_T thresholds for .1 mm W target at 200 GeV/nucleon.

The observed smearing of the sharp on-line digitized E_T thresholds is to be understood as a convolution of a step function (the "ideal threshold") with an approximate gaussian measured as the normalized difference between the on-line, fast analog (flash ADC's) sum and the off-line sum performed using the charge integrating ADC's. The smearing is mainly caused by fluctuations of the calorimeter uranium radioactivity signal and partly by the limited precision of the resistors forming the on-line E_T weights (see section 3.5.5 on page 80). The uranium noise constitutes the ultimate limitation on the transverse energy trigger resolution.

Since we are not limited by statistics in the region of overlap of events from two different E_T thresholds, we decided not to attempt correcting for the efficiency losses (e.g. by a rather simple deconvolution) but rather accept only the events having an E_T well above their respective trigger

threshold. We request the E_T to be at least 3.9σ (gaussian width of the FADC-ChADC asymmetry, ~ 2.7 GeV) above threshold. For such an E_T , less than 0.01% of the events were rejected at trigger level. The ratio of the flux normalized raw E_T distribution for events of two subsequent thresholds converges to 1 safely below the off-line E_T requirement for events of the highest threshold. The observables in the overlap region of N triggers are treated as N measurement of the same quantity. The cuts ~ 10 GeV above E_T thresholds leave about 50% of the events. For the building up of the transverse energy differential cross-section $d\sigma/dE_T$, the final ^{16}O -Al, -Ag, and -W samples consist of 2869, 11432, and 32050 events at 60 GeV/n and 772, 2393, and 50094 events at 200 GeV/n. Finally, one should note that the E_T scale for the raw E_T differential cross-sections is the one resulting from an electron calibration. It has to be corrected for the differences in the relative response to electrons and hadrons (e/π ratio) and for the energy leakage. These corrections are performed using a Monte Carlo procedure that will be discussed in section 4.4 on page 99.

4.2.2 The subtraction of empty target contamination

The possible non-resolved remaining contamination from non-target interactions is studied using data taken in absence of a target. The ratios of the dN/dE_T distributions measured without and with a target, and normalized to the integrated incident flux, are shown in Figure 52 on page 96 for the Al, Ag and W targets at 60 GeV/nucleon (a) and 200 GeV/nucleon (b). At both incident energies, the remaining no-target contamination varies from about 75% at $E_T \sim 10$ GeV to $\leq 1\%$ at $E_T > 50$ GeV.

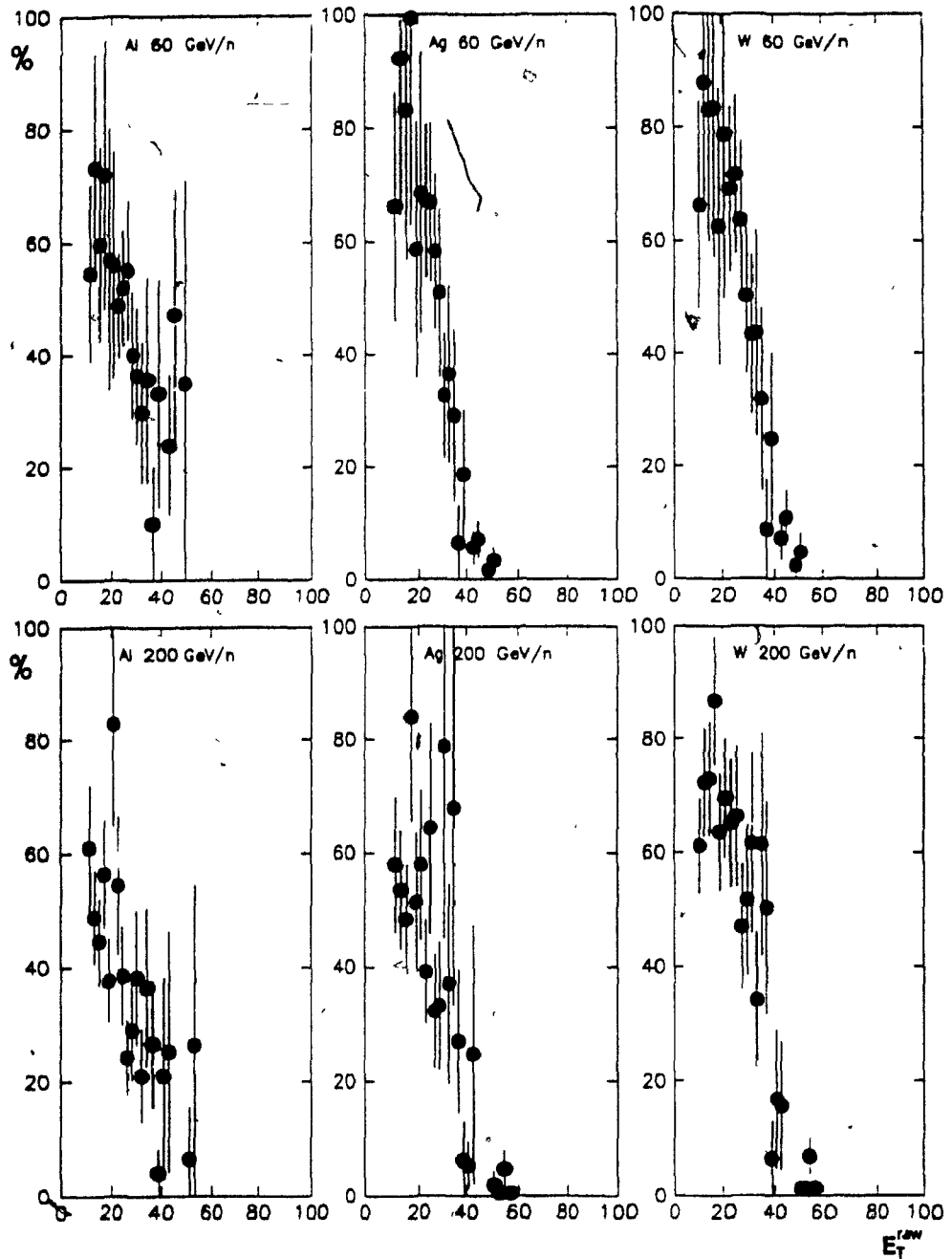


Figure 52: The ratio of the $1/\text{flux } dN/dE_T$ distributions taken in absence or presence of a target. This ratio is a measure as a function of E_T of the remaining no-target contamination for the data taken with Al, Ag and W targets at 60 GeV/nucleon (a) and 200 GeV/nucleon (b).

The high-energy tails of the E_T distributions are thus essentially background free. In the low E_T regions, the true target differential distribution is obtained by subtracting the corresponding $(1/\text{flux}) dN/dE_T$ distribution measured in absence of a target.

4.2.3 The absolute normalization

The differential cross-sections (in mb/GeV) are obtained by rescaling the $(1/\text{flux}) dN/dE_T$ distributions, to take into account the fraction of the measured incident flux which is identified as ^{16}O by the E_{tot} and dE/dx cuts, and by normalizing for the target thicknesses. We thus have

$$\frac{d\sigma}{dE_T} (\text{mb/GeV}) = \frac{1}{\text{flux}} \frac{dN}{dE_T} \times \frac{1}{\tau} \times \frac{1}{f(^{16}\text{O})} \quad (37)$$

The target thicknesses are calculated in the thin target approximation as $\tau = (\rho \cdot N_A \cdot L)/A \times 10^{-24}$ (in mb^{-1}) where ρ is the density in gr/cm^3 , N_A is the Avogadro number of atoms per mole, L is the thickness of the target in cm along the beam direction, and A is the atomic weight in gr/mole.

4.3 The transverse energy pseudorapidity distributions

The transverse energy density distribution in pseudorapidity is simply built by mapping each individual tower in the (η, ϕ) plane. Such a mapping in bins of .2 units of η and 15° of ϕ is shown in window (a) of Figure 53 on page 98 for a plane at mid-depth ($2.1 \lambda_r$) of the wall (forward face of the box). The projection of the calorimeter modules in the (η, ϕ) space is shown in window (b).

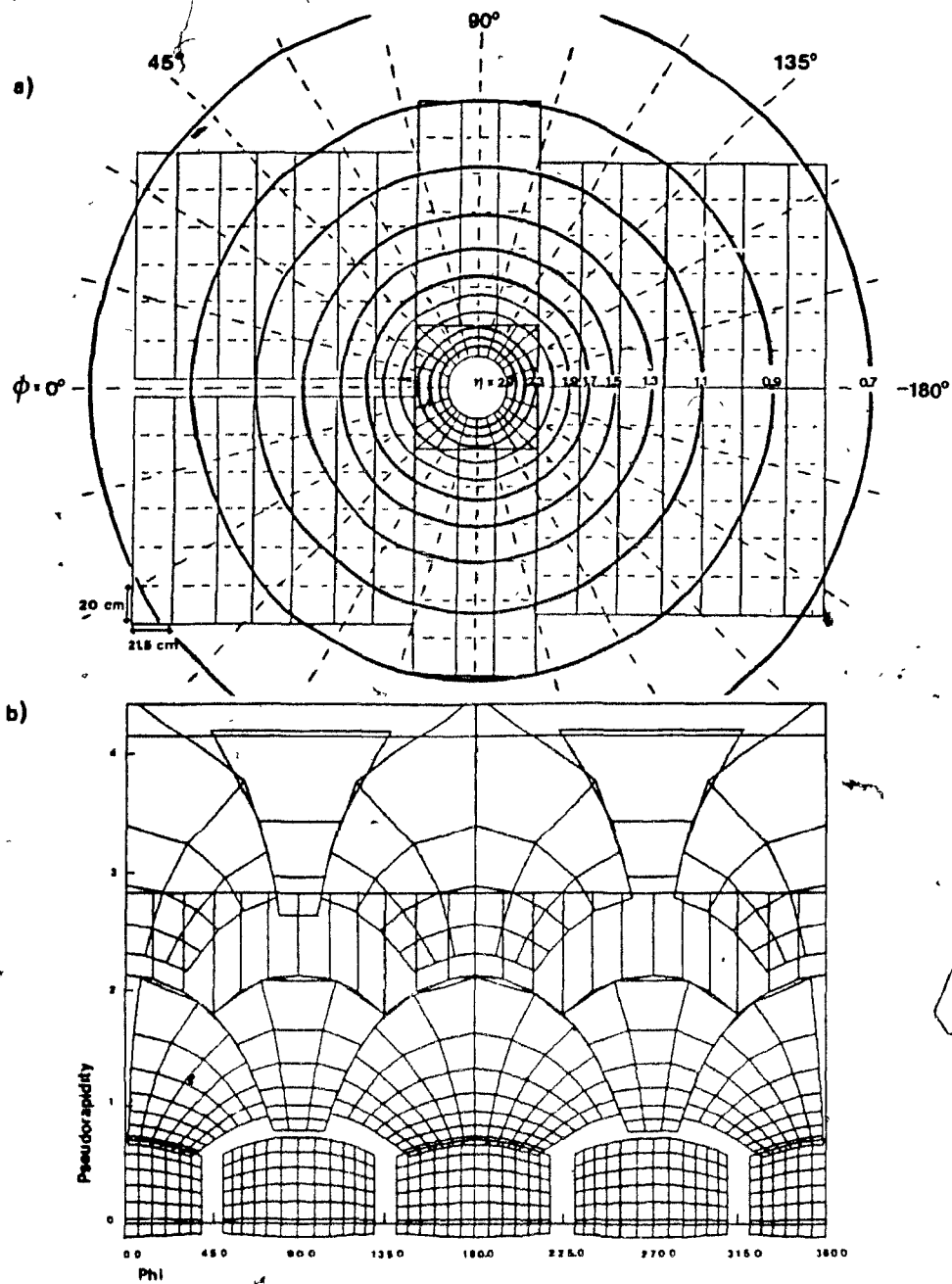


Figure 53: (a) Mapping of the calorimeter towers of the forward face of the box in pseudorapidity (η) and azimuth (ϕ). The solid circles are equipotentials in η spaced by .2 units. The dashed lines are equipotentials in ϕ spaced by 15° . (b) Projection in the (η, ϕ) space. The curves are drawn for a plane at a depth of $2.1 \lambda_c$.

The E_T of a given tower is split in fractional contributions to the various (η, ϕ) cells. The sum of all contributions to a cell forms the density of E_T in that cell. For detailed event-by-event studies (e.g. the fluctuations of the energy flow topology), one would need to ensure exact azimuthal symmetry in each $\Delta\eta$ band for an average event. But as we are mainly interested here in the projection on the rapidity axis, it will be sufficient to note that for a large number of events (e.g. all events in a given E_T window), the raw azimuthal distribution integrated over all η was found to be uniform; i.e. the dispersion around the mean E_T per $\Delta\phi$ bin is smaller than $1 - 2\% \cdot \langle E_T \rangle$. Further confidence on the required overall symmetry of an average event was gained by inspecting the P_x ($\sum E \cdot \sin\theta \cdot \cos\phi$) and P_y ($\sum E \cdot \sin\theta \cdot \sin\phi$) observables. We found that $\langle P_x \rangle \sim 0$ and $\langle P_y \rangle \sim 0$ within statistical errors (≤ 0.1 GeV) for all calorimeters elements (i.e. sides of the box, forward wall of the box, beam calorimeters) and independently of the E_T trigger requirement, except for the wall where $\langle P_x \rangle$ varies with E_T up to ~ -4 GeV ($^{16}\text{O} - \text{W}$, $E_T^{\text{RAW}} \geq 120$ GeV). This offset is due to energy leakage through the slit ($x > 0$) which allows the particle identification in the external spectrometer. The offset of the mean P_x in the wall (as well as the width of the P_x and P_y distributions) is well reproduced by Monte Carlo simulations. It does not bring a trigger bias, in the sense of favouring events with distorted energy flow topology.

4.4 The Monte Carlo corrections on transverse energy flow

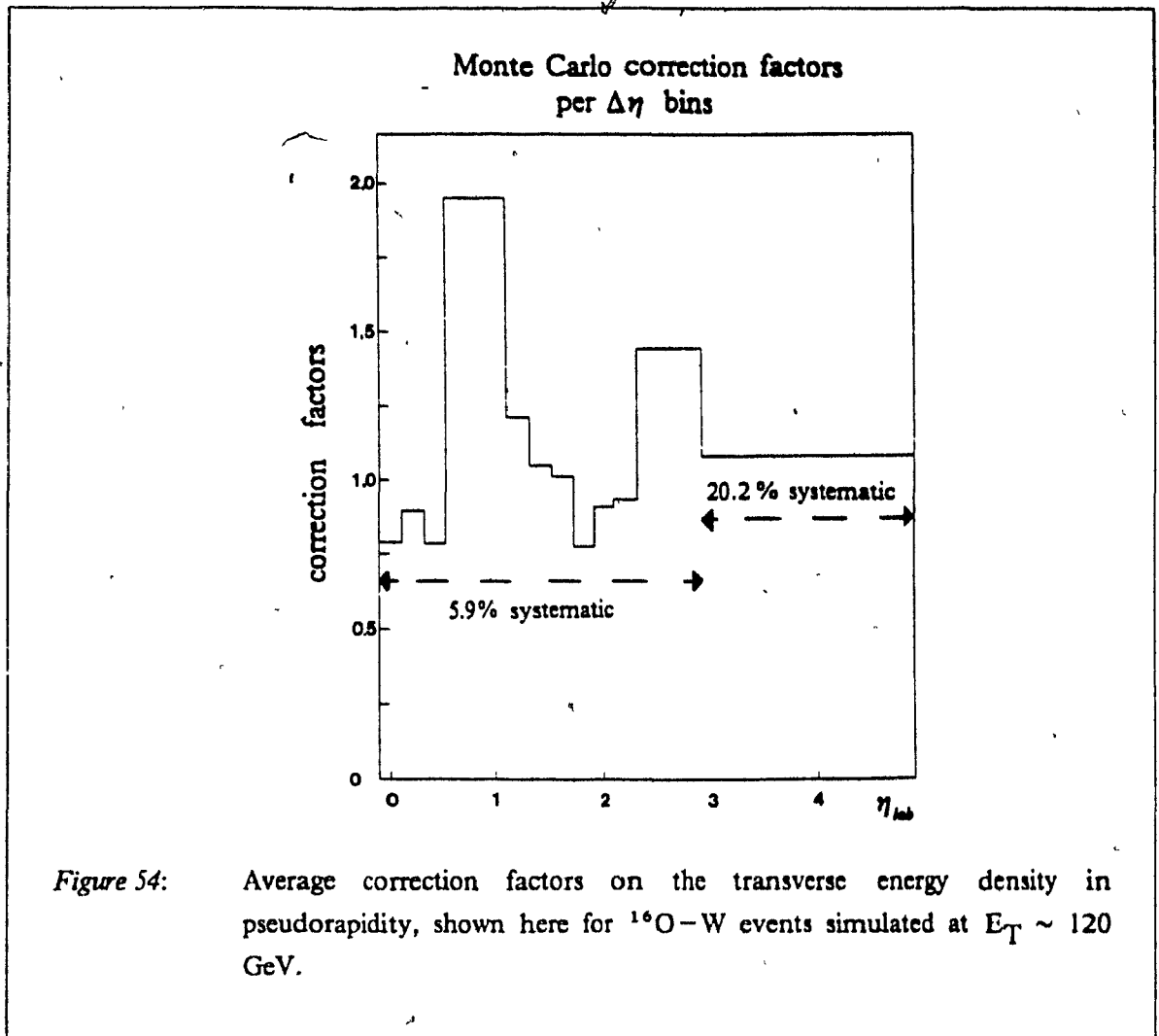
In order to obtain true E_T distributions, we have to unfold the measured spectrum from the transverse energy response and finite resolution of the calorimeters. It was seen in section 3.5.2 on page 57 that this is in general difficult in a environment where clusters due to individual particles are not resolved, since the relationship between the signal in the readout and the true energy deposited in the calorimeter depends strongly on the type, energy, and shower history of the individual incident particles.

An event generator was developed in order to reproduce the measured transverse energy density $dE_T/d\eta$ as realistically as possible and to study the effect of a change in particle composition (π , p , etc.) on the response function. The events were generated at given E_T , and the pseudorapidity densities were subsequently generated according to the measured $dE_T/d\eta$ distributions. The E_T density was further shared among individual particles assuming transverse momentum distributions based on $p - p$ data and conserving energy and momentum.

The showers in the calorimeter were simulated using a shower parametrization tuned to fit the longitudinal and lateral properties. We here again used an adapted form of the parametrization from Bock et al. [124] (see section 3.5.5 on page 80) for the longitudinal shower development and a gaussian distribution for the transverse energy spread with a FWHM of $\lambda/2$ ($X_0/2$) for hadronic (electromagnetic) showers. The response to low energy hadrons (≤ 1 GeV) was carefully simulated.

At such an energy, a proton loses a sizeable fraction of its energy by dE/dx before it undergoes an interaction initiating a shower. The signal-to-energy conversion for dE/dx losses, electromagnetic and hadronic showers was scaled according to the measured e/mip and e/π ratios.

The Monte Carlo simulations showed that the corrections on the E_T scale were dominated by leakage through the corner of the calorimeter "box", by e/π uncertainties and leakage through the calorimetrized dipole magnet, and by the response to low energy hadrons. The overall rescaling factors needed for the calculation of a true E_T from the measurement of E_T^{RAW} in the trigger region $-0.1 < \eta_{lab} < 2.9$ (i.e. after integration over pseudorapidity densities) are found to be essentially independent of E_T and similar within statistical errors for all targets at both incident energies. They amount to a multiplicative correction factor of ≈ 1.147 with a statistical uncertainty of 0.3% and a systematic uncertainty of 5.9%. The main contributions to the systematic uncertainty are: an overall uncertainty of 3% on the e/π ratios, 3% on the event generator model dependence, 3.7% from lateral spread of showers, shower leakage and effects of non-uniformity in light collection, and 1.7% on the e/μ ratio. The average Monte Carlo correction factors on the transverse energy density per bin of pseudorapidity are shown in Figure 54 on page 101.



The E_T resolution in the region $-0.1 < \eta_{lab} < 2.9$ is found to follow the simple scaling law $\sigma = (29 \pm 2) \% \times \sqrt{E_T(\text{GeV})}$.

In view of the poor forward pseudorapidity granularity, we will only be considering the mean E_T in the region $2.9 < \eta_{lab} < 4.9$ when selecting events according to E_T measured in the trigger region. The systematic uncertainty on E_T in that range is rather large (20%). It is mainly due to the uncertainty on the relative fraction of incident electromagnetic transverse energy and on the shape of the pseudorapidity distribution (mainly leading baryons) in the region $\eta > 4.9$. These determine the contribution of side-leakage from the interior of the $\eta = 4.9$ cone.

4.5 The multiplicity differential and pseudorapidity density distributions

The events selected by the amount of transverse energy in the pseudorapidity region $-0.1 < \eta_{lab} < 2.9$ (which covers the target fragmentation region and part of the central region for the ^{16}O -nucleus collisions) can be further analyzed in terms of the multiplicity observable, over the extended effective pseudorapidity coverage $0.9 < \eta_{lab} < 4.9$ provided by the silicon detectors. We here use the transverse energy to fix the "geometry" of the collisions prior to the analysis of this other observable characterizing the particle flow. The transverse energy is expected to be strongly correlated to the total number of participant nucleons or the total number of inelastic collisions.

For the multiplicity analysis, the correlation cuts were made stronger than the ones applied for the E_T analysis in order to further reduce the "no-target" background. This reduction was essential since we only have small statistical samples of pure no-target events and correspondingly cannot precisely determine their characteristics. Furthermore, the no-target contamination creates strong distortions in the pseudorapidity distributions since the effective pseudorapidity coverage of the silicon detectors is very different for events having a vertex displaced in Z . Figure 55 on page 103 shows the final sample of events for the $^{16}\text{O}-\text{W}$ data at 200 GeV/nucleon, displayed in correlation plots of the raw E_T versus the raw multiplicity in the Si-pad (a) and the Si-ring (b).

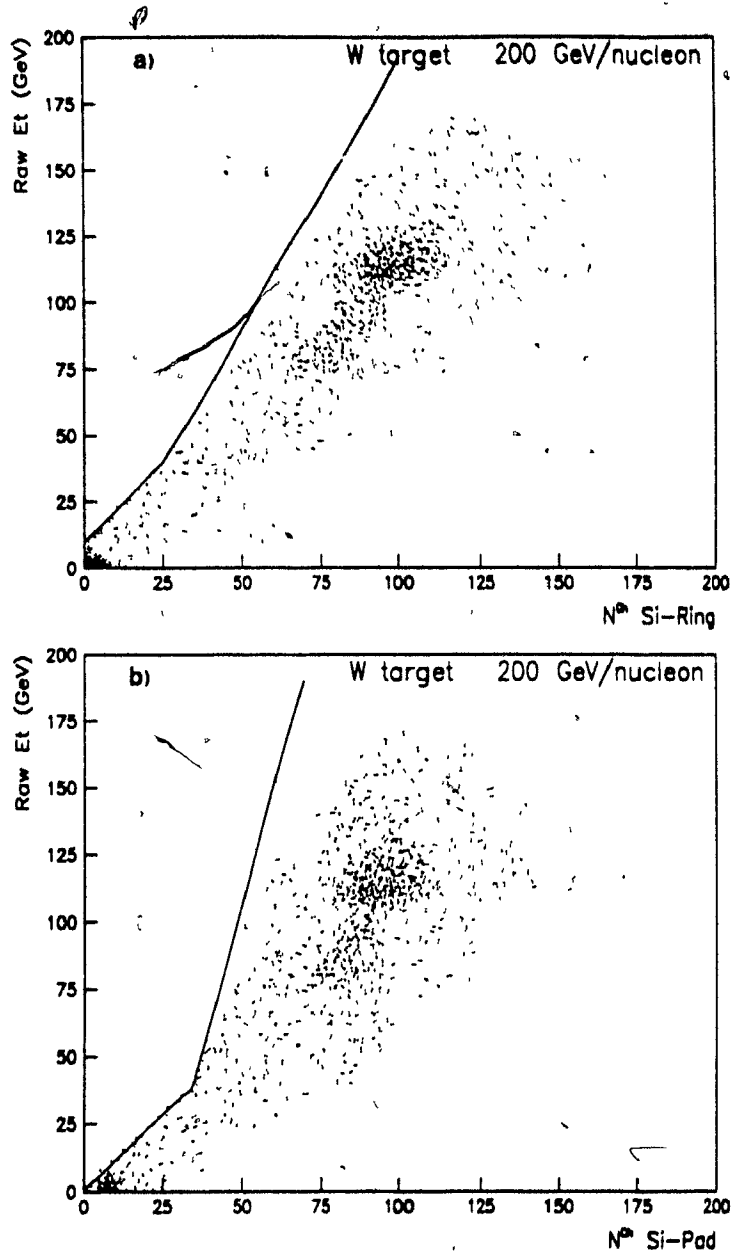


Figure 55: The raw E_T (E_T^{RAW}) versus the raw multiplicity (M^{RAW}) measured with the Si-ring (a) and the Si-pad (b) detectors. The solid lines are the cuts applied to reduce the contamination from pathological "no-target" events.

A certain number of spurious events are seen on the high multiplicity side (right of the main correlation axis in Figure 55). For these events, the distribution of the hits in the silicon segments showed slightly abnormal patterns that could be the sign of an electronic noise triggered by high currents. However, the interpretation remains suspicious and these events cannot safely be

distinguished from normal events. The analysis and physics interpretation of the very high multiplicity tails, where the density of normal events decreases, is thus severely hampered.

Inefficiencies of various origins (i.e. geometrical losses due to inactive silicon segments, multiple hits, charge sharing) have to be overcome before obtaining an estimate of the true multiplicity N_{TRUE}^{ch} associated with a given raw multiplicity N_{RAW}^{ch} . The efficiency losses due to multiple hits in a single detector segment could in principle be avoided by extracting the multiple hit information from the pulse-height distributions of each individual segment. But since we are mainly interested in the average properties (e.g. the true multiplicity associated to a subsample of events satisfying some E_T constraints), we rather chose to work with average analytical corrections. If, for a sample of events, a is the mean occupancy for a given cell (silicon segment) and if it is built up by essentially uncorrelated minimum ionizing particles (mip), the average response of that cell will be a sum of Landau functions corresponding to the energy loss of 1, 2, ..., n particles with relative contributions given by Poisson statistics. For a mean occupancy a , the probability of having any number of hits ≥ 1 can be written as

$$P(\text{any}) = P(1) + P(2) + \dots + P(n)$$

$$P(\text{any}) = 1 - P(0) \tag{38}$$

where $P(n) = (e^{-a} a^n) / n!$. Using equation (38) one can thus deduce the true mean a from the measured mean $P(\text{any})$,

$$a = -\ln(1 - P(\text{any})) \tag{39}$$

Having a we can then evaluate $P(n)$ for any number n . In the forward pseudorapidity regions ($\eta_{lab} \geq 2.9$), the pulse-height distributions are found to be satisfactorily described by Poisson distributed multi-hit probabilities. This is seen in window (a) of Figure 56 on page 105, where we compare the sum (solid curve) of the Poisson weighted contributions for 1, 2, ..., n particles (dashed and dotted curves) to the pulseheight distribution measured in a Silicon-ring segment situated near the lower edge of the forward region for high multiplicity $^{16}\text{O} - \text{W}$ events. At more forward angles, a $\sim 2 \pm 1\%$ systematic excess of double pulseheights is seen, consistent with the rate expected from fast $e^+ e^-$ pairs originating from γ -conversions in the targets.

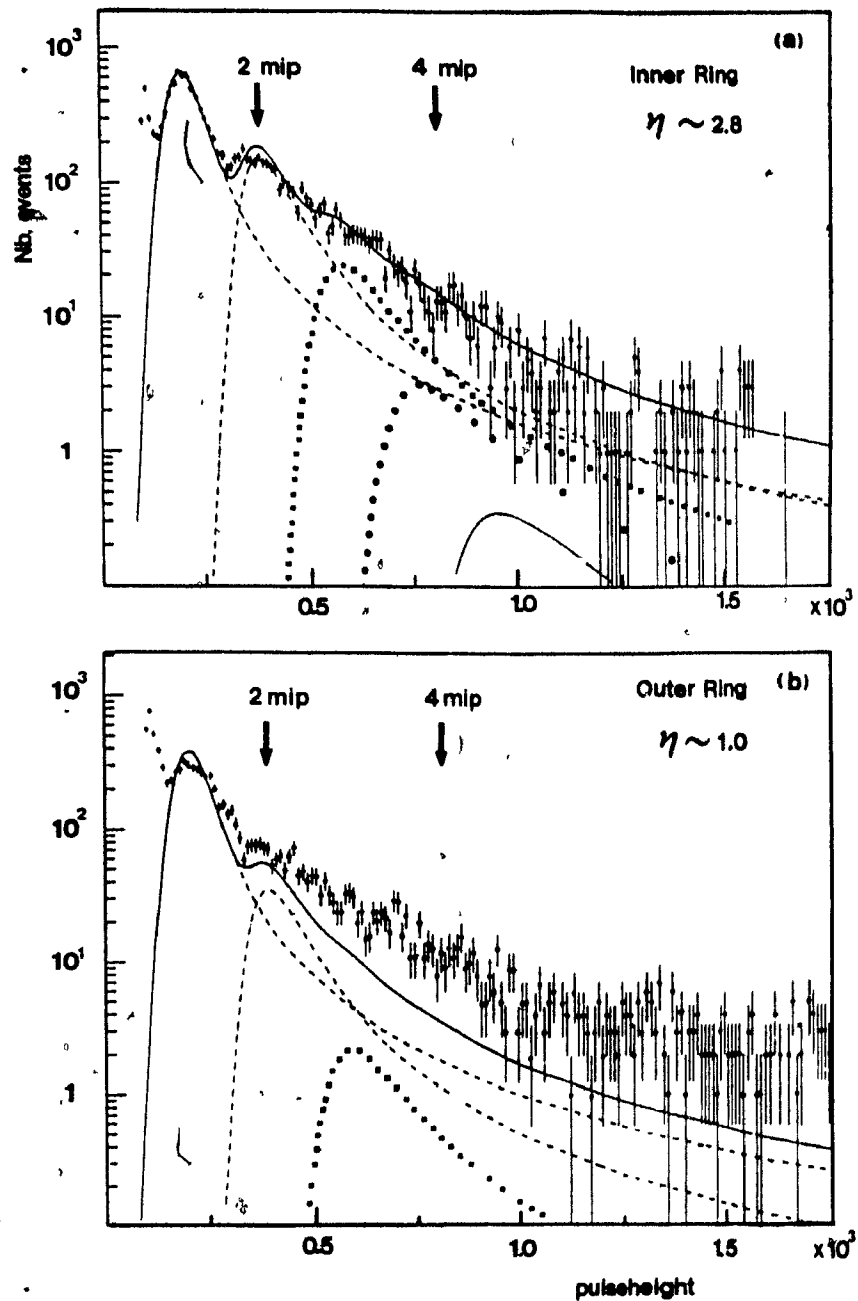


Figure 56: The pulseheight distributions in silicon segments for high multiplicity $^{16}\text{O}-\text{W}$ events at 200 GeV/nucleon. The distribution in window (a) was measured for a segment at central pseudorapidity $\eta \sim 2.8$ ($\theta \sim 7^\circ$), whereas window (b) shows the distribution for a segment closer to the target fragmentation region, at $\eta \sim 1.0$ ($\theta \sim 40^\circ$). The solid curve is the sum of the Poisson distributed multi-hit Landau functions (dotted curves).

Going towards the target fragmentation region, we find an increasing excess of high pulse-heights (≥ 4 mip's). This is seen for instance in window (b) of Figure 56 on page 105 for a silicon segment at $\eta \sim 1.0$. Given the angular distribution, multiplicity and target mass dependence of the hits with very high pulseheights, we tentatively attribute the excess above the multi-hit probabilities to densely ionizing slow target fragments, i.e. to knock on protons and evaporation heavy fragments. The densely ionizing tracks have a high probability of generating large correlated signals in neighbouring elements (cross-talk). Since we don't possess yet a precise knowledge of their associated pulse-height distribution, and since their spatial distribution as a function of impact parameter and target mass is yet unknown, we could not safely modelize the contribution of the slow fragments in order to treat them in our statistical approach. More precise information concerning these slow fragments will have to await for event-by-event pulseheight analysis. We thus simply exclude the hits with an associated energy loss ≥ 4 mip's and correct the resulting inefficiency for true multiple mip's on a statistical basis. This "slow fragment" subtraction reduces the total charged multiplicity by $\leq 1\%$ in the forward region ($\eta_{lab} > 2.9$) and 3–5% in the central region ($\eta_{lab} < 2.9$). At the lower edge of our pseudorapidity acceptance it amounts to $\sim 10\%$ of the observed multiplicity density. Our results are correspondingly depleted from target fragments, but the systematic uncertainty on the remaining fraction may be as large as the effective depletion. The hit probabilities have finally to be corrected for the 2–5% loss of singly charged particles due to our low pulseheight threshold. From the measurement of the overall number of silicon segments having one or more hits, one can calculate the true multiplicity in the acceptance of the silicon ring or the silicon pad detectors from the equation

$$N_{TRUE}^{ch} = \frac{1}{\epsilon_1} \cdot \frac{a}{P(any)} \cdot N_{RAW}^{ch} \quad (40)$$

where a is again the true mean occupancy, but $P(any)$ is now taken as

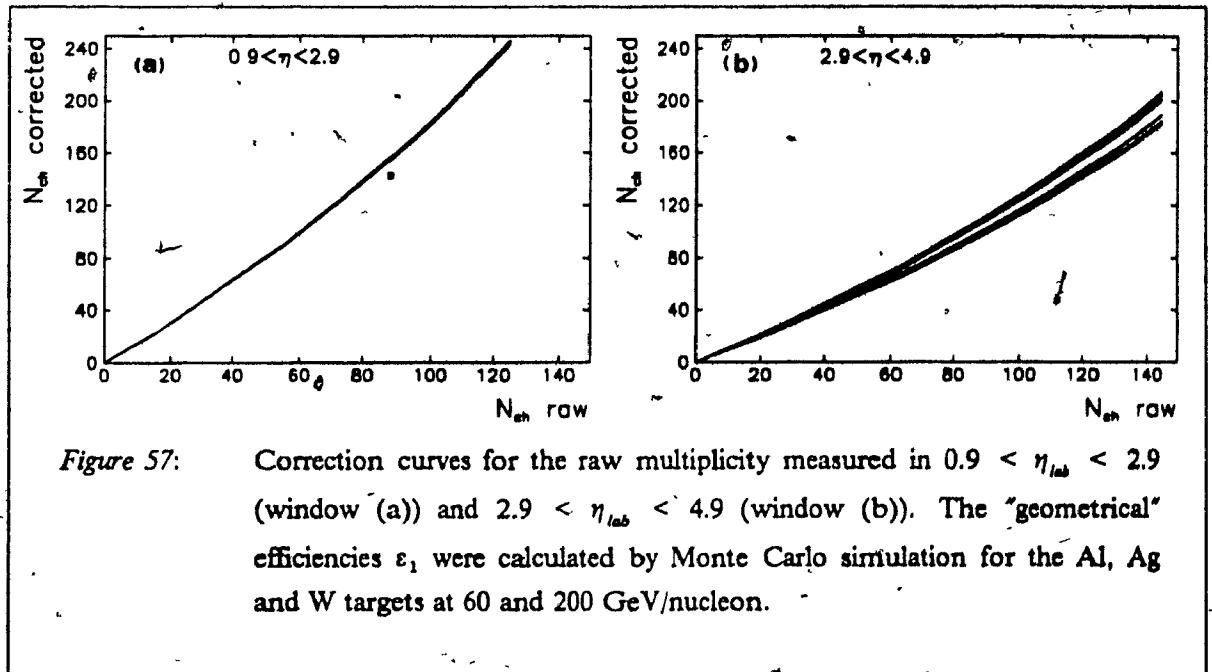
$$P(any) = \frac{\text{number of hits}}{\text{number of segments alive}} \equiv R$$

In formula (40), ϵ_1 is an efficiency function that includes the geometrical losses due to inactive segments, the corrections for charge sharing and the corrections for beam width and beam misalignment. These effects were simulated by an iterative Monte Carlo procedure, which further took into account the varying size and shape of the segments, and for which the uncorrected charged particle pseudorapidity distribution as a function of charged multiplicity, target, and incident energy, was used as an input at the first iteration. Note that the rather large beam offset, $(\bar{x}, \bar{y}) \sim (0.51\text{mm}, -0.43\text{mm})$, and width, $(\sigma_x, \sigma_y) \sim (0.5\text{mm}, 1.2\text{mm})$, introduce strong event-by-event changes of the effective pseudorapidity and azimuthal coverage of the segments. For the building up of the differential cross-sections, the corrections were calculated in an effective pseudorapidity coverage fixed to $0.9 < \eta_{lab} < 2.9$ for the silicon ring and $2.9 < \eta_{lab} < 4.9$ for the silicon pad. The Monte Carlo simulations showed that the efficiency ϵ_1 could well be approximated by a constant to be fixed

separately for the chosen coverage of each silicon detector, and for each target and incident energy. From equations (40) and (38) we thus have

$$N_{TRUE}^{ch} = \frac{-1}{\varepsilon_1(\Delta\eta, A, E_{inc})} \frac{\ln(1-R)}{R} N_{RAW}^{ch} \quad (41)$$

The resulting rescaling functions for the transformation of N_{RAW}^{ch} into N_{TRUE}^{ch} are plotted in Figure 57 for the central (window (a)) and forward (window (b)) pseudorapidity coverages, and for the various target masses for the 60 and 200 GeV/nucleon incident beams.



The overall corrections are rather large, reaching $\sim 220\%$ for the highest measured multiplicity (i.e. in the tail of the $^{16}\text{O}-\text{W}$ distribution at 200 GeV/nucleon) and the remaining systematic uncertainty on the corrected multiplicity scale is estimated to be as large as 10%. The resolution on the true multiplicity is calculated as the quadratic sum of the contributions due to "geometrical" inefficiencies (ε_1) and pile-up inefficiencies (ε_2). It can be well approximated as

$$\frac{\sigma}{N_{TRUE}^{ch}} = \sqrt{\frac{1 - \varepsilon_1 \varepsilon_2}{\varepsilon_1 \varepsilon_2}} \frac{1}{\sqrt{N_{TRUE}^{ch}}}$$

The resulting charged multiplicity resolution functions are plotted in Figure 58 on page 108 for the central (window (a)) and forward (window (b)) pseudorapidity coverages, and for the various targets

and incident energies. Note that the pile-up inefficiencies are strongly dependent on the measured charged multiplicity, $\epsilon_1 = \text{Constant} \times \{\ln(1 - R)/R\}$, so that the resolution $\sigma(N_{TRUE}^{ch})$ does not scale with $\sqrt{N_{TRUE}^{ch}}$.

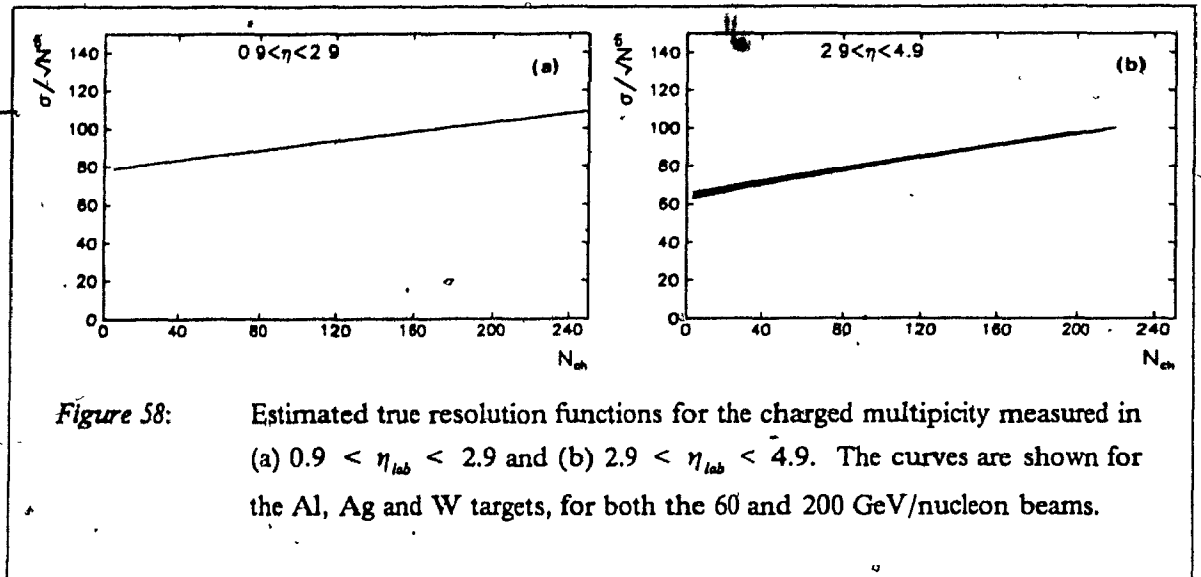


Figure 58: Estimated true resolution functions for the charged multiplicity measured in (a) $0.9 < \eta_{lab} < 2.9$ and (b) $2.9 < \eta_{lab} < 4.9$. The curves are shown for the Al, Ag and W targets, for both the 60 and 200 GeV/nucleon beams.

The resolutions are varying from $\sim 70\%$ to $\sim 110\%/\sqrt{N^{ch}}$ over the measured range, and the corrections (see section 4.6 on page 109) for the resolution smearing will be large, especially in the steeply falling tails of the differential cross-sections, at large multiplicities.

The charged multiplicity pseudo-rapidity density distributions are obtained by projecting the silicon segments into the $\eta - \phi$ space and distributing the hits in the various $(\Delta\eta, \Delta\phi)$ cells with relative weights computed by Monte Carlo simulation. Here again, the procedure took into account the effect of charge sharing, the beam profile and offset, and the geometrical and multiple-hit inefficiencies. The average efficiency of each $(\Delta\eta, \Delta\phi)$ cell was calculated for a large sample of events selected by splitting the E_T scale into ~ 15 GeV windows (that is for events which are to some degree physically equivalent). The corrections were calculated over an extended pseudorapidity coverage of $0.9 < \eta_{lab} < 5.5$. Above the 10% systematic uncertainty on the integrated charged multiplicity, we estimate that the remaining uncertainty on the localization of the multiplicity density varies from $\sim 3\%$ in the $\Delta\eta \sim .2$ bins at small η , to up to $\sim 10\%$ in the most forward bins ($\eta > 4.5$) where the granularity is poor and where the effective coverage in η and ϕ is only partial. The two silicon detectors were treated separately and were found to agree to within 4% in the region where they overlap ($2.5 < \eta < 2.9$). In all cases, the corrected azimuthal distributions for a large sample of events are symmetric within statistical errors.

4.6 Deconvolution of the differential cross-sections for finite resolution

The differential cross-sections have to be corrected for the finite resolution in the measurement of transverse energy or charged multiplicity. These corrections ought to be particularly important for the steeply falling high tails of the $d\sigma/dE_T$ and $d\sigma/dN^{ch}$ distributions.

The philosophy of the procedure developed for the deconvolution consists of first finding a judiciously chosen representation of the data, i.e. a parametrization that fits the data with a $\chi^2/ndf \sim 1$ when considering the entire range of E_T (or N^{ch}), or when splitting the E_T (N^{ch}) scale in 4 or 5 windows. This optimal continuous representation is then deconvoluted analytically and the ratio of the deconvoluted to the undeconvoluted representation gives multiplicative factors for the cross-section as a function of E_T (N^{ch}). The question of the exact nature of the initial representation is a priori irrelevant, but the task can be considerably simplified if one possesses a guidance towards a stable family of representations. Such a guidance was provided by the Nucleon Collision Model [21] [34] (see section 2.2 on page 20) where the nuclear collision is described as a superposition of independent collisions. Such a model offers the advantage of the possibility to implement in a simple manner a precise description of the geometry of the collisions (i.e. sampling over the impact parameters, spatial extent of the colliding objects in terms of the nuclear density profiles, etc.). We used the model with great liberty, adjusting within reasonable limits the overall normalization, the nuclear deformation and density profiles, or introducing a damping for the contribution of successive inelastic collisions. Such a tuning would obviously not be permitted if attempting to use the model as a basis for physics analysis (as done in section 5.2.2 on page 119), but it should be stressed again that here we are only interested in finding a quality representation with the best fitted slope of the $d\sigma/dE_T$ or $d\sigma/dN^{ch}$ distributions over the full E_T or N^{ch} range. In all cases, we could tune the underlying geometrical differential cross-section in order to be left with the need of only two free parameters characterizing the E_T (N^{ch}) scale and the softening from the pure geometrical distribution. We used a minimization code to obtain the best fitted values of the two free parameters. The code also provided a 70% confidence level contour in the free parameter space. All representations obtained by circling around the confidence level contour were also deconvoluted and the resulting deconvoluted/undeconvoluted ratios form, as a function of E_T or N^{ch} , an envelope around the corresponding ratio for the best fitted representation. The half-width of this envelope is used to propagate the error introduced by our deconvolution procedure.

Figure 59 on page 110 exemplifies the main steps of the procedure as applied to the $d\sigma/dE_T$ distribution measured for $^{16}\text{O} - \text{W}$ collisions at 60 GeV/n. This distribution has a particularly steep tail so the correction factors and their associated errors are correspondingly large. Window (a) in Figure 59 on page 110 shows the best fit (solid curve) to the undeconvoluted differential cross-section (closed circles) together with an ensemble of representations (dotted lines) obtained by following the 70% confidence level contour in the parameter space. Window (b) shows the corresponding ratios of the deconvoluted over undeconvoluted representations. The solid line is the correction curve by

which we multiply the differential cross-section, and the half width at a given E_T of the envelope formed by the dotted curves is the error at that E_T on the deconvolution procedure.

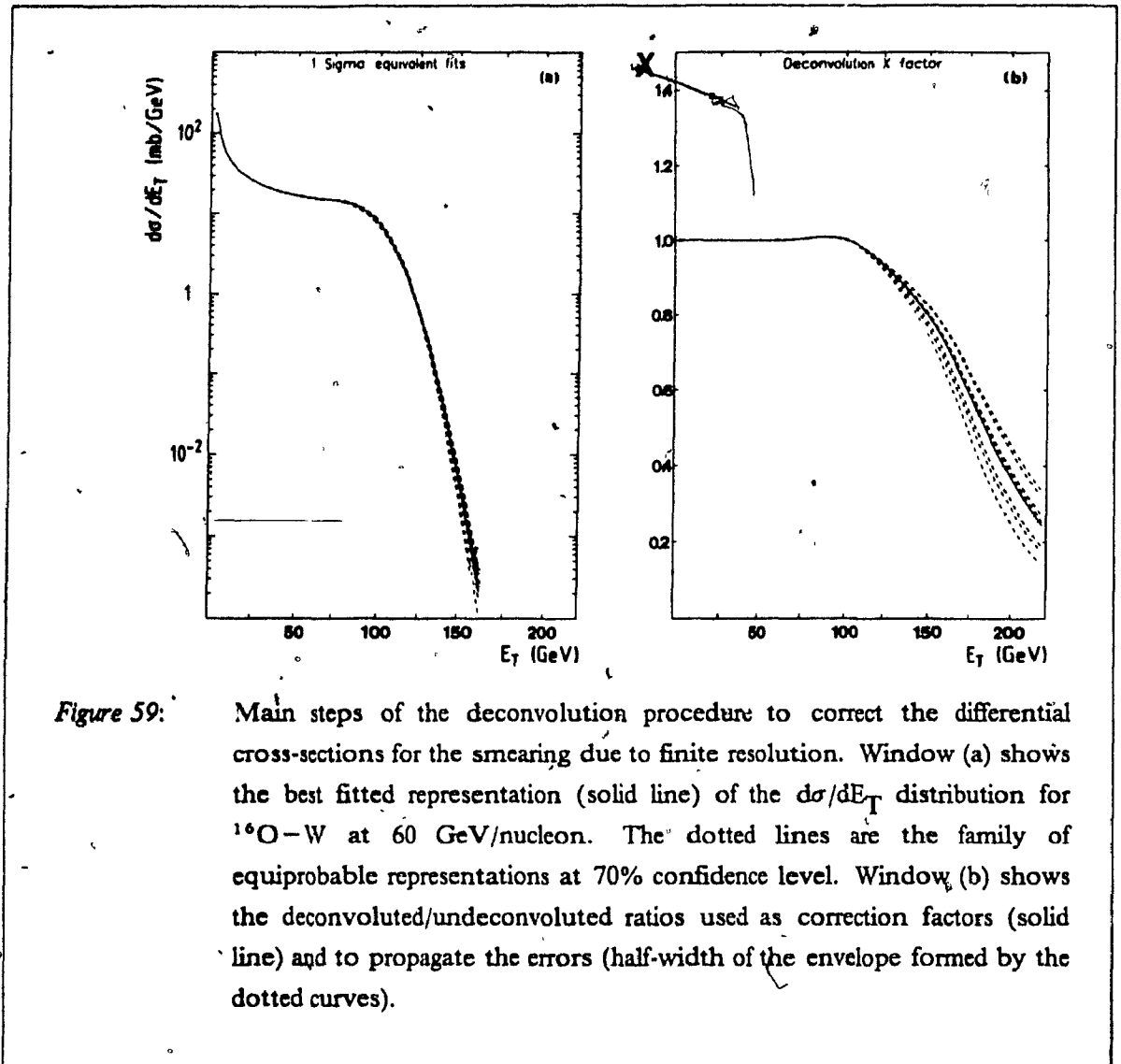


Figure 59: Main steps of the deconvolution procedure to correct the differential cross-sections for the smearing due to finite resolution. Window (a) shows the best fitted representation (solid line) of the $d\sigma/dE_T$ distribution for $^{16}\text{O}-\text{W}$ at 60 GeV/nucleon. The dotted lines are the family of equiprobable representations at 70% confidence level. Window (b) shows the deconvoluted/undeconvoluted ratios used as correction factors (solid line) and to propagate the errors (half-width of the envelope formed by the dotted curves).

The deconvolution procedure, as it should by its very nature, exactly conserves the integral of the differential cross-sections. This was explicitly checked in all cases.

Chapter 5

Experimental results and discussion

5.1 Introduction

The presentation of the experimental results on ultra-relativistic ^{16}O –nucleus collisions will mainly focus on the study of global physical observables. The transverse energy (E_{T}) flow is the natural starting point. First of all, it constitutes the main tool for the event selection, which was performed in all cases by requiring a given E_{T} in the pseudorapidity interval $-0.1 < \eta_{\text{lab}} < 2.9$ where we expected the highest density $dE_{\text{T}}/d\eta_{\text{lab}}$. Besides providing an efficient control of the geometry (impact parameter) of the nuclear collision, the E_{T} flow allows us, through the comparison with QCD-inspired parton models, to explore the space-time evolution of the nuclear collision at a microscopic level. The analysis of the corresponding charged particle contents will further extend this comparison and provide new information over the full rapidity domain on the mechanisms of particle production and energy loss of the incident baryons.

In approaching the conditions for the formation of quark-gluon matter, we are seeking for event candidates signaling, ideally, the achievement of full thermodynamic equilibrium at the highest possible energy density. The measurement of high multiplicity of particles, carrying momentum at large angles relative to the beam direction, is an indicator of such a state of matter. A state for which the incident partons should have suffered numerous scatterings so that their initial ordered motion would have become sufficiently randomized. I will consequently attempt to interpret the measured characteristics of the particle production in terms of the early energy density of a thermodynamic macrosystem. This estimate will quantify the degree of achievement of the critical initial conditions required for a local deconfinement of coloured quarks and gluons. The correlations between the transverse energy and multiplicity flow will be finally discussed as a possible source of information concerning the nature of the collective hydrodynamic expansion and cooling that such a thermalized macrosystem (if formed) could undergo.

5.2 Transverse energy production in ^{16}O - nucleus collisions at 60 and 200 GeV/n

5.2.1 The differential cross-sections $d\sigma/dE_T$

The differential cross-sections versus E_T in the pseudorapidity region $-0.1 < \eta_{lab} < 2.9$ for ^{16}O nuclei at 60 and 200 GeV/nucleon incident on Al, Ag and W targets are given in Table 2 to Table 7 on page 116, and shown in Figure 60 on page 117 and Figure 61 on page 118, for the two incident energies²². As mentioned in the preceding chapter, E_T is defined here as $\Sigma E^{tr} \times \sin\theta$ where E^{tr} is the kinetic energy for the baryons and the total energy for all other particles including antibaryons. The remaining systematic uncertainty on the E_T scale is estimated to be 7.1% (5.9% from the Monte Carlo rescaling factor and 4% from the overall energy calibration). The relative comparison of the various data sets is essentially free of these systematic uncertainties. The overall systematic uncertainty on the normalization of the differential cross-sections is of order 2-3% and increases to 5-10% in the low E_T regions (< 50 GeV) due to the uncertainty on the no-target contamination.

Table 2: ^{16}O -Al transverse energy differential cross-section.

The distribution $d\sigma/dE_T$ is measured in $-0.1 < \eta_{lab} < 2.9$ for 60 GeV/nucleon ^{16}O -Al collisions.

E_T [GeV]	Bin half width [GeV]	$d\sigma/dE_T$ [mb/GeV]	Error [mb/GeV]
14.9	3.4	$2.20 \times 10^{+1}$	$6.51 \times 10^{+0}$
21.8	3.4	$1.30 \times 10^{+1}$	$4.78 \times 10^{+0}$
28.7	3.4	$1.23 \times 10^{+1}$	$1.70 \times 10^{+0}$
35.6	3.4	$8.86 \times 10^{+0}$	$1.13 \times 10^{+0}$
42.4	3.4	$4.02 \times 10^{+0}$	5.89×10^{-1}
49.3	3.4	$1.29 \times 10^{+0}$	1.30×10^{-1}
56.2	3.4	1.62×10^{-1}	4.36×10^{-2}
61.9	2.3	4.17×10^{-2}	2.09×10^{-2}
66.5	2.3	1.01×10^{-2}	1.01×10^{-2}

²² The results on transverse energy probability distributions have been presented at the *XXII^e* Rencontres de Moriond [125] and accepted for publication in Z. Phys. C. [126].

Table 3: $^{16}\text{O} - \text{Ag}$ transverse energy differential cross-section.

The distribution $d\sigma/dE_T$ is measured in $-0.1 < \eta_{\text{lab}} < 2.9$ for 60 GeV/nucleon $^{16}\text{O} - \text{Ag}$ collisions.

E_T [GeV]	Bin half width [GeV]	$d\sigma/dE_T$ [mb/GeV]	Error [mb/GeV]	E_T [GeV]	Bin half width [GeV]	$d\sigma/dE_T$ [mb/GeV]	Error [mb/GeV]
14.9	3.4	$2.32 \times 10^{+1}$	$1.73 \times 10^{+1}$	83.7	1.1	$4.88 \times 10^{+0}$	2.67×10^{-1}
21.8	3.4	$1.78 \times 10^{+1}$	$1.18 \times 10^{+1}$	86.0	1.1	$3.35 \times 10^{+0}$	2.21×10^{-1}
28.7	3.4	$1.81 \times 10^{+1}$	$4.50 \times 10^{+0}$	88.3	1.1	$2.27 \times 10^{+0}$	7.18×10^{-2}
35.6	3.4	$1.88 \times 10^{+1}$	$3.13 \times 10^{+0}$	90.6	1.1	$1.97 \times 10^{+0}$	6.71×10^{-2}
42.4	3.4	$1.67 \times 10^{+1}$	$1.73 \times 10^{+0}$	92.9	1.1	$1.22 \times 10^{+0}$	2.24×10^{-1}
49.3	3.4	$1.58 \times 10^{+1}$	7.11×10^{-1}	95.2	1.1	$1.08 \times 10^{+0}$	4.97×10^{-2}
56.2	3.4	$1.31 \times 10^{+1}$	6.22×10^{-1}	97.5	1.1	7.85×10^{-1}	4.22×10^{-2}
60.8	1.1	$1.29 \times 10^{+1}$	$1.04 \times 10^{+0}$	99.8	1.1	5.85×10^{-1}	3.64×10^{-2}
63.1	1.1	$1.20 \times 10^{+1}$	$1.00 \times 10^{+0}$	102.1	1.1	3.01×10^{-1}	1.92×10^{-2}
65.4	1.1	$1.08 \times 10^{+1}$	9.48×10^{-1}	104.4	1.1	2.04×10^{-1}	1.57×10^{-2}
67.7	1.1	$1.25 \times 10^{+1}$	$1.02 \times 10^{+0}$	106.7	1.1	1.67×10^{-1}	1.41×10^{-2}
70.0	1.1	$9.51 \times 10^{+0}$	3.76×10^{-1}	109.0	1.1	8.51×10^{-2}	9.88×10^{-3}
72.3	1.1	$8.49 \times 10^{+0}$	3.55×10^{-1}	111.3	1.1	5.29×10^{-2}	7.70×10^{-3}
74.6	1.1	$7.95 \times 10^{+0}$	3.43×10^{-1}	113.6	1.1	3.45×10^{-2}	6.17×10^{-3}
76.8	1.1	$7.18 \times 10^{+0}$	3.26×10^{-1}	117.0	2.3	1.11×10^{-2}	2.44×10^{-3}
79.1	1.1	$6.21 \times 10^{+0}$	3.02×10^{-1}	121.6	2.3	6.82×10^{-3}	2.34×10^{-3}
81.4	1.1	$5.73 \times 10^{+0}$	2.90×10^{-1}				

Table 4: $^{16}\text{O}-\text{W}$ transverse energy differential cross-section.

The distribution $d\sigma/dE_T$ is measured in $-0.1 < \eta_{\text{lab}} < 2.9$ for 60 GeV/nucleon $^{16}\text{O}-\text{W}$ collisions.

E_T [GeV]	Bin half width [GeV]	$d\sigma/dE_T$ [mb/GeV]	Error [mb/GeV]	E_T [GeV]	Bin half width [GeV]	$d\sigma/dE_T$ [mb/GeV]	Error [mb/GeV]
14.9	3.4	$4.65 \times 10^{+1}$	$2.70 \times 10^{+1}$	99.8	1.1	$7.57 \times 10^{+0}$	2.85×10^{-1}
21.8	3.4	$3.25 \times 10^{+1}$	$2.08 \times 10^{+1}$	102.1	1.1	$6.83 \times 10^{+0}$	2.70×10^{-1}
28.7	3.4	$2.80 \times 10^{+1}$	$7.90 \times 10^{+0}$	104.4	1.1	$5.59 \times 10^{+0}$	1.21×10^{-1}
35.6	3.4	$2.71 \times 10^{+1}$	$4.70 \times 10^{+0}$	106.7	1.1	$4.74 \times 10^{+0}$	1.12×10^{-1}
42.4	3.4	$2.36 \times 10^{+1}$	$2.84 \times 10^{+0}$	109.0	1.1	$4.05 \times 10^{+0}$	1.03×10^{-1}
49.3	3.4	$1.93 \times 10^{+1}$	$1.16 \times 10^{+0}$	111.3	1.1	$3.26 \times 10^{+0}$	9.29×10^{-2}
56.2	3.4	$1.76 \times 10^{+1}$	5.27×10^{-1}	113.6	1.1	$2.57 \times 10^{+0}$	8.26×10^{-2}
60.8	1.1	$1.66 \times 10^{+1}$	7.82×10^{-1}	115.8	1.1	$1.92 \times 10^{+0}$	7.14×10^{-2}
63.1	1.1	$1.45 \times 10^{+1}$	7.31×10^{-1}	118.1	1.1	$1.64 \times 10^{+0}$	6.61×10^{-2}
65.4	1.1	$1.64 \times 10^{+1}$	7.76×10^{-1}	120.4	1.1	$1.09 \times 10^{+0}$	5.37×10^{-2}
67.7	1.1	$1.58 \times 10^{+1}$	7.62×10^{-1}	122.7	1.1	8.40×10^{-1}	4.70×10^{-2}
70.0	1.1	$1.48 \times 10^{+1}$	7.38×10^{-1}	125.0	1.1	7.05×10^{-1}	4.30×10^{-2}
72.3	1.1	$1.50 \times 10^{+1}$	7.43×10^{-1}	127.3	1.1	4.56×10^{-1}	1.61×10^{-2}
74.6	1.1	$1.55 \times 10^{+1}$	7.57×10^{-1}	129.6	1.1	3.19×10^{-1}	1.33×10^{-2}
76.8	1.1	$1.47 \times 10^{+1}$	7.38×10^{-1}	131.9	1.1	2.05×10^{-1}	1.04×10^{-2}
79.1	1.1	$1.38 \times 10^{+1}$	7.14×10^{-1}	134.2	1.1	1.46×10^{-1}	8.68×10^{-3}
81.4	1.1	$1.42 \times 10^{+1}$	3.91×10^{-1}	136.5	1.1	9.11×10^{-2}	6.71×10^{-3}
83.7	1.1	$1.36 \times 10^{+1}$	3.84×10^{-1}	138.8	1.1	6.87×10^{-2}	5.77×10^{-3}
86.0	1.1	$1.27 \times 10^{+1}$	3.71×10^{-1}	141.1	1.1	3.34×10^{-2}	3.89×10^{-3}
88.3	1.1	$1.23 \times 10^{+1}$	3.64×10^{-1}	143.4	1.1	2.01×10^{-2}	2.98×10^{-3}
90.6	1.1	$1.08 \times 10^{+1}$	3.42×10^{-1}	145.7	1.1	1.86×10^{-2}	2.90×10^{-3}
92.9	1.1	$9.65 \times 10^{+0}$	5.34×10^{-1}	149.1	2.3	5.10×10^{-3}	1.05×10^{-3}
95.2	1.1	$9.87 \times 10^{+0}$	3.26×10^{-1}	154.8	3.4	1.46×10^{-3}	4.47×10^{-4}
97.5	1.1	$8.64 \times 10^{+0}$	3.05×10^{-1}	161.7	3.4	2.80×10^{-4}	1.99×10^{-4}

Table 5: ^{16}O - Al transverse energy differential cross-section.

The distribution $d\sigma/dE_T$ is measured in $-0.1 < \eta_{lab} < 2.9$ for 200 GeV/nucleon ^{16}O - Al collisions.

E_T [GeV]	Bin half width [GeV]	$d\sigma/dE_T$ [mb/GeV]	Error [mb/GeV]
16.1	4.6	$1.80 \times 10^{+1}$	$8.85 \times 10^{+0}$
25.2	4.6	$1.39 \times 10^{+1}$	$3.44 \times 10^{+0}$
34.4	4.6	$1.50 \times 10^{+1}$	$2.78 \times 10^{+0}$
43.6	4.6	$7.33 \times 10^{+0}$	$1.32 \times 10^{+0}$
52.8	4.6	$2.59 \times 10^{+0}$	6.72×10^{-1}
61.9	4.6	1.76×10^{-1}	1.47×10^{-1}
71.1	4.6	3.92×10^{-2}	1.32×10^{-2}

Table 6: ^{16}O - Ag transverse energy differential cross-section.

The distribution $d\sigma/dE_T$ is measured in $-0.1 < \eta_{lab} < 2.9$ for 200 GeV/nucleon ^{16}O - Ag collisions.

E_T [GeV]	Bin half width [GeV]	$d\sigma/dE_T$ [mb/GeV]	Error [mb/GeV]	E_T [GeV]	Bin half width [GeV]	$d\sigma/dE_T$ [mb/GeV]	Error [mb/GeV]
18.4	6.9	$3.36 \times 10^{+1}$	$9.45 \times 10^{+0}$	103.2	2.3	$3.36 \times 10^{+0}$	3.30×10^{-1}
32.1	6.9	$2.40 \times 10^{+1}$	$5.20 \times 10^{+0}$	107.8	2.3	$2.00 \times 10^{+0}$	1.25×10^{-1}
45.9	6.9	$1.58 \times 10^{+1}$	$3.10 \times 10^{+0}$	112.4	2.3	$1.43 \times 10^{+0}$	1.05×10^{-1}
57.4	4.6	$1.35 \times 10^{+1}$	$3.02 \times 10^{+0}$	117.0	2.3	7.98×10^{-1}	7.85×10^{-2}
65.4	3.4	$1.42 \times 10^{+1}$	$3.61 \times 10^{+0}$	121.6	2.3	5.47×10^{-1}	6.46×10^{-2}
72.3	3.4	$9.03 \times 10^{+0}$	$1.37 \times 10^{+0}$	126.2	2.3	3.15×10^{-1}	4.87×10^{-2}
79.1	3.4	$1.05 \times 10^{+1}$	6.08×10^{-1}	130.8	2.3	1.18×10^{-1}	3.05×10^{-2}
84.9	2.3	$7.61 \times 10^{+0}$	6.33×10^{-1}	135.3	2.3	8.69×10^{-2}	2.19×10^{-2}
89.5	2.3	$6.68 \times 10^{+0}$	5.93×10^{-1}	139.9	2.3	2.54×10^{-2}	4.82×10^{-3}
94.1	2.3	$4.77 \times 10^{+0}$	5.06×10^{-1}	144.5	2.3	1.41×10^{-2}	3.79×10^{-3}
98.6	2.3	$4.24 \times 10^{+0}$	4.71×10^{-1}	152.6	5.7	4.76×10^{-3}	1.35×10^{-3}

Table 7: $^{16}\text{O}-\text{W}$ transverse energy differential cross-section.

The distribution $d\sigma/dE_T$ is measured in $-0.1 < \eta_{\text{lab}} < 2.9$ for 200 GeV/nucleon $^{16}\text{O}-\text{W}$ collisions.

E_T [GeV]	Bin half width [GeV]	$d\sigma/dE_T$ [mb/GeV]	Error [mb/GeV]	E_T [GeV]	Bin half width [GeV]	$d\sigma/dE_T$ [mb/GeV]	Error [mb/GeV]
14.9	3.4	$4.02 \times 10^{+1}$	$4.09 \times 10^{+0}$	120.4	1.1	$6.79 \times 10^{+0}$	2.00×10^{-1}
21.8	3.4	$3.01 \times 10^{+1}$	$4.15 \times 10^{+0}$	122.7	1.1	$5.93 \times 10^{+0}$	1.86×10^{-1}
28.7	3.4	$2.93 \times 10^{+1}$	$3.58 \times 10^{+0}$	125.0	1.1	$5.45 \times 10^{+0}$	1.79×10^{-1}
35.6	3.4	$2.47 \times 10^{+1}$	$2.89 \times 10^{+0}$	127.3	1.1	$4.70 \times 10^{+0}$	1.66×10^{-1}
42.4	3.4	$1.82 \times 10^{+1}$	$3.34 \times 10^{+0}$	129.6	1.1	$4.30 \times 10^{+0}$	1.58×10^{-1}
49.3	3.4	$2.02 \times 10^{+1}$	$2.03 \times 10^{+0}$	131.9	1.1	$3.77 \times 10^{+0}$	1.48×10^{-1}
56.2	3.4	$1.72 \times 10^{+1}$	$1.40 \times 10^{+0}$	134.2	1.1	$3.25 \times 10^{+0}$	1.37×10^{-1}
60.8	1.1	$1.54 \times 10^{+1}$	7.22×10^{-1}	136.5	1.1	$2.81 \times 10^{+0}$	5.08×10^{-2}
63.1	1.1	$1.28 \times 10^{+1}$	7.77×10^{-1}	138.8	1.1	$2.38 \times 10^{+0}$	4.68×10^{-2}
65.4	1.1	$1.35 \times 10^{+1}$	6.80×10^{-1}	141.1	1.1	$2.07 \times 10^{+0}$	4.37×10^{-2}
67.7	1.1	$1.48 \times 10^{+1}$	6.80×10^{-1}	143.4	1.1	$1.67 \times 10^{+0}$	3.93×10^{-2}
70.0	1.1	$1.37 \times 10^{+1}$	6.55×10^{-1}	145.7	1.1	$1.38 \times 10^{+0}$	3.58×10^{-2}
72.3	1.1	$1.37 \times 10^{+1}$	6.53×10^{-1}	148.0	1.1	$1.21 \times 10^{+0}$	3.34×10^{-2}
74.6	1.1	$1.45 \times 10^{+1}$	6.74×10^{-1}	150.3	1.1	9.78×10^{-1}	3.01×10^{-2}
76.8	1.1	$1.45 \times 10^{+1}$	6.72×10^{-1}	152.6	1.1	7.79×10^{-1}	2.68×10^{-2}
79.1	1.1	$1.26 \times 10^{+1}$	6.27×10^{-1}	154.8	1.1	6.30×10^{-1}	2.41×10^{-2}
81.4	1.1	$1.33 \times 10^{+1}$	6.44×10^{-1}	157.1	1.1	5.20×10^{-1}	2.18×10^{-2}
83.7	1.1	$1.34 \times 10^{+1}$	6.47×10^{-1}	159.4	1.1	4.11×10^{-1}	1.94×10^{-2}
86.0	1.1	$1.26 \times 10^{+1}$	6.28×10^{-1}	161.7	1.1	3.08×10^{-1}	1.67×10^{-2}
88.3	1.1	$1.20 \times 10^{+1}$	6.13×10^{-1}	164.0	1.1	2.31×10^{-1}	1.44×10^{-2}
90.6	1.1	$1.15 \times 10^{+1}$	5.99×10^{-1}	166.3	1.1	1.81×10^{-1}	1.27×10^{-2}
92.9	1.1	$1.20 \times 10^{+1}$	6.12×10^{-1}	168.6	1.1	1.37×10^{-1}	1.10×10^{-2}
95.2	1.1	$1.16 \times 10^{+1}$	6.03×10^{-1}	170.9	1.1	1.03×10^{-1}	5.93×10^{-3}
97.5	1.1	$1.22 \times 10^{+1}$	6.19×10^{-1}	173.2	1.1	7.35×10^{-2}	4.96×10^{-3}
99.8	1.1	$1.10 \times 10^{+1}$	2.54×10^{-1}	175.5	1.1	5.82×10^{-2}	4.39×10^{-3}
102.1	1.1	$1.06 \times 10^{+1}$	2.50×10^{-1}	177.8	1.1	4.07×10^{-2}	3.64×10^{-3}
104.4	1.1	$1.04 \times 10^{+1}$	2.48×10^{-1}	180.1	1.1	3.20×10^{-2}	3.21×10^{-3}
106.7	1.1	$9.71 \times 10^{+0}$	2.39×10^{-1}	182.4	1.1	2.11×10^{-2}	2.60×10^{-3}
109.0	1.1	$8.98 \times 10^{+0}$	2.30×10^{-1}	184.7	1.1	1.46×10^{-2}	2.14×10^{-3}
111.3	1.1	$8.65 \times 10^{+0}$	2.26×10^{-1}	187.0	1.1	1.22×10^{-2}	1.96×10^{-3}
113.6	1.1	$7.96 \times 10^{+0}$	2.16×10^{-1}	190.4	2.3	5.87×10^{-3}	9.54×10^{-4}
115.8	1.1	$7.75 \times 10^{+0}$	2.13×10^{-1}	195.0	2.3	2.89×10^{-3}	6.79×10^{-4}
118.1	1.1	$6.91 \times 10^{+0}$	2.02×10^{-1}	200.7	3.4	1.33×10^{-3}	4.02×10^{-4}

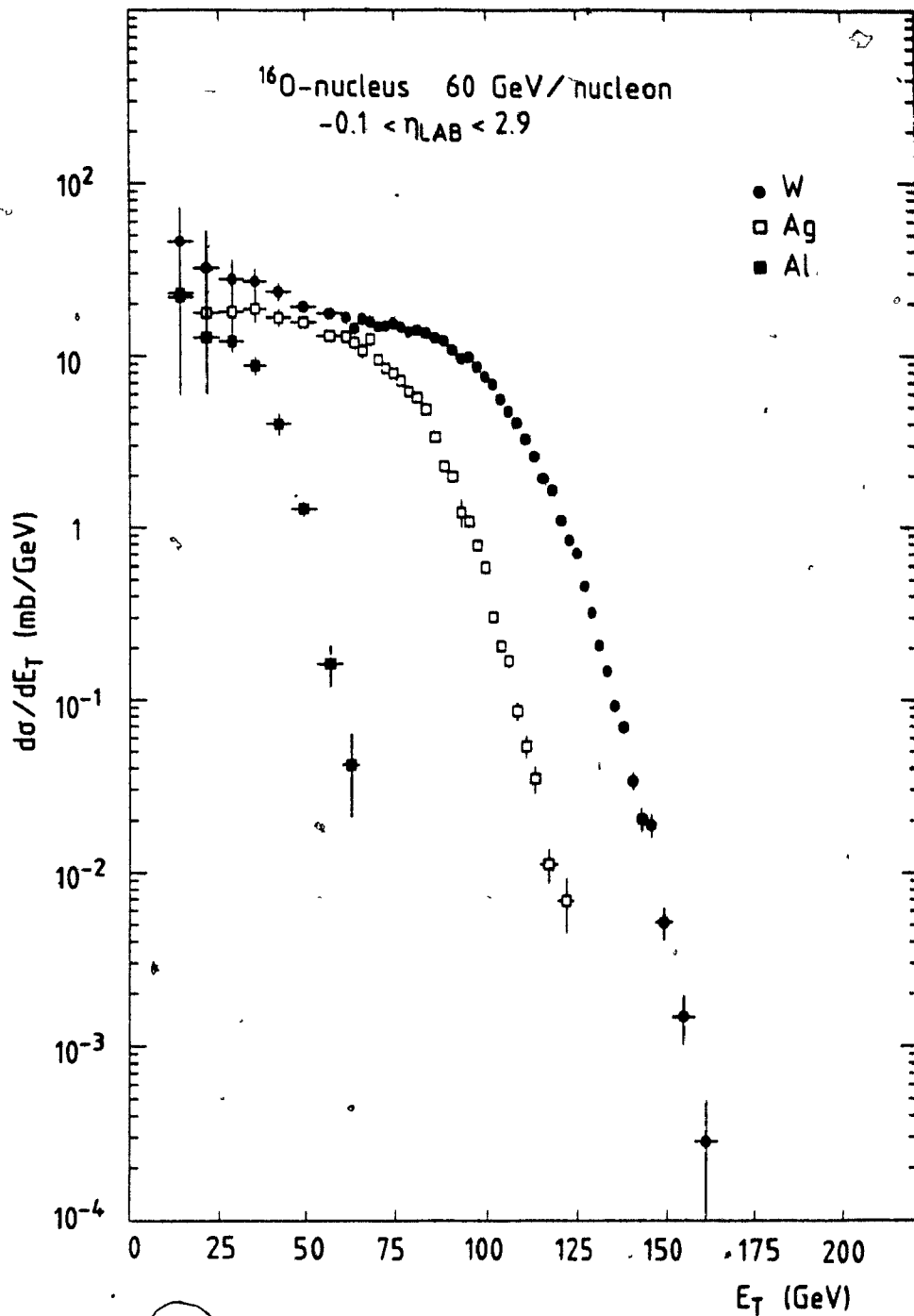


Figure 60:

Transverse energy differential cross-section measured in $-0.1 < \eta_{\text{lab}} < 2.9$ for a 60 GeV/nucleon ^{16}O beam. The distributions $d\sigma/dE_T$ are shown for W (closed circles), Ag (open squares) and Al (closed squares) target. E_T is defined as $\Sigma E_i^{\text{tr}} \sin\theta$ where $E_i^{\text{tr}} = \sqrt{p^2 + m^2}$ except for nucleons where $E_i^{\text{tr}} = \sqrt{p^2 + m^2} - m$.

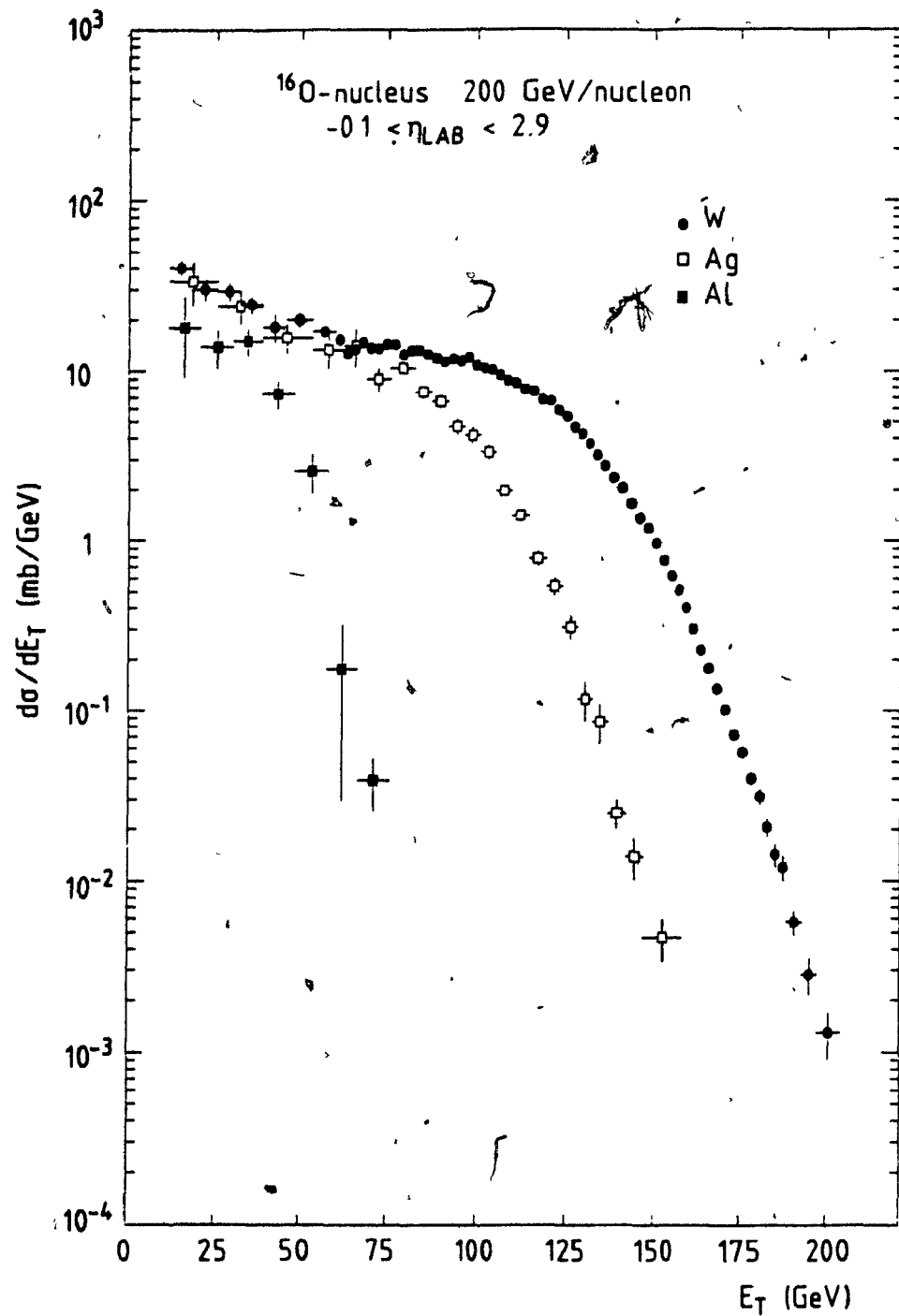
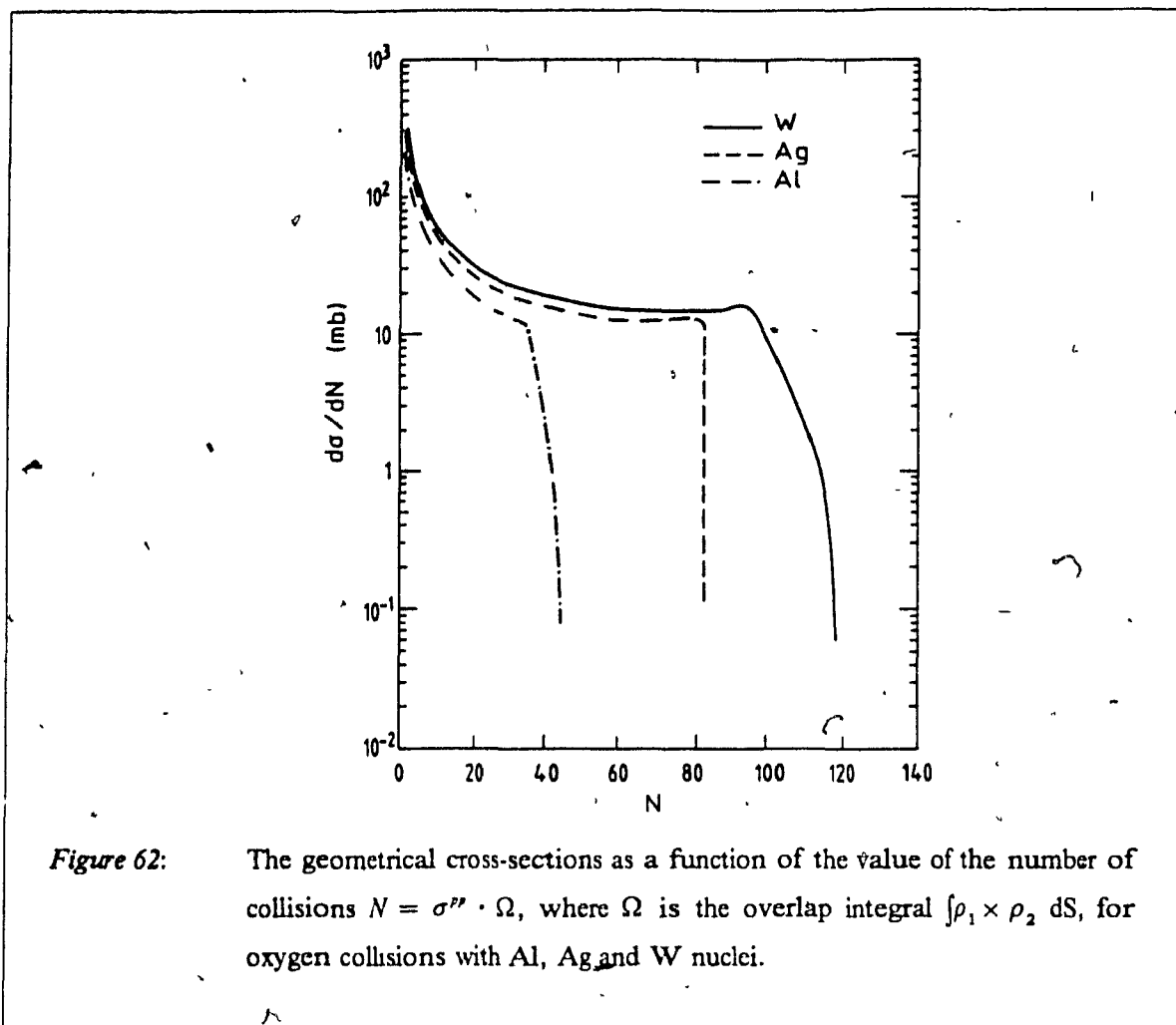


Figure 61: Transverse energy differential cross-section measured in $-0.1 < \eta_{\text{lab}} < 2.9$ for a 200 GeV/nucleon ^{16}O beam. The distributions $d\sigma/dE_T$ are shown for W (closed circles), Ag (open squares) and Al (closed squares) target.

5.2.2 Qualitative features and geometrical parametrizations

The striking common characteristic of the $d\sigma/dE_T$ distributions in Figure 60 on page 117 and Figure 61 on page 118 is a rather flat plateau region extending to a shoulder followed by a steep fall. These features are particularly clear for the heavier target nuclei (Ag and W). The plateau is a manifestation of the sampling over impact parameters and the tail above the shoulder is caused by fluctuations in E_T production for central collisions. The general features are thus reminiscent of the geometry of collisions between objects with a spatial extent such as nuclei.

For spherical nuclei, the geometry is determined by the impact parameter b . For non-spherical target nuclei, two angles are also required to define the geometry. The shape of the density distribution of protons is very well measured by electron scattering, and the neutron distribution is known to be very similar. It is clear that the nature of a collision must depend to a great extent on the value of the overlap integral $\int \rho_1 \times \rho_2 dS$, where $\rho_{1,2}$ are the densities of nucleons per unit area of the two colliding nuclei in the plane transverse to the collision. The overlap integral can be converted into an effective number N of collisions by multiplying by an appropriate hadronic cross-section. A plausible choice is the inelastic nucleon-nucleon cross-section $\sigma_m \sim 32$ mb. That amounts to assume that each incident nucleon interacts with every target nucleon it encounters in a cylinder of cross-sectional area σ_m . The geometrical cross-section as a function of N is shown in Figure 62 on page 120, for oxygen collisions with our target nuclei. For the calculation of these geometrical cross-sections, we used trapezoidal nuclear density profiles deduced from elastic electron scattering, and took into account the nuclear deformation deduced from the intrinsic quadrupole moments. It should be noted that the W nucleus is substantially deformed, and this has a significant effect in the overlap integral.



8. The geometrical cross-sections of Figure 62 show the main features seen in the data. For these cross-sections, the rather flat "plateau" region continues until the colliding objects overlap fully, corresponding to "central" collisions with $b \leq 2-3$ fm.

The similarity of the geometrical cross-sections to the measured E_T distributions suggests that the geometrical overlap integral be used as the basis of a fit to the data [33] [34]. The total E_T is assumed to be produced by N independent nucleon-nucleon collisions. By the central limit theorem, the total E_T produced by any reasonably large number N of such collisions is approximately gaussian distributed with mean $N \cdot \epsilon_0$ and variance $\sigma^2 = \omega \cdot N \cdot \epsilon_0^2$, where ϵ_0 is an effective average E_T for nucleon-nucleon collisions in a nucleus, and both ϵ_0 and ω are free parameters. The probability distribution for N is dictated by geometry as explained above. We obtain an excellent description of the data, as shown in windows (a) and (b) of Figure 63 on page 121 for 60 and 200 GeV/nucleon incident energies respectively.

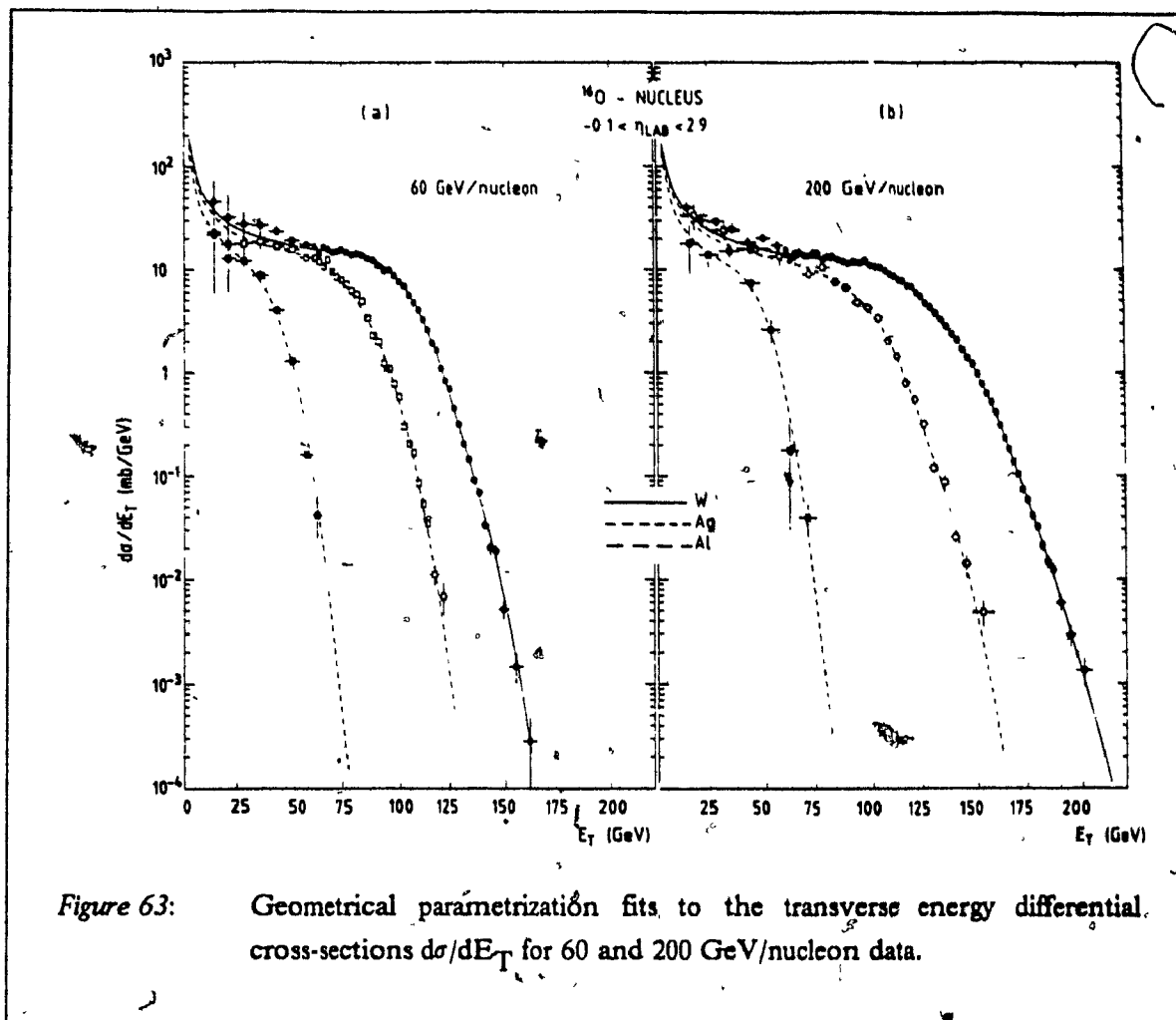


Figure 63: Geometrical parametrization fits to the transverse energy differential cross-sections $d\sigma/dE_T$ for 60 and 200 GeV/nucleon data.

I should stress that the quality of the description is rather insensitive to the absolute value assumed for σ_m . The geometrical superposition of independent nucleon-nucleon interactions is thus seen to provide a simple heuristic picture of the E_T production in nuclear collisions. The free parameters ϵ_0 and ω provide a convenient compact parametrization of the data, but cannot be fully interpreted as physics parameters since too many important effects are hidden or ignored (e.g. energy conservation and nature of the objects participating to the multiple-scattering processes, cascading of secondary particles, etc.).

The fitted values found for ϵ_0 and ω are given in Table 8 on page 122.

Table 8: Parametrization of the $d\sigma/dE_T$ distributions.

The best fit values of the free parameters ϵ_0 and ω for the geometrical parametrization of the E_T differential cross-sections are given for the Al, Ag and W targets at 60 and 200 GeV/nucleon incident energies.

	60 GeV/nucleon			200 GeV/nucleon		
	Al	Ag	W	Al	Ag	W
ϵ_0 [GeV]	1.02	0.95	0.98	1.26	1.14	1.19
ω	1.99	2.20	1.75	1.05	2.64	2.53

The values of ϵ_0 are around 1 GeV, which may be compared to the mean E_T of ~ 1.4 GeV found by fitting [34] $p-p$ data at $\sqrt{s} = 20$ GeV and extrapolating to the pseudorapidity coverage considered here. If ϵ_0 is viewed as some kind of effective E_T production per "elementary" nucleon-nucleon scatters, it should be lower than the $p-p$ value because of the energy degradation during the multiple inelastic scattering process, although intranuclear cascading of secondaries would tend to increase it. The variance parameter, ω , is larger for the 200 GeV/nucleon data than for the 60 GeV/nucleon data for the heavier targets Ag and W, reflecting the fact that the fall of the cross-section beyond the plateau is less steep at the higher incident energy (except for the Al target, but there the fall-off region is not well determined statistically at the higher energy). This may be partly due to the fact that with increasing incident energy, the effective center-of-mass of the collisions is shifted towards larger rapidities and one may expect the fluctuations, in the (smaller) fraction of the total E_T production contained in the region $-0.1 < \eta_{lab} < 2.9$, to be larger. The signs of excess variance observed at 200 GeV/nucleon are nevertheless of special interest since this has been emphasized as a possible signal of collective behaviour (see section 1.4.3 on page 14). The global "geometrical" features of the transverse energy distributions can alternatively be studied in the framework of the naive Wounded Nucleon Model (WNM) (see section 2.2 on page 20). Such a framework has been considered [49] [51] to analyse the properties of the $^{16}\text{O}-\text{Pb}$ transverse energy distribution measured at 200 GeV/nucleon in the region $2.2 < \eta_{lab} < 3.8$ by the NA35 Collaboration [35]. The E_T distribution was found to be well described by a 16-fold convolution of nucleon-nucleus collisions [51], whereas a convolution of independent nucleon-nucleon collisions lead to an underestimate of the E_T production [49]. In the WNM, the simplifying assumption is made that the particle production emerges independently and with equal weights from each participating (wounded) nucleon. For any given impact parameter, one calculates the probability to have w wounded nucleons, and the contribution of these to the differential cross-section is described by a

two parameters (α and β) analytical expression (equ. (17)). The prescriptions of the WNM were used as a basis for a fit to our data in [127]. The values of the α and β parameters were fixed by fitting the O-W distributions in order to benefit from the high statistical precision of these data, and for those fixed parameter values, predictions were made for the O-Al and O-Ag distributions. A convolution in the spirit of a simple Additive Quark Model (AQM) (see section 2.2 on page 20) was also performed [127] with the assumption that the transverse energy production should scale with the total number of wounded valence quarks in the target nuclei. Figure 64 shows the resulting fits (solid curves) and predictions (dashed and dotted curves) for the simplified AQM and for the WNM at 60 GeV/nucleon (windows (a) and (b) respectively) and 200 GeV/nucleon (windows (c) and (d) respectively).

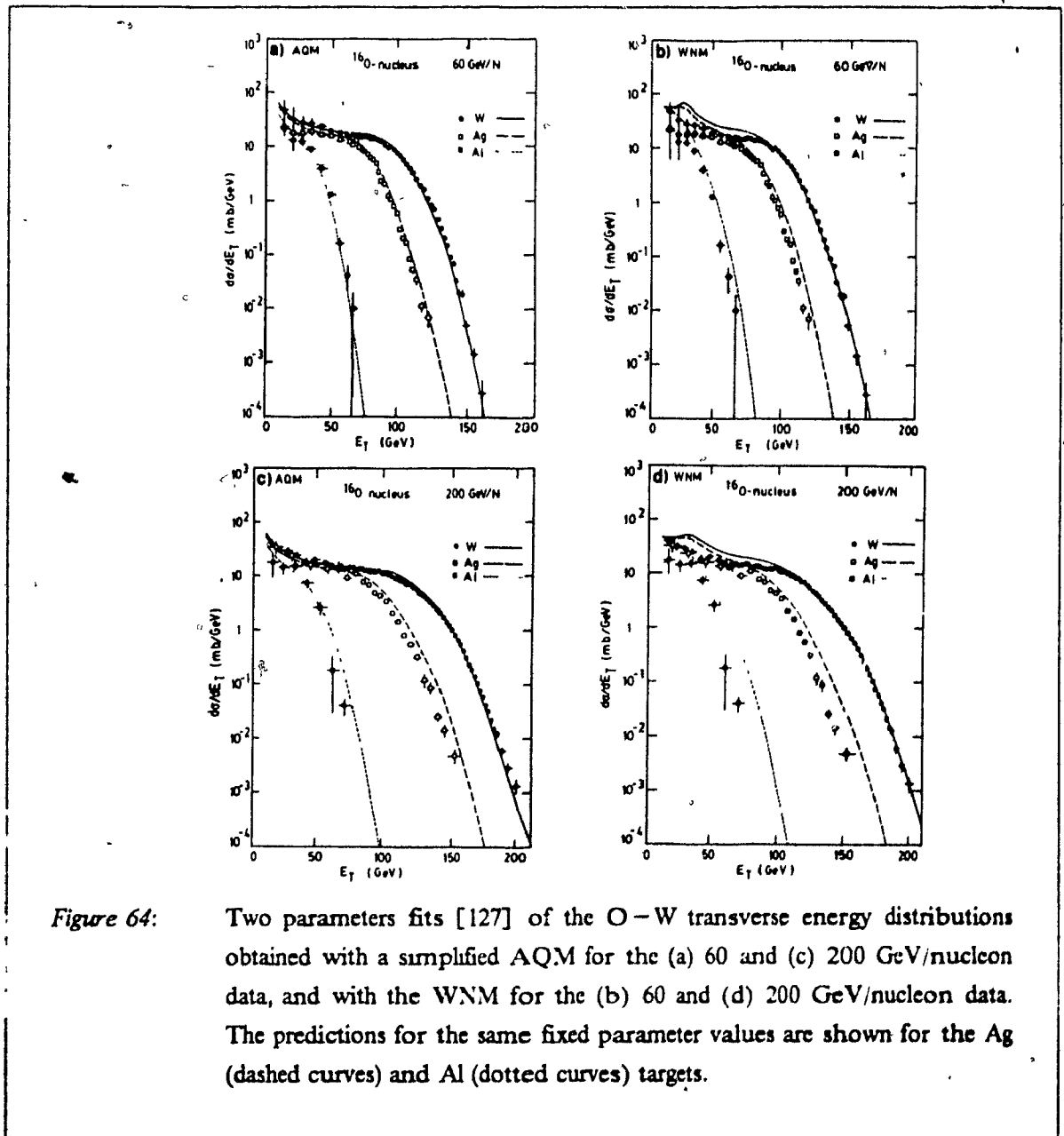


Figure 64: Two parameters fits [127] of the O-W transverse energy distributions obtained with a simplified AQM for the (a) 60 and (c) 200 GeV/nucleon data, and with the WNM for the (b) 60 and (d) 200 GeV/nucleon data. The predictions for the same fixed parameter values are shown for the Ag (dashed curves) and Al (dotted curves) targets.

The global features of the spectra are well described, showing again the dominance of the geometrical aspects of the collisions, which translate into a strong correlation between the transverse energy production and the impact parameter. The fits and predictions of the simplified AQM offer better descriptions of the data, in particular at low transverse energy. This may reflect the fact that more weight was given there to the participants of the target nuclei, and the pseudorapidity coverage considered is oriented towards the target fragmentation region. An interesting aspect of the predictions in Figure 64 on page 123 is that they systematically overestimate the transverse energy production for the Al and Ag targets, and more at 200 GeV/nucleon than at 60 GeV/nucleon. In other words, the transverse energy production in the "central-target fragmentation" region rises faster than expected from a naïve superposition of independent nucleon-nucleon collisions (e.g. faster than with the increasing number of participants in the WNM), and relatively faster at 200 GeV/nucleon than at 60 GeV/nucleon incident energy. Here again, I stress that these "geometrical" parametrizations cannot pretend to give a full physical description of the data since, for instance, they include no provision of a mechanism for energy-momentum conservation or for possible rescattering of secondaries. The discrepancies may signal the necessity for a proper treatment of such physical effects.

5.2.3 The A-dependence of the transverse energy production

The geometrical cross-sections of Figure 62 on page 120 show a sharp edge followed by a steep fall beyond the point where the colliding nuclei overlap fully ($b \leq 2.3\text{fm}$). Given the strong correlation between the geometrical impact parameter and the transverse energy production, we may make use of this step-function-like characteristic to fix the geometry of the nuclear collisions, and consequently study the A-dependence of the E_T production. Hence, for the E_T distributions, it is natural to define E_T^{central} as that value of E_T for which the cross-section is one-half that of the "plateau". We define the plateau cross-section as that for which the rate of change with energy (averaged over a 15 GeV interval) is minimal.

The values of E_T^{central} , as a function of the atomic number A of the target nuclei, can be used to parametrize the target dependence of the average central collisions. These values are shown in Figure 65 on page 125 as a function of A and for both incident energies, together with a fit of the form A^α with $\alpha = 0.48 \pm 0.02$ and 0.53 ± 0.04 for 60 and 200 GeV/nucleon incident energy respectively. The E_T in the trigger region acceptance is evidently still increasing with energy at these rather high beam energies, and is increasing somewhat faster than linearly with the nuclear thickness of the target (i.e. $A^{1/3}$), even at the lower energy. In other words, the increase of E_T^{central} , as measured in the pseudorapidity region $-0.1 < \eta_{\text{lab}} < 2.9$, is somewhat faster than the corresponding increase of the number of participant nucleons.

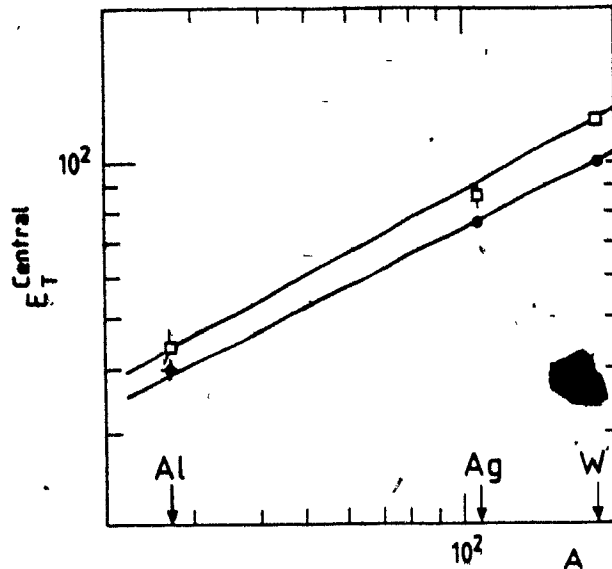


Figure 65: The E_T for average central collisions ($b \leq 2-3$ fm, corresponding to full geometrical overlap between the colliding nuclei) versus the atomic mass number of the target nuclei for 60 (lower curve) and 200 (upper curve) GeV/nucleon incident energies. The solid lines are fits to the data of the form $constant \cdot A^\alpha$. The best estimates of the free parameter α are $\alpha = 0.48 \pm .02$ and $0.53 \pm .04$ for the 60 and 200 GeV/nucleon incident energies.

This result is in contrast with the dependence measured by the NA35 Collaboration [128] in the more forward region $2.2 < \eta_{lab} < 3.8$ and for which the data is compatible with $\alpha \sim 1/3$. This suggests a rather strong rapidity dependence of the rate of change of $dE_T/d\eta$ as a function of target nuclei. Such a strong dependence was observed by the WA80 Collaboration [129] for the charged particles pseudorapidity densities. They observed that although the target mass dependence could be well parametrized as $A^{\alpha(\eta)}$ in any $\Delta\eta$ sub-region, the exponent $\alpha(\eta)$ varied considerably with η . For 60 and 200 GeV/nucleon ^{16}O -nucleus collisions, they found that $\alpha(\eta)$ slightly rises from $\alpha \sim 0.5$ at $\eta \sim -1.7$ to a maximum of $\alpha \sim 0.8$ at $\eta \sim 0$ (e.g. at the lower edge of our trigger coverage), after which it decreases rapidly with η , reaching $\alpha \sim 0.15$ at $\eta \sim 2.9$ (e.g. upper edge of our trigger coverage) and finally a particle yield essentially independent of the target mass at $\eta \sim 4$. The "A-dependence" is thus strongly dependent, and possibly in a non-trivial way, on the considered pseudorapidity sub-region. It was seen in section 2.3 on page 26 that in nucleon-nucleus collisions, a contribution to similar A-dependence of the particle production as a function of rapidity was thought to arise from the degradation of the incident nucleon's energy. Hence, we may expect that an increasing fraction of the total E_T production will be pulled at larger angles as the number of target nucleon participants increases, thus contributing to an apparent excess of A-dependence at

smaller pseudorapidities.

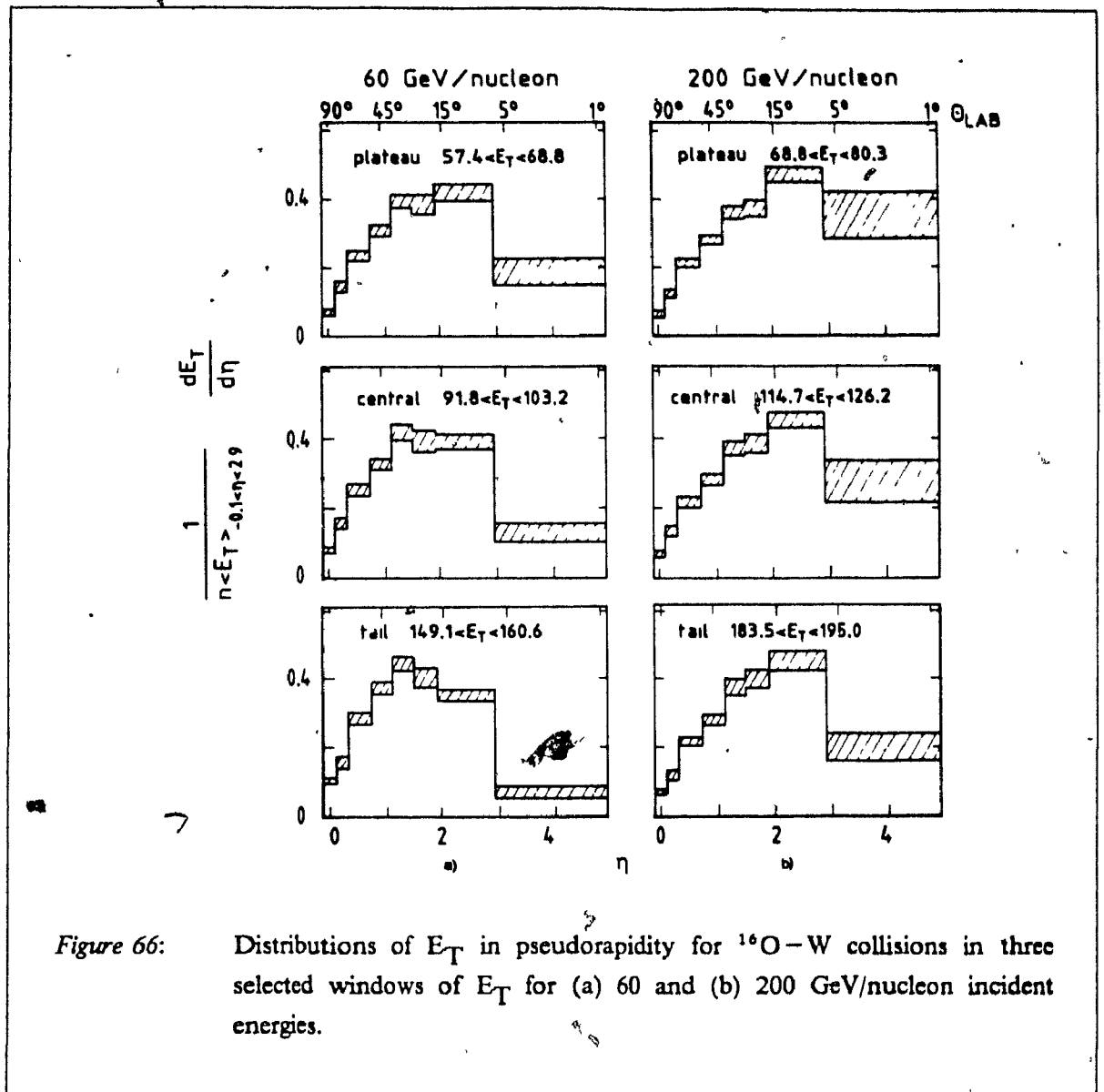
The fact that $E_T^{central}$ rises as a function of A indicates that we are in an energy regime above that where the projectile energy is largely dissipated before it completely traverses a large target nucleus, sometime called the "fully stopping" regime²³. In the case of full stopping, the E_T for central collisions would cease to rise beyond a certain size of target. Evidently, even 60 GeV/nucleon incident energy is above this regime.

It is interesting to compare the scale of E_T production in nucleus-nucleus collisions to the one of hadron-nucleus collisions. At 200 GeV/nucleon incident energy, the E_T distribution measured [130] in the region $0.6 < \eta_{lab} < 2.2$ for p-Pb collisions extends to about 40 GeV when exploring 5 decades of the differential cross-section (down to $\sim 10^{-3}$ mb/GeV), which should be contrasted to ~ 200 GeV reached for O-W collisions in the larger region $-0.1 < \eta_{lab} < 2.9$. This indicates that the transverse energy production per incident nucleon is on average much less extreme in nuclear collisions as is trivially expected from probability considerations. Correspondingly, one expects that the average amount of stopping of the incident baryons (as measured by the mean energy loss or the average rapidity shift after a given nuclear thickness) is smaller in nucleus-nucleus collisions. Such difference between the average strength of the degradation of the incident baryons momenta in p-A and A-B collisions has been emphasized in theoretical studies, based on multichain extensions of the Dual Parton Model [47], where one addresses the question of the nuclear stopping power. The stopping power plays a determinant role [55] in the evaluation of the energy domain in which nuclear collisions may allow the formation of a baryon rich quark-gluon plasma, or in the study of the separation between the fragmentation regions which could lead to the formation of a hot baryon free central region.

5.2.4 Fractional E_T density in pseudorapidity

The distributions of the density of E_T in pseudorapidity, $dE_T/d\eta$, for a W target at 60 and 200 GeV/nucleon incident energies are shown respectively in windows (a) and (b) of Figure 66 on page 127. The distributions are normalized to 1 in the trigger region $\eta < 2.9$. Three regions of E_T are selected, corresponding to the plateau region of $d\sigma/dE_T$, the $E_T^{central}$ region, and the highest E_T measured.

²³ If the multiple inelastic collisions remove only a relatively small fraction of the incident nucleons energy, the production of particles that populate the central region in the center-of-mass frame would increase essentially in proportion to the total number of inelastic collisions. At asymptotically high energies, this should ultimately scale with the target nuclear thickness, $\propto A^{1/3}$. This would be the case, for instance, in the high energy limit of the Dual Parton Model, as discussed in section 2.5.1.3 on page 45.



As mentioned in chapter 4, our η resolution is poor in the region $\eta > 2.9$, i.e. forward of the trigger region, so this region is plotted as one bin in Figure 66. The integral (i.e. the total E_T in this region) is however reasonably reliable.

The η -distributions are moving towards lower pseudorapidities (large angles) with E_T in the region $-0.1 < \eta_{lab} < 2.9$, i.e. the fraction in the forward region, $R \equiv E_T(2.9 \leq \eta \leq 4.9) / E_T(-0.1 \leq \eta \leq 2.9)$, decreases with increasing E_T . The backward shift is sharper at 60 GeV/nucleon.

For the E_T bin centered on $E_T^{central}$, the values of $E_T^{central}$ and R are presented in Table 9 on page 128 for the three targets and both incident energies. We observe that R decreases with increasing A for both incident energies, and is always smaller at 60 GeV/nucleon.

Table 9: Target mass dependence of the E_T production.

Average E_T for central collisions ($b \leq 2-3$ fm) and the corresponding $R \equiv E_T(2.9 \leq \eta \leq 4.9) / E_T(-0.1 \leq \eta \leq 2.9)$ as a function of the atomic mass number A of the targets for 60 and 200 GeV/nucleon incident energies.

	60 GeV/nucleon			200 GeV/nucleon		
	Al	Ag	W	Al	Ag	W
$E_{T, \text{central}}$	39.8 ± 1.5	76.5 ± 0.6	99.5 ± 0.4	44.3 ± 3.4	86.0 ± 4.8	119.9 ± 0.5
R_{central}	0.54 ± 0.11	0.36 ± 0.08	0.27 ± 0.06	0.95 ± 0.19	0.66 ± 0.14	0.57 ± 0.12

The $dE_T/d\eta$ distributions do not show the extended plateau that would be characteristic of the "ultra-high energy regime". I recall (see section 1.4.2 on page 11) that the existence of such an extended plateau is assumed in most theoretical hydrodynamic calculations [10] [20]. It is thought to be reminiscent of the properties of individual nucleon-nucleon [132] or nucleon-nucleus [133] collisions at ultra-high energies, for which the particle production at large angles is largely independent of the particular center-of-mass-like frame chosen for observation. The assertion is made that in nuclear collisions, the system should look essentially the same in all frames where the emergent excited nuclei are, shortly after the collision, highly Lorentz-contracted pancakes receding in opposite direction from the collision point at nearly the speed of light. A cylindrical boost symmetry is thus imposed as an initial condition and this leads to simple solutions of the hydrodynamic equations. The absence of a plateau structure in the distributions of Figure 66 on page 127 implies that the prescriptions provided by the models for interpreting the characteristics of the particle flow in terms of thermodynamic macro-variables may not be applicable, or at least their interpretation be severely weakened. We should note that an extended plateau is not yet expected to be fully developed for nucleon-nucleon collisions at the maximum center-of-mass energies available in our experiment ($\sqrt{s_{NN}} \sim 19.4$ GeV). Furthermore, the results of Table 9 and Figure 66 on page 127 may be seen to show characteristics more proper to stopping than to scaling domain. In this connexion, it is instructive to compare the measured E_T with its kinematical limit estimated via a simple full-stopping calculation. Let's take for example an ^{16}O nucleus incident on a W target. A central collision involves a minimum of about 50 W nucleons and we may consider an effective number A_{eff} of target participants ranging from 50 to 80 nucleons. If we suppose that the kinematic is the one of a collision between two objects of 16 and 50-80 nucleon masses, and further assume that the available energy is re-emitted isotropically in the center-of-mass frame, the kinematic limits for the

E_T production at 200 GeV/nucleon range from $(\pi/4)(\sqrt{s} - 66m_n) = 384$ to 477 GeV. Furthermore, under these assumptions, the $dE_T/d\eta$ distribution shows no plateau, but is a broad peak centered at $\eta_{OW} \approx \ln(2 \cdot E_{inc} / \sqrt{s_{OW}}) \approx 2.4$. Our highest E_T point for $^{16}\text{O} - \text{W}$ collisions at 200 GeV/nucleon is 200 GeV in the pseudorapidity region $\eta_{lab} < 2.9$. Adding in the forward E_T measured in $\eta_{lab} > 2.9$ increases this to 280 GeV, which is ≈ 0.73 of the kinematic limit for $A_{eff} \sim 50$. This fraction goes down to ≈ 0.59 for an effective mass number $A_{eff} \sim 80$, which may actually be more appropriate for the extreme tail of the W spectrum. For average central collisions, we measure (Table 9 on page 128) $E_T \sim 120$ GeV for O - W collisions at 200 GeV/nucleon, which represents, after rescaling for the forward transverse energy, a fraction of 0.49 ($A_{eff} = 50$) of the kinematic limit. The corresponding fractions for 60 GeV/nucleon $^{16}\text{O} - \text{W}$ are 0.97 ($A_{eff} = 50$) or 0.79 ($A_{eff} = 80$) at the highest E_T , and 0.67 ($A_{eff} = 50$) for $E_T^{central}$. The observed E_T production at 60 GeV/nucleon represents a larger fraction of the full-stopping limit. From similar data, the NA35 [128] and the WA80 [134] collaborations have recently also inferred a higher relative stopping for the lower beam energy. At both incident energies, we are considering E_T 's which are by no means small fractions of the kinematic limit and the narrowness of the observed pseudorapidity distribution is not surprising.

5.3 Charged multiplicity flow in $^{16}\text{O} - \text{nucleus}$ collisions at 60 and 200 GeV/n

5.3.1 The differential cross-sections $d\sigma/dN^{ch}$

The differential cross-sections in charged multiplicity ($d\sigma/dN^{ch}$) for $^{16}\text{O} - \text{nucleus}$ collisions at 60 and 200 GeV/nucleon incident energies are shown in Figure 67 on page 130 and Figure 68 on page 131 respectively, for Al, Ag and W target nuclei²⁴. The corrections for multiple hits, charge sharing, and electronic cross-talk introduce an estimated $\sim 10\%$ systematic uncertainty on the multiplicity scale. The distributions have been deconvoluted to remove the distortions introduced by the multiplicity resolution ($\sigma \sim 80 - 120\%/\sqrt{N^{ch}}$). The very high multiplicity tails of the distributions have been omitted. This is justified considering the yet unresolved contamination from electronic noise, and since the multiplicity resolution and efficiency corrections are still under investigation for these high tails.

²⁴ The W results at 200 GeV/nucleon have been submitted for publication in Z. Phys. C. [135].

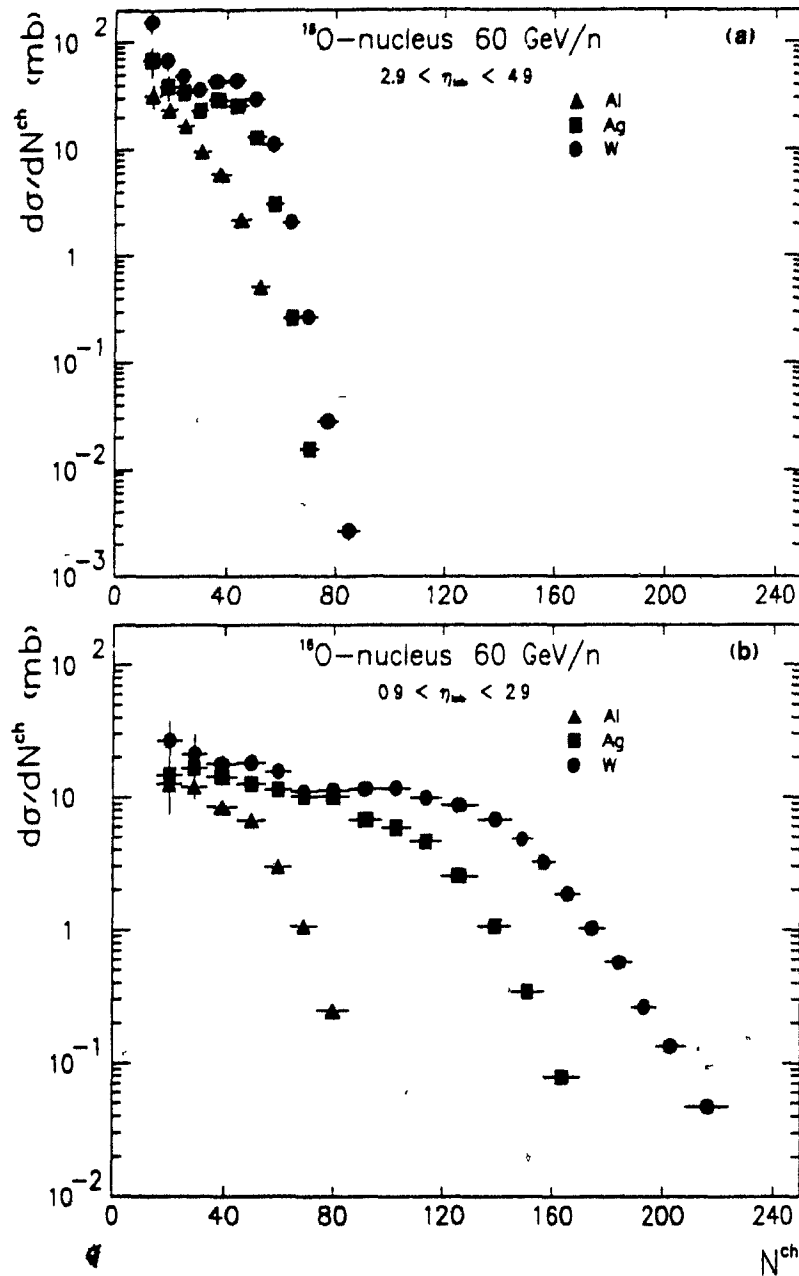


Figure 67: Charged multiplicity differential cross-sections, $d\sigma/dN^{ch}$, measured in the pseudorapidity region $2.9 < \eta_{lab} < 4.9$ (a) and in $0.9 < \eta_{lab} < 2.9$ (b) for 60 GeV/nucleon ^{16}O nucleus incident on Al (triangles), Ag (boxes) and W (circles) targets.

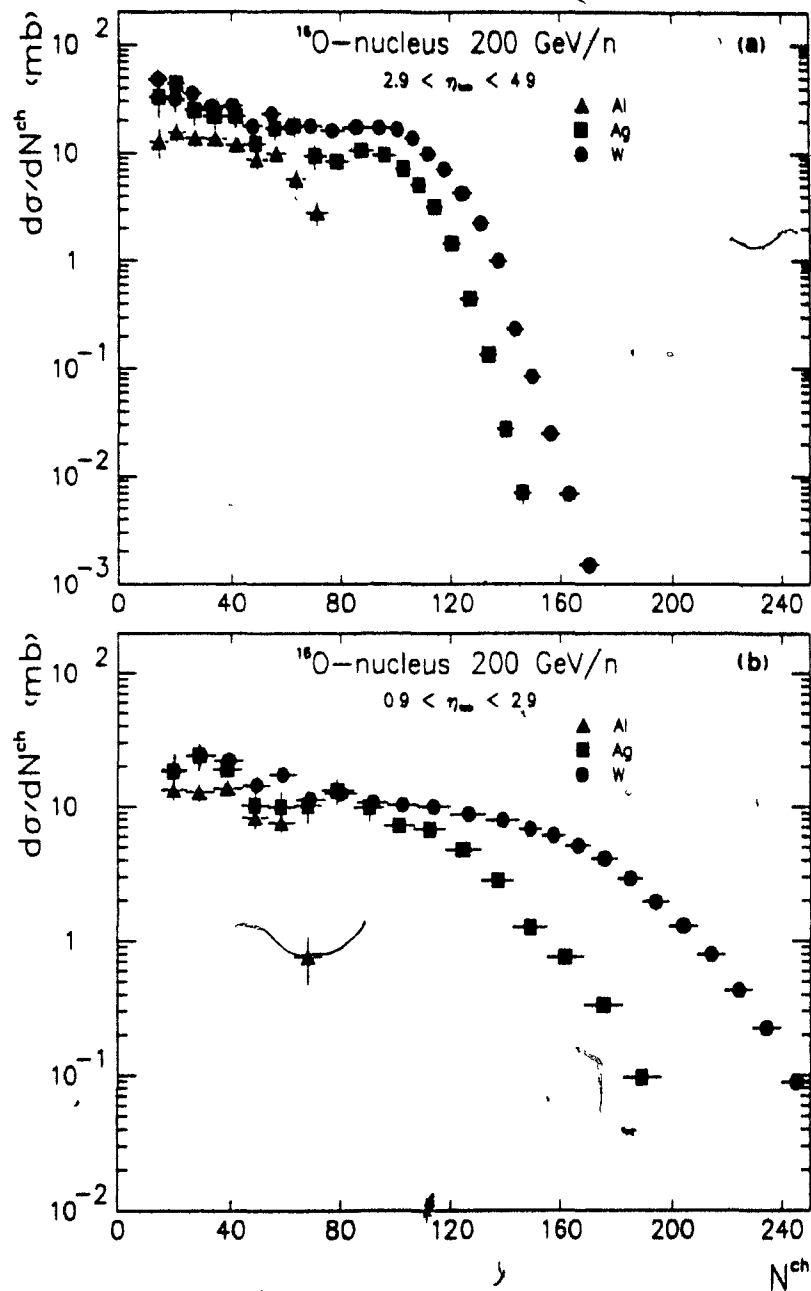


Figure 68: The distributions $d\sigma/dN^{\text{ch}}$ measured in the region $2.9 < \eta_{\text{lab}} < 4.9$ (a) and in $0.9 < \eta_{\text{lab}} < 2.9$ (b) for 200 GeV/nucleon ^{16}O nucleus incident on Al (triangles), Ag (boxes) and W (circles) targets.

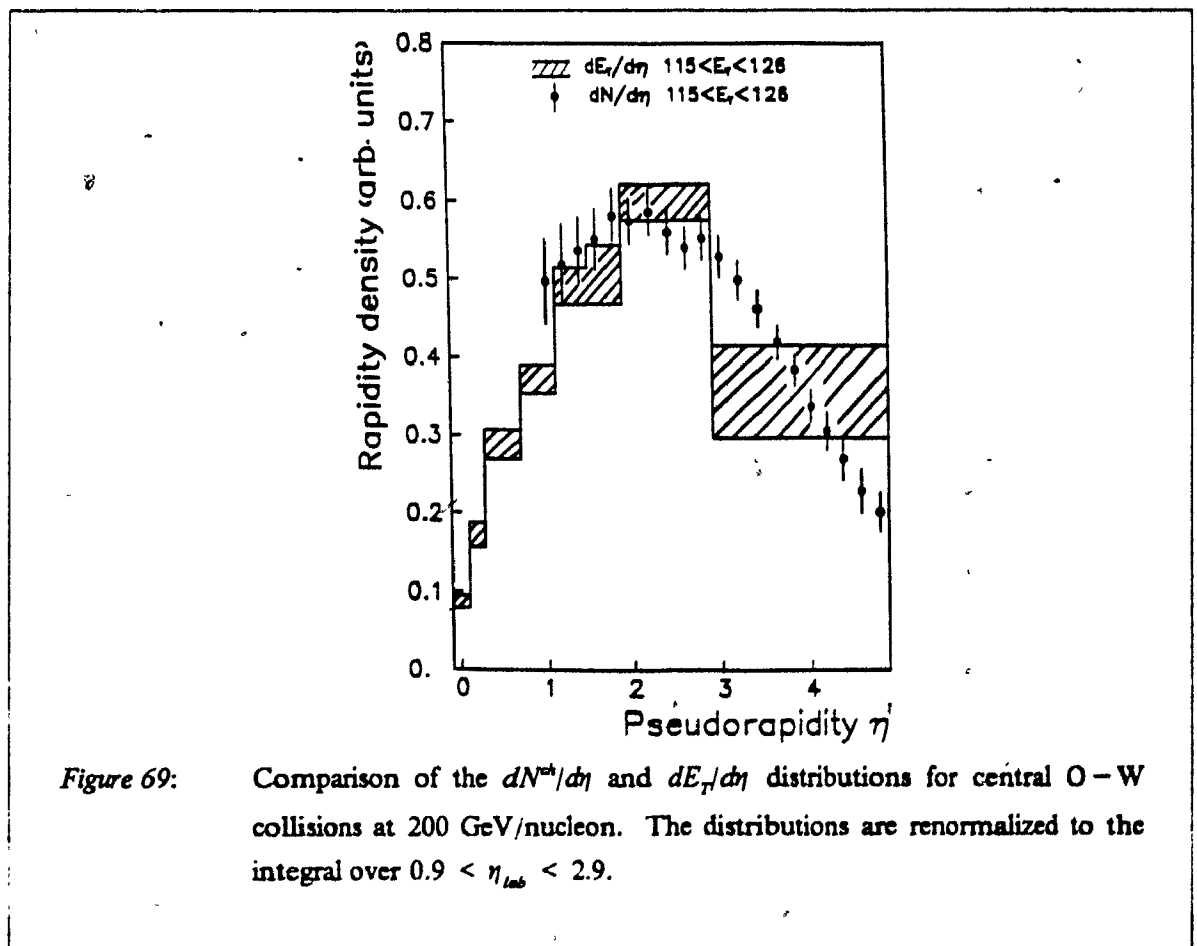
The cross-sections are presented separately for two "hemispheres": the forward pseudorapidity interval ($2.9 < \eta_{\text{lab}} < 4.9$), which covers mostly the beam fragmentation region and extends to the central

region for the ^{16}O -nucleus collisions considered, and the central interval ($0.9 < \eta_{lab} < 2.9$) covering mainly the central region and part of the target fragmentation region. The central coverage overlaps fully with the E_T trigger acceptance, whereas the forward coverage is precisely the region in which we identify an interaction via a minimal requirement on charged multiplicity ($N^{ch} \geq 10$). We stress that we observed no difference between a sample of events selected either by the E_T or by the interaction trigger. In other words, as long as we go far enough above the E_T thresholds (on-line or off-line), the triggering on E_T does not appear to introduce a specific bias in the event selection. Accordingly, the events used for building the differential cross-sections $d\sigma/dN^{ch}$ are those for which N^{ch} is high enough so that there is no significant ($< 0.01\%$) truncation, by a nearby E_T threshold, of the E_T physical fluctuations corresponding to that given N^{ch} . Such a selection was feasible since E_T and N^{ch} are strongly correlated quantities. The general characteristics of the $d\sigma/dN^{ch}$ distributions are similar to the ones observed for the $d\sigma/dE_T$ distributions. They reflect again the geometry of the nuclear collisions which engender a plateau extending to a shoulder that is followed by a rather steep fall. The shoulder region is at the point where the colliding nuclei fully overlap, and beyond that point it gets harder to increase the particle production by increasing the number of inelastic collisions and/or by increasing the number of participating nucleons. The A^* dependence of the N^{ch} scale in the region $0.9 < \eta_{lab} < 2.9$ is compatible with the one observed for E_T in the same pseudorapidity region (i.e. $\alpha \geq 1/3$). In the forward region $2.9 < \eta_{lab} < 4.9$, this dependence is strikingly weaker, thus confirming the observation [129] that in the region dominated by the projectile influence, the net particle yield becomes essentially independent of the target mass. The exact mechanisms leading to this relative depletion in the beam fragmentation region cannot be fully disentangled without a detailed particle identification with its associated Lorentz-invariant rapidity units, and we can only speculate on their possible nature. It is known that similar relative depletion for the production of fast forward secondaries is observed in p-A collisions (see section 2.3 on page 26). Moreover, the A-dependence of the multiplicity rapidity density distributions in nuclear collisions (discussed above in section 5.2.3 on page 124) has characteristics very much alike the ones of p-A collisions (see for instance Figure 11 on page 29). Consequently, it is plausible to assume that the mechanisms leading to the forward depletion in hadron-nucleus and nucleus-nucleus collisions are of a common nature. As the incident baryons are progressively slowed down by the multiple scattering processes while travelling through the target nuclei, the particle production is increasingly shifted backward, towards smaller pseudorapidities. In that sense, the observed most forward fast secondaries would be preferably created by early inelastic collisions, i.e. when the incident nucleons encounter the first "rows" of target nucleons. These fast secondaries have a formation time (see section 2.4 on page 29) which is strongly dilated in the target rest frame. Most of them are formed well after having escaped the target nuclear volume, largely uninfluenced if increasing the length of traversed nuclear matter via a change of the target nucleus mass. Under those conditions, all impact parameters for which the colliding nuclei fully overlap would correspond to essentially equivalent nuclear collisions when looking at fast secondaries through a forward rapidity window. Such an accumulation of impact parameters could explain the rise observed at the shoulder of the $d\sigma/dN^{ch}$ distributions in the region $2.9 < \eta_{lab} < 4.9$. It would also result in steeper slopes for the tails of these distributions. These

slopes are indeed seen in Figure 67 on page 130 and Figure 68 on page 131 to be much steeper than for the backward coverage. But there an additional source of fluctuations may come from the rescattering of slow secondaries. To go above these qualitative arguments would require one to consider the nuclear collisions in their full complexity, where each nucleon forming a system of valence quarks with its associated cloud of sea quarks, antiquarks and gluons, undergoes several parallel interactions with the surrounding nucleons.

5.3.2 Fractional multiplicity density in pseudorapidity

The charged multiplicity pseudorapidity distribution $dN^{ch}/d\eta$, for central O-W collisions at 200 GeV/nucleon, is overlaid in Figure 69 with the $dE_T/d\eta$ distribution measured for the same event sample. The distributions are arbitrarily renormalized to the absolute value of the integral over $0.9 < \eta_{lab} < 2.9$.



The shapes of the E_T and N^{ch} distributions are found to be very similar. The poorer pseudorapidity granularity for the E_T measurements precludes a detailed study of the rapidity dependence of the E_T per charged particles. As discussed in greater details in section 4.5 on page 102, the remaining systematic uncertainties (included in Figure 69 on page 133) on the η -localization of the multiplicity density are rather large. They range from $\sim 10\%$ at $\eta \sim 0.9$ to $\sim 4\%$ around $\eta \sim 2.9$, and rise up again to $\sim 10\%$ for $\eta > 4.5$. At small pseudorapidities, they are mainly due to the unknown remaining contribution from slow nuclear fragments, whereas at forward pseudorapidities the precision on the absolute densities is limited by the poor geometrical efficiency. The distributions of the charged multiplicity density in pseudorapidity, $dN^{ch}/d\eta$, are shown in Figure 70 on page 135 for three selected windows in E_T corresponding to the plateau, the shoulder and the tail of the $d\sigma/dE_T$ distributions for the Al, Ag and W target nuclei, at 60 GeV/nucleon (a) and 200 GeV/nucleon (b) incident ^{16}O energies.

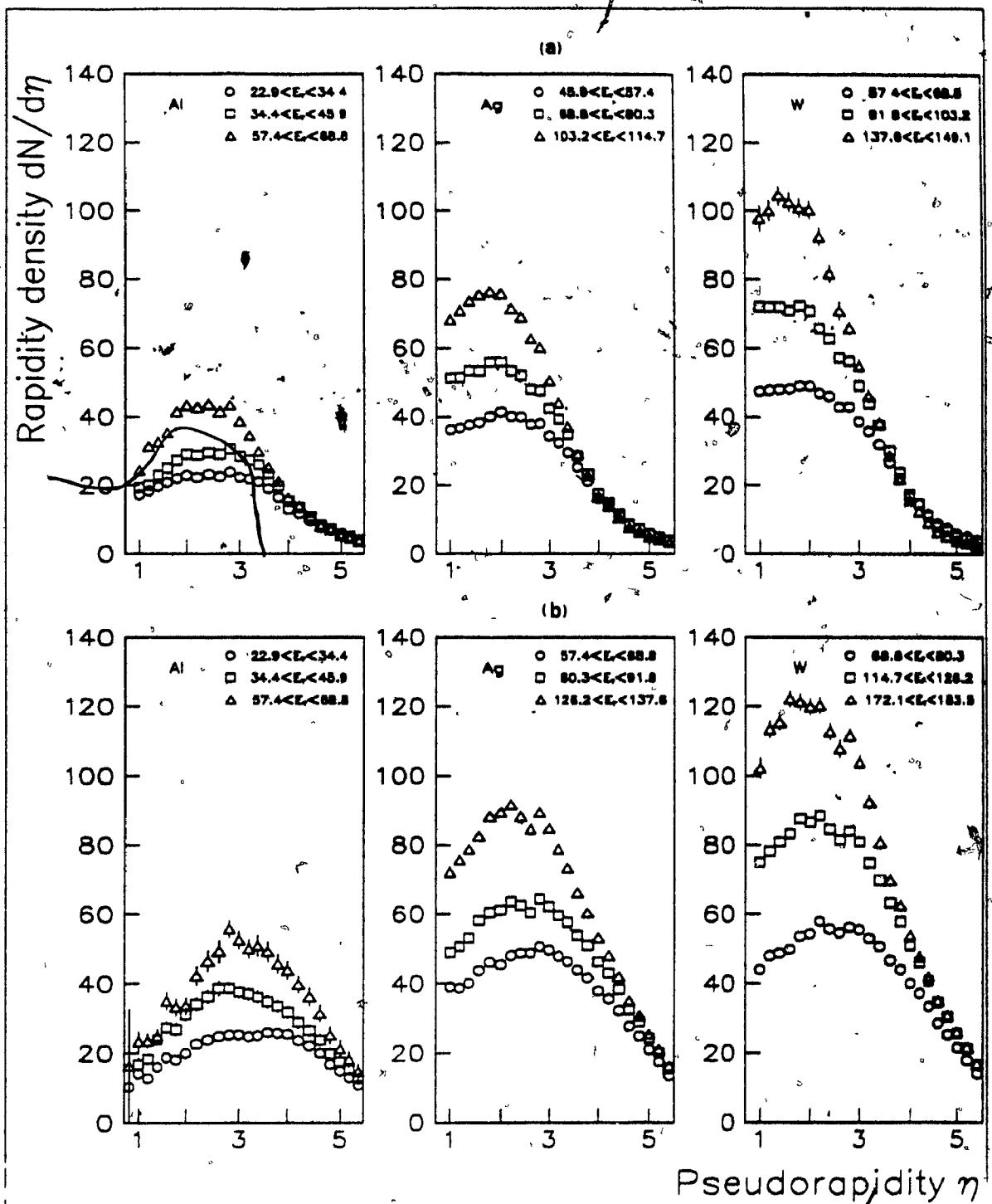


Figure 70: The charged multiplicity pseudorapidity density ($dN^{\text{ch}}/d\eta$) distributions for ^{16}O -nucleus collisions at 60 GeV/nucleon (a) and 200 GeV/nucleon (b) incident energies, and for Al, Ag and W target nuclei. The distributions are shown for three selected E_{T} intervals corresponding to the plateau, the average central collisions and the tail of the respective $d\sigma/dN^{\text{ch}}$ distributions.

The pseudorapidity granularity for the N^{ch} measurement is much finer than for the E_T measurement. Hence the global evolution in rapidity of the produced particle flow is more strikingly illustrated. First of all, at forward angles (large η) for both incident energies, it is seen in Figure 70 on page 135 that the charged particles pseudorapidity density is largely independent (within systematic errors) of both E_T and the target mass number. This was to be expected given the very weak A-dependence of the N^{ch} scale when integrating over $2.9 < \eta_{lab} < 4.9$ (see Figure 67 on page 130 and Figure 68 on page 131), and the strong correlation between the impact parameter and the transverse energy production. With increasing E_T and increasing A, the multiplicity production is significantly shifted backward, towards smaller pseudorapidities. This is reflecting the displacement, as seen from the laboratory reference frame, of the effective center-of-mass for an increasing number of participating target nucleons. The backward displacement is accompanied by a progressive narrowing of the pseudorapidity distributions. It was seen in section 5.2.4 on page 126 that the highest E_T values correspond to a significant fraction of the full-stopping limit. Hence, the narrowing of the $dN^{ch}/d\eta$ distributions could be the sign of an approach towards the "bell shape" characteristics resulting from a spherical-like "fireball" expansion in the center-of-mass frame. From the backward rapidity shift and narrowing of the pseudorapidity distributions of produced particles in the laboratory (target) rest frame, one indirectly measures the nuclear matter capacity to stop the incident baryons via complex multiple-parallel scattering processes.

In order to quantify the rapidity displacement, we have plotted in Figure 71 on page 137, as a function of transverse energy, the mean charged multiplicity pseudorapidity

$$\bar{\eta} = \left(\sum_i \Delta N_i^{ch} \cdot \Delta \eta_i \right) / \left(\sum_i \Delta N_i^{ch} \right)$$

calculated over $0.9 < \eta_{lab} < 5.5$ for the Ag and W targets at 60 and 200 GeV/nucleon. Note that the absolute values of $\bar{\eta}$ are larger than the true mean pseudorapidity because of the truncation at small η .

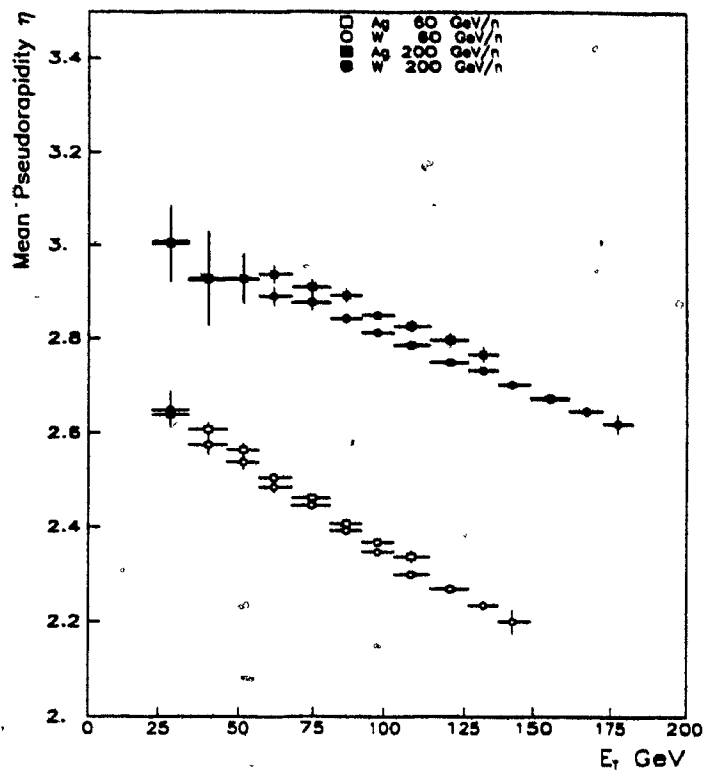


Figure 71: The mean charged particles pseudorapidity, calculated over $0.9 < \eta_{lab} < 5.5$, as a function of E_T measured in the trigger region $0.9 < \eta_{lab} < 2.9$. The lower bands are the values for the Ag (open boxes) and W (open circles) targets at 60 GeV/nucleon. The upper bands are the values for the Ag (closed boxes) and W (closed circles) targets at 200 GeV/nucleon.

For both incident energies, the $\bar{\eta}$ values are seen to be independent of the target mass when measuring at the same given E_T . The $\bar{\eta}$ values move considerably with increasing E_T . At low E_T , they correspond to the p-p center-of-mass values, i.e. $\eta_{pp}^{c.m.} \sim 3.04$ at 200 GeV/nucleon and ~ 2.74 at 60 GeV/nucleon. At the highest E_T , they approach the values obtained in a full-stopping O-W scenario (see section 5.2.4 on page 126), i.e. $\eta_{OW} \sim 2.4$ at 200 GeV/nucleon and 1.8 at 60 GeV/nucleon for $A_{eff}^{target} \sim 50$. Similar dependence is observed as a function of the target mass for minimum-bias events [129].

5.4 Comparison with Monte Carlo multichain Dual Parton models

The data are now compared to the predictions for nuclear collisions of Monte Carlo physics models which perform a non-trivial superposition of the known characteristics of soft-hadronic processes in hadron-hadron interactions. The models considered use the phenomenology of the Dual Parton Model for the colour separation mechanisms. The nucleon-nucleon interactions give rise to colour neutralizing chains that link valence or sea quarks. The rules governing the evaluation of the number and nature of such chains were discussed in detail in section 2.5 on page 32. The models are completed by the implementation of the fragmentation processes by which the chains breaking leads to hadronization into colourless observable particles. The fundamental physics motivations of such models were discussed in Chapter 2. They provide us with a better understanding of what to expect *a priori* from a "conventional" picture of ultra-relativistic nuclear collisions. We stress that there is yet no unique "conventional" description of the multiple soft-hadronic processes giving rise to the particle production in the nuclear collisions. The deviations between the predictions of the models and the observed properties of the particle flow may thus simply signal an unexpected underestimation of a subtle "standard" physical effect as well as point to more interesting new aspects of the space-time evolution of the hadronic interactions in nuclear collisions.

We shall first compare the observed characteristics of the transverse energy flow to the predictions of the IRIS event generator [105] which combines the Dual Parton Model (DPM) for non-diffractive inelastic scattering [92] [98] [99] with the Lund Fragmentation [70] [74] as implemented in the Monte Carlo code JETSET [136], adding a form of diffraction scattering in the spirit of the DPM. The DPM is based on colour exchange with a long formation time. The IRIS parameters have been adjusted to give a representation of proton-proton and PETRA e^+e^- data. The extension to proton-nucleus and nucleus-nucleus interactions involves an algorithm with no new parameter except in the description of the nucleus, using a Woods-Saxon radial density distribution but ignoring nuclear deformation. Energy and momentum are conserved.

The absolute predictions for the $d\sigma/dE_T$ distributions measured in the region $-0.1 < \eta_{lab} < 2.9$ for ^{16}O -nucleus collisions at 200 GeV/nucleon are shown for the different targets in Figure 72 on page 139.

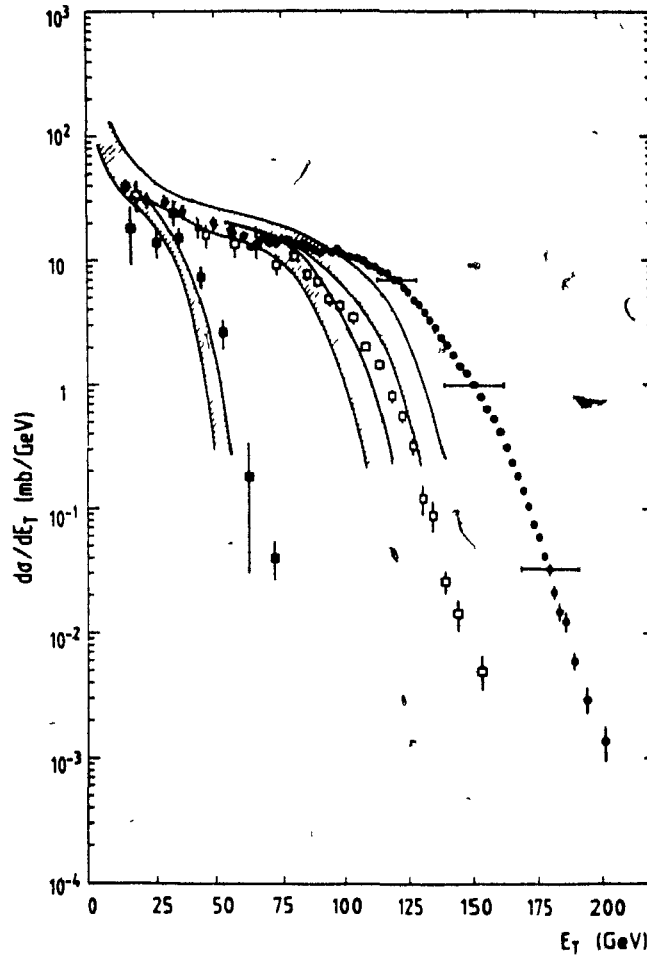


Figure 72: Comparison of the IRIS Monte Carlo predictions (shaded bands) with the $d\sigma/dE_T$ distributions measured at 200 GeV/nucleon. The comparison is made to the ^{16}O -Al (closed boxes), Ag (open boxes) and W (closed circles) data.

Although the qualitative features of the data are described correctly, the IRIS predictions underestimate the values of E_T at the fall-off for each of the target nuclei. The discrepancy appears to be significantly larger than the overall experimental systematic error on the E_T scale. Nevertheless, bearing in mind that the IRIS predictions are absolute, i.e. with no allowed tuning of free parameters, the degree of agreement could be considered satisfactory. It should be noted here that the IRIS predictions [137], as well as the predictions of the Monte Carlo Multi-Chain Fragmentation Model developed by Ranft [138] which is also based on the Dual Parton Model colour separation mechanisms, were found to be in reasonable agreement with the $d\sigma/dE_T$ distribution measured by the NA35 Collaboration in the somewhat more forward η region $2.2 < \eta_{\text{lab}} < 3.8$ for ^{16}O -Pb collisions at 200 GeV/nucleon [35]. The apparent discrepancy could

be due to cascading of slow produced particles in the nucleus, an effect enhanced in the target fragmentation region and not included in IRIS. The absence of rescattering in IRIS is a consequence of the formation time which is assumed to be much larger than the time needed by the virtual fragments to escape the interaction volume.

The effect of rescattering can be studied in the framework of the Dual Parton Model. Such a study was initiated by Ranft [97], who extended his Multichain Monte Carlo Fragmentation Model (MCFM) to allow the possibility of reinteractions of low energy secondaries inside the target nucleus. The MCFM uses the Glauber multiple scattering theory and the prescriptions of Zadorozhnyi et al. [139] for sampling the number of inelastic collisions of the participating beam and target nucleons. The colour separation mechanism follows from the DPM scheme [92] [98] [99] and the multiparticle chains are given an intrinsic transverse momentum chosen from a sample distribution with a mean of ~ 0.4 GeV/c [91] [97]. The procedure for the chain fragmentation is a function of its invariant mass. All chains having masses above the mesons (or baryons for chains linking a diquark) are fragmented via the decay code BAMJET [140]. BAMJET fragments the chains linking quark - antiquark, quark - diquark and diquark - antidiquark pairs into pseudoscalar, vector mesons and baryons. The hadronic resonances are then decayed using DECAY [141]. The (eventual) secondary interactions are often very low energy (~ 1 GeV) inelastic collisions and these are treated separately using the HADRIN [142] code, which performs quasi two body reactions and subsequent resonance decay. Energy-momentum and additive quantum numbers like charge, strangeness and baryon number, are conserved in each individual event. The model was introduced in section 2.5.1.3 on page 45 to study the influence of the hadronic formation time τ_0 on the contribution of intranuclear rescattering to the particle production in nucleon-nucleus interactions. The Monte Carlo simulation of the MCFM follows the full space-time history of the secondaries. These are allowed to reinteract only after an average time τ_0 (in their own rest frame), which is Lorentz-dilated to $\gamma\tau_0$ in the target rest frame. The formation time τ_0 is kept as the sole free parameter of the model.

The predictions of the MCFM for different values of $\tau_0 \cdot c$ are compared in Figure 73 on page 141 to measured $d\sigma/dE_T$ distributions for p-Pb collisions ($0.6 < \eta_{lab} < 2.4$) [130] and for O-Ag and O-W collisions ($-0.1 < \eta_{lab} < 2.9$) at 200 GeV/nucleon incident energy.

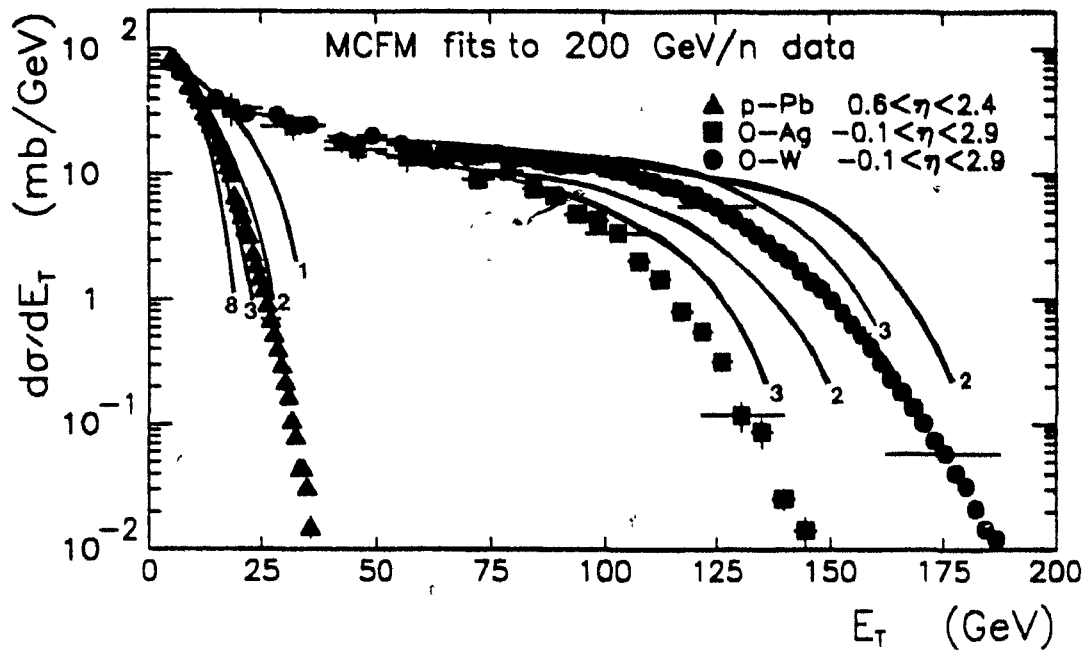
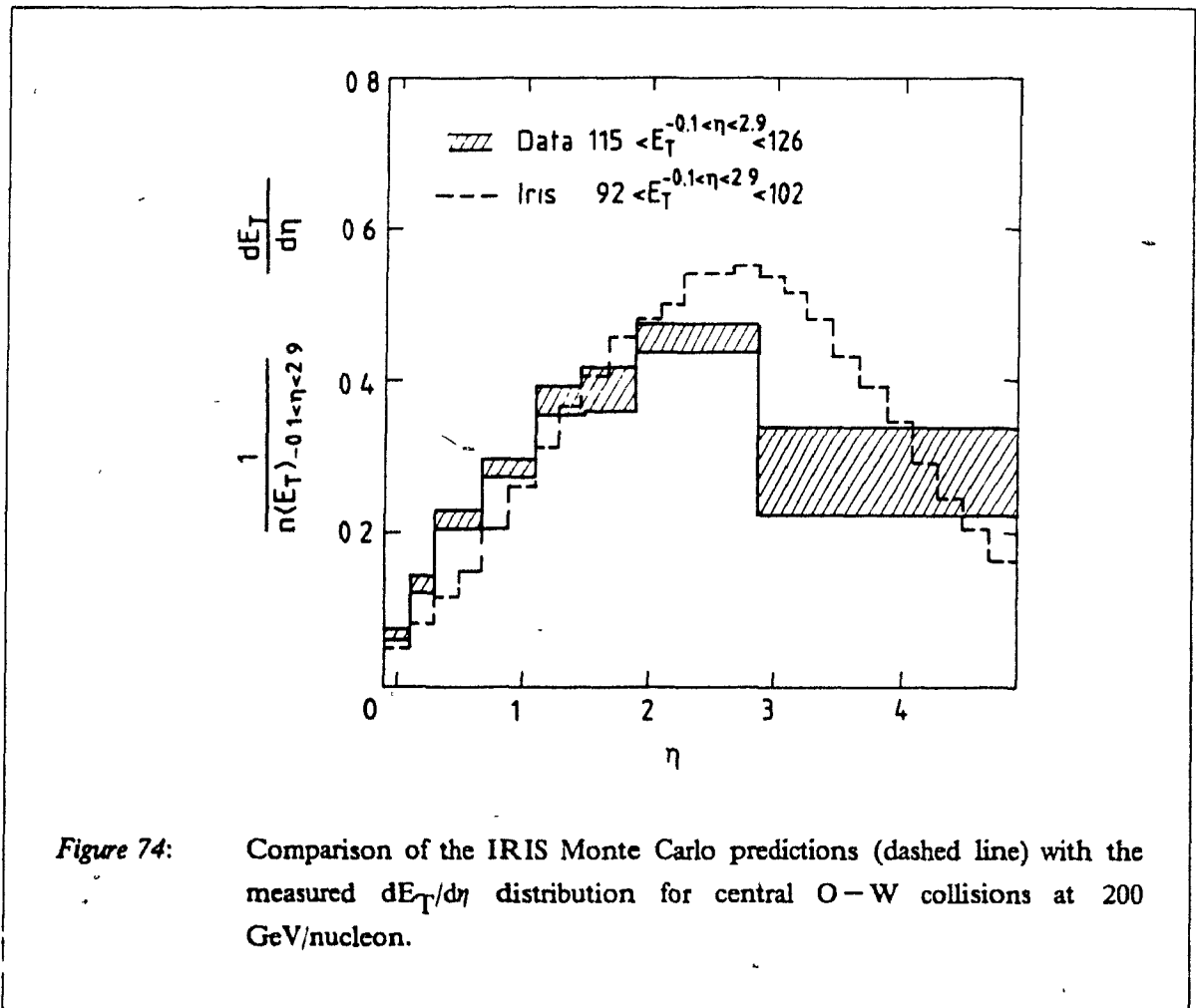


Figure 73: Effect of the inclusion of a finite formation time on the $d\sigma/dE_T$ distributions as studied in the Dual Monte Carlo Multi-Chain Fragmentation Model [97]. The Monte Carlo predictions are shown for O-Ag collisions and O-W collisions at 200 GeV/nucleon, for a formation time parameter τ fixed to $\tau_0 \cdot c = 2$ fm (dotted lines) or $\tau_0 \cdot c = 3$ fm (solid lines). Also shown are the comparison, for $\tau_0 \cdot c = 1, 2, 3$ and 8 fm, with the $d\sigma/dE_T$ distribution measured [130] in p-Pb collisions.

The intranuclear cascade corrections are seen to significantly influence the E_T production for both nucleon-nucleus and nucleus-nucleus collisions. For similar values of the formation time parameter (2-3 fm/c in the p-Pb case and ~ 3 fm/c in the ^{16}O -nucleus cases), the model is in fairly good agreement with both sets of data. The optimal values for τ_0 are slightly larger than the values (1-2 fm/c) that were needed to reproduce the rapidity density ratios (p-Xe)/(p-p) (see Figure 17 on page 44)

If rescattering of slow secondaries plays an important role in nuclear collisions, it could significantly influence the charged particles and transverse energy pseudorapidity distributions. We shall now compare those distributions with the predictions of IRIS in which cascading is neglected. Ideally, such comparison should be carried at a well defined impact parameter. In order to select

event samples corresponding to approximately equivalent geometrical conditions, we chose to scale the transverse energy requirements in proportion to the $E_T^{central}$ values²⁵. The $E_T^{central}$ values obtained from the IRIS $d\sigma/dE_T$ distributions (Figure 72 on page 139) are $\sim 15\%$ to 20% lower than the data values (Table 9 on page 128). These offsets are treated as overall geometrical offsets. Hence the IRIS events are selected at $15-20\%$ lower E_T values. The IRIS prediction for the average $dE_T/d\eta$ distribution produced in central O-W interactions at 200 GeV/nucleon is shown in Figure 74. The IRIS and the measured distributions have been divided by the mean E_T in the region $-0.1 < \eta_{lab} < 2.9$ (i.e. normalized separately to 1 over the trigger region).



²⁵ The $E_T^{central}$ is defined as the values of E_T at which the cross-section has fallen to half of the plateau's height (see 5.2.3 on page 124).

The shape of the measured distribution is reasonably reproduced. The integral of the IRIS distribution in the forward region ($\eta > 2.9$) is in reasonable agreement with the data, but there the poor resolution in η forbids any more extensive comparison. Within the trigger region, the IRIS prediction is seen to underestimate the weight of the smallest rapidity bins ($\eta \leq 1.5$).

More detailed comparisons are made with the measured $dN^{ch}/d\eta$ where we benefit from a much finer granularity in η . Such comparisons are shown in Figure 75 on page 144. The IRIS predictions were renormalized to the measured total charged multiplicity integrated over $0.9 < \eta_{lab} < 5.5$. In window (a), I show the evolution of the IRIS and measured distributions as a function of the target mass number for central collisions. IRIS describes very well the $dN^{ch}/d\eta$ distribution for the Al target nucleus. But for increasing A, IRIS increasingly overestimates the charged particle production at central pseudorapidities and underestimates it in the target fragmentation region. The same comments apply to the evolution as a function of E_T shown in window (b).

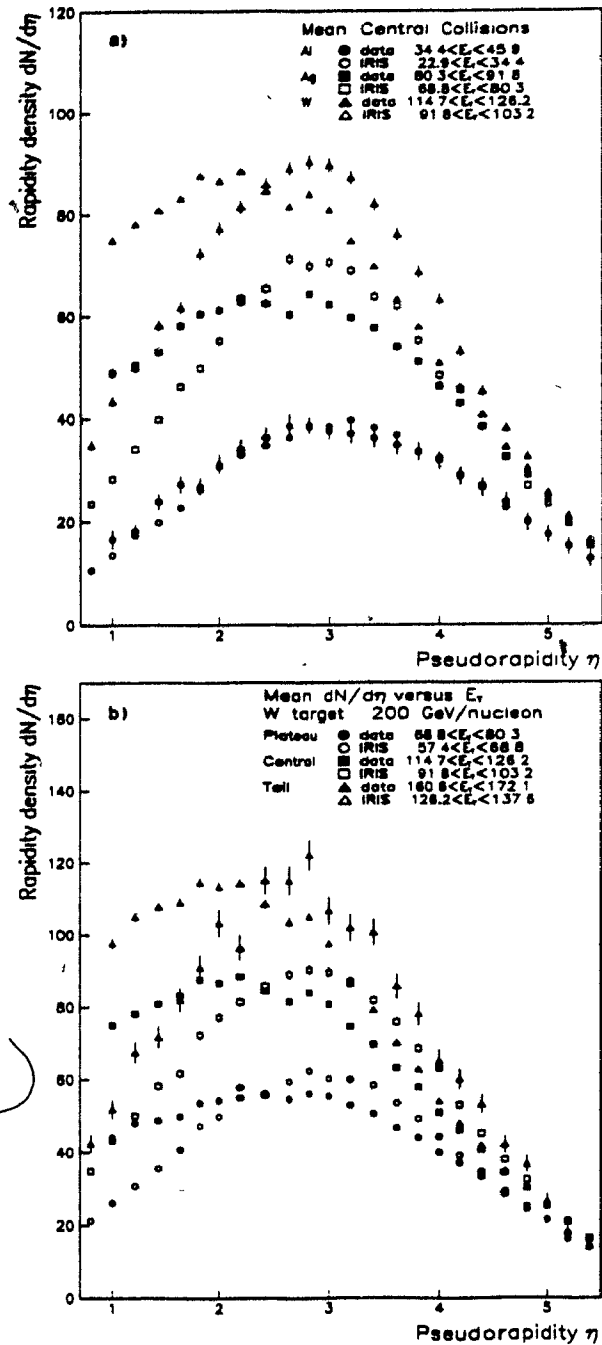


Figure 75: Comparison of the IRIS Monte Carlo predictions with the $dN/d\eta$ distributions. The distributions are shown for (a) mean central collisions in $^{16}\text{O} - \text{Al}$, Ag , and W collisions at 200 GeV/nucleon incident energy and for (b) three windows of E_T for $^{16}\text{O} - \text{W}$ collisions at 200 GeV/nucleon incident energy.

While the underestimate in the target fragmentation region may be due to the negligence of the rescattering of slow secondaries, the systematic deviations in the more central and forward regions cannot be easily explained off. They could be the signal of new phenomena. It is interesting to note that similar deviations are observed by the WA80 Collaboration [129] when comparing their charged particles pseudorapidity density distributions with the FRITIOF [143] QCD-inspired Monte Carlo fragmentation model.

The similarity between the A and the E_T dependence of the particle production was to be expected from the equivalence, for various targets, of the mean rapidity shift as a function of E_T (see section 5.2.4 on page 126). It should be added that this shift of the mean charged particles pseudorapidity is fairly well reproduced by IRIS. The mean pseudorapidity (calculated over $0.9 < \eta_{lab} < 5.5$) for IRIS O-W events moves backward by $\Delta\eta \sim 0.25$ over a 100 GeV E_T interval. That compares favorably with the measured strength of the rapidity shift (see Figure 71 on page 137). In IRIS, the DPM multiple scattering processes involve the quarks and antiquarks of the virtual cloud surrounding the leading fragments. It is the formation of these sea quark chains that is responsible for the energy degradation (stopping) of the incident nucleons. It seems that the resulting overall rapidity shift of the particle production predicted by such an approach is sufficiently strong to explain the data, without the necessity to invoke effects of a collective nature.

5.5 Estimate of energy density achieved for the 200 GeV/n data

One of the fundamental motivations for studying ultra-relativistic nuclear collisions is the possibility that such collisions allow the thermalization of large volumes of matter in which the critical conditions of temperature, energy and/or baryon densities required for quark-gluon plasma formation would be fulfilled. It was seen in section 1.4 on page 7 that under favorable circumstances, the critical conditions could be reached either in the baryon rich nuclear fragmentation regions [9] or within a hot firetube of mesonic matter in the central region [10].

Yet, little is known empirically on the fundamental questions of the degree of thermalization of the energy density and lifetime of an eventual system at equilibrium. No experiment has found clear evidence that some degree of thermal equilibrium has been attained in ultra-relativistic nuclear collisions, nor is there evidence that the created states have a fluid behaviour rather than acting as a more-or-less independent collection of freely streaming particles. The data presented above on the characteristics of the particle flow appear to show no clear sign of global collective (hydrodynamical) effects. Nevertheless, although we cannot yet speak of "thermal energy" density, it is interesting to evaluate the extent to which the energy density approached at some early time during the collision the critical conditions necessary for a deconfinement phase transition. Unfortunately, one cannot go beyond a rough estimate of the early energy density achieved. Large uncertainties occur in the definition of the interaction volume if the transverse dimensions are significantly blown up by

cascading secondaries, and the calculation of the collision kinematics is not unambiguous.

One can consider again the simple full stopping scenario (see section 5.2.4 on page 126) applied to the case of a central O-W collision at 200 GeV/nucleon. In such a scenario, the interaction volume is a cylinder through the W nucleus, with the transverse dimension of the ^{16}O nucleus, giving in the target reference frame a total volume of about 300 fm^3 containing about 50 target nucleons and 16 projectile nucleons. The collision kinematics is calculated treating the two groups of nucleons collectively. In the c.m. frame, the interaction volume is Lorentz contracted by $\gamma_{c.m.}$, leading to an effective volume of about 52 fm^3 . The kinematic limit for the total E_T production (calculated as in section 5.2.4 on page 126 but without subtracting the nucleon masses) is $\approx 446 \text{ GeV}$, corresponding to a transverse energy density of $\approx 8.75 \text{ GeV/fm}^3$. If we assume that the energy density scales linearly down to only partial stopping, the extreme tail of the W spectrum can be interpreted as corresponding to an energy density of up to $0.73 \times 8.75 = 6.4 \text{ GeV/fm}^3$. For a system of 16 projectile nucleons and 80 target nucleons, which occupy a larger volume, this value reduces to 3.1 GeV/fm^3 .

Alternatively, the prescriptions of scaling hydrodynamic models [10] [17] can be used to estimate the early energy density. Although, as discussed in section 5.2.4 on page 126, it is not clear that the symmetry conditions imposed in such models which are reminiscent of the Shuryak-Bjorken [7] [10] kinematics of ultra-high energy collisions, are more appropriate than the estimate for the case of energy deposit in a fixed frame corresponding to the observed rapidity peak. According to Bjorken's formulation (section 1.4.2 on page 11), the energy density for central nuclear collisions can be estimated for an early time τ_0 as

$$\epsilon_{Bjorken} \sim \frac{\bar{m}_T}{c\tau_0 \cdot f(A_{\min})} \frac{dN(y=0)}{dy} \text{ GeV/fm}^3$$

where $f(A_{\min})$ is the transverse dimension of the smallest of the colliding nuclei. Since pions should be the dominating particles produced in the central rapidity region, we can use the fact that for such particles

$$\frac{dE_T}{d\eta} = \bar{p}_T \frac{dN}{dy}(y=\eta) \times \left\{ 1 - O\left(\frac{m^2}{\bar{p}_T^2}\right) \right\}$$

and work with a Bjorken-like formula

$$\epsilon_0 \sim \frac{1}{c\tau_0 \cdot f(^{16}\text{O})} \left(\frac{dE_T}{d\eta} \right)_{\max} \text{ GeV/fm}^3$$

This ϵ_0 is an underestimate of $\epsilon_{Bjorken}$ since

$$m_T = p_T \{1 + (m/p_T)^2\}^{1/2} \geq p_T$$

From Figure 61 on page 118 and Figure 66 on page 127, we find that $(dE_T/d\eta)_{\max} \approx 90 \text{ GeV}$ at $\eta \sim 2.4$ in the tails of the E_T distribution for the W target. This gives an energy density of $\varepsilon_0 \approx 3.6 \text{ GeV/fm}^3$, for a transverse area of $f(^{16}\text{O}) = 25 \text{ fm}^2$ and the usual assumption on the formation time [41] $\tau_0 \approx 1 \text{ fm/c}$. Note that in Bjorken's approach, the entropy per unit rapidity is a conserved quantity because of the imposed cylindrical boost symmetry. This implies in turn that the particle production per unit rapidity does not depend on the details of the hydrodynamic evolution, but only on the energy deposited in the early stage of the collision. In more detailed calculations taking into account the work done by the fluid during expansion [20], the estimated early energy density could be as large as $2 \cdot \varepsilon_{\text{Bjorken}}$ for $\varepsilon_{\text{Bjorken}} \geq 3 \text{ GeV/fm}^3$. On the other hand, further extension of the models to take into account early transverse collective flow could significantly lower these estimates [144].

We should finally mention that the measured pseudorapidity density of transverse energy is affected by the hadronization (parents) and subsequent decay processes (children). For example, the IRIS event generator predicts that a substantial contribution to the E_T production will arise from the decay processes ($E_T^{\text{parents}} \sim 0.7 E_T^{\text{children}}$).

Despite the very large uncertainties on the estimates of the early energy density, it is probably safe to say that we are considering densities within the range required for the deconfinement phase transition (i.e. $\sim 2.5 \text{ GeV/fm}^3$ as seen in section 1.2 on page 2), and certainly much larger than the energy density inside a nucleon.

5.6 Multiplicity dependence of the transverse momentum

The variations of the mean transverse momentum as a function of multiplicity have been considered in many theoretical studies as a possible indirect probe of a deconfinement phase transition. This was originally proposed by Shuryak, Zhurov and Van Hove [7] [24] who advocated that these variations should reflect the general properties of the equation of state of the high-temperature hadronic matter. Their argument was that during the fluid-like expansion of the dense matter, because of the pressure gradient at the boundary between the vacuum and the matter in the fluid, the fluid had to work on the particles to push them into the vacuum. An increase of the pressure gradient driven by an increase of the energy density would result in a rise of the mean transverse momentum of secondary particles. The multiplicity of produced particles would be in turn closely related to the energy density (and entropy) achieved in a collision. Hence, the correlation between the transverse momentum and the multiplicity would be reflecting the pressure *versus* energy density (entropy) properties of the equation of state. Van Hove conjectured that anomalous effects would be most dramatically seen in the case of a first order phase transition. For such a transition, the transverse momentum increases with the energy density (produced multiplicity) and pressure up to the transition. During the transition, the pressure remains constant while the energy density continues to increase, resulting in a flattening of the mean p_T *vs* multiplicity curve. This flattening would thus signal the transition phase, a phase mixture of pion gas and quark-gluon plasma. It would be followed by a steep rise in the pure quark matter phase. Detailed predictions [27] were made in attempting to explain in such a framework the \bar{p}_T *versus* multiplicity measured in cosmic ray experiments for ultra-high energy nuclear collisions [25] (see section 1.4.3 on page 14).

More recent calculations showed that the change of slope would be considerably softened, in particular for mesons, as the system spends more and more time in the mixed phase while the energy density increases [28]. It could be further attenuated by longitudinal cooling [145] or even completely blurred by the hadronization process [146]. But the issue is controversial, since even a generally soft transition could be occasionally followed by violent explosion-like phenomena leading to dramatic changes of slopes in the \bar{p}_T *versus* multiplicity (energy density) correlations [147].

The measurements of the transverse energy and multiplicity flow allows us to study the variations of \bar{E}_T/N^{ch} (closely related to \bar{p}_T) as a function of E_T (closely related to the energy density). Figure 76 on page 149 shows the ratio of the mean E_T over the charged multiplicity (both measured in $0.9 < \eta_{lab} < 2.9$), as a function of E_T (measured in $-0.1 < \eta_{lab} < 2.9$). The systematic uncertainties on the \bar{E}_T/N^{ch} values are of the order of 12% (7.1% from the E_T scale and $\sim 10\%$ from the multiplicity scale).

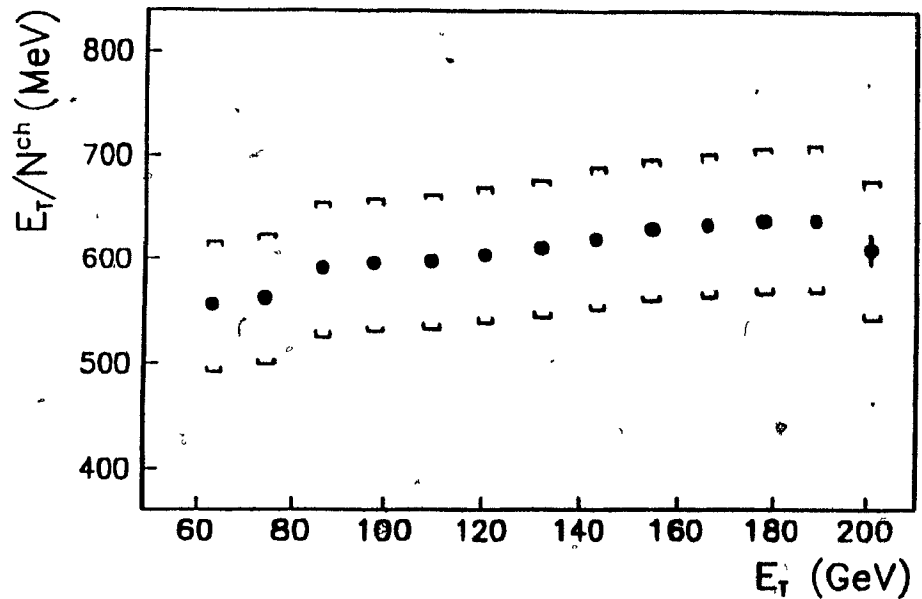


Figure 76: The average E_T per charged particles in the central pseudorapidity interval $0.9 < \eta_{lab} < 2.9$ versus E_T in the trigger acceptance $-0.1 < \eta_{lab} < 2.9$. The combined systematic uncertainty on the E_T and N^{ch} scales is indicated as horizontal square parenthesis.

Within systematic errors, we observe no apparent variation of the mean transverse energy per charged particle up to the highest E_T measured, although the energy densities reached (section 5.5 on page 145) are within the domain of critical values required for a phase transition.

Given a constant charged to neutral ratio, and since $E_T = p_T(1 + (m/p)^2)^{1/2}$ and $(m/p)^2 \ll 1$ for most charged particles (mainly pions) populating our central pseudorapidities, the \bar{E}_T/N^{ch} can be interpreted as some kind of \bar{p}_T averaged over all charged particles species. The IRIS event generator predicts that $E_T^{ch}/E_T^{all} \sim 0.59$, independent of E_T . Using this value, we find from Figure 76 a constant average effective $\bar{p}_T = 0.36 \pm .04$ GeV/c. This may be compared to the value of $\bar{p}_T \sim 0.35$ GeV/c observed at central rapidities in p-p collisions for similar nucleon-nucleon c.m. energies.

The fact that \bar{E}_T^{ch}/N^{ch} is apparently independent of E_T seems to be in opposition to the dramatic change of \bar{p}_T observed by the JACEE Collaboration [25] for comparable maximum estimated energy densities. It could be argued that a change in the particle composition, or different p_T -dependence for different particle species, could obscure a change of slope when attempting to measure it via

\bar{E}_T/N^{\pm} vs E_T . From our preliminary external spectrometer results, there appears to be no strong variation of this kind. This can be seen in Figure 77, which shows the (a) ratio of positive to negative particles versus E_T and (b) the average p_T per particle as a function of E_T for protons, π^+ and π^- , measured in the pseudorapidity region $0.9 < \eta_{lab} < 2.0$.

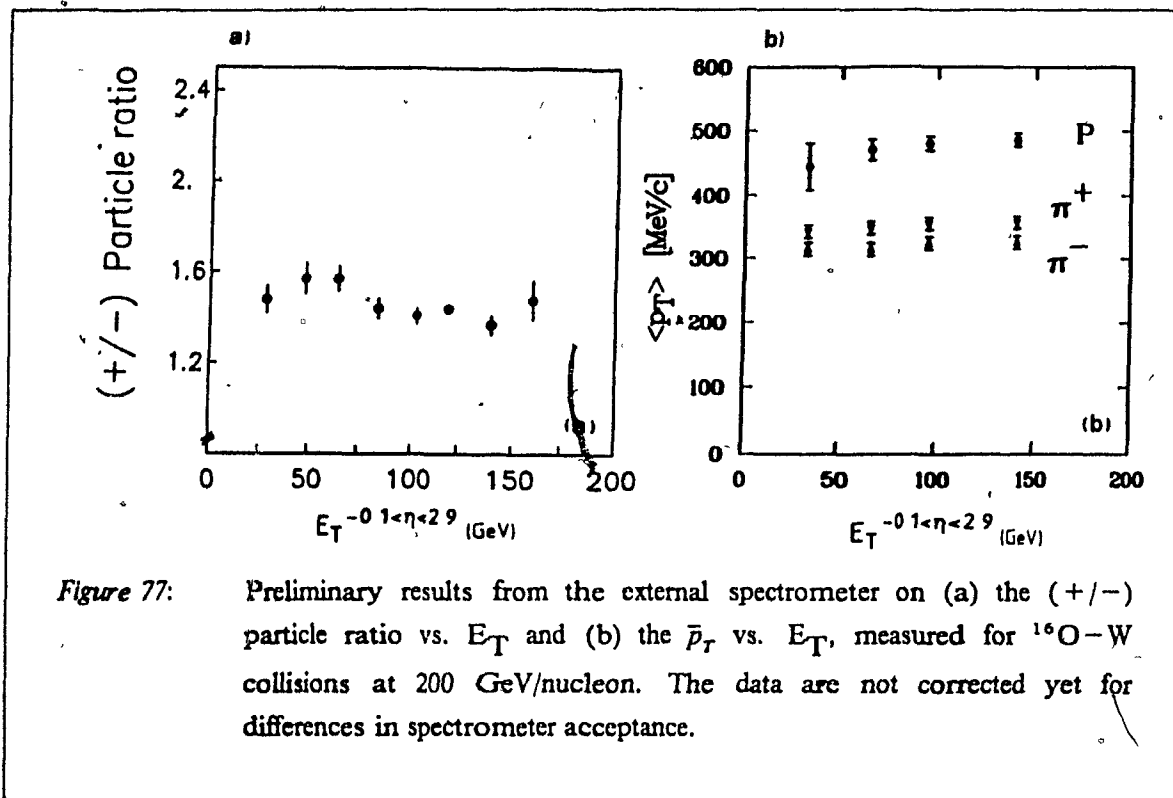


Figure 77: Preliminary results from the external spectrometer on (a) the (+/-) particle ratio vs. E_T and (b) the \bar{p}_T vs. E_T , measured for $^{16}\text{O}-\text{W}$ collisions at 200 GeV/nucleon. The data are not corrected yet for differences in spectrometer acceptance.

Furthermore, recent results from the NA35 Collaboration [148] also show significant variations of the mean transverse momentum as a function of multiplicity, for negative particles measured in $0.45 < y < 4.55$ in $^{16}\text{O}-\text{Au}$ collisions at 200 GeV/nucleon.

The absence of anomalous effects specific to nuclear collisions is strikingly exemplified in Figure 78 on page 151, showing the external spectrometer measurement of the p_T distribution for negative particles measured for central $^{16}\text{O}-\text{W}$ collisions ($E_T > 110$ GeV), divided by the distribution measured for "minimum bias" $p-\text{W}$ collisions [149].

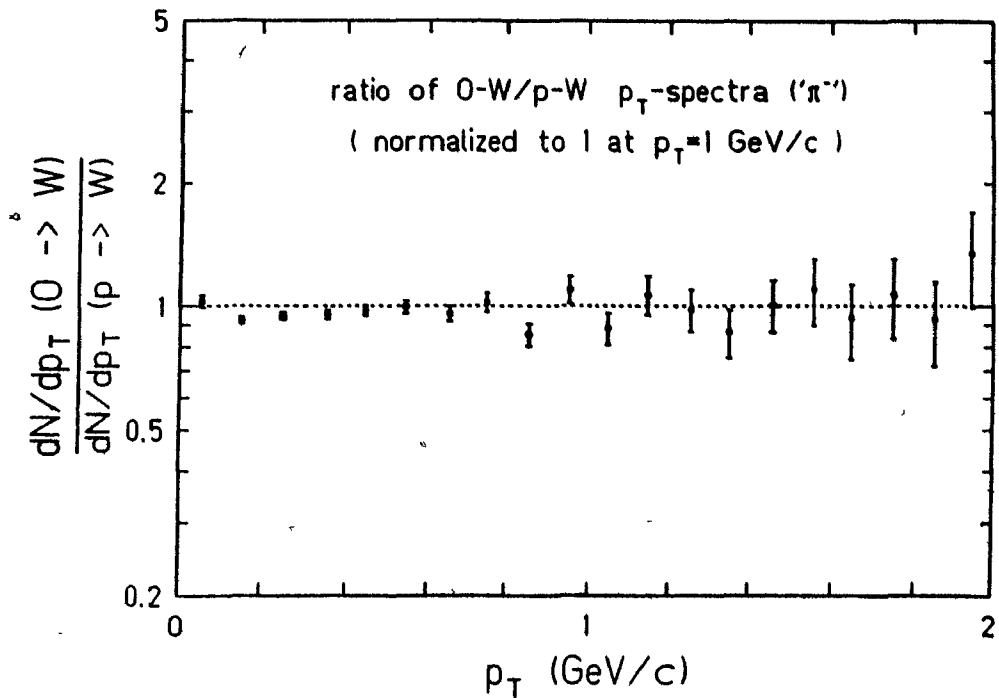


Figure 78: The p_T spectrum of negative particles for $^{16}\text{O}-\text{W}$ collisions divided by the corresponding spectrum for $p-\text{W}$ collisions. The $^{16}\text{O}-\text{W}$ spectrum is obtained for $E_T > 110$ GeV (\sim central collisions) whereas the $p-\text{W}$ spectrum is obtained, with a relatively low E_T requirement of $E_T > 10$ GeV (E_T is measured in $-0.1 < \eta_{\text{lab}} < 2.9$).

In the range of p_T values shown in Figure 78, which covers five orders of magnitude in cross-section, the spectra are found to be identical within errors. Similar results are obtained for photon spectra.

Chapter 6

Conclusion

In this thesis, I presented the measurement principles, the analysis and the results of a first generation experiment on ultra-relativistic nuclear collisions. The transverse energy and multiplicity flow produced in ^{16}O -nucleus collisions at 60 and 200 GeV/nucleon were measured using high precision calorimetry and silicon-array detectors. Complementary information on particles identification and momenta was provided, over a small solid angle, by a magnet, drift chambers, time of flight and Cherenkov counters. The nuclear collisions were used to bring extended volumes of matter to extreme conditions of temperature, baryon and energy densities, conditions under which one expects the creation of short-lived systems where hadronic matter could undergo a deconfinement phase transition towards a new state of quark-gluon plasma matter. States corresponding to a maximum energy deposition and thermalization in the interaction volume should be characterized by high multiplicity of particles carrying momentum at large angles relative to the beam direction. We attempted to select such states by requiring a maximal transverse energy production.

Careful optimization and studies of the calorimeter performances allowed a unique exploration of the transverse energy differential cross-sections, $d\sigma/dE_T$, over up to 5 orders of magnitude in the target-central fragmentation region $-0.1 < \eta_{lab} < 2.9$ for ^{16}O -Al, Ag and W collisions. The general features of the E_T distributions were shown to be largely reflecting the geometry of the nuclear collisions. Given such a strong correlation of the particle production with the impact parameter, it was shown that naive convolutions of independent nucleon-nucleon interactions could provide compact parametrizations allowing a qualitative description of the probability distributions, indicating that the particle production is built from an accumulation (not necessarily trivial) of soft hadronic interactions.

The particle production was found to have a rich structure that translated into strong rapidity-dependent variations of the rapidity density of E_T and charged multiplicity (N^{ch}) as a function of target mass number A or transverse energy. From the $d\sigma/dE_T$ and the $d\sigma/dN^{ch}$ distributions it was found that, for central collisions, the E_T production in $-0.1 < \eta_{lab} < 2.9$ and the charged multiplicity in the sub-domain $0.9 < \eta_{lab} < 2.9$ increased faster than with the target

nuclear thickness. This apparent enhancement appeared to be limited to large angles (small pseudorapidities). In the forward region $2.9 < \eta_{lab} < 4.9$, dominated by the projectile influence, the net charged particles yield was found to be largely independent of the target mass. The relative depletion of fast forward secondaries could be seen from the pseudorapidity density distributions $dN^{ch}/d\eta$ and $dE_T/d\eta$. With increasing E_T and/or increasing A , these distributions were found to be progressively shifted towards small η 's, reflecting the displacement, as seen from the laboratory reference frame, of the effective center-of-mass for an increasing number of participating target nucleons. The backward shift was accompanied by a narrowing of the pseudorapidity distributions, which could be the sign of an approach towards a spherical-like "fireball" expansion in the center-of-mass frame. The mean pseudorapidity of the particle production was shown to be similar for various targets when measured at the same E_T value. It was seen to vary from values close to the $p-p$ center-of-mass values down to values close to the ones predicted by a simple "full stopping" scenario in which particles are assumed to be emitted isotropically in the center-of-mass, and the kinematic of a collision is assumed to be the one of two objects with masses given by the total number of participating beam and target nucleons. Depending on the number of target nucleons involved, the highest transverse energies produced in the $^{16}\text{O}-\text{W}$ collisions were found to correspond to 60–70% of the "full stopping" kinematic limit at 200 GeV/nucleon and 80–100% of the limit at 60 GeV/nucleon. This indicates a higher relative stopping for the lower beam energy.

The observed characteristics of the rapidity, A and E_T dependence of the particle flow were mentioned to be in agreement with recent results from the NA35 and WA80 collaborations. Moreover, they were seen to be similar to the characteristics of the particle production in hadron-nucleus collisions, and could be qualitatively explained by invoking the concepts of nuclear stopping power and hadronic formation time. The energy-momentum of an incident baryon is progressively degraded by the multiple scattering processes while it travels through the target nucleus. The increasing shift towards smaller rapidities of the resulting particle production contributes to an apparent depletion of the net forward production. Hence, the rapidity characteristics of the particle flow indirectly measure the nuclear capacity to stop the incident baryon via complex multiple scattering processes. The proper formation time of the fast secondaries is strongly Lorentz-dilated in the target rest frame and they may leave the interaction volume largely unperturbed. The slow secondaries populating the target fragmentation region have large rescattering probabilities and can contribute to the excess target dependence.

I advocated that in order to be able to identify abnormal phenomena, a model should consider the nuclear collision in its full complexity, treating nucleons as full system of valence quarks surrounded by a cloud of virtual sea quarks, antiquarks and gluons, undergoing "simultaneous" interactions with several other nucleons. This is achieved in the QCD-inspired IRIS Monte Carlo model, which uses the Dual Parton Model for the colour separation mechanism, and where the hadronization uses fragmentation codes tuned to fit hard scattering processes. In IRIS, the colour exchange interaction gives rise to the formation of strings which are formed independently and decay independently into secondaries. The model neglects final state interaction of the secondaries. The

model was found to reproduce the mean rapidity shift of the $dN^{ch}/d\eta$ distributions, indicating that the energy loss mechanisms are sufficiently strong to explain the data without the necessity to invoke effects of a collective nature. On the other hand, the model appeared to systematically overestimate the charged particles production in the central region and underestimate it in the target fragmentation region. The E_T production in the target-central region appeared to be systematically underestimated. The possible contribution of secondary rescattering to the E_T production was investigated by comparing to the predictions of the Dual Parton Monte Carlo Multichan Fragmentation Model, in which the full space-time history of secondaries is followed and provision is made to include an average formation time parameter. The rescattering of secondaries was shown to significantly influence the transverse energy production in the target-central fragmentation region.

Rough estimates of the achieved early energy density were performed for the events in the extreme tail of the E_T distribution for $^{16}\text{O}-\text{W}$ collisions at 200 GeV/nucleon. The estimates based on the simple "full-stopping" scenario or on the prescriptions of scaling hydro-dynamic models yielded comparable results. It was mentioned that large uncertainties occur in such estimations. Nevertheless, it seemed that energy densities within the critical domain for a deconfinement phase transition could have been reached in the early stage of the collisions processes. But there exists yet no experimental evidence that some degree of thermal equilibrium has been attained, nor is there any clear sign of collective behaviour.

Anomalies in the multiplicity dependence of the transverse momentum have been considered as a possible means of identifying the occurrence of a mixed phase signaling the deconfinement phase transition. For the N^{ch} and \bar{E}_T measured in the region $0.9 < \eta_{lab} < 2.9$ as a function of E_T , the mean E_T per charged particle was found to be essentially independent of E_T up to the highest E_T measured in $^{16}\text{O}-\text{W}$ collisions at 200 GeV/nucleon. Moreover, preliminary results from the external spectrometer indicated that the particle composition, as well as the mean transverse momenta of protons, π^+ and π^- , were largely independent of E_T .

The absence of strong variations of the \bar{p}_T versus particle multiplicity appeared to be in contradiction with cosmic ray measurements by the JACEE Collaboration, but was confirmed by recent results from the NA35 experiment.

References

1. Quark Matter Formation and Heavy Ion Collisions, Proceedings of the Bielefeld Workshop May 1982, M Jacob and H. Satz (Editors), [World Scientific, Singapore, 1982];
Quark Matter '83, Brookhaven, T.W Ludlam and H.E. Wegner (Editors), Nucl. Phys. A418(1984),
Quark Matter 1984, Helsinki, K Kajantie (Editor), Lecture notes in Physics 221(1984), Springer, Heidelberg;
Quark Matter '86, Asilomar, L.S. Schroeder and M Gyulassy (Editors), Nucl. Phys. A461(1987).
2. L. Van Hove, "Quark matter formation and heavy ion collisions, the theoretical situation", in proceedings of the 1982 Quark Matter conference, ref. [1].
3. F. Karsh, "Lattice QCD at finite temperature, a status report", to be published in the proceedings of the 1987 Quark Matter conference.
4. H. Satz, "Critical behaviour in finite temperature QCD", Phys. Rep. 88, 5(1982)349.
5. H. Stöcker and W Greiner, "High energy heavy ion collisions — Probing the equation of state of highly excited hadronic matter", Phys. Rep. 137, 5-6(1986)277.
6. J. Cleymans, R.V. Gavai and E. Suhonen, "Quarks and gluons at high temperatures and densities", Phys. Rep. 130, 4(1986)217.
7. E.V. Shuryak, "Quantum chromodynamics and the theory of superdense matter", Phys. Rep. 61, 2(1980)71.
8. J. Engels et al., "High temperature SU(2) gluon matter on the lattice", Phys. Lett. B101(1981)89.
9. R. Anishetty, P. Koehler and L. McLerran, "Central collisions between heavy nuclei at extremely high energies: The fragmentation region", Phys. Rev. D22, 11(1980)2793.

10. J.D. Bjorken, "Highly relativistic nucleus - nucleus collisions: The central rapidity region", *Phys. Rev. D* 27, 1(1983)140.
11. L.D. McLerran and T. Toimela, "Photon and dilepton emission from the quark-gluon plasma: Some general considerations", *Phys. Rev. D* 31, 3(1985)545;
R.C. Hwa and K. Kajantie, "Diagnosing quark matter by measuring the total entropy and the photon or dilepton emission rates", *Phys. Rev. D* 32, 5(1985)1109,
K. Kajantie et al., "Transverse-flow effects in dilepton emission", *Phys. Rev. D* 34, 3(1986)811.
K. Kajantie et al., "Dilepton emission and the QCD phase transition in ultrarelativistic nuclear collisions", *Phys. Rev. D* 34, 9(1986)2746;
C.P. Singh, "Signal for a quark-gluon plasma in the fragmentation region", *Phys. Lett. B* 188, 3(1987)369;
12. M.I. Gorenstein and O.P. Pavlenko, "Correlation between dilepton emission and hadronic multiplicity in ultrarelativistic nuclear collisions as the signal of a deconfinement phase transition", *Phys. Lett. B* 192(1987)198.
13. J. Rafelski and B. Müller, *Phys. Rev. Lett.* 48, 16(1982)1066; P. Koch, B. Müller and J. Rafelski, *Phys. Rep.* 142, 4(1986)167, C. Greiner, P. Koch and H. Stöcker, *Phys. Rev. Lett.* 58, 18(1987)1825, U. Heinz, K.S. Lee and M.J. Rhoades-Brown, *Phys. Rev. Lett.* 58, 22(1987)2292.
14. R.D. Pisarski, "Phenomenology of the chiral phase transition", *Phys. Lett. B* 110(1982)155.
15. T. Matsui and H. Satz, " J/ψ suppression by quark - gluon plasma formation", *Phys. Lett. B* 178(1986)416.
16. K. Kajantie, "Parameters and signals for quark-gluon matter formation in nucleus - nucleus collisions", in proceedings of the 1982 Quark Matter conference, ref. [1].
17. K. Kajantie and L. McLerran, *Phys. Lett. B* 119(1982)203; K. Kajantie and R. Raitio, *Phys. Lett. B* 121(1983)415, K. Kajantie, P. Raitio, and P. V. Ruuskanen, *Nucl. Phys. B* 222(1983)152.
18. A. Bialas, "Models for particle production in nucleus - nucleus collisions at high energies", in proceedings of the 1982 Quark Matter conference, [1].
19. B. Andersson et al., "Relativistic heavy ion reactions", *Phys. Scr.* 34, 6A(1986)451.

20. M. Gyulassy and T. Matsui, "Quark-gluon-plasma evolution in scaling hydrodynamics", Phys. Rev. D29, 3(1984)419.
21. G. Baym, "Thermal equilibration in ultra-relativistic heavy-ion collisions", Phys. Lett. B138(1984)18.
22. J.P. Blaizot and A.H. Mueller, "The early stage of ultra-relativistic heavy ion collisions", Saclay preprint, PhT/87-022, 1987, submitted for publication to Nucl. Phys. B.
23. T. Matsui, "Dynamical evolution of the quark-gluon plasma and phenomenology", in proceedings of the 1986 Quark Matter conference, ref. [1].
24. L. Van Hove, "Multiplicity dependence of p_T spectrum as a possible signal for a phase transition in hadronic collisions", Phys. Lett B118(1982)138; see also E.V. Shuryak and O.V Zhirov, Phys Lett B89(1980)253.
25. JACEE Collaboration, T.H Burnett et al, "High energy cosmic ray events of ultra-relativistic nucleus - nucleus collisions", Nucl. Phys. A447(1985)189c; see also V. Takahashi in proceedings of the 1986 Quark Matter conference, ref. [1].
26. UA1 Collaboration, G. Arnison et al., "Transverse momentum spectra for charged particles at the CERN proton - antiproton collider", Phys. Lett B118(1982)167.
27. J. Kapusta et al., "Correlation between transverse momentum and multiplicity for spherically exploding quark - gluon plasmas", Phys. Lett. B163(1985)253
28. M. Kataja et al., Phys. Rev. D34, 9(1986)2755; H. Von Gersdorff, in proceedings of the 1986 Quark Matter conference, ref. [1].
29. K. Kajantie and L. McLerran, "Energy densities, initial conditions and hydrodynamic equations for ultra-relativistic nucleus - nucleus collisions", Nucl. Phys. B214(1983)261.
30. M. Gyulassy et al., "Deflagrations and detonations as a mechanism of hadron bubble growth in supercooled quark-gluon plasmas", Nucl. Phys. B237(1984)477.
31. L. Van Hove, "Hadronization model for quark - gluon plasma in ultra-relativistic collisions", Z. Phys. C27(1985)135.
32. H. Ehtamo, J. Lindfors and L. McLerran, "Can the fluctuations in head-on ultra-relativistic nuclear collisions be large?", Z. Phys. C18(1983)341.

33. G. Baym, P. Braun-Munzinger and V. Ruuskanen, "Transverse energy production in proton - nucleus and nucleus - nucleus collisions", Phys. Lett. B190(1987)29.
34. A.D. Jackson and H. Boggild, "A model of transverse energy production in high energy nucleus - nucleus collisions", Nucl. Phys. A470(1987)669.
35. NA35 Collaboration, A. Bamberger et al., "Multiplicity and transverse energy flux in $^{16}\text{O} + \text{Pb}$ at 200 GeV per nucleon", Phys. Lett. B184(1987)271.
36. H. Brody et al., "Nuclear cross sections at high transverse energy", Phys. Rev. D28, 9(1983)2334.
37. K. Gottfried, "Space-time structure of hadronic collisions and nuclear multiple production", Phys. Rev. Lett. 32, 17(1974)957.
38. A. Bialas, M. Bleszynski and W. Czyz, "Multiplicity distributions in nucleus - nucleus collisions at high energies", Nucl. Phys. B111(1976)461.
39. W. Busza, "Review of experimental data on hadron - nucleus collisions at high energies", Acta Phys. Pol. B8, 5(1977)333.
40. M. A. Faessler, "Experiments with alpha particles at the CERN intersecting storage rings", Phys. Rep. 115(1984)1.
41. D. Kisielewska, "Intranuclear cascade in high energy collisions", Acta Phys. Pol. B15, 12(1984)1111.
42. T. Ochiai, "Energy flow in ultra-relativistic nucleus - nucleus collisions and comparison between models", Z. Phys. C35(1987)209.
43. M. Fuki and H. Sumiyoshi, "Increase of the number of wounded nucleons due to energy and baryon stoppings in nucleus - nucleus collisions", Prog. Theor. Phys. 76, 4(1986)879.
44. V.V. Asinovich, Yu.M. Shabelsky and V.M. Shekhter, Nucl. Phys. B133(1978)477; A. Bialas and E. Bialas, Phys. Rev. D20, 11(1979)2854; A. Dar and F. Takagi, Phys. Rev. Lett. 44, 12(1980)768; A. Bialas and W. Czyz, Nucl. Phys. B194(1982)21.
45. A. Bialas and W. Czyz, "Constituent quark model and production of particles from nuclear targets", Acta Phys. Pol. B10, 9(1979)831.

46. A. Bialas and A. Kolawa, "Distribution of wounded nucleons and of colored strings in $\alpha - \alpha$ collisions at high energies", Z. Phys. C22(1984)231; see also *idem*, Z. Phys. C25(1984)102.
47. S. Daté, M. Gyulassy and H. Sumiyoshi, "Nuclear stopping power at high energies", Phys. Rev. D32, 3(1985)619.
48. T. Ochiai, "Large transverse energy production in high energy proton - nucleus collisions", Rikkyo Univ. preprint RUP-87-4 (1987).
49. T. Ochiai, "Transverse energy production in central rapidity region in $^{16}\text{O} - \text{Pb}$ collisions", Prog. Theor. Phys. 78, 4(1987)741.
50. N. Pisutova, P. Lichard and J. Pisut, "A simple model of large transverse-energy events in proton - nucleus interactions", Phys. Lett. B172(1986)451.
51. J. Ftáčnik et al, "On the transverse energy distributions in the central rapidity region of $^{16}\text{O} + \text{Pb}$ collisions at 200 GeV per nucleon", Phys. Lett. B188(1987)279.
52. E.O. Abdrahamanov et al, Z. Phys. C5(1980)1; T.F. Hoang, B. Cork and H.J. Crawford, Z. Phys. C29(1985)611.
53. J. Babecki and G. Nowak, Acta Phys. Pol. B9, 5(1978)401; I. Otterlund et al., Nucl. Phys. B142(1978)445, M.A. Faessler et al., Nucl. Phys. B157(1979)1.
54. B. Brown et al, "Production of high-transverse-energy events in p - nucleus collisions at 400 GeV/c", Phys. Rev. Lett. 50, 1(1983)11.
55. W. Busza and A.S. Goldhaber, "Nuclear stopping power", Phys. Lett. B139(1984)235; see also W. Busza, in proceedings of the 1984 Quark Matter conference, ref. [1].
56. R.C. Hwa, Phys. Rev. Lett. 52, 7(1984)492; L.P. Csernai and J. I. Kapusta, Phys. Rev. D29, 11(1984)2664, *idem*, Phys. Rev. D31, 11(1985)2795; C.-Y. Wong, Phys. Rev. Lett. 52, 16(1984)1393; *idem*, Phys. Rev. D30, 5(1984)961, *idem*, Phys. Rev. D30, 5(1984)972, *idem*, Phys. Rev. D32, 1(1985)94; J. Hüfner and A. Klar, Phys. Lett. B145(1984)167; R.C. Hwa and M.S. Zahir, Phys. Rev. D31, 3(1985)499, M. Jezabek, J. Karczmarczuk and M. Rozanska, Z. Phys. C29(1985)55, M. Jezabek and M. Rozanska, Phys. Lett. B175(1986)206; J.B. Bowlin and A.S. Goldhaber, Phys. Rev. D34, 3(1986)778; S. Frankel and W. Frati, Univ. of Philadelphia preprint UPR-0319T(1986); *idem*, Univ. of Philadelphia preprint UPR-0320T(1986).

57. D.S. Barton et al., "Experimental study of the A dependence of inclusive hadron fragmentation", Phys. Rev. D27, 11(1983)2580; see also R. Bailey et al., Z. Phys. C29(1985)1.
58. C. De Marzo et al., "Multiparticle production on hydrogen, argon and xenon targets in a streamer chamber by 200-GeV/c proton and antiproton beams", Phys. Rev. D26, 5(1982)1019.
59. A. Bialas and W. Czyz, "Quark model and nucleus - nucleus collisions at high energies", talk given at the Workshop on Future Experiments with High Energy Heavy ions, Darmstadt, October 1980, unpublished.
60. V.V. Anisovich, Yu.M. Shabelsky and V.M. Shekhter, "Yields of projectile fragments in hadron - nucleus interactions and the quark structure of hadrons", Nucl. Phys. B133(1978)477
61. E.L. Feinberg, Sov. Phys. JETP 23(1966)132; O.V. Kancheli et al, JETP Lett. 18(1973)274; K. Gottfried, Phys. Rev. Lett. 32, 17(1974)957; L. Stodolsky, Max Planck Inst preprint MPI - PAE/Pth 23/75 (1975), N.N. Nikolaev, Sov. J. Part. Nucl. 12(1981)63.
62. K. Fialkowski and W. Kittel, "Parton models of low momentum transfer processes", Rep. Prog. Phys. 46(1983)1283.
63. M.A. Faessler, "Nucleus - nucleus collisions at high energies", lectures given at the Summer School on Heavy Ions, Cargèse, 2 - 15 September (1984).
64. K.P. Das and R.C. Hwa, Phys. Lett. B68(1977)459, T.A. DeGrand, Phys. Rev. D19, 5(1979)1398; R.C. Hwa and R.G. Roberts, Z. Phys. C1(1979)81; J. Kalinowski, S. Pokorski and L. Van Hove, Z. Phys. C2(1979)85; R.C. Hwa, Phys. Rev. D22, 3(1980)759; *idem*, Phys. Rev. D22, 7(1980)1593.
65. B. Andersson, G. Gustafson and C. Peterson, "The relationship between the meson, baryon, photon and quark fragmentation distributions", Phys. Lett. B69(1977)221.
66. S.J. Brodsky and J.F. Gunion, "Hadronic fragmentation as a probe of the underlying dynamics of hadron collisions", Phys. Rev. D17, 3(1978)848
67. A. Capella et al., "Jets in small- p_T hadronic collisions, universality of quark fragmentation, and rising rapidity plateaus", Phys. Lett. B81(1979)68.

68. W. Ochs, "Hadron fragmentation at high energies and quark constituents", Nucl. Phys. B118(1977)397.
69. K.P. Das and R.C. Hwa, "Quark - antiquark recombination in the fragmentation region", Phys. Lett. B68(1977)459.
70. B. Andersson, G. Gustafson and T. Sjöstrand, "A three-dimensional model for quark and gluon jets", Z. Phys. C6(1980)235.
71. B. Andersson, G. Gustafson and T. Sjöstrand, Phys. Lett. B94(1980)211; B. Andersson et al., Nucl. Phys. B178(1981)242.
72. H. Minakata, "Universal quark-jet fragmentation in soft hadronic reactions", Phys. Rev. D20, 7(1979)1656.
73. G. Cohen-Tannoudji et al., "Partons at low p_T ", Phys. Rev. D21, 9(1980)2699.
74. T. Sjöstrand, Lund preprint LU TP 80-03(1980); B. Andersson et al., Z. Phys. C9(1981)233; B. Andersson et al., Phys. Rep. 97, 2-3(1983)31.
75. B. Andersson, G. Gustafson and B. Nilsson-Almqvist, "A model for low- p_T hadronic reactions with generalizations to hadron - nucleus and nucleus - nucleus collisions", Nucl. Phys. B281(1987)289.
76. R.T. Van de Walle (editor), "Partons in soft-hadronic processes", Proceedings of the Europhysics Study Conference, Erice, Italy, World Scientific, March 1981.
77. A. Capella, U. Sukhatme and J. Trân Thanh Vân, "Soft multihadron production from partonic structure and fragmentation functions", Z. Phys. C3(1980)329.
78. G. 't Hooft, "A planar diagram theory for strong interactions", Nucl. Phys. B72(1974)461.
79. H.-M. Chan et al., Nucl. Phys. B86(1975)479, *idem*, Nucl. Phys. B92(1975)13; G.F. Chew and C. Rosenzweig, Nucl. Phys. B104(1976)290; *idem*, Phys. Rep. C41, 5(1978)263.
80. G. Veneziano, Nucl. Phys. B74(1974)365; *idem*, Nucl. Phys. B117(1976)519.
81. See A. Capella, "Dual fragmentation models of soft hadron - hadron and hadron - nucleus interactions", in ref. [76].

82. A. Capella and J. Trân Thanh Vân, "Hadron - nucleus interactions and the leading particle effect in a Dual-Parton Model", *Z. Phys.* C10(1981)249.
83. J. Ranft and S. Ritter, "Particle production and correlations in hadron - hadron collisions in the dual Monte - Carlo chain fragmentation model", *Z. Phys.* C27(1985)413
84. A. Capella, U P. Sukhatme and J. Trân Thanh Vân, "Evidence for "held-back" valence quarks from particle ratios in pp and $\bar{p}p$ collisions", *Phys. Lett.* B125(1983)330.
85. A. Capella and J. Trân Thanh Vân, "New results in the Dual Parton Model", in Proceedings of the XV International Symposium on Multiparticle Dynamics, June 1984, G. Gustafson and C. Peterson (Editors), [World Scientific, Lund, 1984].
86. K. Fialkowski and A. Kotanski, *Phys. Lett.* B107(1981)132; A. Capella and J. Trân Thanh Vân, *Phys. Lett.* B114(1982)450.
87. P. Aurenche and F.W. Bopp, *Phys. Lett.* B114(1982)363; A. Capella and J. Trân Thanh Vân, *Phys. Lett.* B114(1982)450, A.B. Kaidalov and K.A. Ter-Martirosyan, *Phys. Lett.* B117(1982)247; A. Pagnamenta and S. Sukhatme, *Z. Phys.* C14(1982)79; K. Fialkowski and A. Kotanski, *Z. Phys.* C20(1983)1; P. Aurenche, F.W. Bopp and J. Ranft, *Z. Phys.* C23(1984)67; A. Capella and J. Trân Thanh Vân, *Z. Phys.* C23(1984)165; T. Kanki, *Nucl. Phys.* B243(1984)44; J. Ranft, P. Aurenche and F.W. Bopp, *Z. Phys.* C26(1984)279; A. Capella, A. Staar and J. Trân Thanh Vân, *Phys. Rev.* D32, 11(1985)2933
88. A. Capella et al., "New results in the Dual Parton Model: diffraction and KNO scaling violations", in Proceedings of the XVIIth International Symposium on Multiparticle Dynamics, June 1986, M. Markytan et al. (Editors), [World Scientific, Seewinkel, 1986].
89. A. Capella and J. Trân Thanh Vân, *Z. Phys.* C18(1983)85; P. Aurenche, F.W. Bopp and J. Ranft, *Z. Phys.* C23(1984)67; A. Capella and J. Trân Thanh Vân, *Phys. Rev.* D29, 11(1984)2512.
90. J. Ranft, "The diffractive component of particle production in the dual multistring fragmentation model", *Z. Phys.* C33(1987)517.
91. A. Capella and A. Krzywicki, *Phys. Rev.* D29, 5(1984)1007; F.W. Bopp, P. Aurenche and J. Ranft, *Phys. Rev.* D33, 7(1986)1867; A. Capella, J. Trân Thanh Vân and J. Kwecinski, *Phys. Rev. Lett.* 58, 20(1987)2015.
92. A. Capella and J. Trân Thanh Vân, "A new parton model description of soft hadron-nucleus collisions", *Phys. Lett.* B93(1980)146.

93. J. Ranft and S. Ritter, "Particle production in hadron - nucleus collisions in a multi-chain fragmentation model", Z. Phys. C20(1983)347.
94. J. Ranft and S. Ritter, "Rapidity ratios, Feynman-x distributions and forward - backward correlations in hadron - nucleus collisions in a dual Monte Carlo multi-chain fragmentation model", Z. Phys. C27(1985)569.
95. C. Halliwell et al., "Energy dependence of the pseudorapidity distributions in proton - nucleus collisions between 50 and 200 GeV/c", Phys. Rev. Lett. 39, 24(1977)1499.
96. W.Q. Chao et al., "Simple space-time description of high-energy hadron - nucleus collisions", Phys. Rev. Lett. 44, 8(1980)518.
97. J. Ranft, "Hadron production in hadron - nucleus and nucleus - nucleus collisions in the Dual Monte Carlo Multi-Chain fragmentation Model", preprint of the SSC Central Design Group, SSC - 143 (1987)
98. A. Capella, J. Kwiecinski and J. Trần Thanh Vân, "High-energy nucleus - nucleus inelastic interactions in the Dual Parton Model", Phys. Lett. B108(1982)347.
99. A. Capella, C. Pajares and A.V. Ramallo, "High energy nucleus - nucleus collisions in the Dual Parton Model", Nucl. Phys. B241(1984)75.
100. K. Kinoshita, A. Minaka and H. Sumiyoshi, "Very high energy nucleus - nucleus collisions and multi-chain model", Z. Phys. C8(1981)205.
101. A. Capella et al., "Multiplicity distributions in nuclear collisions", Phys. Rev. D35, 9(1987)2921.
102. A. Capella et al., "Multiplicity, E_T and minijets distributions in the Dual Parton Model", talk given by C. Pajares (1987).
103. A. Capella and J. Trần Thanh Vân, "Nuclear collisions in the Dual Parton Model", in proceedings of the 1986 Quark Matter conference, ref. [1].
104. W. Bell et al., Phys. Lett. B128(1983)349; *idem*, Z. Phys. C27(1985)191.
105. J.P. Pansart, IRIS (version 200), "A Monte Carlo for nucleon - nucleus and nucleus - nucleus collisions at very high energies", DPhPE 86-06, Saclay (1986); also in Quark Matter 1986, Nucl. Phys. A461(1987)521c.

106. R.H. Beuttenmuller et al., "Performance of a novel silicon detector", Nucl. Inst. Meth. A252(1986)471.
R.H. Beuttenmuller et al., "Silicon position sensitive detectors for the HELIOS (NA34) experiment", Nucl. Inst. Meth. A253(1987)500.
107. P. Giubellino et al., "Performance of the Silicon Ring Counters for the HELIOS Experiment at CERN", to be submitted to Nucl. Inst. Meth.
108. J.F. Janji, At. Data. Nucl. Data Tables 27(1982)147.
109. C.W. Fabjan, "Calorimetry in high-energy physics", CERN preprint EP/85-54(1985), published in "Techniques and concepts of high-energy physics III", T. Ferbel (Editor), New York, Plenum Press, 1985.
110. K. Pinkau, "Errors in electromagnetic cascade measurements due to the transition effect", Phys. Rev B139, 6(1965)1548
111. U. Amaldi, "Fluctuations in calorimetry measurements", CERN preprint EP/80-212.
112. R.L. Ford and W.R. Nelson, "The EGS code system: Computer programs for the Monte Carlo simulation of electromagnetic cascade showers", SLAC report, no. 210 (1978); see also W.R. Nelson, H. Hirayama and D.W.O. Royers, SLAC report no. 165 (1985).
113. R. Wigmans, "On the energy resolution of uranium and other hadron calorimeters", Nucl. Inst. Meth. A259(1987)389.
114. C.W. Fabjan, "Calorimeters: gaseous readouts and alternatives", CERN preprint EP/86-45 (1986).
115. T. Akesson et al., "Properties of a fine-sampling uranium-copper scintillator hadron calorimeter", Nucl. Inst. Meth. A241(1985)17.
116. C. Leroy, Y. Sirois and R. Wigmans, "An experimental study of the contribution of nuclear fission to the signal of uranium hadron calorimeters", Nucl. Inst. Meth. A252(1986)4.
117. E. Bernardi et al., "Performance of a compensating lead-scintillator hadronic calorimeter", DESY preprint DESY-87-041(1987).
118. Y. Sirois and R. Wigmans, "Effects of long-term low-level exposure to radiation as observed in acrylic scintillator", Nucl. Inst. Meth. A240(1985)262.

119. H. Brueckmann and H. Kowalski, "The dependence of calorimeter responses on the gate width", ZEUS int. note 86/026(1986).
120. T. Akesson et al., "Performance of the uranium/plastic scintillator calorimeter for the HELIOS experiment at CERN", Nucl. Inst. Meth. A262(1987)243.
121. H. Brueckmann, "Hadron calorimetry (puzzle of physics)", in proceedings of the Workshop on Compensated Calorimetry, Pasadena, CALT 68 - 1305(1985).
122. H. Abramowicz et al., "The response and resolution of an iron-scintillator calorimeter for hadronic and electromagnetic showers between 10 GeV and 140 GeV", Nucl. Inst. Meth. A180(1981)429.
123. T. Ludlam, BNL report, RHIC-PH-8 OG882(1986).
124. R.K Bock, T. Hansl-Kozanecka and T.P. Shah, "Parametrization of the longitudinal development of hadronic showers in sampling calorimeters", Nucl. Inst. Meth. 186(1981)533.
125. Y. Sirois, "Transverse energy flow and multiplicity in ^{16}O -nucleus collisions at 200 GeV/N", in proceedings of the Hadronic Session of the XXIVth Rencontre de Moriond, J. Trân Thanh Vân (editor), Editions Frontières, March 15-21 (1987).
126. HELIOS Collaboration, T. Akesson et al., "The transverse energy distribution in ^{16}O -nucleus collisions at 60 and 200 GeV per nucleon", CERN preprint EP/87-176, accepted for publication in Z. Phys. C.
127. T. Ochiai, "Transverse energy production in target fragmentation region in ^{16}O -nucleus collisions", Dalhousie University preprint (1988).
128. NA35 Collaboration, A. Bamberger et al., "Study of the energy flow in ^{16}O -nucleus collisions at 60 and 200 GeV/nucleon", Darmstadt preprint GSI-88-08(1988), submitted to Z. Phys. C.
129. WA80 Collaboration, R. Albrecht et al., "Charged-particle distributions in ^{16}O induced nuclear reactions at 60 and 200 A GeV", Darmstadt preprint GSI-87-81(1987), submitted to Phys Lett. B.
130. T. Akesson et al., "The transverse energy distribution in hadron-lead collisions", CERN preprint EP/87-170, submitted to Z. Phys. C.

131. A. Capella et al., Orsay preprint LPTHE 86/10 and contribution to the of the *XVIIth* International Symposium on Multiparticle Dynamics, Austria, June 1986 [World Scientific].
132. UA5 Collaboration, K. Alpgard et al., Phys Lett. B107(1981)310, *idem*, Phys Lett. B107(1981)315.
133. A. Bujak et al., "Proton-helium elastic scattering from 45 to 400 GeV", Phys. Rev. D23, 9(1981)1895.
134. WA80 Collaboration, R. Albrecht et al., "Forward and transverse energy distributions in oxygen-induced reactions at 60 A GeV and 200 A GeV", Phys. Lett. B199(1987)297.
135. HELIOS Collaboration, T. Akesson et al., "Measurement of multiplicity distributions in oxygen-tungsten collisions at 200 GeV per nucleon", submitted to Z Phys. C. (presented by J Schukraft at the 1987 Quark Matter Conference held in Nordkirchen)
136. T. Sjöstrand, "The Lund Monte Carlo for jet fragmentation and e^+e^- physics - JETSET version 6.2", Comput. Phys. Commun. 39(1986)347; see also revised version 6.3 by T Sjöstrand and M. Bengtsson, Comput. Phys Commun. 43(1987)367.
137. G.W. London, N.A. McCubbin and R. Stock, "Perspectives for ultra-relativistic nucleus-nucleus physics at CERN in the 1990's", CERN preprint SPSC 87-52(1987).
138. J. Ranft, "Transverse energy distributions in nucleus-nucleus collisions in the dual Monte Carlo Multi-Chain fragmentation Model", Phys. Lett. B188(1987)379.
139. A.M. Zadorozhny, V.V. Uzhinskii and S.Yu. Shmakov, "Interaction of constituent quarks in nucleus-nucleus collisions", JINR Dubna preprint P2-86-361(1986), unpublished.
140. S. Ritter and J. Ranft, Acta Phys Pol. B11, 4(1980)259; S. Ritter, Z. Phys C16(1982)27, S. Ritter, Comput. Phys Commun 31(1984)393.
141. K. Hänßgen and S. Ritter, "The Monte Carlo code decay to simulate the decay of baryon and meson resonances", Comput. Phys. Commun. 31(1984)411.
142. K. Hänßgen and J. Ranft, Nucl Sci. Eng. 88(1984)537.
143. B. Nilsson-Almqvist and E. Stenlund, Comput. Phys. Commun. 43(1987)387.
144. L. Van Hove, "Prospects for production and detection of a quark-gluon plasma", in proceedings of the 1986 Quark Matter conference, ref. [1].

145. J.-P. Blaizot and J.-Y. Ollitrault, "Hydrodynamics of a quark-gluon plasma undergoing a phase transition", Nucl. Phys. A458(1986)745.
146. X.-N. Wang and R.C. Hwa, "Transverse momentum in high-energy nuclear collisions: Collective expansion", Phys. Rev. D35, 11(1987)3409.
147. E.V. Shuryak and O.V. Zhironov, "Is the explosion of a quark-gluon plasma found?", Phys. Lett. B171(1986)99.
148. NA35 Collaboration, A. Bamberger et al., "Negative particle production in nuclear collisions at 60 and 200 GeV/nucleon", Darmstadt preprint GSI-88-07(1988), submitted to Z. Phys. C.
149. HELIOS Collaboration, T. Akesson et al., "Spectra of negative particles and photons in collisions of p-W and ^{16}O -W at 200 GeV/n", submitted to Z. Phys. C. (presented by H.-W. Bartels at the Quark Matter 1987 Conference, Nordkirchen, West Germany, August 1987).